

University of Nottingham
UK | CHINA | MALAYSIA

MECHANICAL CHARACTERISATION OF ADHESIVE BONDS IN MEMS INERTIAL SENSORS

Peter Kendall, BEng, MSc

Submitted to The University of Nottingham for the Degree of Doctor of Philosophy

School of Mechanical, Materials and Manufacturing Engineering

October 2018

Abstract

Micro-Electro-Mechanical Systems (MEMS) inertial sensors are used to measure acceleration and rate of angular rotation based on the deformation of a small sensitive structure, and are widely used from low-cost commercial to high-performance space and defence applications. Packaging processes can induce thermo-mechanical stresses and curvature within the MEMS die, leading to stressing and deformation of the sensitive MEMS element, which change over time and temperature. These effects cause performance changes over time and temperature, including zero-g offsets and bias and scale factor changes in MEMS accelerometers and quadrature bias changes in MEMS gyroscopes. The die bond, a small adhesive bond attaching the die to the package, can induce significant stresses and deformation in the die that have potential to cause these effects.

This thesis focuses on the die curvature induced by the die bonding process, the mechanical properties of bonds, and investigates the changes in properties over temperature and time. The effects of bond design parameters are investigated to evaluate the performance of 4-dot and 9-dot bond shapes to reduce stress and reduce changes in curvature and mechanical properties over temperature and time. The behaviour of these bond shapes and the traditional square full coverage bond with thickness reductions is also investigated.

Methods to characterise the mechanical properties of bonds are developed based on vibration testing of plain bonded dies, in bounce and shear directions, and using a single degree of freedom Kelvin-Voigt model with hysteretic damping. These methods are used to characterise different bond designs over the typical operating temperature range of a MEMS inertial sensor, in terms of apparent modulus and loss factor, as well as over time caused by thermal cycling and high temperature storage. White light interferometry is used to assess the die deformation induced by bonding and changes over time. The influence of imperfection effects on the dynamic response of the die is investigated, including coupling between translational and rotational coordinates and the resulting errors induced in the characterised properties.

Finite Element models are developed to investigate the bond design parameters and their effect on bond induced curvature and translational die mode frequencies, along with their change over

temperature. The results indicate the bond design parameters that are expected to reduce die curvature and property changes over temperature, as well as beneficial bond material properties. It was found that a bond material with a reduced thermal expansion coefficient provided the most significant reduction in die curvature from varying the bond material properties, and greatly reduced the percentage change in bond properties over temperature. It is thought that minimisation of performance effects would be achieved through matching of the bond and adherends thermal expansion rates.

The 9-Dot bond was observed to induce the lowest die curvature of the bond shapes investigated and it was indicated that further discretisation would lead to further improvements. To reduce the temperature dependency of the bond properties, the bond should be designed such that it does not experience significant slenderness stiffening effects. To achieve the small thicknesses used in MEMS devices a very low shape factor is required, this can be achieved through a high perimeter to cross-sectional area ratio of the bond shape.

Improvements and future works are proposed to allow full assessment of bond design effects experimentally and using finite element modelling. It is recommended for future investigations into die bond designs, to use larger-scale bonded samples, but maintaining slenderness ratios, to reduce the effects of imperfections and noise observed in the experiments, through reduced coupling and increased vibration response and die curvature.

Acknowledgements

I would like to thank my supervisors Prof. Atanas Popov and Dr. Stewart McWilliam for their support and guidance during the project, especially through the writing up period.

Many thanks to UTC Aerospace Systems for their sponsorship of this research and providing me with this opportunity, as well as, for their input and support through the project and welcoming me to their site to gain first-hand experience and knowledge of their company and devices.

Finally, my immense appreciation and gratitude for the continuous love and support of my partner, Annie, without whom this would never have been achieved, thank you.

Contents

Abstract.....i

Acknowledgements.....iii

Nomenclature.....xiii

List of Figures.....xvi

List of Tables.....xxvii

Chapter 1: Literature Review and Introduction

1.1. MEMS Technology 1

1.2. Inertial Sensors 1

1.2.1. Gyroscopes 1

1.2.1.1. Operation of MEMS Gyroscopes 2

1.2.2. Accelerometers 5

1.2.2.1. Operation of MEMS Accelerometers 5

1.3. Development of MEMS Inertial Sensors 7

1.3.1. Packaging of MEMS 8

1.3.1.1. Role of MEMS Packaging 9

1.3.1.2. Wafer Level Packaging 10

1.3.1.3. Die-Level Packaging – Die Attach 13

1.3.1.4. Effects of Packaging on Sensor Performance 17

1.3.2. Possible Research into Packaging and Residual Stress 18

1.3.2.1. Die Attach Effects on MEMS Performance 19

1.4. Plan of Work 21

1.4.1. Aims and Objectives 22

1.4.2. Methodologies 22

1.4.3. Deliverables 23

1.4.4. Thesis Outline 24

1.4.4.1. Chapter 2: Trial Experiments 24

1.4.4.2. Chapter 3: Enhanced Loss Factor Analysis and Characterising Bond Imperfections 24

1.4.4.3. Chapter 4: Finite Element Model Development 25

1.4.4.4. Chapter 5: Bond Design Variations - FEM 25

1.4.4.5. Chapter 6: Bond Design Variations - Experimental 25

1.4.4.6. Chapter 7: Project Conclusions and Evaluation with Proposed Improvements and Future Work 26

Chapter 2: Trial Experiments

2.1. Introduction 27

2.2. Main Aims 28

2.2.1. Objectives 28

2.3. Overview of Experiments 29

2.3.1. Test Sample 29

2.3.2. Vibration Test Setup 32

2.4. Vibration Test Methods 33

2.4.1. Sine Sweep 33

2.4.2. Fast Fourier Transform (FFT) 34

2.5. Analysis Methodology 36

2.5.1. Transmissibility Function (TF) 36

2.5.2. Material Model 37

2.5.2.1. Kelvin-Voigt Viscous Damping Model 37

2.5.2.2. Kelvin-Voigt Hysteretic Damping Model 37

2.5.3. Material Property Analysis 39

2.5.3.1. Storage Modulus (Young's and Shear) 39

2.5.3.2. Hysteretic Loss Factor 40

2.6. Trial Results 42

2.6.1. Multipoint – Mode Shape Characterisation 42

2.6.1.1. Bounce Transmissibility 43

2.6.1.2. Shear Transmissibility 46

2.6.2. Mechanical Loading 49

2.6.2.1. Bounce 50

2.6.2.2. Shear 52

2.6.3. Environmental Temperature 55

2.6.3.1. Bounce 56

2.6.3.2. Shear 59

2.6.4. Response Linearity with Excitation Magnitude 61

2.6.4.1. Bounce 61

2.6.4.2. Shear 64

2.6.5. Surface Profile Measurement 65

2.7. Summary and Conclusions 68

Chapter 3: Enhanced Loss Factor Analysis and Characterising Bond Imperfections

3.1. Introduction 71

3.2. Loss Factor Analysis Using Bandwidth Methods 72

3.2.1. Half-Power Bandwidth method 72

3.2.2. Multi-Power Bandwidth method 73

3.3. Comparison of Loss Factor Analysis Methods 74

3.3.1. Inverse Maximum Transmissibility Methods and Improvements 74

3.3.1.1. Quadratic Interpolation of Natural Frequency and Maximum Transmissibility 75

3.3.2. Frequency Bandwidth Methods and Improvements 77

3.3.2.1. Linear Interpolation of Power Bandwidth Frequencies 77

3.3.2.2. Bandwidth of Squared Frequency (removal of small loss assumption) 78

3.3.3. Effect of Noisy Transmissibility Function on Loss Factor Errors 80

3.3.3.1. Noise Reduction – Transmissibility Function Smoothing 83

3.3.3.2. Excessive Noise 85

3.3.4. Other Signal Issues – Artefacts 88

3.3.4.1. Side of Peak Artefact 88

3.3.4.2. Centre of Peak Artefact 91

3.4. Imperfect Samples – Coupled Motion 93

3.4.1. Analytical Model 94

3.4.1.1. Perfect Bond Geometry 94

3.4.1.2. Sloped Bond Geometry 96

3.4.2. Finite Element Modelling 100

3.4.2.1. Perfect Bond 101

3.4.2.2. Sloped Bond 102

3.4.2.3. Die Misplacement 104

3.4.2.4. Combined sloped bond and misplaced die imperfections 106

3.4.2.5. Measured Bond Property Errors Induced by Imperfect Samples 108

3.5. Concluding Remarks on Loss Factor Calculation Methods 111

Chapter 4: Finite Element Model Development

4.1. Introduction 115

4.2. Theory 115

4.3. Model description 117

4.3.1. Overview 117

4.3.1.1. Free Expansion 117

4.3.1.2. Constrained Contraction 118

4.3.1.3. Dynamic Response 118

4.3.2. Detailed Model Description 119

4.3.2.1. Finite Element Software Implementation 119

4.3.2.2. Assembly Geometry 119

4.3.2.3. Contact Algorithm and Detection 120

4.3.2.4. Contact Parameters 124

4.3.2.5. Mesh 131

4.3.2.6. Requirements due to Bonding stress 139

4.3.2.7. Summary of Model Requirements 141

4.4. Results 143

4.4.1. Temperature Effects 143

4.4.1.1. Geometrical Effects only 143

4.4.1.2. Effect of Material Properties 146

4.4.1.3. Estimated Young's Modulus Temperature Dependency 153

4.5. Conclusions 156

4.5.1. Model Parameters 156

4.5.2. Model Outputs as a function of Temperature 157

4.5.2.1. Geometrical Effects 157

4.5.2.2. Material Properties 157

4.5.2.3. Temperature Dependent Young's Modulus 158

4.5.3. Concluding Remarks 159

Chapter 5: Bond Design Variation - FEM

5.1. Introduction 161

5.2. Design Variables 163

5.2.1. Bond Thickness 163

5.2.2. Bond Shape 165

5.2.3. Bond Material 167

5.2.4. Die Parameters 168

5.3. Model Descriptions 168

5.3.1. Overview 168

5.3.2. Detailed 169

5.3.3. Mesh Convergence for Most Slender Bond Models 170

5.4. Results 172

5.4.1. Shape and Thickness effects at room temperature 172

5.4.1.1. Comparison with Empirical Slenderness Expressions 177

5.4.2. Thickness effects as a function temperature 179

5.4.2.1. Bounce Mode 179

5.4.2.2. Shear Mode 181

5.4.2.3. Die Bow 183

5.4.3. Shape effects as a function of temperature 185

5.4.3.1. Bounce Mode 185

5.4.3.3. Shear Mode 187

5.4.3.3. Die Bow 189

5.5. Conclusions 191

5.5.1. Die Bow 192

5.5.2. Bounce Mode 193

5.5.3. Shear Mode 194

Chapter 6: Bond Design Variation - Experimental

6.1. Introduction 196

6.1.1. Objectives 196

6.2. Overview of Experiments 197

6.2.1. Testing Types and Description 198

6.2.1.1. Vibration 198

6.2.1.2. Surface Profile – Die Curvature 200

6.2.2. Test Samples 202

6.2.3. Test Procedure 203

6.3. Mechanical Characterisation of Bond Properties 204

6.3.1. Apparent Storage Modulus 205

6.3.2. Hysteretic Loss Factor 205

6.4. Results and Discussions 206

6.4.1. Initial Sample Characterisation and Mechanical Property Trends 206

6.4.1.1. Sample and Mode Shape Characterisation (multipoint) 206

6.4.1.2. Linearity with Excitation Amplitude 215

6.4.1.3. Environmental Temperature 218

6.4.2. Sample Changes over Time, Temperature cycling and High Temperature Storage 223

6.4.2.1. Linearity Trends with Excitation Amplitude 223

6.4.2.2. Environmental Temperature Trends 227

6.4.2.3. Die Surface Profile Change 230

6.5. Conclusions 234

6.5.1. Characterising Bond Imperfections 234

6.5.2. Linearity 234

6.5.3. Temperature 235

6.5.4. Property changes over time 235

6.5.5. Surface Profiles and change over time 236

6.5.6. FE model validation 237

Chapter 7: Project Conclusions and Evaluation

7.1. Introduction 238

7.1.1. Aims 238

7.1.2. Methodologies 238

7.2. Project Work, Outcomes and Evaluation 240

7.2.1. Finite Element Modelling 240

7.2.1.1. Development 240

7.2.1.2. Environmental Temperature 241

7.2.1.3. Material Properties 241

7.2.1.4. Bond Geometry 242

7.2.2. Vibration Experiments and Analysis 245

7.2.2.1. Property Analysis 245

7.2.2.2. Design Variations and Full Test Regime 246

7.2.3. Die Curvature Measurements 248

7.2.4. Comparisons between FE model and Experimental 249

7.3. Bond Design for Improved Performance 250

7.4. Improvements and Future Works 251

7.4.1. Finite Element Modelling 251

7.4.2. Experimental 253

References 256

Nomenclature

α_1	Imperfect bond incline angle about shear axis 1
α_2	Imperfect bond incline angle about shear axis 2
β	Imperfect bond incline direction
Υ	Shear strain
ε	Compressive strain
η	Hysteretic loss factor
θ_x	Twist coordinate about bounce axis
θ_1	Rocking coordinate about shear axis 1
θ_2	Rocking coordinate about shear axis 2
ν	Poisson's ratio
σ	Compressive stress
τ	Shear stress
ϕ	Imperfect bond incline angle magnitude
ω	Frequency (rad/s)
ω_1	Power-point bandwidth frequency
ω_2	Power-point bandwidth frequency
A	Bond cross-sectional area
A_{FF}	Force free bond area (perimeter surface area)
a	Constant
a_1	Bond width in shear direction 1
a_1	Bond width in shear direction 2
c	Viscous damping coefficient
c_H	Hysteretic damping coefficient
E	Bond Young's Modulus
E_a	Bond apparent Young's modulus - incompressible

E'_a	Bond apparent Young's modulus with compressibility effects
F	Resultant Force
f	Frequency (Hz)
G	Bond Shear modulus
G_a	Bond apparent shear modulus
h_G	Perpendicular distance to centre of die mass from bond surface
K	Bond bulk modulus
k	Spring stiffness
k^*	Complex stiffness
M	Resultant moment
m	Modal mass
m_{bond}	Bond mass
m_{die}	Die mass
p	Fractional power level
r	Radius of bond dot
S	Shape factor
T	Motion transmissibility magnitude
T_{max}	Motion transmissibility magnitude at natural frequency
T^*	Complex transmissibility
T^*_{max}	Complex transmissibility at natural frequency
T_g	Glass transition temperature
t	Time
t	Bond Thickness
t_0	Nominal bond thickness
w	Width of slender bond
X	Response displacement magnitude
X_0	Base displacement magnitude
X^*	Complex response displacement

X^*_0	Complex base displacement
x	Instantaneous response displacement
x_0	Instantaneous base displacement
x	Bounce coordinate
y_1	Shear coordinate 1
y_2	Shear coordinate 2
z_1	Axis 1 parallel to inclined bond surface
z_2	Axis 2 parallel to inclined bond surface

List of Figures

Figure 1 – Wafer of etched MEMS inductive gyroscope structures [5] 1

Figure 2 - Packaged MEMS Capacitive Vibratory Ring Gyroscope, with and without lid [10] 2

Figure 3 - Diagram showing the primary and secondary 2-theta modes of vibration of a ring resonator [14].....3

Figure 4 - Diagram showing example of drive, sense and tuning electrode configuration around the ring's circumference [10] 4

Figure 5 - Packaged MEMS capacitive comb structure accelerometers, a) 1-axis with part of packaged removed for testing exposing the die bond, b) 2-axis 5

Figure 6 - Piezo-resistive accelerometer design showing deformation under given loads [19].....6

Figure 7 - Diagram showing the principle of a capacitive accelerometer [21].....6

Figure 8 - Diagram showing an example of a comb geomerty used in a Capacitive MEMS accelerometer.....7

Figure 9 – a) Wafer level packaging of a silicon on glass and b) silicon on insulator, gyroscopes [38] 10

Figure 10 - Epoxy moulding compound encapsulation of a silicon on insulator gyroscope [26] 12

Figure 11 – a) Deformation of the top surface of a MEMS die after adhesive die bond, b) Profiles along x and y axes [41] 14

Figure 12 - Deformation after Die Bonding a) Die and Substrate b) Die with undeformed shape from FE [41] 15

Figure 13 - Relationship between deflection and adhesive layer thickness for a) silver glass, b) polyimide adhesives [41] 15

Figure 14 - Variation of Youngs modulus and CTE of a die attach adhesive [34] 16

Figure 15 - Deformation of MEMS die with and without a stress isolating guard ring from FEA [19] 17

Figure 16 - Variation of microbridge natural frequency (1st and 3rd modes) before and after bonding [53] 20

Figure 17 - a) Photo of bonded trial test sample, b) Creo model image showing bond geometry 30

Figure 18 - Diagram of the stencil used to manufacture the trial bond, incorporating possible bond shapes 31

Figure 19 - Test setup schematic 33

Figure 20 - Comparison of Transmissibility Functions measured using Swept Sine and FFT with chirp Test Methods.....35

Figure 21 - Representative diagram for a Single-Degree-Of-Freedom Kelvin-Voigt model with viscous damping 37

Figure 22 - Representative diagram for a Single-Degree-Of-Freedom hysteretic damping model 38

Figure 23 - Representative diagram for a Single-Degree-of-Freedom model with complex stiffness.....38

Figure 24 - Percentage error in loss factor using 1st order approximation for different system loss factors.....41

Figure 25 -Measurement points and coordinate system 43

Figure 26 - Compressive Transmissibility Function and Phase for trial specimen at various points on the die surface.....44

Figure 27 - Comparison of Compressive transmissibility function from testing and complex SDOF generated using derived parameters 46
Figure 28 – Shear Transmissibility Functions and Phase plots for trial specimens at various points on the die surface, in both shear directions (a+b – y1, c+d – y2) 47
Figure 29 - Comparison of Shear transmissibility functions from testing and hysteretic SDOF generated using measured parameters (dashed), at various measurement points and directions (a – y1, b – y2) 49
Figure 30 – Comparison of Transmissibility functions and Phase Plots before (black) and after (red) mechanical loading 50
Figure 31 – Comparison of Transmissibility Functions generated with measured properties before (black) and after (red) mechanical loading 52
Figure 32 – Comparison of Transmissibility functions and Phase Diagrams before and after mechanical loading in shear direction y1 (a+b) and y2 (c+d) 53
Figure 33 – Comparison of Transmissibility Function generated with SDOF model before (black) and after (red) mechanical loading in shear direction y1 (a) and y2 (b) 55
Figure 34 - Diagram and photographs of chamber setup 56
Figure 35 – Measured Bounce Transmissibility Functions for varying Environmental Temperature 57
Figure 36 – Measured Bounce Properties over temperture 58
Figure 37 – Bounce Transmissibility functions generated using the complex stiffness model and comparison with Test data 59
Figure 38 – Measured Shear Transmissibility Functions for varying Environmental Temperature 60
Figure 39 – Measured Bond Shear Properties over Temperature 60
Figure 40 – Shear Transmissibility Functions Generated using the Complex Stiffness model and comparison with Test data 61
Figure 41 – Comparison of Bounce Transmissibility Functions measured and generated using the complex stiffness model, a) test data only, b) comparison with generated (dashed) 62
Figure 42 – Measured Bounce Bond Properties over excitation acceleration 63
Figure 43 – Backbone-like plot showing linear bond bounce properties and their change with the onset of non-linear behaviour, Marker colour denotes increasing accelerations (blue-red) 63
Figure 44 – Comparison of Shear Transmissibility Functions measured and generated using the complex stiffness model, a) test data only, b) comparison with generated (dashed) 64
Figure 45 – Measured Shear Bond Properties over excitation acceleration 64
Figure 46 – Backbone-like plot showing linear bond shear properties and their change with the onset of non-linear behaviour, Marker colour denotes increasing accelerations (blue-red) 65

Figure 47 - Surface profile of the copper die before (left) and after (right) bonding measured using mechanical stylus Zeiss O-Inspect 66
Figure 48 - Surface profile scan of the copper die before (top) and after (bottom) bonding using white light interferometry 67
Figure 49 - Improved die design and manufacture, with reference features and greater flatness 68
Figure 50 – Illustration of the Half power bandwidth on a modal peak 72
Figure 51 - Loss Error for Inverse Transmissibility Methods, 1st order (a) and exact (b), for raw 'test' data of varying loss factor and frequency resolution 75
Figure 52 - Natural Frequency Error over frequency resolution for various loss factors, from raw 'test' data (a) and 'test' data incorporating quadratic interpolation of frequency and transmissibility (b).....76
Figure 53 - Loss Error for Inverse Transmissibility Methods, 1st order (a) and exact (b), for 'test' data with quadratic interpolation of natural frequency and maximum transmissibility, over varying loss factor and frequency resolution 76
Figure 54 - Loss Error Frequency Bandwidth Methods, half-power (a) and multi-power (b), for 'test' data with quadratic interpolation of natural frequency and maximum transmissibility, over varying loss factor and frequency resolution 77
Figure 55 - Loss Error for Frequency Bandwidth Methods, half-power (left) and multi-power (right), for 'test' data with quadratic interpolation of natural frequency and maximum transmissibility and linear interpolation of the power bandwidth frequencies, over varying loss factor and frequency resolution.....78
Figure 56 - Loss Error for Frequency Bandwidth Methods, half-power (a) and multi-power (b), for 'test' data with quadratic interpolation of natural frequency and maximum transmissibility, linear interpolation of power bandwidth frequencies, and using the squared frequency bandwidth, over varying loss factor and frequency resolution 79
Figure 57 - Noisy FRF using the frequency resolution and loss factor typically found in the experiments, a) full frequency range, b) detailed view at peak 80
Figure 58 – Average natural frequency error (a), and Average loss factor error using exact inverse (b), second order half power (c) and multipower (d) calculation methods for noisy transmissibility functions (with quadratic interpolation of natural frequency and maximum transmissibility, and linear interpolation of power bandwidth frequencies) 82
Figure 59 – Perfect (black), Noisy (red) and Smoothed (blue) Transmissbility Functions, noise applied is 1% of the maximum transmissibility magnitude, a) full frequency range, b) detailed view of peak 83
Figure 60 – Average natural frequency error (a), and Average loss factor error using exact inverse (b), second order half power (c) and multipower (d) calculation methods for smoothed noisy transmissibility functions (with quadratic interpolation of natural frequency and maximum transmissibility, and linear interpolation of power bandwidth frequencies).....84
Figure 61 – Perfect (black), Noisy (red) and Smoothed (blue) Transmissbility Functions, noise applied is 2.5% of the maximum transmissibility magnitude, a) full frequency range, b) detailed view of peak 86

Figure 62 – Average natural frequency error (a), and Average loss factor error using exact inverse (b), second order half power (c) and multipower (d) calculation methods for smoothed noisy (2.5%) transmissibility functions (with quadratic interpolation of natural frequency and maximum transmissibility, and linear interpolation of power bandwidth frequencies) 86
Figure 63 – Perfect (black), Noisy (red) and Smoothed (blue) Transmissbility Functions, noise applied is 5% of the maximum transmissibility magnitude, a) full frequency range, b) detailed view of peak 87
Figure 64 – Average natural frequency error (a), and Average loss factor error using exact inverse (b), second order half power (c) and multipower (d) calculation methods for smoothed noisy (5%) transmissibility functions (with quadratic interpolation of natural frequency and maximum transmissibility, and linear interpolation of power bandwidth frequencies) 87
Figure 65 – Transmissibility functions with artefacts likely to affect the analysis, a) side and b) central artefacts 88
Figure 66 – Fit using various loss calculation methods (a) and loss factors calculated across power range for side artefact (b) 90
Figure 67 – Fit of TFs using various loss calculation methods, a) using points above artefact, b) using points below 90
Figure 68 - Fit of TF using various loss calculation methods for a central artefact 92
Figure 69 – a) Fit of TF for various loss calculations, using manual estimate of natural frequency and maximum gain, b) loss factors calculated across power range for central artefact 93
Figure 70 – Diagram – asm and plan of bond showing dz elements 94
Figure 71 – Plan and side (perpendicular to incline direction θ) view defining bond incline 97
Figure 72 – side views of the sloped bond in y1 and yy directions, showing definition of the tilt angles α1 and α2 97
Figure 73 - Tetra mesh used for Creo Simulate FE models (shown is the perfect geometry case) 101
Figure 74 -Transmissibility functions simulated using Creo Simulate model of a perfect bond, a) bounce, b) shear y1 and c) y2 101
Figure 75 – Multipoint Transmissibility Functions for a sloped bond aligned with y2 or β=0° excited in bounce x (a), shear y1 (b) and shear y2 (c), for ~1° (row 1) and 5° (row 2) slope angles 103
Figure 76 – Multipoint Transmissibility Functions for a misaligned sloped bond (β=60°) excited in bounce x (a), shear y1 (b) and shear y2 (c), for ~1° (row 1) and 5° (row 2) slope angles 104
Figure 77 - Diagram of die offset definition 105
Figure 78 – Multipoint Transmissibility Functions for a die misplaced -0.3mm in the y2 direction excited in bounce x (a), shear y1 (b) and shear y2 (c) 105
Figure 79 – Multipoint Transmissibility Functions for a die misplaced 0.4mm in the y1 direction and -0.3mm in the y2 direction excited in bounce x (a), shear y1 (b) and shear y2 (c) 106
Figure 80 - Diagrams Defining Combined Imperfections 107

Figure 81 - Multipoint Transmissibility Functions for case 1 of a combination of sloped bond and misplaced die excited in bounce x (a), shear y1 (b) and shear y2 (c) 107
Figure 82 - Multipoint Transmissibility Functions for case 2 of a combination of sloped bond and misplaced die excited in bounce x (a), shear y1 (b) and shear y2 (c) 108
Figure 83 - Diagram of Die attachment via Die Bond, showing layers of the bonded structure 116
Figure 84 - Diagram showing typical deformations in the Die and Bond after bonding 116
Figure 85 - Deformation and misalignment in capacitive electrodes due to induced curvature after bonding 117
Figure 86 - Temperature increase stage of the modelling, showing original and expanded geometries 118
Figure 87 - Bonding and cooling stage of the modelling, showing expanded and deformed geometries, with definition of the output metric corner bow 118
Figure 88 – Translational Die modes calculated during modal stage of the modelling, left, bounce, right, shear 119
Figure 89 - ANSYS Workbench model flowcharts, left, expansion, right, contraction and modal 119
Figure 90 - Modelled geometries in Creo, left, whole, right, 1/8 model using 4 lines of symmetry 120
Figure 91 - Contacting bodies showing contact detection points, blue, nodal detection, red, gauss point detection 122
Figure 92 - Model Quality metrics Gap (a) and Penetration (b) for various contact algorithms and detection schemes, 0 – gauss point, 1 – nodal (contact), 2 – nodal (target), 3 – surface projection 122
Figure 93 – Bounce (a) and Shear (b) Mode Frequencies of the Die for various contact algorithms and detection schemes, 0 – gauss point, 1 – nodal (contact), 2 – nodal (target), 3 – surface projection 123
Figure 94 – a) Bow in Die's top surface (centre to corner height differential) using various contact algorithms and detection schemes, 0 – gauss point, 1 – nodal (contact), 2 – nodal (target), 3 – surface projection, and FE image of distribution (b) 123
Figure 95 - Model Quality metrics, Maximum Gap (a) and Penetration (b) when contact parameters are varied individually 125
Figure 96 - Die translational mode frequencies, Bounce (a) and Shear (b), when contact parameters are varied individually 126
Figure 97 - Corner bow when contact parameters are varied individually 127
Figure 98 – Variation of model quality metrics, Maximum gap (a) and penetration (b), with parameter control level, using contact algorithms Augmented Lagrange (blue) and Multipoint Constraint (red), for both 1/8 (dotted) and 1/4 (solid) models 129
Figure 99 - Variation of Die Bounce mode frequency with parameter control level, using contact algorithms Augmented Lagrange (blue) and Multipoint Constraint (red), for both 1/8 (dotted) and 1/4 (solid) models 129

Figure 100 - Variation of Die Shear mode frequency with parameter control level, using contact algorithms Augmented Lagrange (blue) and Multipoint Constraint (red), for both 1/8 (dotted) and 1/4 (solid) models, a) wide frequency range, b) detailed view of convergence trend with smaller frequency range 130
Figure 101 - Variation of Corner Bow with parameter control level, using contact algorithms Augmented Lagrange (blue) and Multipoint Constraint (red), for both 1/8 (dotted) and 1/4 (solid) models 131
Figure 102 - Various mesh regimes investigated for 1/8 and 1/4 models, a) 1/8 contact sized tetra elements, b) 1/8 part sized tetra elements, c) 1/4 contact sized tetra elements, d) 1/4 part sized tetra elements, e) 1/4 part sized quad elements 132
Figure 103 - Variation in Die bounce and shear mode frequencies for various mesh regimes and contact algorithms ...133
Figure 104 - Variation in corner bow for various mesh regimes and contact algorithms 133
Figure 105 - Bounce mode frequency convergence with element size refinement, including 1/8th (dotted) and 1/4 (solid) models, AL default (light blue), controlled AL (dark blue) and MPC (red) contact algorithms, for contact sized tetra mesh (square), part sized tetra mesh (circle) and part sized quad mesh (triangle – ¼ only), a) wide frequency range, b) fine frequency range showing detail in AL controlled and mpc results 135
Figure 106 - Shear mode frequency convergence with element size refinement, including 1/8th (dotted) and 1/4 (solid) models, AL default (light blue), controlled AL (dark blue) and MPC (red) contact algorithms, for contact sized tetra mesh (square), part sized tetra mesh (circle) and part sized quad mesh (triangle – ¼ only) 137
Figure 107 - Corner Bow convergence with element size refinement, including 1/8th (dotted) and 1/4 (solid) models, AL default (light blue), controlled AL (dark blue) and MPC (red) contact algorithms, for contact sized tetra mesh (square), part sized tetra mesh (circle) and part sized quad mesh (triangle – ¼ only).....138
Figure 108 - Modal Frequencies, a) bounce and b) shear, as the contact parameter set is varied for 1/4 geometry models using 250um elements, for the pre-stressed (solid) and unstressed (dotted) cases, using the MPC (red) and AL (blue) contact algorithms and for contact sized tetra (square), part sized tetra (circle) and part sized quad (triangle) mesh regimes 140
Figure 109 – a) Bounce and b) Shear Modal Frequencies as the mesh size is varied for 1/4 geometry models, for pre-stressed (solid) and unstressed (dotted) cases, using MPC (red) and controlled AL (blue) contact algorithms and for contact sized tetra (square), part sized tetra (circle) and part sized quad (triangle) mesh regimes.....141
Figure 110 – a) Variation in Bounce mode frequency over temperature for the pre-stressed and unstressed cases, and b) difference in the bounce mode frequencies over temperature 144
Figure 111 – a) Variation in Shear mode frequency over temperature for the pre-stressed and unstressed cases, and b) difference in the shear mode frequencies over temperature 145
Figure 112 – a) Variation in Die Bow over temperature for the pre-stressed and unstressed (at RT) cases, and b) difference in the deiffering bows over temperature 146

Figure 113 – a) Bounce Mode Frequency b) Pre-stress Effect over temperature when Young's Modulus is varied.....146
Figure 114 – a) Shear Mode Frequency and b) Pre-stress effect over temperature when Young's Modulus is varied 147
Figure 115 – a) Die Curvature and b) Pre-stress effect over temperature when Young's Modulus is varied 147
Figure 116 – a) Bounce Mode Frequency, b) Pre-stress Effect and c) normalised Bounce Frequency over temperature when Thermal Expansion Coefficient is varied 148
Figure 117 – a) Shear Mode Frequency, b) Pre-stress Effect and c) normalised Shear Frequency over temperature when Thermal Expansion Coefficient is varied 149
Figure 118 – a) Die curvature and b) Pre-stress Effect over temperature when Thermal Expansion Coefficient is varied 150
Figure 119 – a) Bounce Mode Frequency, b) Pre-stress Effect and c) normalised Bounce Frequency over temperature when Poisson's Ratio is varied 151
Figure 120 – a) Shear Mode Frequency, b) Pre-stress Effect and c) normalised Shear Frequency over temperature when Thermal Poisson's Ratio is varied 152
Figure 121 – a) Die curvature and b) Pre-stress Effect over temperature when Poisson's Ratio is varied 152
Figure 122 – a) Bounce Mode Frequency and b) Pre-stress Effect over temperature when Estimated temperature dependent Young's Modulus is used, with comparison to constant properties.....154
Figure 123 – a) Shear Mode Frequency and b) Pre-stress Effect over temperature when Estimated temperature dependent Young's Modulus is used, with comparison to constant properties 154
Figure 124 - Bow over temperature when Estimated temperature dependent Young's Modulus is used, with comparison to constant properties.....155
Figure 125 - Comparison of Die bow induced over temperature for Pre-stressed and Unstressed cases using temperature dependent Young's modulus and the comparison of Pre-stress effects between constant and temperature dependent 156
Figure 126 – Variation in Apparent Modulus and corrected Apparent Modulus over thickness for a square bon.....164
Figure 127 – Variation of Bulk Modulus with Poisson's Ratio for Silicone Adhesive.....165
Figure 128 – Variation of Apparent Moduli over thickness for differing Poisson's Ratio values 165
Figure 129 – Bond Shapes to be investigated in FE modelling study.....166
Figure 130 – Shape Factor variation over thickness for differing bond shapes 166
Figure 131 – Apparent Modulus variation over thickness for various bond shapes.....167
Figure 132 – Mesh regimes used for various bond shapes, 1mm thick bond examples shown 169
Figure 133 - Normalised Bounce Mode Frequencies for 250µm (a) and 100µm (b) thick bonds 170
Figure 134 - Normalised Shear Mode Frequencies for 250µm (a) and 100µm (b) thick bonds 171
Figure 135 - Normalised Bow values for 250µm (a) and 100µm (b) thick bonds.....172

Figure 136 - Bounce Mode Frequency trends with frequency of the various bond shapes at room temperature.....173
Figure 137 - Shear Mode Frequency trends with thickness of the various bond shapes at room temperature.....173
Figure 138 - Die Bow trends with thickness of the various bond shapes at room temperature.....174
Figure 139 - Deformation probe locations used in curvature variation, follow a circular path with 7.5mm diameter about the centre of the die at 15° intervals.....175
Figure 140 - Height Variation of die top surface (compared to die centre) 7.5mm circle around centre of die for square bond of various thicknesses.....175
Figure 141 - Height Variation of die top surface (compared to die centre) 7.5mm circle around centre of die for 4-dot bond of various thicknesses.....176
Figure 142 - Height Variation of die top surface (compared to die centre) 7.5mm circle around centre of die for 9-dot bond of various thicknesses.....176
Figure 143 - Height Variation of die top surface (compared to die centre) 7.5mm circle around centre of die for various bond shapes of typical die bond thicknesses.....177
Figure 144 - Comparison of Bounce Mode Frequencies for various bond shapes over thickness, using various Modulus values, E – Elastic modulus, Ea – Apparent modulus, E'a – Apparent modulus with compressibility correction 178
Figure 145 – Comparison between FE and theoretical Shear Mode Frequencies for various bond shapes over thickness 179
Figure 146 - Bounce mode frequency variation, a) magnitude and b) normalised, over temperature for a square bond of varying thickness 180
Figure 147 - Bounce mode frequency variation, a) magnitude and b) normalised, over temperature for a 4-dot bond of varying thickness 181
Figure 148 - Bounce mode frequency variation, a) magnitude and b) normalised, over temperature for a 9-dot bond of varying thickness 181
Figure 149 - Shear mode frequency variation, a) magnitude and b) normalised, over temperature for a square bond of varying thickness 182
Figure 150 - Shear mode frequency variation, a) magnitude and b) normalised, over temperature for a 4-dot bond of varying thickness 183
Figure 151 - Shear mode frequency variation, a) magnitude and b) normalised, over temperature for a 9-dot bond of varying thickness 183
Figure 152 – Die bow variation, a) magnitude and b) normalised, over temperature for a square bond of varying thickness 184
Figure 153 – Die bow variation, a) magnitude and b) normalised, over temperature for a 4-dot bond of varying thickness 184

Figure 154 – Die bow variation, a) magnitude and b) normalised, over temperature for a 9-dot bond of varying thickness 185
Figure 155 - Bounce mode frequency variation, a) magnitude and b) normalised, over temperature for a 1mm thick bond of varying shape 186
Figure 156 - Bounce Mode Frequency variation, a) magnitude and b) normalised, over temperature for a 0.5mm thick bond of varying shape 187
Figure 157 - Bounce mode frequency variation, a) magnitude and b) normalised, over temperature for a 0.1mm thick bond of varying shape 187
Figure 158 - Shear mode frequency variation, a) magnitude and b) normalised, over temperature for a 1mm thick bond of varying shape 188
Figure 159 - Shear mode frequency variation, a) magnitude and b) normalised, over temperature for a 0.5mm thick bond of varying shape 188
Figure 160 - Shear mode frequency variation, a) magnitude and b) normalised, over temperature for a 0.1mm thick bond of varying shape 189
Figure 161 – Die bow variation, a) magnitude and b) normalised, over temperature for a 1mm thick bond of varying shape 190
Figure 162 - Die bow variation, a) magnitude and b) normalised, over temperature for a 0.5mm thick bond of varying shape 190
Figure 163 – Die bow variation, a) magnitude and b) normalised, over temperature for a 0.1mm thick bond of varying shape 190
Figure 164 – Diagram illustrating link between E'a thickness sensitivity to Temperature dependency of bounce mode frequency.....194
Figure 165 - Figure of multipoint positions bounce and shear 199
Figure 166 - Multipoint Transmissibility Functions for sample 1 (1.3mm square) in bounce (a) and shear (b).....207
Figure 167 - Multipoint Transmissibility Functions for sample 2 (1.1mm square) in bounce (a) and shear (b).....208
Figure 168 - Multipoint Transmissibility Functions for sample 3 (0.5mm square) in bounce (a) and shear (b).....208
Figure 169 - Multipoint Transmissibility Functions for sample 4 (0.3mm square) in shear 209
Figure 170 - Multipoint Transmissibility Functions for sample 5 (0.6mm 4-dot) in bounce (a) and shear (b) 209
Figure 171 - Multipoint Transmissibility Functions for sample 6 (0.4mm 4-dot) in bounce (left) and shear (right) 210
Figure 172 - Multipoint Transmissibility Functions for sample 7 (0.2mm 9-dot) in shear 210
Figure 173 - Multipoint Transmissibility Functions for sample 8 (0.4mm 9-dot) in bounce (a) and shear (b) 211
Figure 174 - Multipoint Transmissibility Functions for sample 9 (1.1mm square, thin die) in bounce (a), shear (b).....211
Figure 175 - Multipoint Transmissibility Functions for sample 10 (0.4mm square, thin die) in shear 212

Figure 176 – Comparison of Experimental and FE Bounce mode frequencies of various bond shapes over thickness 214
Figure 177 – Comparison of Experimental and FE Shear mode frequencies of various bond shapes over thickness 215
Figure 178 – a) Absolute and b) Normalised Bounce Property changes with excitation amplitude (0.1g (blue)-17.6g (red)) 216
Figure 179 – a) Absolute and b) Normalised Shear Property changes with excitation amplitude (0.1g (blue)-17.6g (red)), A, B, C, and D illustrate differing non-linearity trends observed 217
Figure 180 - Individual Normalised shear property trends over excitation magnitude for various bond designs, a) normalised modulus, b) normalised loss factor, normalised using properties within linear range 218
Figure 181 - Backbone style graphs, showing changes in a) absolute and b) normalised (to ambient) bounce properties, modulus against loss factor when environmental temperature is varied (Shown by marker colour from blue to red (-40-120oC)) 219
Figure 182 – Normalised (to ambient) bounce property trends over environmental temperature for varying samples, markers denoting bond shapes, colour for bond thickness and dotted lines showing thinner dies, a) normalised modulus, b) normalised loss factor 220
Figure 183 - Backbone style graphs, showing changes in a) absolute and b) normalised (to ambient) shear properties, modulus against loss factor when environmental temperature is varied (Shown by marker colour from blue to red (-40-120oC)) 221
Figure 184 – Normalised (to ambient) Shear property backbone graphs, for environmental temperatures between 20-120oC 222
Figure 185 – Normalised (to ambient) shear property trends over environmental temperature for varying samples, markers denoting bond shapes, colour for bond thickness and dotted lines showing thinner dies, a) normalised modulus, b) normalised loss factor 222
Figure 186 – Linearity trends over time for sample 5 in bounce 224
Figure 187 – Linearity Trends over time in shear for samples 4 (a), 6 (b), 7 (c) and 9 (d) 225
Figure 188 – Normalised (to initial linear properties from test L1) linear bounce properties from linearity tests over time, a) modulus, b) loss factor, grey box highlights the significant stiffening after temperature storage 226
Figure 189 – Normalised (to initial linear properties from test L1) linear shear properties from linearity tests over time, a) modulus, b) loss factor, grey box highlights the significant stiffening after temperature storage 226
Figure 190 – Temperature Trends over time in bounce for samples 5 (a) and 8 (b) 227
Figure 191 - Temperature Trends over time in shear for samples 3 (a), 6 (b), 7 (c) and 10 (d) 228
Figure 192 – Normalised (to initial from test T1) ambient bounce properties from temperature tests over time, a) modulus, b) loss factor, grey box highlights the significant stiffening after temperature storage 229

Figure 193 – Normalised (to initial from test T1) ambient shear properties from temperature tests over time, a) modulus, b) loss factor, grey box highlights the significant stiffening after temperature storage 229
Figure 194 – Example of initial (unbonded) surface scan for sample 1, a) before and b) after filling of bad measurements 230
Figure 195 - 2D profile of surface measurements, illustrating noise before (left) and after (right) filling process 231
Figure 196 – Change in Die Shape after Bonding for each sample 232
Figure 197 – Change in Die Shape after High Temperature Storage for each sample 233

List of Tables

Table 1 - Measured material properties from Transmissibility Function at each point in compression 45

Table 2 - Measured material properties from Transmissibility Function at each point in both shear directions 48

Table 3 – Apparent Young's modulus values and changes before and after mechanical loading.....51

Table 4 – Compressive Hysteretic loss factor values and changes before and after mechanical loading.....51

Table 5 – Apparent shear modulus values and changes before and after mechanical loading 54

Table 6 – Shear Hysteretic loss factor values and changes before and after mechanical loading 54

Table 7 - Percentage errors in natural frequency and loss from various calculation methods, for an artefact to the side of the peak.....91

Table 8 - Percentage errors for natural frequency and loss from various calculations for a centrally located artefact 93

Table 9 – Percentage errors (compared to the FE perfect bond case) in modulus and loss, calculated using various methods, for the central measurement points in bounce and shear directions 109

Table 10 – Average of absolute errors across die surface/edge (all measurement points), for modulus and loss factor using various calculation methods.....111

Table 11 – Spread in % errors across die surface/edge (all measurement points), for modulus and loss factor using various calculation methods 111

Table 12 - Material Properties used in FE models 120

Table 13 - Table containing the various parameters varied and the values tested 125

Table 14 - Contact Parameter values for bonded contact default and those initially chosen from sensitivity analyses ..128

Table 15 - Contact Parameter values used when parameters are varied together, from default bonded to 200% of chosen 128

Table 16 - Table showing chosen model features and parameters 143

Table 17 - Estimated Temperature Dependent Young's Modulus used in FE Model.....153

Table 18 - Properties of Tested Samples 203

Table 19 - Full Test Procedure for each sample.....203

Table 20 - Coupling observations and inferred imperfection types for the tested samples, along with property error estimates.....213

Chapter 1: Literature Review and Introduction

1.1. MEMS Technology

MEMS or Micro-Electro-Mechanical Systems are small devices comprised of mechanical and electrical components; these devices have many applications, particularly as sensors. The advantages of these systems are their highly compact size, low power consumption and capability of low cost high-volume manufacture [1] [2]. With continuing improvements in their performance these micro devices are used widely from low cost commercial to high precision aerospace and defence applications [3]. Typical MEMS devices include: microphones, pressure sensors, switches, energy harvesters, thermometers, small motors and inertial sensors [4], such as gyroscopes, an example of which is shown in Figure 1. MEMS sensors operate by using an electrical sensing circuit, such as magnetic inductors, capacitive transducers, or piezoelectric materials, to detect the deformations/displacements of a mechanical system, such as a membrane or resonator structure, caused by changes in an object's motion or environmental variable. This thesis focuses on MEMS inertial sensors and these are described in detail in the following sections.

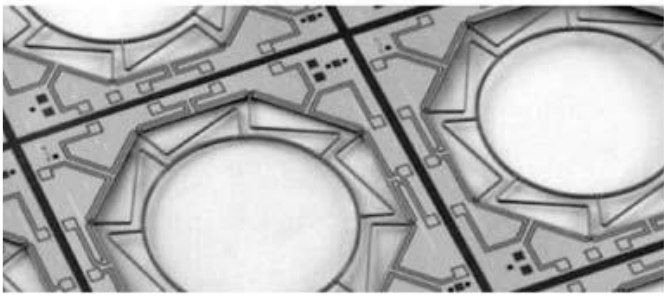


Figure 1 – Wafer of etched MEMS inductive gyroscope structures [5]

1.2. Inertial Sensors

1.2.1. Gyroscopes

Gyroscopes are commonly used sensors for measuring an angular velocity of interest in a component or system [2], such as traction and stability control systems in vehicles, consumer electronics like cameras or phones, or in aerospace guidance and control systems [1] [6] [7]. They can also be used alongside other inertial sensors such as accelerometers in standalone inertial navigational

systems (or Inertial Measurement Units, IMUs), or in conjunction with Global Positioning Systems (GPS) [6] [8]. Conventional gyroscopes such as rotating wheel or optical systems (fibre optic, laser ring) are highly precise but have high power consumption and are too large and expensive to be widely used in many applications [1] [8]. Advances in micromachining techniques have enabled the production of MEMS gyroscopes with low cost batch fabrication, significant size reductions of orders of magnitude, as well as greatly minimising power consumption and enabling integration with the required control circuitry [8] [1] [2] [9]. An example of a packaged MEMS gyroscope is shown in Figure 2. These developments have allowed the use of gyroscopes in a much larger range of applications, previously thought to be non-cost effective [1]. However, these systems are not yet capable of the same resolution as conventional gyros, and for this reason much development is focussed on improving the sensitivity of MEMS systems to inertial grade, i.e. a resolution and bias stability better than 1-10°/h [1] [6].



Figure 2 - Packaged MEMS Capacitive Vibratory Ring Gyroscope, with and without lid [10]

1.2.1.1. Operation of MEMS Gyroscopes

MEMS gyroscopes use the transfer of energy from a primary mode of vibration (drive) to a secondary mode (sense) when a rate of turn is applied about a particular (normal) axis. The transfer of energy is caused by Coriolis coupling [1] [11] [12] [13] which ensures that the resulting amplitude of the secondary mode is proportional to the rate of turn applied [6]. Different vibrating elements (resonators) have been used, including tuning forks, plates, disks, hemispheres and simple cantilever beams. The work presented here focuses on ring resonators which are an example of an axisymmetric resonator [2].

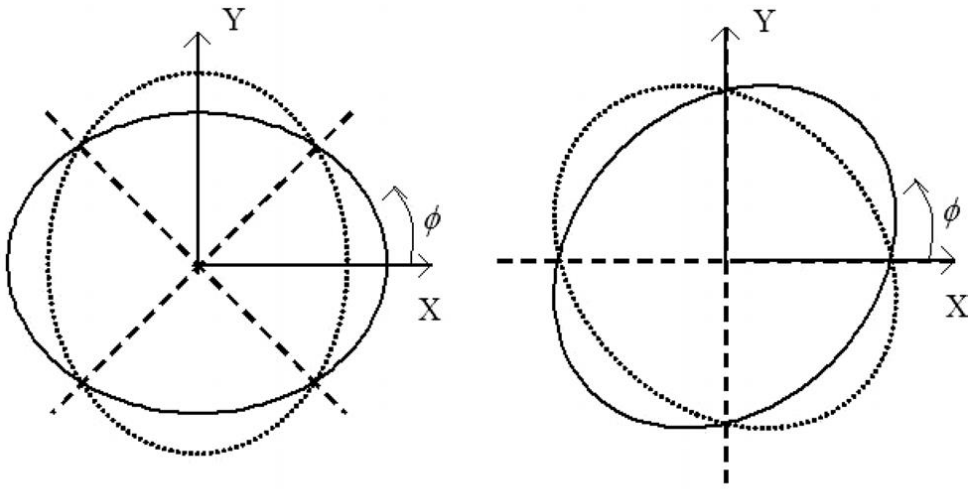


Figure 3 - Diagram showing the primary and secondary 2-theta modes of vibration of a ring resonator [14]

Axisymmetric resonators have advantages compared to other resonators because its structure is balanced so it is symmetrical about the central axis of the structure. This ensures the natural frequencies occur in degenerate pairs, such that the drive and sense modes have the same natural frequency and mode shapes which are orthogonal to each other [6] [7] [13]. It is important for the resonator to have equal natural frequencies to maximise energy transfer between the modes and maximise sensitivity to rotation [2] [15]. In ring resonator gyroscopes the in-plane 2-theta flexural modes are normally used in operation - these modes are separated by an angle of 45° and are shown in Figure 3 [6]. A significant advantage of using these flexural modes is that they are effectively uncoupled from rigid body motions, which reduces the sensitivity of the device to external spurious vibrations [6] [2] [15].

Vibratory gyroscopes operate at resonance and various drive methods are available to excite the drive mode in the resonator. These include piezoelectric, inductive (electromagnetic) and electrostatic (capacitive). For the vibrating ring gyroscopes investigated in this thesis electrostatic actuation is used based on parallel plate capacitors arranged around the circumference of the ring. In practice the ring is used as a moving plate, with fixed plate electrodes embedded in the substrate around the ring circumference; the electrodes are manufactured from the same silicon wafer and so have equal thicknesses [16]. A harmonic excitation force is generated by applying a constant bias voltage with time varying component to the drive electrodes. The amplitude of motion of the sense mode is detected capacitively by measuring the change in capacitance between the ring and sense electrodes as the ring-electrode gap changes [6] [15]. Figure 4 shows the arrangement of drive and

sense electrodes for a typical ring-based gyroscope, as well as tuning electrodes used to negate the effects of imperfection and align the drive and sense modes with the electrodes.

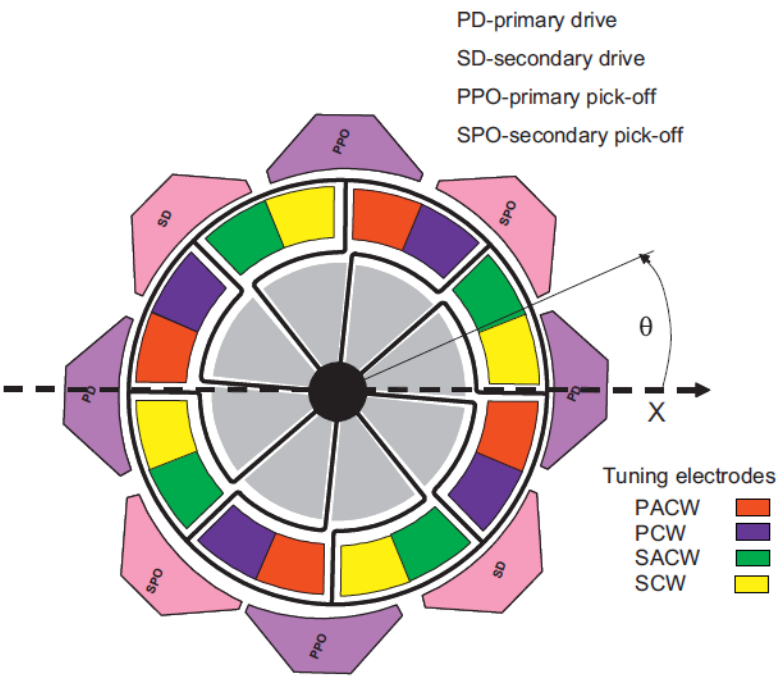
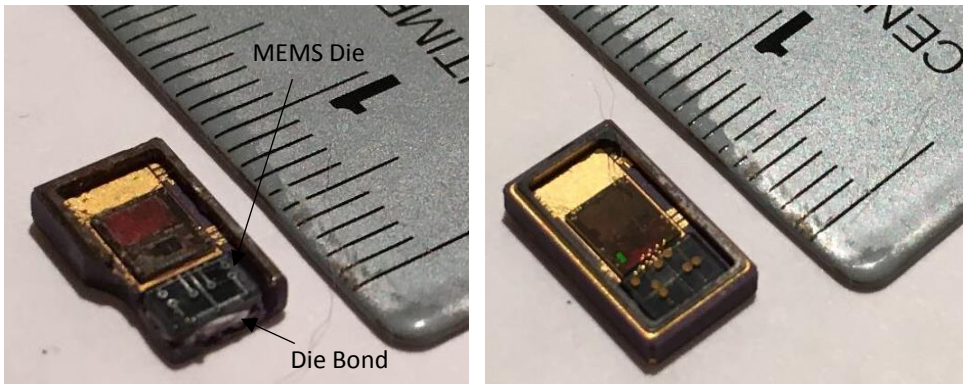


Figure 4 - Diagram showing example of drive, sense and tuning electrode configuration around the ring's circumference [10]

Manufacturing tolerances in the ring resonator, the support legs and electrodes result in small structural imperfections that compromise the cyclic symmetry (degeneracy) of the resonator. The imperfections cause the natural frequencies of the ring to be mistuned so that a frequency split appears between the two flexural modes, the sense amplitude reduces, and the device sensitivity significantly degrades, compared to a perfect ring [16]. Techniques are available to retune the ring frequencies such as laser ablation and electrostatic correction. In laser ablation material is removed from the neutral axis of the ring at particular locations to negate the effect of imperfections. A perceived disadvantage of this approach is that the trimming process is irreversible and can only be achieved before packaging occurs, and so cannot be used as part of an active control method [16]. Electrostatic correction uses tuning electrodes located around the ring circumference, as seen in Figure 4 [6], to modify the stiffness of the ring at particular locations by varying the potential differences across capacitors. The advantage of this method is that it can be achieved pre- or post-packaging and does not permanently modify the resonator [16].

1.2.2. Accelerometers

Accelerometers are used to measure linear motion, specifically the rate of change in linear velocity [17]. For the same reasons as gyroscopes, MEMS accelerometers provide high performance and low cost, with low power consumption, small size and integrated functionality [4] [18]. They are used in a variety of applications, such as navigational systems, control systems, anti-lock braking systems and airbag deployment, as well as low-cost commercial applications such as image stability in digital cameras. Figure 5 shows examples of packaged capacitive MEMS accelerometers.



a) b)

Figure 5 - Packaged MEMS capacitive comb structure accelerometers, a) 1-axis with part of packaged removed for testing exposing the die bond, b) 2-axis

1.2.2.1. Operation of MEMS Accelerometers

In general, MEMS accelerometers consist of a suspended proof-mass system [19] which experiences deflection due to its inertia resisting the motion of an applied acceleration [4] . An electrical sensing system is used to measure the induced deflection and convert the signal into an acceleration reading. A wide range of different accelerometer designs are available incorporating different proof mass configurations, simple beam and plate suspension systems, electrostatic comb drive geometries, and piezo-resistive and capacitive sensing systems. Piezo-resistive systems use only a moving mass, with the acceleration being measured through the change in resistance of the deformed springs suspending the proof mass, as seen below in Figure 6 [19].

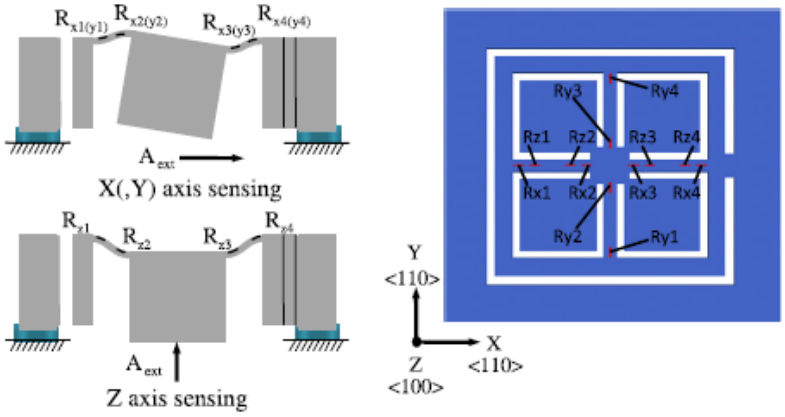


Figure 6 - Piezo-resistive accelerometer design showing deformation under given loads [19]

The accelerometers considered within this thesis utilise capacitive sensing, and the principle of their measurement is similar to that described for capacitive MEMS gyroscopes. Capacitive systems use two electrodes, one stationary and one moving (proof mass), in which the change in the electrode gap due to the induced deformation of the moveable mass results in a change of capacitance producing an electrical signal proportional to the experienced acceleration [4] [20]. The principle of capacitive systems is shown in Figure 7. To maximise the displacements of the proof mass and so the magnitude of the output signal, the damping in the support structure could be reduced. However, this results in proof-mass displacements that overshoot the steady-state response corresponding to the applied acceleration and produce long settling times (open-loop) [20]. Ideally the proof mass should reach its steady state value as quickly as possible with no oscillations, so that it is ready to measure another acceleration [20]. In practice, this is achieved by introducing closed loop feedback into the system via electrostatic forces from the capacitors to increase the damping ratio and reduce the settling time. Closed loop accelerometers [20] tend to have improved bias stability as they are able to maintain a better zero position of the proof mass [20] [18].

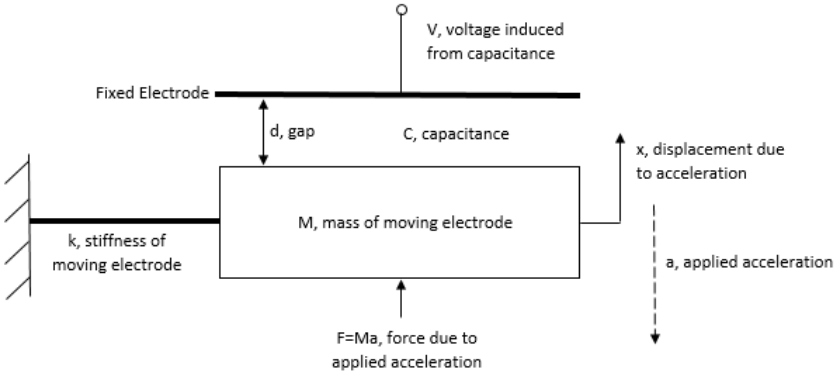


Figure 7 - Diagram showing the principle of a capacitive accelerometer [21]

The accelerometer design considered in this thesis uses a closed-loop capacitive comb drive structure, an example of this MEMS element geometry is shown in Figure 8. The large capacitor area leads to higher capacitance readings and so offers better Signal to Noise Ratios (SNR) compared to other designs. Differential capacitors are utilised to improve accuracy by using two fixed electrodes (instead of one) either side of the electrodes of the proof mass [22]. Proof mass displacement is calculated from the capacitance readings either side of each finger based on differential capacitance [4]. Movement of the proof mass opens/closes the electrode gaps, leading to differing capacitance changes in the two fixed electrodes, one positive the other negative and results in an output voltage that is a linear function of the gap changes [22] [23].

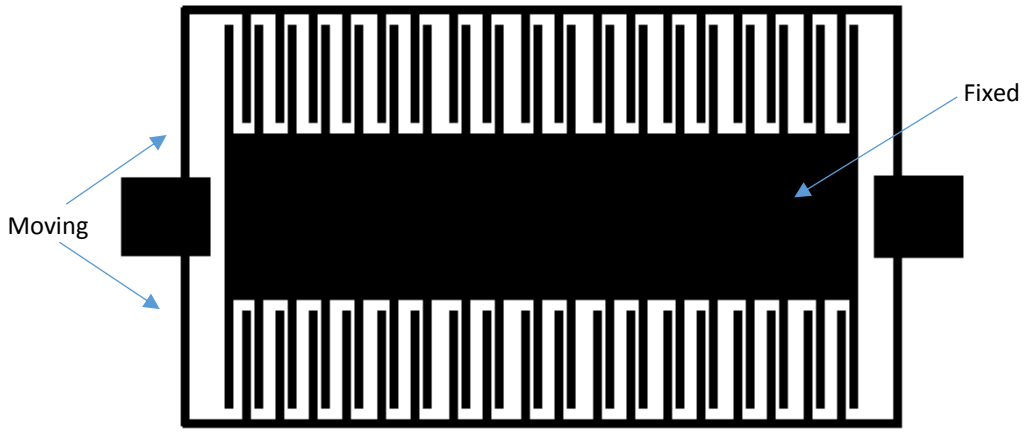


Figure 8 - Diagram showing an example of a comb geomerty used in a Capacitive MEMS accelerometer

1.3. Development of MEMS Inertial Sensors

There is much interest in the development of MEMS inertial sensors due to their numerous advantages over their conventional counterparts. The sensitivity of devices is a key area of improvement if they are to be used in high precision environments such as space applications. This is of particular interest in gyroscope design where recent research [24] aims to reduce damping in the resonator, to maximise the amplitude of motion and improve measured signal quality. A literature review into damping mechanisms in vibrating MEMS gyroscopes revealed that research tools are available to predict the most important damping mechanisms (thermoelastic and support) and further research into damping is not required in an industrial context.

Another key area of interest is packaging which can have a significant impact on the design and performance of MEMS inertial sensors. It is well known that sensor packaging can have a significant

influence on sensor performance over time and temperature, particularly when the sensor is subjected to environmental shock and vibration. In essence this is because there are many different thermal and mechanical requirements to be considered and balanced when designing the package [3]. The following sub-sections provide an introduction into the packaging of MEMS, including descriptions of the functions and the differing levels of packaging, common processes used and their effects on sensor performance.

1.3.1. Packaging of MEMS

MEMS have been developed from the integrated circuit (IC) and microelectronics industry, where packaging is less of a necessity and there are fewer requirements on its functionality. A consequence of this is that packaging in the microelectronics industry is more standardised and 'off-the-shelf' packages can be used [25], with little or no forethought into the packaging type and processes throughout the chip design cycle. In contrast, MEMS devices are highly diverse incorporating delicate moving parts and complex geometries [26], and so require packaging to be custom designed for specific designs and applications [3] [27] [28] [29]. This makes the packaging stage much more expensive, and on average packages comprises 80% of total device cost (max 95%) [27] [28]. On this basis packaging is an integral part of MEMS devices and it is important to consider packaging throughout the whole design process, and not be considered as just an 'add-on' [27] [29]. Taking packaging into account from the outset of the design process allows reductions to be made in device complexity which can yield reductions in fabrication time and cost [30] [31].

A lack of focussed research into MEMS packaging in the past has limited market applicability, due to the cost, performance and reliability issues induced from poor packaging [32] [28] [31]. Advancements in the process and knowledge of packaging design are vital for MEMS devices to reach their full market and performance potential [28]. In the last 10 years this issue has been addressed and MEMS packaging has become a keen area of research [30]. A large proportion of this research is concerned with the evolution and effect of residual stresses induced in the fabrication and packaging processes of the devices. This is due to inertial sensor performance being highly sensitive to these stresses, therefore understanding their origin and effect is key to improving their reliability [33] [34].

1.3.1.1. Role of MEMS Packaging

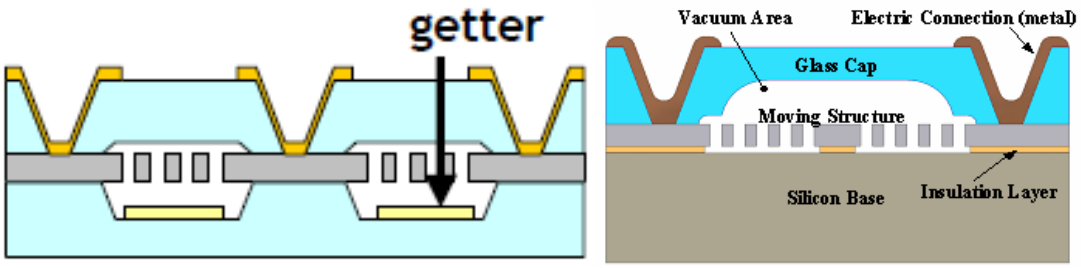
Packaging has many functions, the primary function is to protect its contents from hostile environmental operating conditions that could damage the delicate mechanical components (sensing element) and electrical circuits [27] [25] [28]. Damaging conditions include temperature changes and heat generated by the integrated circuits, humidity or moisture, spurious mechanical vibrations and shocks, as well as electromagnetic radiation and particulates [25] [27]. The packaging also protects internal components from damaging fabrication processes such as dicing, where coolant is required to flow over the die surface which can contain silicon and diamond particles (from wafer and saw) [28].

The package also provides silicon components with mechanical support, provides electrical connections to power the electrical circuits and to distribute the electrical energy to the required components [3] [25] [27], as well as providing a means of handling the die safely [28]. MEMS packaging as mentioned previously is highly application specific and therefore the requirements of a specific package should be defined thoroughly, but care should be taken not to over specify the needs so that no unnecessary cost is incurred [31]. For example many MEMS devices require access to the environment to perform their function, such as pressure sensors; however inertial sensors do not, but they do need an evacuated environment due to the significant effect of fluid damping, and so require hermetic packages [28] [31] [30] [29]. Finally packaging integrates all of the required components minimising cost, size, mass and complexity [25].

MEMS packaging consists of three levels: i) wafer-level, ii) die-level and iii) system or device level [26] [27] [35], with each level having specific functions at particular points in fabrication and operation or working as a combination, for example, providing thermal and electrical paths through each layer for heat removal and electrical transmission [3] [25] [35]. System level packaging consists of a robust casing to protect the device from handling and being dropped after fabrication and during assembly into the required system, as well as providing an assembly interface and electromagnetic shielding (if metal) [25] [27]. Wafer-level and die-level functions and processes are discussed in detail in the following two sections.

1.3.1.2. Wafer Level Packaging

Wafer-level packaging protects the delicate components (electrical and mechanical) of the device during fabrication and packaging processes via encapsulation by glass or Pyrex capping wafers (see Figure 9) [3] [36], and then possibly encased by an epoxy moulding compound [28] [26] [32]. Die separation or dicing is often carried out using a diamond saw which requires a coolant flow over the die, the fluid and contained particulates can damage or destroy exposed features on the surface of the wafer [32] [28] [31] [37]. Alternative solutions to reduce the risk of damage at die separation include temporary plastic packaging, laser dicing or wafer cleaving. However, these lead to increases in cost and/or lead time [28] [31]. The cap wafer/wafers also provide more robust surfaces for die handling [28], as well as providing a cavity with suitable clearance for movement of the sensing element [31]. These can be attached to the silicon substrate via anodic or glass frit bonding in a vacuum to generate a hermetic and evacuated operating environment. The use of gettering materials within the package also removes unwanted gas and water vapour through chemisorption or physisorption, and can be seen in Figure 9 [32] [28]. As the device is now packaged within its required atmosphere, full testing can be carried out earlier (after capping, before dicing) to identify faulty dies, reducing the cost associated with packaging bad chips, for the same reason electrical testing should be carried out prior to release [28].



(a) (b)

Figure 9 – a) Wafer level packaging of a silicon on glass and b) silicon on insulator, gyroscopes [38]

1.3.1.2.1. Anodic Bonding

Anodic bonding is a common method of joining the glass cap and silicon wafers rigidly. Due to the presence of heat (420°C) in the process, the glass is chosen to have a coefficient of thermal expansion (CTE) similar to that of silicon [39] [26] [36]. The glass and silicon are placed in contact with one another and an electric potential applied, with the cathode placed on the glass and the anode on the silicon [39]. This results in the mobile positive ions migrating through the silicon and 2% by mass sodium (in Pyrex) diffusing towards the electrode on the surface. This also results in a depleted silicon

dioxide layer (negatively charged) at the glass contact surface and a positive charge on the silicon surface [39]. The opposing charges on the contacting surfaces produce an attractive electrostatic force that provides high enough pressure to initiate a Si-O-Si chemical bond at the interface [39]. The strength of this bond is controlled through the applied voltage and temperature [27].

Anodic bonding leads to several mechanisms for inducing stresses within the device. Firstly, there are thermal effects, where stresses are induced due to the CTE mismatch between Pyrex and silicon, even though these materials are chosen due to their similar CTE values over a large temperature range [27] [39]. The CTE for silicon is slightly higher than Pyrex in the temperature range 140-500°C, which results in silicon shrinking relative to the Pyrex, putting the silicon under tensile stress. This stress is highly sensitive to the processing temperature due to changes in CTE mismatch with temperature [27]. The heating of the wafers during bonding also leads to thermal inhomogeneities (gradients) leading to non-uniform stresses being generated [39]. Viscoelasticity of the Pyrex at elevated temperatures (above the glass transition temperature) causes structural relaxation and glass shrinkage leading to the evolution of stresses. These stresses are sensitive to the processing time of the bond [39], oppose those induced by the CTE mismatch, and can be used to reduce the final wafer bow [27]. The last mechanism leads to significant changes to the stress profiles generated. This is caused by migration of sodium ions within the Pyrex that causes compositional gradients and hence variations in the CTE through the Pyrex cap [39] [27]. These compositional gradients are dependent on the electrode arrangement (providing the electric potential for bonding) and are seen through the thickness of the wafer as well as across its plane, with the maximum Na accumulation at the electrode position [27] [39]. The stresses induced by compositional gradients compensate for the stresses induced by the CTE mismatch, and their effects are seen mainly in the centre of the wafer with reduced effects on the outer devices [39]. Therefore, assessment of these stresses requires modelling at the wafer level, i.e. wafer containing 50-60 devices [39].

1.3.1.2.2. Glass Frit Bonding

This is an alternative bonding method to anodic bonding which is less rigid but still provides good hermeticity [36]. Small glass particles are suspended in a paste which is screen printed onto the glass cap wafer while in a 'soft' state and then glazed, which solidifies the suspension by removing the

volatiles [36] [37]. The silicon and glass are then put into contact with the frit sandwiched between them and heated to similar temperatures as anodic bonding (450-500°C [28]) so that the frit softens [36]. Force is then applied allowing the paste to reflow, creating a seal, upon cooling the paste hardens and contracts [36] [37]. This bond is self-planarizing, with insensitivity to the particles and surface condition. However, there are alignment issues due to movement of the upper wafer during force application (5µm accuracy) [36].

1.3.1.2.3. Eutectic Metal

This defines a metal alloy that remains in a single phase when transitioning from solid to liquid (i.e. there is no intermediate 2 phase equilibrium) [36]. Once the alloy is applied to the surface of a wafer via electroplating, sputtering or dual source evaporation, the cap and device are put into contact while in an inert atmosphere (with 4% hydrogen) and heated under uniform pressure, melting the alloy [36]. The bond is planarized, with the surface roughness and small particles becoming contained within the bond [36]. This type of bond is suitable for very small devices, due to the high hermeticity of the alloy, and has good alignment accuracy of ≤2µm [36].

1.3.1.2.4. Epoxy Moulding Compound Encapsulation

MEMS devices are sometimes encapsulated by an epoxy moulding compound after a capping wafer has been fitted, as shown in Figure 10 [34]. The curing of the epoxy produces shrinkage of the package, leading to deformation of the MEMS structure and non-uniform stresses, with low levels of stress seen in the centre and rapidly increasing at the edges [26]. The encapsulation occurs at 175°C and is then cured at 125°C followed by cooling to room temperature. This leads to two major stress sources: shrinkage due to curing (0.15-0.6% in volume or 0.05-0.2% in linear dimension) and thermo-mechanical loading due to CTE mismatch [26].

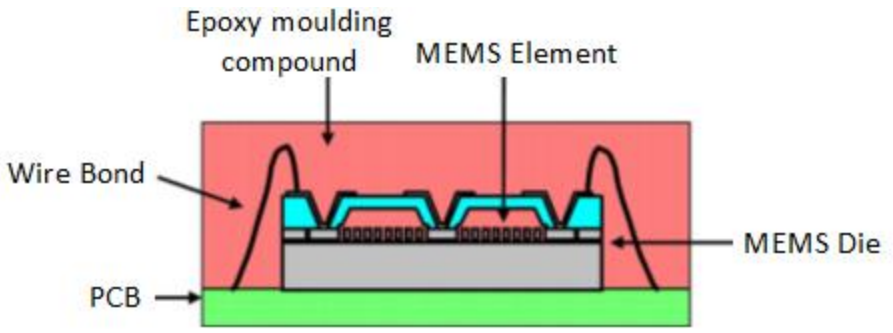


Figure 10 - Epoxy moulding compound encapsulation of a silicon on insulator gyroscope [26]

1.3.1.3. Die-Level Packaging – Die Attach

Die level packaging attaches the MEMS die (glass encapsulated silicon wafer) to a rigid substrate (metal/ceramic package base) [36] and results in a good mechanical attachment providing support, ensuring the MEMS device does not move relative to the package base [25]. Also accomplished at this stage is the wire bonding of the electrical connections between the die and the base, to which the pins for the socket interface are attached (or flip chip in the accelerometer case) [27]. Wire bonding is commonly achieved using solder or adhesive [25]. When considering the stresses induced during fabrication and packaging processes, die-attachment is key, as this step induces the highest stresses, and causes deformation of the die [33]. Examples of the die deformation induced by an adhesive die bond, measured experimentally and simulated using FE modelling can be seen in Figure 11 and Figure 12 respectively.

1.3.1.3.1. Solder Bond

An Au-Sn (80/20) solder is used, and a eutectic metal bond is achieved when heated at 250°C in a forming gas [25]. Soldering produces a solid metal bond, resulting in a single rigid part which has low thermal and electrical resistances [25]. However, due to the rigidity of the bond, the CTE of the attached materials must be well matched as the solder cannot accommodate any induced stresses from differences in the expansion, which often results in failure [25].

1.3.1.3.2. Adhesive Bonding

Adhesive bonding is the most common die-attach method. This is characterised by the use of a curing process in which the liquid polymer becomes solid. During this process full development of the adhesives physical properties occurs, and the extent of cure has a strong influence on these properties [40] [27]. The curing process is made up of two steps: i) the gel step is a short duration process in which the polymer is dimensionally set into position, and ii) the cure step, which occurs at a higher temperature for a longer duration [27]. During the cure step, the high temperature causes an opening of the anhydride rings leading to free carboxyl ions having the ability to react with the epoxy group. This results in a multitude of linear polymers with hydroxyl groups providing reactive sites [27]. These sites enable the cross linking of the linear polymers into a cross linked matrix. This occurs at a higher temperature and results in adhesive shrinkage, which is a source of residual stress in adhesive bonding

[27]. The phase transition of the epoxy from a liquid to solid polymer is not instant across the material leading to thermal and degree of cure gradients and non-uniform shrinkage [27]. In some cases the adhesive is filled with metal flakes (typically silver) to enhance its electrical conductivity and to enable wafer level 3D packaging [25] [36].

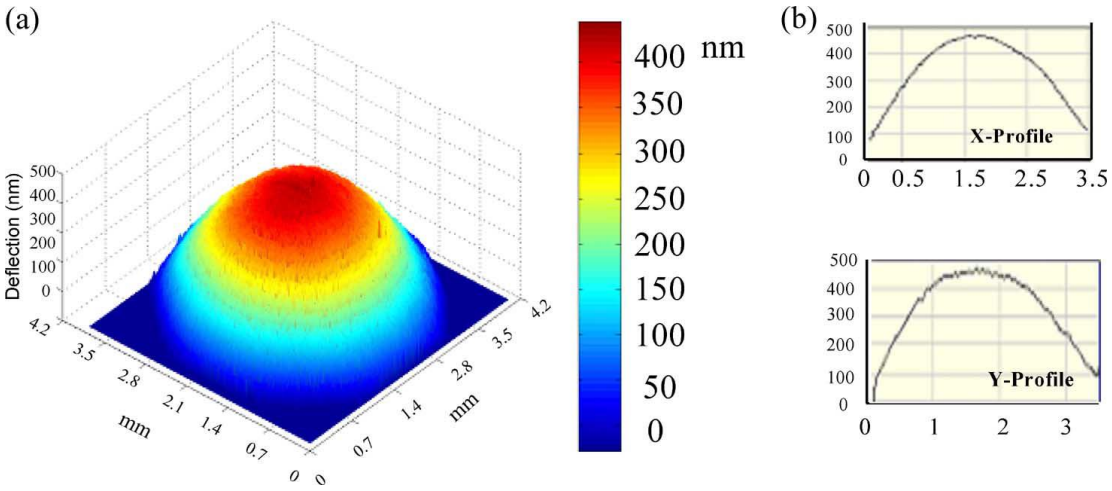


Figure 11 – a) Deformation of the top surface of a MEMS die after adhesive die bond, b) Profiles along x and y axes [41]

Unlike the rigid bond produced via soldering, an adhesive bond is able to accommodate stresses induced by the CTE mismatch between the die and package base due to its low modulus [33] [42]. Therefore for stress reduction, the adhesive's flexibility is a key parameter. It is also highly important that the bond retains this flexibility after temperature cycling to avoid failure of the MEMS device [43]. Epoxies are a commonly used adhesive because of their high bond strength [44]. However standard chemistries have a relatively high Young's modulus of approximately 1GPa, and flexible epoxies can have a Young's modulus as low as 100MPa [43]. Silicone adhesives with a modulus of about 1MPa are used to create low stress die bonds, but suffer from greatly reduced bond strength as compared to epoxies and can have a CTE of up to 400ppm/°C, resulting in a large CTE mismatch with the die and substrate [43] [44] [45]. DELO [43], an industrial adhesives developer, have created new solutions having a good balance of bond strength and flexibility. These new adhesives are based on mCDs (methacrylated beta-cyclodextrins) and acrylates having Young's modulus of 25MPa and 5MPa respectively and have improved bond strength compared to flexible epoxies [43]. The stresses induced during the temperature drop after curing are larger than those during operating temperature variation, and the new mCD and acrylate chemistries cure at 100°C as opposed to the 150°C of silicones and

epoxies (adhesives have much lower processing temperatures compared to solder) [43] [40]. A multi-step cure can reduce the final cure stress by stepping the temperature down in stages [40].

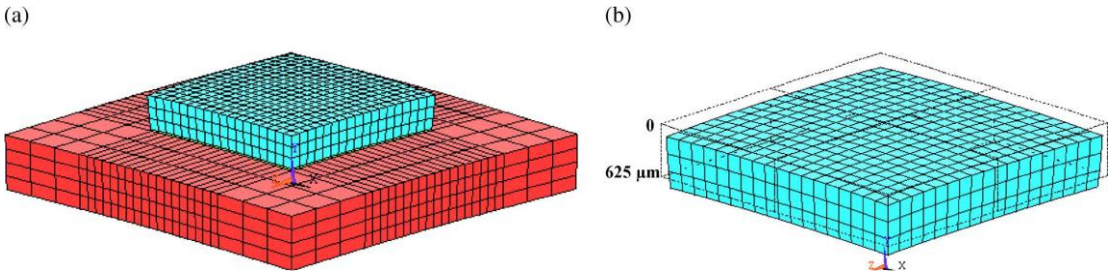


Figure 12 - Deformation after Die Bonding a) Die and Substrate b) Die with undeformed shape from FE [41]

The thickness of the adhesive is an important consideration and can play a major role in stress reduction. This is because an increase in thickness tends to reduce the induced stress, as more is accommodated for within the adhesive due to its lower stiffness, as shown in Figure 13 [33]. An increase in thickness also leads to a more uniform stress distribution, and this is thought to be due to a decoupling of the die and substrate which causes the stresses within the die to be wholly reliant on the properties of the adhesive layer [33]. It is found that packaging processes result in large variations in adhesive thickness across the bond, which induces non-uniform stresses and hence unsymmetrical deformation and warpage [33] [46]. For this reason, it is important to maintain a constant bond thickness, and this can be achieved by incorporating a layer of ceramic balls within the adhesive layer [27]. It has been observed that die attachment causes tensile strain on the die surface which compensates for the compressive strain induced in manufacture, giving a possible method of tuning through design of the packaging processes [46]. Tseng and Li [37] observed that using a four dot adhesive scheme for the die bond instead of one large bond shape with full coverage significantly reduced stress levels in a MEMS accelerometer - this was demonstrated numerically and experimentally [42] [19].

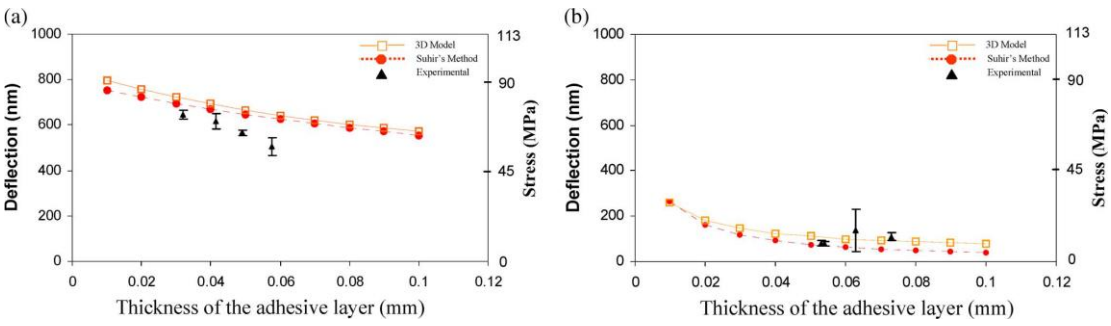


Figure 13 - Relationship between deflection and adhesive layer thickness for a) silver glass, b) polyimide adhesives [41]

Adhesives exhibit changes in physical properties and behaviour at various temperatures as shown in Figure 14 [34]. At low temperatures the adhesive can be considered to be solid glass. However, at temperatures close to its glass transition temperature (T_g) the adhesive begins to display viscoelastic behaviour. At temperatures above T_g the adhesive enters its 'rubber region' and this is the operating region where the adhesive is flexible [27]. To avoid large variations in die bond properties over temperature, it is preferable to have T_g outside the normal operating temperature range, and this can be achieved using mCDs, acrylates and some silicones [43].

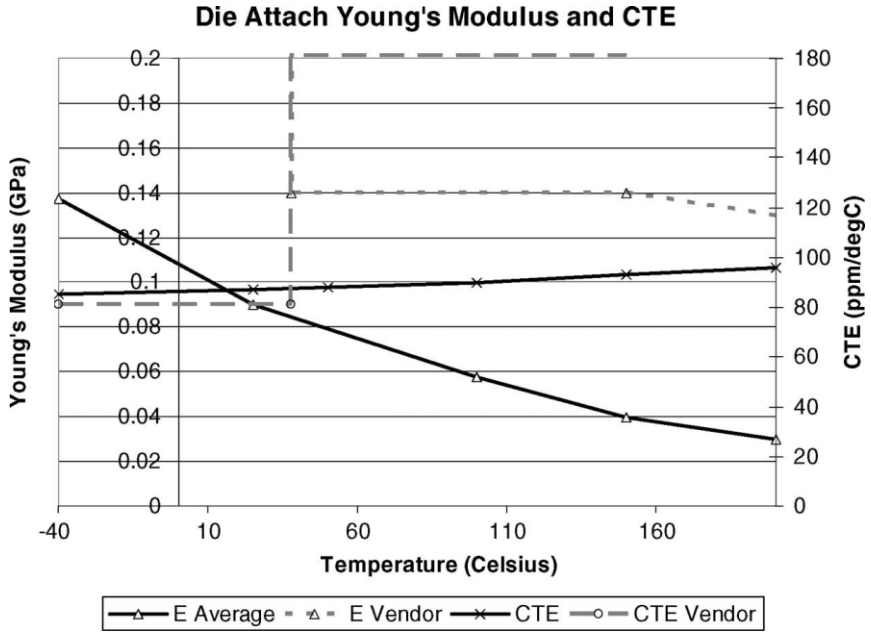


Figure 14 - Variation of Youngs modulus and CTE of a die attach adhesive [34]

Viscoelastic behaviour leads to transient effects such as stress relaxation and creep, which leads to changes in deformations and hence dynamical behaviour and performance over time [27] [47] [48] [42] [33]. Farley and Dasgupta [49] state that these viscoelastic effects in a MEMS die bond are significant. It is important to understand this performance drift and ensure that the drift does not exceed the performance specification limits over the device lifetime [47]. The drift can be reduced significantly through the use of flexible interposers, which can isolate the device from the changing package stresses and deformations [47]. These interposers deform to relieve the induced stresses, leaving the die unstressed or at significantly lower stress [50]. This has also been achieved using various structures such as a deformable guard ring, see Figure 15 [19]. These structures can significantly reduce the effect on the die or MEMS element and any performance change over temperature and time [19] during operation.

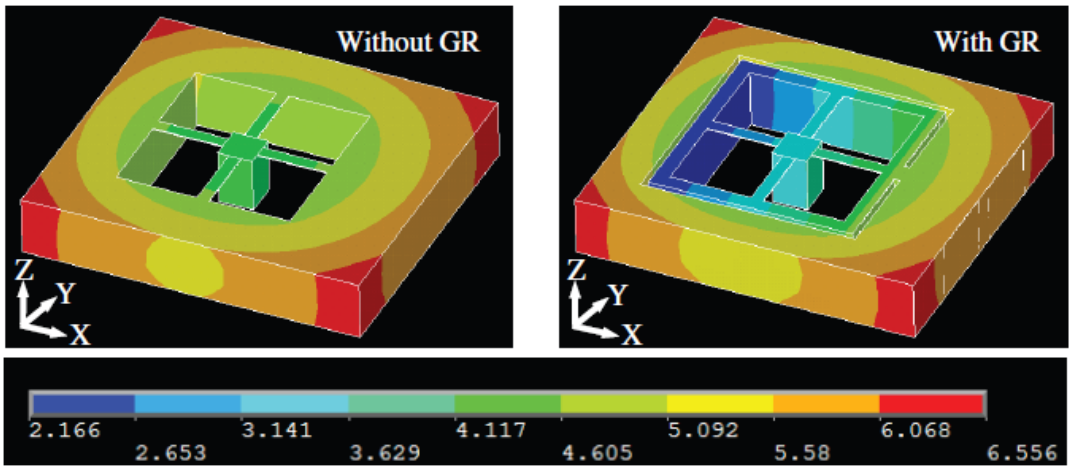


Figure 15 - Deformation of MEMS die with and without a stress isolating guard ring from FEA [19]

The use of curing adhesives in the die-attach leads to outgassing, in which water and organic vapours are released during and after curing within the package [28] [42]. The products of outgassing can settle within the package and cause failure through corrosion of electrical circuits. Stiction of the moving element is avoided as the wafer level packaging is hermetic, protecting the MEMS structure from potentially harmful vapours [28]. This outgassing can be countered through the use of gettering materials, which remove the unwanted gasses and moisture [28].

1.3.1.4. Effects of Packaging on Sensor Performance

It has been observed that packaging processes induce thermo mechanical stresses and geometric deformations within the sensor die [51] through a variety of mechanisms described in Sections 1.3.1.2. and 1.3.1.3. These effects can have a significant influence on sensor performance due to changes in the structural and dynamic behaviour of components [26] [52], especially under varying temperature loading [53]. For the simple case of a micro-bridge (double-clamped beam) the induced stresses cause curvature of the die and therefore bridge, which stiffens the beam and changes the natural frequency [54].

For MEMS Gyroscopes the induced stresses can lead to temperature dependent frequency splits, mode angle changes (orientation of mode shapes), sensitivity reduction and relative movement of transducers caused by sensing offsets [26] [28] [29] [55] [34]. If the stresses or deformations are too large and any of these performance parameters are outside an acceptable range, the device is considered to have failed and is scrapped [38]. As devices are miniaturised by reducing the diameter

and thicknesses to save space and potentially reduce dissipation from thermoelastic damping, the impact of the induced stresses on performance has become significant [26].

In MEMS accelerometers, stresses cause changes to the dynamics of the proof mass due to changes in stiffness and curvature of the die resulting in sensing offsets. This includes zero-g offsets where the static deformation causes a change in capacitance which is measured and interpreted as acceleration even though no acceleration is applied [43]. This is a key issue for high performance accelerometers designed for navigation purposes as even a very small sensing offset will result in large velocity or displacement error post integration [4].

As the environmental temperature changes the resonator dynamics vary non-linearly [53] and the mechanical properties of the die bond change. This causes the die to react differently to shocks/vibrations/loads etc and influences the sensor measurements. In addition, the stresses and deformations change over time due to the viscoelastic nature of the adhesives used in the die bonding, leading to performance drift over time. Thermally cycling the devices after die-attach, as would occur in operation, produces large variations in the natural frequencies over time [53]. This in turn will change the temperature effects on sensor performance over time.

1.3.2. Possible Research into Packaging and Residual Stress

It is clear from the above that packaging of MEMS inertial sensors provides a multitude of possible research opportunities, all with significant applications in the development of devices. Each packaging process induces stress within the device, which can lead to changes in resonator dynamics over temperature and time. Understanding the effects of each packaging process during manufacture is important in the design of low stress devices to reduce any performance drifts experienced. Manufacturing variations within each packaging process yield differences between individual devices from the same batch and across the wafer they are produced from. As it would be difficult to model and simulate the influence of a combination of variations, this thesis focuses on a single package process. Noting that the die attach is the dominant stress source [33], the die attach will form the main focus of this thesis.

1.3.2.1. Die Attach Effects on MEMS Performance

The literature review has shown that packaging processes induce thermo-mechanical stresses that lead to deformation/curvature of the sensor die [42] [46], and that the dominant mechanism inducing these stresses is the die attach [33]. Inertial sensor performance is highly sensitive to these stresses [41] [34] and the induced stresses affect the sensor performance in 3 ways: i) changing the die dynamics, ii) changing the resonator dynamics and iii) changing the static displacement (curvature) of the resonator. This section describes in more details the influence of the die attach on sensor performance.

It was noted earlier that methods have been developed to reduce these stresses. The use of highly flexible (low modulus) adhesives, such as silicones [42] [33] [44] or, through design of the bond geometries by using a 4-dot bond [42] [37] and bonds of greater thickness [46] [41]. However, Rusanen and Torkkeli also made clear that silicones despite their very low moduli can induce greater stresses/deformations due to their high CTE values, which can be in excess of 300ppm/°C [44]. It was found that all tested MEMS microphones failed from buckling of their membranes due to the stresses induced from a large CTE mismatch of the bond compared to the die and substrate coupled with a large drop from the curing temperature (150°C) [44]. Further to this stress, polymer-based adhesives suffer from cure shrinkage, which occurs due to outgassing, where vapours are released during curing, inducing further stresses [42] [33]. Walwadkar et al. observed that for a silicone adhesive the curvature induced was relatively constant over a small range of thicknesses tested experimentally, attributing this to effects of cure shrinkage and CTE mismatch [33]. In Figure 16 a small offset can be seen in the 1st mode before and after bonding at the curing temperature, and this may be caused by cure shrinkage.

This thermo-elastic coupling between the die and the package can affect MEMS sensor performance under varied temperature loading, leading to temperature effects such as zero-g offsets and temperature coefficient of offset [53]. Song et al showed that the natural frequency of microbridges varied significantly when die bonded using an epoxy adhesive, as seen in Figure 16 [53]. Shown in the figure is the effect of temperature on the frequencies for the 1st and 3rd mode of vibration of the microbridge before and after bonding. It is clearly seen that the natural frequencies change due to the presence of the bond and the stresses it causes. The natural frequencies increase non-linearly with

temperature, reaching values similar to the unbonded microbridge at the curing temperature (120°C), indicating that the die is uncoupled/unstressed at this temperature [53].

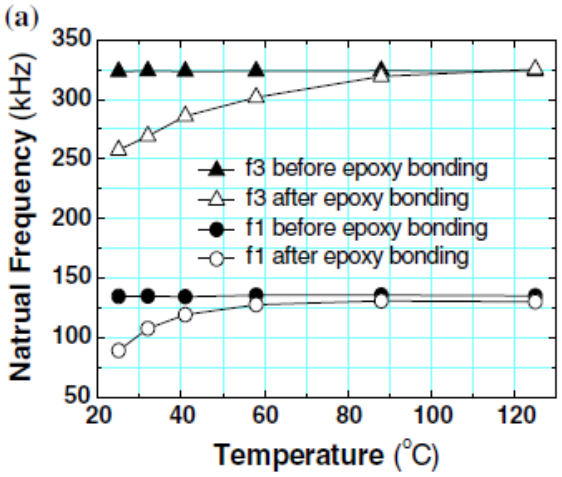


Figure 16 - Variation of microbridge natural frequency (1st and 3rd modes) before and after bonding [53]

Although the effects of the stresses induced in the bond and how these vary over temperature can be significant, in many cases they can be compensated for via calibration of the devices. For the case of accelerometers, the zero-g offset can be measured and a correction applied, even over temperature. However, if the stresses change over time, any corrections made become invalid and in most cases recalibration is not possible. Experimental work by Rusanen and Torkkeli showed that the capacitance of silicone sealed MEMS microphones decreased while held at a single temperature and attributed this change to the presence of viscoelastic mechanisms, relaxation of the packaging stresses and resulting creep of the MEMS structure [44]. Song et al also observed indications of stress relaxation, when thermal cycling caused incremental changes in the natural frequency of microbridges over time [53]. This is of particular interest as a changing temperature-capacitance curve cannot be compensated for over the lifetime of the device, leading to significant errors after storage or cycling in temperature environments. Again, this is a phenomenon observed by the sponsoring company in bias and scale factor accelerometer performance metrics, when devices are held at elevated temperatures for long periods of time.

Another concern having similar effects is aging/further cure, during which the material properties change over time, particularly when subjected to elevated temperatures. It has been observed that the modulus of a silicone elastomer can increase over time [56]. If the material properties of the die bond changes over time, similar effects as a changing stress state will occur. If the bond

stiffens, then the thermo-mechanical coupling between the die and package will change, modifying the temperature effects on performance and invalidating any temperature correction that was applied at calibration.

The stress distribution and deformation variations across the dies surface can have a significant effect on sensor performance, and the die bond design is key to controlling the stress distribution [33]. Frequency shifts of microbridges having the same length differ depending on their position on the die, with the largest shifts seen at the centre of the die decreasing towards the edges [53]. It has been found that different adhesives cause differing stress distributions, with silicone producing maximum stress at the centre, while polyimide and silver glass produce maximum values towards edges of the die [33]. This is of particular concern for dies that have multiple structures at different locations on a single die. For multi-axis inertial sensors, this results in different structures being under differing stress-states and therefore experience different drifts over temperature and time. For ring resonator type gyroscopes, it is important that the stress state is axisymmetric (about the ring centre), as variations in stress and deformation around the ring circumference can lead to performance issues such as quadrature bias. Quadrature errors arise from the direct coupling of the drive and sense motions [57]. Imperfections in the die bond layer, such as thickness or property variations can induce asymmetry in the stress distribution. Lo et al. describes the manufacturing challenges in terms of control and repeatability of the bond geometry and thickness when using highly flexible die attach adhesives [45].

1.4. Plan of Work

The literature review suggests that the die bond is a key area of importance for the successful development of MEMS inertial sensors and holds much potential for improving their performance and reliability. Industry has also identified the die bond as a possible root cause of sensor performance issues, including bias and scale factor changes and drifts over temperature and time respectively. For these reasons, the two mains themes of the thesis are to understand how the die bond properties, including geometrical design and material, affect die dynamics and to consider how the dynamic response and stress-state of the bond change over temperature and time.

1.4.1. Aims and Objectives

The main aim of this project is to quantify and better understand the performance change over time and temperature of a die bond based on a low modulus silicone adhesive currently used in inertial sensors. With the intention of identifying bond designs that improve performance stability over time and temperature. This will be achieved by investigating the changes in dynamic response and static deformation (curvature) of the bond, which have been seen to directly link to sensor performance metrics such as bias and scale factor. Therefore, the ideal bond being sought leads to a die that experiences no change in its curvature or dynamic response over time and temperature. While this may be achieved through extreme bond designs, such as an infinitesimally small bond at the centre of the die, it is essential that the bonds investigated are practical, such that other requirements of the bond are not undermined (i.e. mechanical support, susceptibility to shock and vibration) and are able to be implemented in industry (manufacturable).

The investigations will evaluate the performance of various die bond designs and will include studies into variations in thickness and bond shape (4-dot bond and 9-dot bond designs) to reduce bonding stress and its change over temperature and time. The effects of different temperature environments and treatments will be investigated by observing the changing dynamic response of the die over the operating temperature range of typical sensors and over time due to thermal cycling and storage at high temperature. While, any accompanying change in die curvature over time and temperature will also be investigated.

Secondary objectives include observation of the glass transition temperature of the bond, onset and magnitude of response non-linearity with excitation level and investigating if and how these are affected by bond geometry. As well as the effects of short term mechanical loading and of bond and assembly imperfections on the dynamic behaviour of the die.

1.4.2. Methodologies

The objectives of the project will be achieved through a combination of experimental and finite element modelling methods. Modal testing of ‘dummy’ dies, with different bond designs, of varying shape and thickness, will be used to investigate temperature trends and changes over time due to the various temperature environments. The term ‘dummy’ die refers to a solid, uniform die and are used

to simplify the dynamic responses observed to the rigid body modes of the die, after complex vibratory responses were seen for real sensor dies due to the intricate structures they encapsulate. Surface profile measurements of the same dummy dies will be assessed for evidence of stress reduction using particular bond designs, quantifying the curvature induced by bonding and changes over time due to high temperature storage.

Finite element models emulating the dummy die bonded assemblies will assess the stress effects of bonding and observe both the stress and dynamic property trends over temperature. Changes over time will not be included in the modelling. The modelling will only be concerned with the bond and its design, with performance effects insinuated from the observed curvature and dynamic property changes of the bond, i.e. the resonator geometry will not be included, and so direct performance effects are outside the scope of this project. However, the modelling techniques developed could be used in future investigations to directly assess the trends of sensor performance metrics over temperature caused by the changing bonding stress in alternative die and resonator geometries utilised in other sensors.

1.4.3. Deliverables

Aside from the aims and objectives discussed in Section 1.4.1, some of the most important outcomes of the project will be the tools developed. These include the development of an FE model capable of accurately predicting the stress and deformation state of the die for any die bond design and its resulting modal response. Modelling guidelines will be devised to help design engineers to achieve converged FE models for key output metrics such as die curvature and shear and bounce mode frequencies based on mesh sizes and contact parameter control.

Other key deliverables are the developed testing procedures and analysis models used to characterise the properties of bonds throughout the test regime. The test procedures include methodologies used in differing circumstances for varying objectives, such as identifying the linear response region, and observing temperature trends and coupling of vibration modes. Also developed are practical signal processing methods of the captured test data, and calculation methods for the key parameters leading to the characterisation of bonds in terms of modulus and loss factor properties. The robustness and limitations of the various characterisation methods developed to typical response signal

problems, such as noise and artefacts, and mode coupling are shown. Methods for measuring the curvature induced in the die from bonding and how it may change over time are also developed. Recommendations and advice will be concluded for further improvements to the testing and analysis procedures for small scale bonded structures to achieve improved accuracy in future die bond investigations.

1.4.4. Thesis Outline

The following sub-sections give a brief outline of the work performed in each chapter of this thesis.

1.4.4.1. Chapter 2: Trial Experiments

In Chapter 2, experimental procedures are developed to assess the change in the response of a single bonded die sample under base excitation for varying excitation magnitude, over temperature and due to short-term mechanical loading. Single degree of freedom systems are described and used to characterise the mechanical properties, apparent modulus and loss factor, of the bond in bounce and shear directions. Transmissibility and material property trends are displayed, showing the bond's non-linear behaviour with excitation, temperature dependence and susceptibility to change due to mechanical loading. The capability of contact and non-contact methods to measure the curvature induced in the die through bonding is investigated.

1.4.4.2. Chapter 3: Enhanced Loss Factor Analysis and Characterising Bond Imperfections

In Chapter 3, further loss factor characterisation methods are described, including the half-power and averaged multi-power bandwidth methods. The errors in characterised loss factor from these methods are compared to those of the inverse transmissibility method used in chapter 2 for transmissibility functions of varying frequency resolutions and system loss factor. This error comparison is expanded further for transmissibility functions suffering from signal issues such as noise and artefacts.

Through use of an undamped analytical model of an inclined bond, it is shown that bond imperfections can cause coupling of the rotational and translational coordinates. The effects of geometrical bond imperfections on the differing response observed across the die surface are

investigated with the use of simple FE models, while the errors in characterised properties due to various imperfections are quantified for the differing loss factor calculation methods.

1.4.4.3. Chapter 4: Finite Element Model Development

In Chapter 4, a finite element model is developed in ANSYS to simulate the bonding process inducing curvature in the die and calculate the translational mode frequencies over temperature of the pre-stressed bond. Investigation of the contact algorithms, detection methods, parameters, mesh regime and size required to achieve convergence is conducted and results for key model metrics displayed. The converged model is then used to observe the changes in die curvature and translation mode frequencies over temperature due to inclusion of the bonding stress. Results and discussion for the model output trends for varying bond properties are presented.

1.4.4.4. Chapter 5: Bond Design Variations - FEM

In Chapter 5, the finite element model developed is used to investigate the effects of bond design parameters, shape and thickness. The dependencies of these variables are discussed, including definition of the bond slenderness measure, shape factor and its effect on the stiffness and 'apparent' properties of the bond is described. Results of model output trends are shown for bond of varying designs, with conclusions on the design parameters effects on the differing outputs presented.

1.4.4.5. Chapter 6: Bond Design Variations - Experimental

In Chapter 6, the experimental investigation into bond design parameters is presented. First, the test samples and procedures are described, along with the analysis methods used to characterise bond properties. Results of multi-point response measurements are shown for each sample, identifying the level of coupling observed and the levels of bond imperfections inferred from the results of the FE investigations conducted in Chapter 3, with the impact of these imperfection on the accuracy of characterised properties discussed. Bond property trends over excitation and temperature are shown and discussed for bond of various design, as well as the changes observed over time due to thermal cycling and high temperature storage. Results for the curvature changes experienced in the various bond designs due to bonding and high temperature storage are shown. Comparisons between the experiments and FE are presented.

1.4.4.6. Chapter 7: Project Conclusions and Evaluation with Proposed Improvements and Future Work

In Chapter 7, summaries of the project aims, methodologies and work are presented. Along with key findings of the project work and evaluation of the project aims. Conclusions are drawn on beneficial bond design parameters and material properties to reduce die curvature and the changes in curvature and bond properties over temperature, based on the results of the FE work. Improvements to the work conducted and future investigations are proposed to achieve the full aims and objectives of this project and to gain greater insights and understanding beyond the scope of this thesis.

2. Chapter 2: Trial Experiments

2.1. Introduction

The literature review showed that the die attach process used in the packaging of MEMS devices is the dominant source of thermo-mechanical stresses and deformations in the MEMS die [33]. The performance of MEMS inertial sensors has been seen to be highly sensitive to these stresses and resulting deformations [34] [41]. Literature has suggested methods for reducing these stresses including the use of low modulus adhesives [41] [42]. However, it was also observed that silicones, like those currently used for die bonds in MEMS inertial sensors can induce high stress and curvature despite their low modulus because of their large thermal expansion mismatch to the die and substrate [44]. The induced stresses and curvature change over temperature and time, leading to changes in sensor performance [53] [44] [33].

The stress and deformation induced from the die attach not only affect the MEMS die, but also affect the bond. A stressed bond has different mechanical properties to that of an unstressed bond of the same geometry and material. Therefore, by analysing the mechanical properties of bonds over temperature and time insights can be gained into the changing stress and deformation state of the die. The purpose of this chapter is to investigate experimental methods capable of characterising the mechanical properties of bonds and observing changes over temperature and excitation level, as well as detrimental changes caused by the test methods employed.

The majority of the test methods investigated are vibration test methods, where the die is excited dynamically via a controlled base motion. Vibration test methods were chosen as they replicate normal operating conditions of MEMS inertial sensors. Quasi-static force deflection tests are also investigated as a means of confirmation and comparison with dynamic results. Contact and optical methods for quantifying the curvature of the die induced after die bonding are also considered.

2.2. Main Aims

The main aim is to assess the potential for characterising the material properties of a 'die bond' using harmonic base excitation vibration tests. These tests will consider base excitations applied normal and parallel to the bond to induce compression (bounce) and shear vibrations separately, and will observe changes in the analysed material properties over time, temperature and excitation magnitude.

The outcomes from this chapter and the experiments performed will guide and inform future tests where different bond geometries (shape and thickness) and stress/strain conditions are considered (Chapter 6). For this reason, the processes and procedures developed in this Chapter and results obtained will be analysed in detail to validate their accuracy and limitations. The conclusions drawn will provide valuable insight into the effects of design parameters in future chapters.

2.2.1. Objectives

To achieve the main aims the following objectives must be realised:

- Develop a testing arrangement to measure the dynamic response over frequency of a bonded die under base excitation, generating transmissibility Frequency Response Functions (FRF) in separate compression and shear tests.
- Perform multiple single-point measurements at various locations on the surface/edge of the die and extract the bounce and shear mode shapes.
- Observe changes and trends in the modal response with changing environmental temperature.
- Investigate and characterise the presence of non-linearity in frequency response measurements for each mode by performing vibration tests having different excitation magnitudes, and determine the approximate excitation level at which the response becomes non-linear. This knowledge ensures that other vibration tests are performed within the linear response region and provides a further measure of change occurring over time.
- Develop a Single-Degree-of-Freedom model (SDOF) to analyse the modal response peak in the measured FRFs and identify stiffness and damping coefficient values that can be used to determine the material properties for a given bond in compression/shear vibration tests.

- Investigate contact and optical methods for measuring the curvature induced during bonding.
- Investigate the use of quasi-static force deflection tests and its effects on the specimen.
- Identify any potential issues that could affect the accuracy of the analysis and plan/implement any changes that could eliminate/mitigate these problems in future tests.

2.3. Overview of Experiments

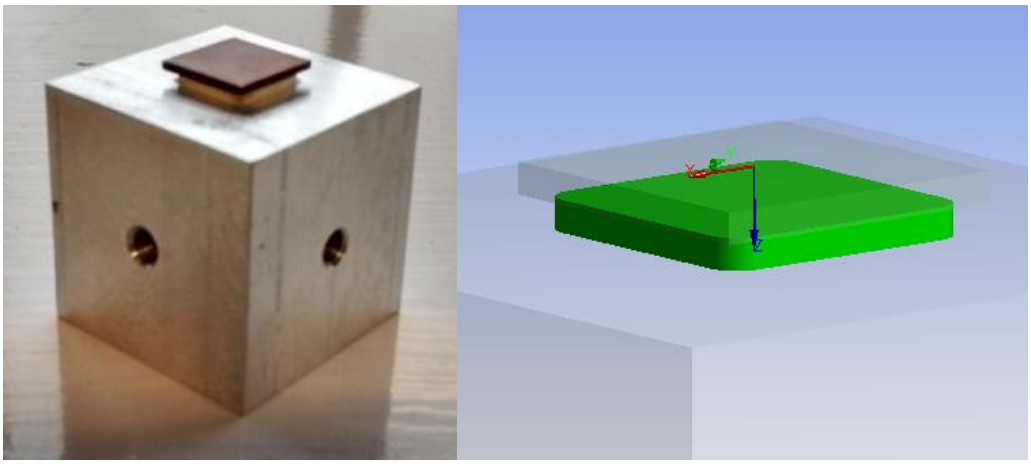
The dynamic response of a bonded 'die' is investigated by measuring its frequency response when subjected to base excitation. The base excitation is generated by an electromagnetic shaker used to provide translational excitation in a single direction. The magnitude of the applied excitation is measured by an accelerometer that is rigidly attached to the substrate of the bond (base). The response of the die is measured using Laser Doppler Velocimetry in the same direction as the applied excitation.

2.3.1. Test Sample

The Test Sample considered in trial experiments comprises a 10x10x1mm copper die bonded to a relatively small 25x25x25mm aluminium base via a 9x9x1mm square silicone die bond (Dow Corning Q1-9225). The dimensions of the copper die were chosen to be of the same order of magnitude as those of a typical MEMS die (often a sandwich of silicon wafers encapsulated on either side by Pyrex glass), which are approximately 5-10mm in depth and width and 1mm in height. The die was chosen to be square for simplicity to allow FE models developed later to be reduced using symmetry conditions. Also, gyroscopes often use square dies (particularly for ring resonator types) to preserve a level of symmetry around the ring. The base was designed to be small to reduce mass, while still providing enough space to attach the control accelerometer and for the 3 M4 tapped holes for attachment to the shaker.

Figure 17a) shows a photograph of the test sample and Figure 17b) shows a Creo computer model illustrating the ideal bond shape used in tests. The bond shape chosen for the trial tests is square with rounded corners (radius 1mm), and the width and depth are slightly smaller than the dimensions of the die to ensure no spillage of adhesive past the edges of the die. The trial bond emulates those currently used in many inertial sensors and provides close to full coverage of the die surface. The main difference between this trial bond and bonds found in typical MEMS devices is the thickness. Typical

die bond thicknesses using a silicone adhesive range from 50-250µm. However, the thickness of the trial bond is chosen to be 1mm. The extra thickness provides greater deformation under dynamic loading and ensures the die bounce mode is within the frequency range of the available test equipment (below 10kHz). Also having a thicker bond provides greater control and accuracy within the manufacturing process, as very slender bonds would be difficult to produce accurately without the use of precision deposition equipment. In later tests where the bond design is varied (Chapter 6), thickness is a key variable and thicknesses down to 100µm will be investigated.



a) b)

Figure 17 - a) Photo of bonded trial test sample, b) Creo model image showing bond geometry

Copper and aluminium were initially chosen as the die and substrate pairing due to their similar thermal expansion mismatch (~5ppm/°C) to a borosilicate glass (Pyrex) and alumina (~4ppm/°C) pairing, as well as their advantages in manufacture and availability. The similar CTE mismatches are expected to produce a similar level of die curvature [33]. However, some literature indicates greater deformations occur when the bond material has an expansion coefficient much greater than that of the adherends [44]. Therefore, as copper and aluminium have CTEs larger in magnitude (factor of 4) than their equivalents, this effect may be reduced, although the expansion coefficient of silicone is still over an order of magnitude greater. The curvature experienced in the trial specimen may be further reduced because of the higher modulus value of copper compared to Pyrex, as well as the thicker silicone layer used.

To manufacture bonds with the required bond shape a stencilling method was developed. This method involved manufacturing a 1mm thick steel stencil. In the trial experiments this stencil was manufactured from a 1mm thick sheet and various bond shapes were milled through its thickness,

providing options for further bond shapes to be produced. The machined stencil was then coated in PTFE using a dry film lubricant aerosol spray to provide a non-stick surface, allowing for easier removal of the stencil, reducing any alteration of the bonds shape or thickness. Figure 18 shows a schematic diagram of the stencil used, highlighted is the square shape used in the trial experiments. The stencilling method has the advantage that the bond dimensions can be controlled and the manufacturing process is repeatable – this is particularly important in future tests, where bond variations are considered.

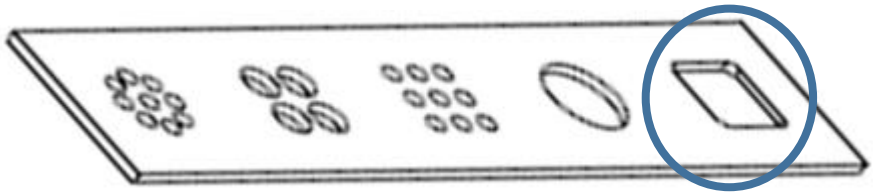


Figure 18 - Diagram of the stencil used to manufacture the trial bond, incorporating possible bond shapes

To manufacture the bond, the adhesive was first mixed thoroughly, following the manufacturers recommended procedure, using a 10:1 ratio of base to catalyst. The stencil was then laid flat on the top surface of the aluminium base such that the square hole was approximately centred, and then filled with the mixed adhesive. A piece of steel sheet with a straight edge was then run over the surface of the stencil to remove any excess adhesive and the stencil removed by slowly lifting vertically. Care must be taken to ensure the shape of the bond is not disturbed by any lateral or twisting motions during removal. The PTFE coating reduces lifting at the edges of the shape caused by sticking of the adhesive to the stencil due to the high viscosity of silicone. The die is then placed on top of the stencilled silicone, with a 0.5mm overhang at each edge, and light pressure is applied to ensure contact occurs across the die surface and remove any small variations in thickness. Small sections of 1mm thick material can be placed under areas of overhang to ensure the thickness and planarity of bonds, and these need to be removed with care so that no levering of the die occurs causing sloping of the bond. The fully assembled bond is then cured, based on the manufacturers recommended cure regime, in a sealed temperature chamber at 150^{o}C (preheated) for 30 minutes. The assembly is then removed and allowed to cool. The temperature chamber used was a SNOL 60/300 LFN Oven, local ventilation is required because hydrogen and formaldehyde vapours are released during curing.

2.3.2. Vibration Test Setup

A schematic of the vibration test setup can be seen in Figure 19. The test sample is subjected to base excitation by mounting it onto an electromagnetic shaker [SignalForce V4 shaker] capable of providing translational excitation in a single axis up to a frequency of 10 kHz. The test sample is attached to the shaker via a single M4 threaded hole in the armature, with a plain threaded rod providing connection between the base and shaker. There are 3 threaded holes (M4) in the base of the test sample - 2 in the side faces of the test sample to provide excitation in the 2 shear directions, and 1 in the bottom face of the test sample for the bounce direction. The threaded holes are designed to allow the direction of the excitation to be changed quickly and easily.

The excitation signal is sent to the shaker by a signal analyser [Stanford Research Systems Dynamic Signal Analyser Model SR785]. The form of signal varies in different tests and is explained in a later section (section 2.4.). The magnitude of the excitation signal is controlled via a reference accelerometer (single-axis, PCB Piezotronics 352C22) which measures the acceleration in the direction of excitation and is attached to the aluminium base by a cyanoacrylate adhesive (super glue). The cyanoacrylate adhesive provides a thin planar bond due to its very low viscosity, ensuring little or no misalignment with the desired measurement direction. The resulting bond has a high stiffness, ensuring there is no relative movement, and allowing accurate measurements of the base motion to be made. The curing time is quick (~10 s) and the bond is weak and brittle in torsion. This allows quick and easy attachment and removal of the accelerometer.

A laser vibrometer [Polytec OFV 055 laser head and 3001S controller] is used to measure the velocity response of the die at a single point in the direction of excitation, with the vibrometer measuring response in the direction of the laser. The laser provides a non-contact method for measuring the response of the die. Unlike an accelerometer this measurement technique does not modify the mass or stiffness of the test specimen and so does not affect the response. This method is essential in this case because the vibrating part (die) has low mass and attaching an accelerometer to the die would significantly modify the dynamic behaviour of the system. The signal analyser is used to record both the excitation signal (acceleration over frequency) measured by the accelerometer and the response signal (velocity over frequency) measured by the vibrometer. These two signals are used later

to produce the displacement transfer function of the system over frequency, known as the displacement transmissibility function, this is discussed in detail in Section 2.5.1.

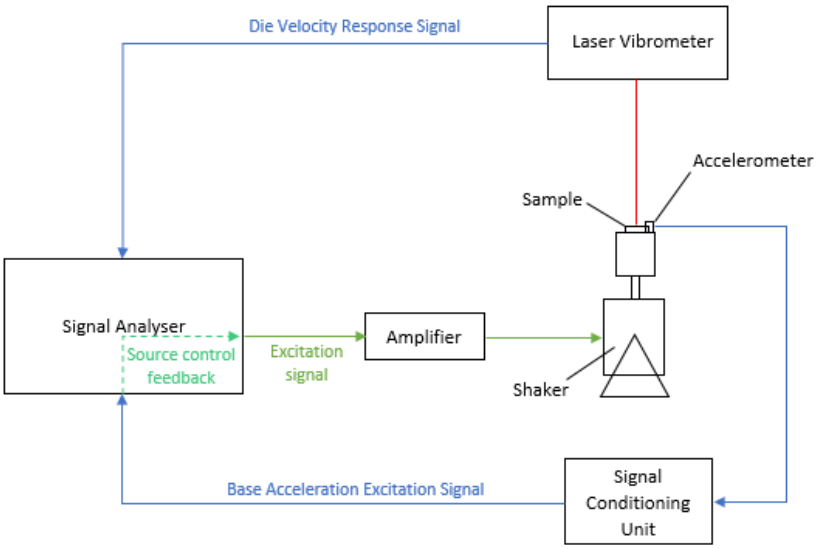


Figure 19 - Test setup schematic

2.4. Vibration Test Methods

Two different testing methods are used to investigate the dynamic behaviour of the die. These are the Sine Sweep Method and the Fast Fourier Transform Method [58] [59] [60]. In this section these methods are described, and their advantages and disadvantages identified and explained in the context of the characterisation work performed in this thesis.

2.4.1. Sine Sweep

The Sine Sweep test is a common modal testing technique used to determine the resonant frequencies of a vibrating structure [58] [59] [60]. The applied excitation consists of a constant amplitude sinusoidal signal, the frequency of which is varied sequentially over time through a range of frequencies. The amplitude of excitation is measured by the reference accelerometer, and the frequency is changed only after an appropriate settling time has passed to ensure the response has reached steady-state. It is important to ensure the settling time is sufficiently long to reach steady state at the lowest frequency tested, and in the trial tests a settling time of 125ms was used. The process of changing the frequency, waiting for the vibration response to reach steady state and measuring the response amplitude continues until measurements at each frequency in the defined frequency range are complete [58] [60].

A sine sweep test has the advantage that high frequency resolution can be achieved by selecting a high number of frequencies over a range, as well as a high signal to noise ratio and dynamic range of measurements [60] – this is achieved by the analyser optimising the measurement signal at each frequency before recording. The control method used in this method allows for a constant acceleration magnitude, under tight control (+/- 0.1dB), at all frequencies in the tested range. This tight constant control of excitation over the full frequency range is a key requirement when performing linearity tests, where different levels of excitation amplitude are considered, making the Sine Sweep Method ideal [59]. The disadvantage of this method is the time taken to perform a full frequency sweep at high frequency resolution. For example, measuring 2000 frequency point with a settling time of 0.125 s will take (0.125x2000=) 250s. The long duration of the test can have implications on the quality of data as there is a longer time for any external disturbance to affect the dynamic behaviour of the system. Possible disturbances experienced could be associated with chamber noise or coolant release and would cause sporadic peaks at specific frequencies in the frequency response.

2.4.2. Fast Fourier Transform (FFT)

The FFT method uses an excitation signal that contains components of all frequencies in the defined test range simultaneously and therefore excites response at all those frequencies. The form of this excitation signal can vary but here a chirp signal is used. This signal provides an equal amplitude sine wave at each frequency simultaneously and each is perfectly periodic within the time record [60] [59]. The control at each frequency is not as tight as in the sine sweep tests, as there is some variation of amplitude over frequency with only the total excitation amplitude controlled [59]. The response is measured as a short time history (typically ~4ms) by the vibrometer. The signal analyser then transforms the response into the frequency domain using the Fast Fourier Transform (FFT).

The FFT algorithm uses Fourier's theorem that any waveform can be represented by the weighted sum of sine waves of all frequencies. The short time records (for excitation and response) can be represented by a magnitude at each frequency component and this results in the ability to capture a large frequency spectrum (0-100kHz) in milliseconds. The disadvantage of the FFT is its resolution. As the FFT utilises frequency 'bins', in which a small range of frequencies may be represented by a single magnitude value, so if a frequency component of interest is between 'bins' its response is split between

the neighbouring 'bins' [60]. In practice the number of bins is limited by the analyser used and so achieving high resolution is only possible by reducing the range of frequencies tested. To improve accuracy and repeatability, averaging is used in which multiple time records are transformed into their component frequency spectra and then averaged. Averaging helps to reduce the level of noise and the effect of any disturbances in the final frequency spectra. Despite the large number of records used, a full frequency range can be tested in a short duration e.g. <1s. This short testing duration is well suited to systems experiencing regular disturbances, such as those experienced during temperature variation tests due to noise from the chamber and the release of coolant. A uniform window is used to ensure that no part of the frequency spectra is artificially attenuated [60].

Figure 20 compares transmissibility functions calculated from test data captured using the sine sweep and FFT test methods. It can be seen that there is good agreement between the results from the differing test methods for each equivalent set of measurement points (i.e. red + dark blue (p1), orange + mid-blue (p3), yellow + cyan (p5)).

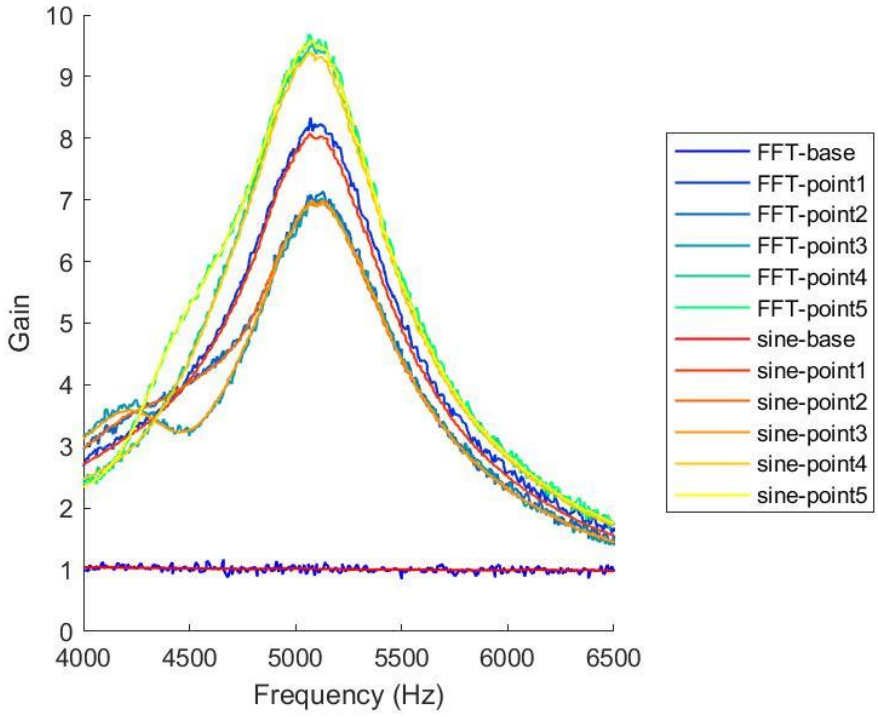


Figure 20 - Comparison of Transmissibility Functions measured using Swept Sine and FFT with chirp Test Methods

2.5. Analysis Methodology

The previous section described the two methods used in the trial dynamic testing. Although the methods are different, both methods provide information about the frequency content of the response, based on the applied excitation measured by the reference accelerometer and the response measured by the vibrometer. To capture the phase relationship between the excitation and response, the signals are recorded as complex quantities, containing both real and imaginary components. The following section describes how the measured excitation and response signals are transformed into a Transmissibility function (TF) or Frequency Response Function (FRF), and how the resulting TF can be analysed to determine the material properties (elastic modulus and loss factor) for the die-bond-base system under test.

2.5.1. Transmissibility Function (TF)

In the experiments, the sample is excited via a base acceleration and the velocity response of the die is measured at different frequencies. To characterise the dynamic response and allow comparisons between tests it is convenient to normalise the response in terms of a transfer function defined as the ratio of response to applied excitation [58] [59]. In the experiments performed, where both excitation and response are defined by motion, i.e. acceleration and velocity respectively, the motion TF is calculated [61]. If the time-varying (sinusoidal) base acceleration (excitation) is $\ddot{x}_0(t)$, and die velocity is $\dot{x}(t)$, the motion transmissibility function, T^*, is determined using the steady state die and base displacement magnitudes, X^*, *and* X_0^* respectively, and is given by:

$$T^* = \frac{X^*}{X_0{}^*} = \frac{\left(\frac{\dot{X}^*}{i\omega}\right)}{\left(\frac{\ddot{X}_0{}^*}{(i\omega)^2}\right)}$$

where complex notation has been used to represent the steady state base acceleration $\ddot{X}_0{}^* e^{i\omega t}$ and velocity of the die $\dot{X}^* e^{i\omega t}$ and complex amplitudes $\dot{X}^*$and $\ddot{X}_0{}^*$ are measured directly in experiments as voltages and then converted to velocity and acceleration. The transmissibility defined is complex containing both magnitude and phase information of the response.

2.5.2. Material Model

To characterise the properties of the bond based on the TF, the stiffness and damping behaviour are determined based on an appropriate material model. In what follows the Kelvin-Voigt and Hysteretic damping models are introduced and discussed for this purpose.

2.5.2.1. Kelvin-Voigt Viscous Damping Model

The Kelvin-Voigt model is commonly used when analysing simple vibrating structures like that investigated in the experimental trials [61] [58] [59]. Figure 21 shows a schematic representation of the Kelvin-Voigt model.

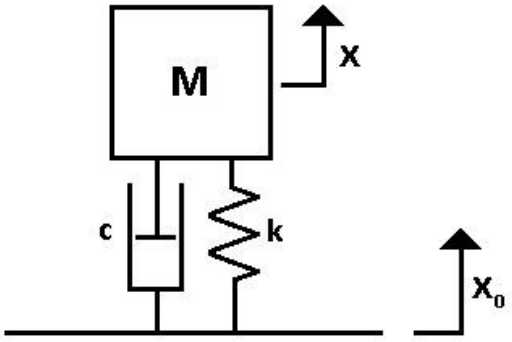


Figure 21 - Representative diagram for a Single-Degree-Of-Freedom Kelvin-Voigt model with viscous damping

The model consists of a lumped mass connected to ground via a spring and viscous dashpot connected in parallel. The spring has stiffness k and the viscous dashpot has damping coefficient c. The mass translates in the x direction and the governing equation of motion under free vibration is given by:

$$m\ddot{x} + c\dot{x} + kx = 0$$

Experiments on solid materials undergoing cyclic stressing have shown that damping forces are independent of frequency [61]. As the viscous damping model generates a damping force that is dependent on frequency, the viscous model is not appropriate for the current application [61]. To correct for this dependence the hysteretic damping model is introduced.

2.5.2.2. Kelvin-Voigt Hysteretic Damping Model

The hysteretic damping model incorporates a damping coefficient c_H divided by the frequency of oscillation [61] [58] [59]. Figure 22 shows a schematic representation of the hysteretic damping model.

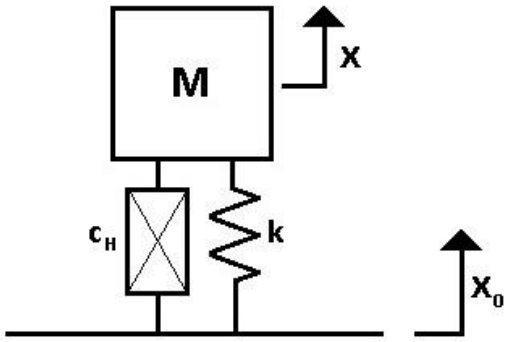


Figure 22 - Representative diagram for a Single-Degree-Of-Freedom hysteretic damping model

The equation of motion for free vibration is:

$$m\ddot{x} + \frac{c_H}{\omega}\dot{x} + kx = 0$$

Assuming that the response is harmonic, such that $x(t) = Xe^{i\omega t}, \dot{x}(t) = i\omega . x(t)$ gives

$$m\ddot{x} + (ic_H + k)x = 0$$

In this case it is not possible to separate the stiffness and hysteretic damping, and so they are considered together as the complex stiffness. Rearranging the equation of motion gives:

$$m\ddot{x} + k(1 + i\eta)x = 0$$

where $\eta = \frac{c_H}{k}$ is the hysteretic loss factor.

Alternatively, we can write:

$$m\ddot{x} + k^*x = 0$$

where the complex stiffness $k^* = k(1 + i\eta)$.

Figure 23 shows a representative diagram of the system considered including base excitation x_0.

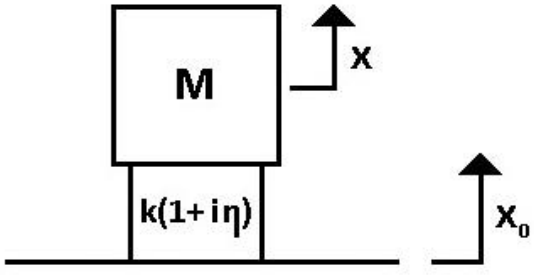


Figure 23 - Representative diagram for a Single-Degree-of-Freedom model with complex stiffness

The equation of motion for the system with base excitation is:

$$m\ddot{x} + k(1 + i\eta)x = k(1 + i\eta)x_0$$

Assuming $x(t) = X^* e^{i\omega t}$ and $x_0(t) = {X_0}^* e^{i\omega t}$ in this equation and rearranging, it can be shown easily that the motion transmissibility of a single degree of freedom Kelvin-Voigt model with hysteretic damping over frequency is:

$$T^*(\omega) = \frac{X^*}{{X_0}^*} = \frac{k(1+i\eta)}{-\omega^2 m + k(1+i\eta)} = \frac{{\omega_n}^2 + {\omega_n}^2 \eta i}{{\omega_n}^2 - \omega^2 + {\omega_n}^2 \eta i} \tag{2.1}$$

where the natural frequency squared ${\omega_n}^2 = \frac{k}{m}$.

This equation is used in Section 2.5.3.2 and later in Chapter 3 to derive expressions to calculate the damping present in the bond from the test transmissibility, in terms of loss factor η.

2.5.3. Material Property Analysis

Assuming that the measured transmissibility functions for the bounce and shear modes have the form derived for a single degree of freedom system with a complex stiffness (hysteretic damping), the material properties of the bond can be estimated.

2.5.3.1. Storage Modulus (Young's and Shear)

The natural frequency of the system can be determined directly from the measured transmissibility magnitude. The natural frequency is the frequency at which the maximum transmissibility magnitude is observed [58]. The static (modal) stiffness, k can be calculated from:

$$k = {\omega_n}^2 m,$$

where m is the (modal) mass of the system.

In many applications the modal mass can be approximated as the physical mass undergoing vibration (i.e. die mass). However, in the case of a micro-engineered die and other small scale bonded structures, the die mass is small enough that the mass of the bond cannot be neglected. For the case when the bond mass is uniformly distributed and the bond deforms as a linear translation, it can be derived (through a simple integration across the bonds thickness) that the modal mass, *m* is given by:

$$m = m_{die} + \frac{m_{bond}}{3}$$

Incorporating the modal mass into equation (2.1), expressing the stiffness in terms of the apparent storage modulus and rearranging, it can be shown that the apparent storage moduli (Young's and shear) can be expressed as:

$$E_a, G_a = \frac{{\omega_{n_{bounce,shear}}}^2 \left(m_{die} + \frac{m_{bond}}{3}\right) t_{bond}}{A_{bond}}$$

(2.2)

where t_{bond} and A_{bond} are the thickness and cross-sectional area of the bond.

The modulus calculated here for a small-scale bond is defined as the apparent Young's or Shear modulus, for excitation in the bounce and shear directions respectively. The term 'apparent' is used as the value calculated is not equal to the material's Young's or Shear modulus because of stiffening effects associated with the constrained bonded surfaces of a slender bond [62] [63] [64]. Further details on this slenderness stiffening effect and empirical relations for the relationship between material moduli and the apparent moduli for differing geometries are discussed in chapter 6 when bond geometries are varied.

2.5.3.2. Hysteretic Loss Factor

As described in Section 2.4.2, damping in the complex stiffness material model is defined by the hysteretic loss factor η, which at resonance is equivalent to twice the viscous damping ratio γ, i.e. η=2γ [59].

In what follows, two methods for calculating the loss factor from the transmissibility of the system are described. These are based on the imaginary component and magnitude of the maximum transmissibility at resonance.

The results derived in Section 2.4.2.1 indicate that the transmissibility for a single degree of freedom system is given by:

$$T^*(\omega) = \frac{{\omega_n}^2 + {\omega_n}^2 \eta i}{{\omega_n}^2 - \omega^2 + {\omega_n}^2 \eta i}$$

Maximum transmissibility occurs at resonance. Setting $\omega = \omega_n$ and rationalising the denominator, the maximum transmissibility is given by:

$${T^*}_{max} = \frac{1 + \eta i}{\eta i} = 1 - \frac{1}{\eta} i$$

Re-arranging this equation it can be shown that the loss factor can be expressed as:

$$\eta = -\frac{1}{Im({T^*}_{max})}$$

This result indicates that the loss factor can be expressed in terms of the imaginary component of the maximum transmissibility at resonance. To use this result, it is necessary to real and imaginary components of excitation and response must be recorded. However, in some cases only the magnitude of the transmissibility is measured, so an alternative method is required.

The magnitude of the maximum transmissibility at resonance is:

$$|T^*_{max}| = \left|1 - \frac{1}{\eta} i\right| = \sqrt{1 + \frac{1}{\eta^2}}$$

Squaring and rearranging this equation, it can be shown that:

$$\eta = \frac{1}{|T^*_{max}| \sqrt{1 - \left(\frac{1}{|T^*_{max}|}\right)^2}}$$

(2.3)

This is an exact result for the loss factor. However, if η is small, $|T^*_{max}|$ is large such that $1/\sqrt{1 - (\frac{1}{|T^*_{max}|})^2} \approx 1$ and

$$\eta \approx \frac{1}{|T^*_{max}|}$$

(2.4)

Figure 24 plots the loss factor prediction errors obtained using the 1st order approximation given by equation 2.4. The error obtained by using equation 2.4 is less than 1% provided the loss factor is less than 0.15. In contrast there is no error obtained using equation 2.3 for any system loss factor as it is an exact solution. The equations 2.3 and 2.4 will be defined as the inverse transmissibility magnitude method exact solution and first order approximation respectively.

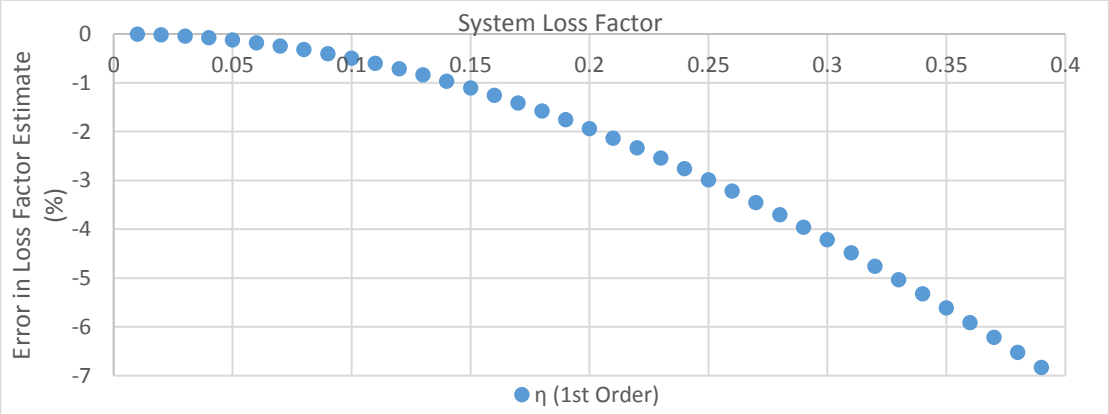


Figure 24 - Percentage error in loss factor using 1st order approximation for different system loss factors

In the trial tests all loss estimates will be calculated using the exact solution, equation 2.3, to ensure consistent analysis across tests. A comparison of the various possible calculations will be performed later, in Chapter 3, when the analysis model is developed further and other complex loss factor calculations are introduced.

2.6. Trial Results

In this section experimentally measured results for the transmissibility and material properties will be presented and discussed for the base excitation tests conducted in the bounce and shear directions. Initially the multi-point responses are used to characterise the mode shapes for the peaks observed in the transmissibility functions, with identification of the translational modes (Section 2.6.1.). The change in response and material properties will be assessed due to mechanical loading from a quasi-static force deflection test (section 2.5.2.). The change in response (transmissibility function) and material properties due to varying environmental temperature (section 2.5.3.) and excitation (section 2.5.4.) will then be investigated, using measurements taken at the centre of the die only.

2.6.1. Multipoint – Mode Shape Characterisation

The aim of the multipoint tests is to characterise the modal responses occurring at the peaks observed in transmissibility measurements and identify the translational modes of interest. This is achieved by measuring the response at various locations on the die surface or edge when base excitation is applied in the compression and shear directions. In the trial experiments 5 points were measured on the die surface for the bounce excitation case and 3 points were measured on the die edge for the shear excitation case. Figure 25 shows locations of the measurement points and definition of the coordinate system. By inspecting the magnitude and phase of the transmissibility at each point, the motion of the die can be inferred and the translational mode identified. For pure translational modes it is expected that the responses at all measurement points will have the same magnitude and phase, in the direction of the excitation. The resulting transmissibility functions at all measurement points are expected to have a single peak at the resonant frequency with identical gain magnitude and phase values.

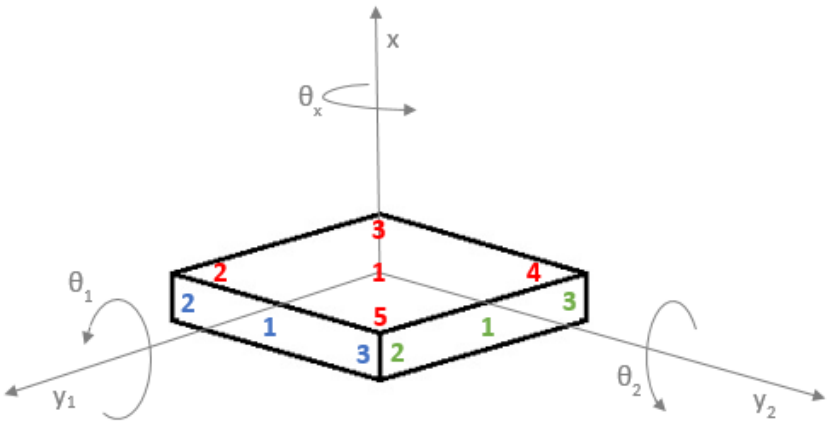


Figure 25 -Measurement points and coordinate system

2.6.1.1. Bounce Transmissibility

Figure 26 shows the bounce Transmissibility Functions (TFs) and phase diagrams for the trial specimen under vertical base excitation measured at various points on the dies surface (located as shown in Figure 25).

A large response peak is observed for all measurement points located at approximately 5.1KHz, indicating the presence of a resonant mode that is highly coupled to the compressive excitation direction. At this frequency all measurement points experience a large increase in gain, and the phase plot shows that these motions are in phase with each other. This is typical of a translational mode of vibration. However, different measurement points experience different levels of gain magnitude at the resonant frequency. Edge 4-5 has the largest gains, followed by central point (1) with edge 2-3 exhibiting the lowest peak gain. This variation in displacement response at resonance indicates that the die is not moving in pure translation, and that there is a superimposed rocking motion about an axis approximately parallel to edges 4-5 and 2-3.

At 4.3 kHz the transmissibility function contains a feature that has a different shape for each of the measurement points. The phase plot also indicates that the phases are different at each of the measurement points. These phase differences indicate the presence of a rocking mode or two rocking modes near this frequency. Note: there will be 2 rocking modes at the same frequency for a perfect square bond.

The observed rocking mode/s and presence of rocking in the translational mode indicates the presence of coupling between the rotational and translational coordinates (i.e. x, θ_1 and θ_2). This

coupling is likely to be caused by the presence of imperfection in the bond or die, resulting in a non-uniform mass or stiffness distribution across the bond/die. The imperfection could be a sloped or non-uniformly cured bond, or be associated with imperfect manufacture or assembly of the die.

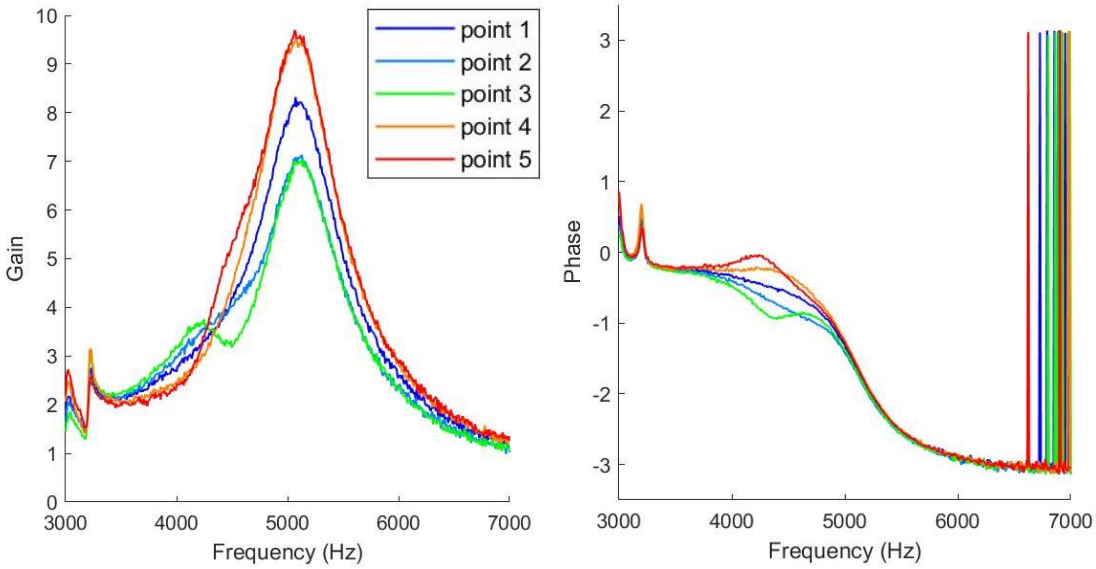


Figure 26 - Compressive Transmissibility Function and Phase for trial specimen at various points on the die surface

The analyses described in Section 2.5.3 are used to determine the apparent material properties in bounce (apparent Young's modulus and loss factor) of the bond using the measured transmissibilities at each measurement point. To improve the accuracy of these calculations, care must be taken to determine an accurate value for the natural frequency, and this process is affected by the presence of noise and frequency resolution in the measured Transmissibility function. To reduce the effects of small noise induced local maxima close to the peak, a low span moving average is used to smooth the data and avoid the presence of local maxima. In addition, quadratic interpolation is applied around the peak to artificially increase the frequency resolution and improve peak frequency identification. Table 1 shows the calculated values for apparent Young's modulus and loss factor, using equations 2.2 and 2.3 respectively.

The apparent Young's moduli lie in the range 11.77MPa to 11.96MPa. The minimum and maximum values are calculated at opposing corners 5 and 3 respectively, the median value is 11.83MPa calculated at the central point 1. The minimum and maximum values correspond to -0.5% and +1.1% variations about the central point.

The hysteretic loss factors lie in the range 0.106 to 0.146. Similar to the Young's modulus, the minimum and maximum values are calculated at corners 5 and 3 respectively. The median value is 0.124 calculated at the central point 1. The variation across measurement points is much greater for the loss factor than for the modulus, and corresponds to -14.7% and +18.3% variations about the central point.

Whilst the variations with measurement location is quite large it is important to realise that the models developed in Section 2.5.3 are only valid for a single degree of freedom system in pure translation. As discussed earlier the bounce mode contains a rocking motion about an axis close to the centre of the die and approximately parallel to die edges 4-5 and 2-3. The rocking contributions are most significant on edges 2-3 and 4-5, whilst central point 1 is least affected by rocking. The rocking contributions alter the maximum transmissibility value used in the property calculations. For this reason, it is expected that the apparent Young's modulus and loss factor for central point 1 are the most accurate of the points considered.

Table 1 - Measured material properties from Transmissibility Function at each point in compression

Measurement Point	1	2	3	4	5
Apparent Young's Modulus (MPa)	11.83	11.89	11.96	11.78	11.77
Compressive Hysteretic Loss Factor	0.124	0.144	0.146	0.107	0.106

Figure 27 shows a comparison between the measured Transmissibility and Transmissibility calculated using the Complex stiffness model with hysteretic damping values from Table 1. It can be seen that the generated Transmissibilities fit the test data well over a frequency range around the translation dominant peak, but without reproducing the other "rocking" modes present in the test data. By fitting to the combined peak value, the influence of loss factor error can be seen over frequency for measurement points with significant rocking measured. Points 4 and 5 have a higher gain due to the addition of the rocking component to the translational displacement and therefore a lower damping value is calculated. This leads to a narrower peak which causes the transmissibility is underestimated away from the centre of the peak. The opposite is true for points 2 and 3. The transmissibility for Point 1, which experiences only a low level of rocking, is replicated almost perfectly over the frequency range by the hysteretic damping model.

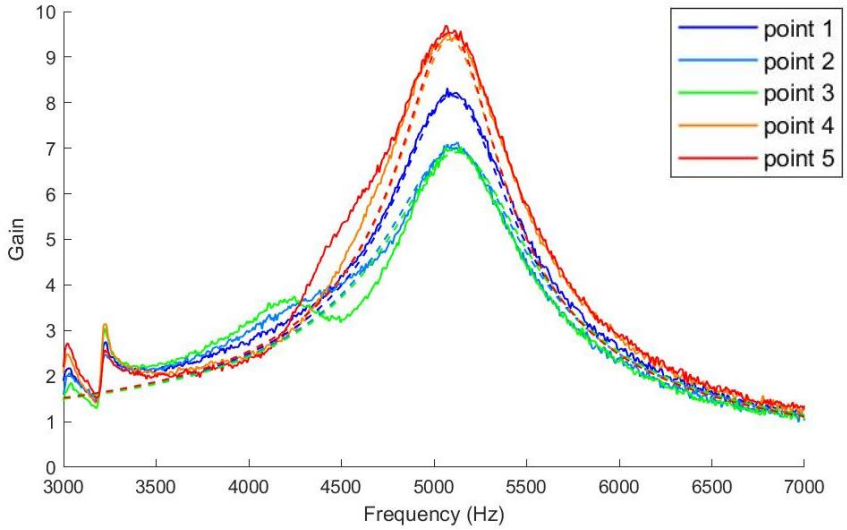


Figure 27 - Comparison of Compressive transmissibility function from testing and complex SDOF generated using derived parameters

2.6.1.2. Shear Transmissibility

Figure 28 shows the tansmissibility and phase plots measured at 3 points on the die edge for the two shear directions (when the shear response and excitation are aligned). Both tansmissibilities have a strong peak at approximately 1.8KHz for all measurement points, indicating the presence of shear modes. Like the rocking modes described earlier, a perfect square bond has 2 translational shear modes in orthogonal directions at the exact same frequency.

Similar to the bounce tests, the maximum gain values at the peaks are different for each measurement point, suggesting the presence of a contaminating non-translational motion. In bounce, the contamination was caused by rocking motion. Although rocking is likely to be present here, the measurement points are unlikely to measure rocking motion. The shear mode is more likely to be contaminated by a torsional motion about an axis through the centre of the die (θ_x). The magnitude of this rotational motion is seen to vary between the two tested shear directions, with shear direction 1 (y_1) experiencing a greater gain variation between measurement points than in shear direction 2 (y_2) at the resonant frequency. The larger rotational component in shear direction 1 can also be seen as there is a second feature at a frequency of approx 1.6 kHz in the transmissibility plot for shear direction 1. This is similar to that observed in bounce tests associated with rocking frequencies, but is much lower in significance. This feature can be seen clearly in the phase plot, where there is a visible difference in phase between the measurements at different locations. These features are also present in shear side 2, but are too small to be visible in the figures.

Similar to the bounce test results, the presence of the torsion mode and the contaminating torsion motions associated with the shear mode peak are due to coupling caused by imperfection in the trial sample. The same imperfection caused coupling between bounce and rocking in the compressive direction, and is seen when observing the rocking magnitudes about the different shear axes. It was stated earlier that the resultant rocking axis was approximately parallel to die edges 2-3 and 4-5 (y), and therefore the largest rocking component is θ_1, with a smaller rocking component θ_z. Therefore the same imperfection causes greater coupling between y_1 and θ_2 (shear direction 1), than between y_2 and θ_x (shear direction 2).

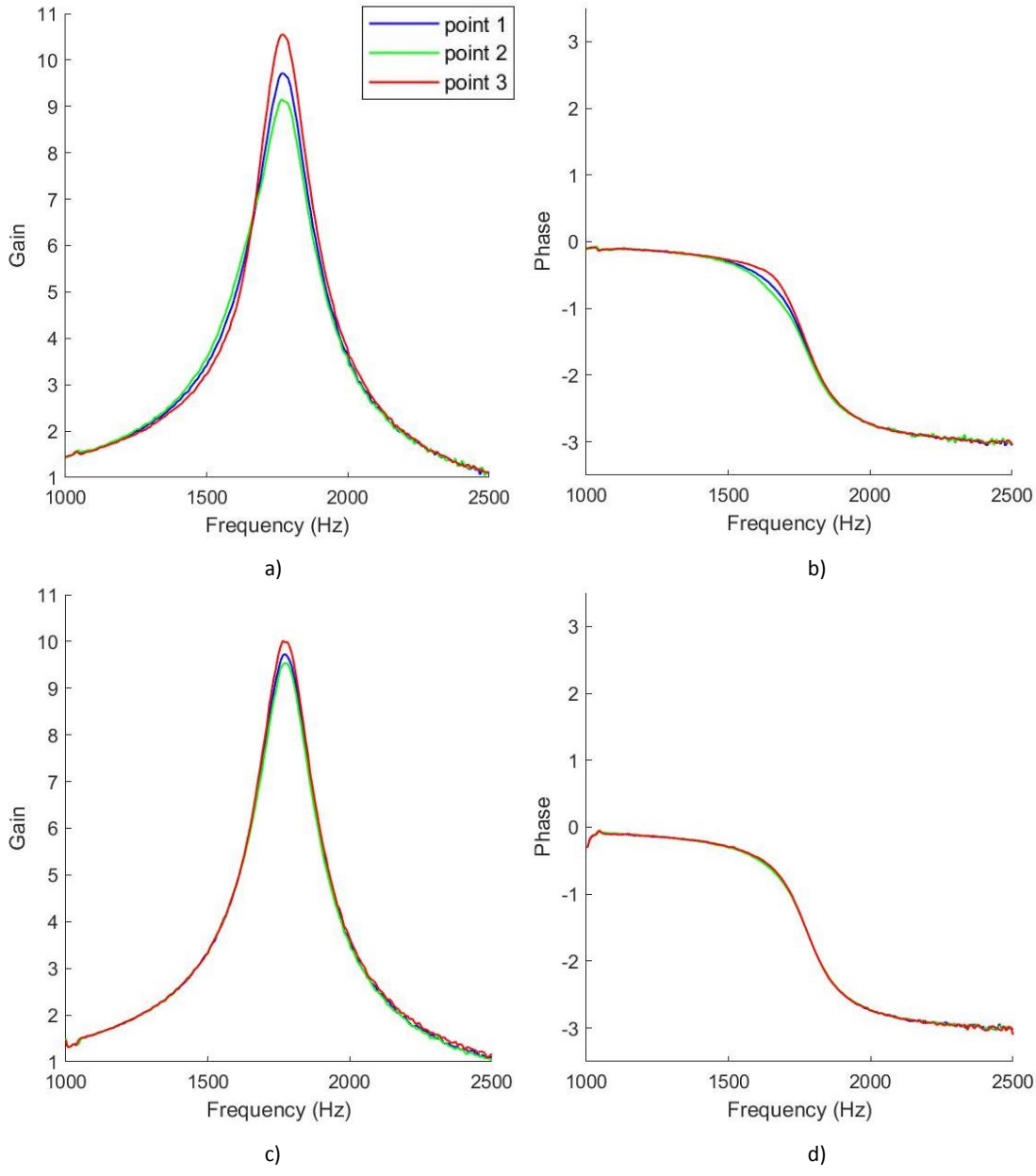


Figure 28 – Shear Transmissibility Functions and Phase plots for trial specimens at various points on the die surface, in both shear directions (a+b – y_1, c+d – y_2)

The analyses described in Section 2.5.3 are used to determine the apparent shear material properties (modulus and loss factor) of the bond using the measured transmissibilities at each measurement point. Similarly to the bounce tests, averaging and interpolation methods are used to smooth the data and improve peak frequency identification. These methods are particularly important in the shear because the peak width is narrower compared to the bounce case. Measurements indicate that the natural frequency is always slightly higher, for shear direction 2 than for direction 1, indicating that the imperfection has split the shear mode frequencies. Table 2 shows the calculated (apparent) values for Young's modulus and loss factor.

The apparent shear modulus for shear direction 1 lies in the range 1.424MPa to 1.428MPa, whilst for shear direction 2 they lie in the range 1.429MPa to 1.436MPa. These ranges are small and correspond to variations of 0.29% and 0.51% respectively. It is interesting to note that the calculated moduli do not follow the same variation behaviour as the peak gains, with edge values (points 2 and 3) both higher than the central values (point 1) in both directions. This backs up the assertion that the moduli are independent of the imperfection. However, this could be due to the much lower response of the torsion mode in the transmissibility, and so limit its ability to interfere with and shift the translation dominated peak of interest at differing measurement points.

The loss factors in shear direction 1 lie in the range 0.096 to 0.111, whilst for shear direction 2 they lie in the range 0.101 to 0.106. Following the same logic as for the bounce tests, the variation is largest when the contaminating torsional component is most significant. This occurs at measurement points 2 and 3, which are furthest from the torsion axis, and shear direction 1, where a larger torsion component was observed. It is expected that central point 1 is least affected by torsion and so is the most accurate point to calculate the loss factor. It is also interesting to note that at the central point the apparent loss factors for the two shear modes are identical.

Table 2 - Measured material properties from Transmissibility Function at each point in both shear directions

Measurement Point	1		2		3	
Shear Direction	1	2	1	2	1	2
Apparent Shear Modulus (MPa)	1.424	1.429	1.428	1.436	1.424	1.430
Shear Hysteretic Loss Factor	0.104	0.104	0.111	0.106	0.096	0.101

Figure 29 shows a comparison between the measured transmissibility and transmissibility calculated using the complex material model with material values from Table 2. The generated data fits the test results very well, with good agreement of the peak values as well as close replication over frequency. Similar to the bounce case, there is some variation away from the peak value for the measurement points experiencing the largest torsion contamination because of the loss factor error induced by including the torsion components in its calculation. The differences are much lower for the shear cases because of the smaller loss factor errors as well as reduced peak width and frequency. The central point (point 1) which experiences the lowest torsion contribution can be seen to be replicated almost perfectly over frequency for both shear directions.

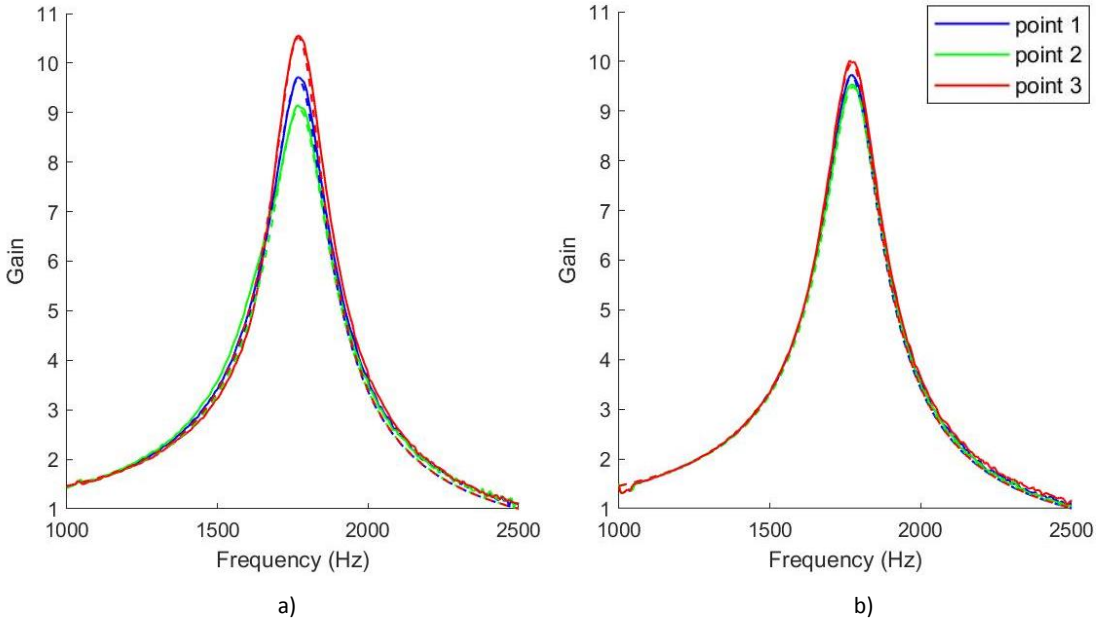


Figure 29 - Comparison of Shear transmissibility functions from testing and hysteretic SDOF generated using measured parameters (dashed), at various measurement points and directions (a – y_1, b – y_2)

2.6.2. Mechanical Loading

In this section, the influence of short term mechanical loading on the trial sample in shear and compression are evaluated. This mechanical loading was conducted initially to provide a second assessment of the material properties, particularly modulus values, and was applied in the form of a quasi-static force deflection test. The sample was subjected to three load and release cycles up to strains of 10, 20 and 25% consecutively at a strain rate of 10%/min (0.1mm/min). The compression tests were performed first, followed by shear tests (shear direction 1 only). A load cell was used to measure the applied force, but excessive levels of noise from the load cell made the force results

unclear. However, the process provided an opportunity to assess changes to bond properties caused by short-term mechanical loading. After the mechanical loading had been applied and released, the sample was retested using the same methods and measuring points as the multipoint vibration tests analysed in the previous section. The following sections compare the transmissibility functions and phase plots at the various measurement points before and after mechanical loading, allowing changes to the bond properties and behaviour to be assessed.

2.6.2.1. Bounce

Figure 30 compares the experimentally measured compressive transmissibility and phase plots, before (black) and after (red) mechanical loading has been applied, at the five measurement points on the surface of the die. It can be seen clearly that the bounce transmissibility changes after the load has been applied. For the translation dominated bounce peak, it can be seen that all measurement points experience a reduction in peak gain amplitude and the peak shifts to a lower frequency. The features corresponding to the possible rocking modes are also enhanced, indicating a greater level of rocking motion and suggesting the imperfection has been worsened by the loading. These changes are also apparent in the phase plots, where it can be seen after loading that the bounce and possible rocking mode frequencies reduce slightly and the phase differences at frequencies coinciding with the possible rocking modes are more significant.

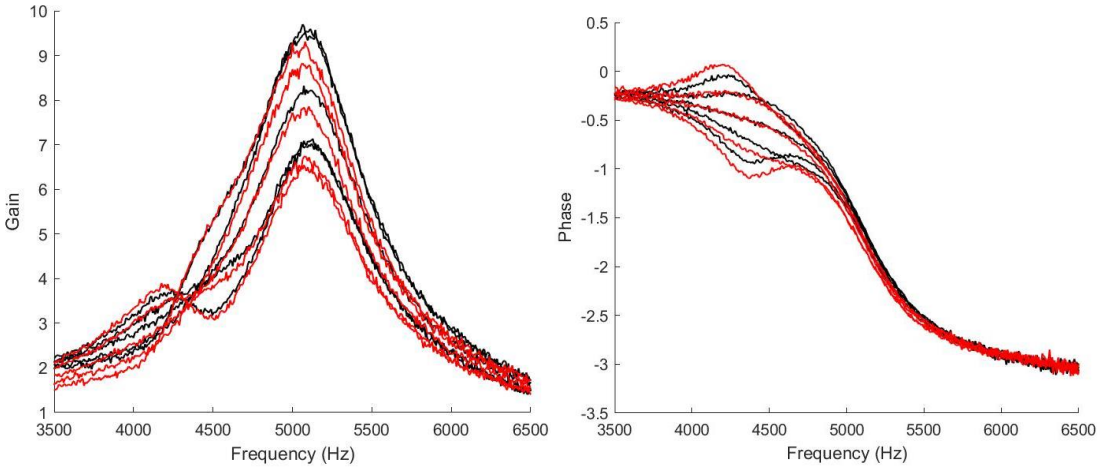


Figure 30 – Comparison of Transmissibility functions and Phase Plots before (black) and after (red) mechanical loading

The post static testing results were analysed using the same methods as the previous section to calculate the material properties. Table 3 and Table 4 show the apparent Young's modulus and

hysteretic loss factors, respectively, for each measurement point, including the absolute and percentage changes in bond properties. Table 3 indicates that the mechanical loading has reduced the apparent Young's modulus by between -0.77% and -1.90%, with a drop of -1.17% observed at central point 1. In absolute terms, these changes correspond to an approximate drop of 0.1-0.2 MPa. This strain-softening behaviour is commonly observed in elastomers and is known as the Mullins effect, where a rubber-like material's mechanical properties change after exposure to an initial deformation [65]. This results in lower stress to be experienced in subsequent deformations to the same strain, i.e. a reduction in modulus [65]. This effect occurs whenever the elastomer is deformed to strains larger than it has previously experienced [65].

Table 3 – Apparent Young's modulus values and changes before and after mechanical loading

	1	2	3	4	5
Initial (MPa)	11.83	11.89	11.96	11.78	11.77
post static (MPa)	11.69	11.80	11.73	11.65	11.61
Change (MPa)	-0.14	-0.09	-0.23	-0.13	-0.16
% change	-1.17	-0.77	-1.90	-1.13	-1.39

Table 4 indicates that the mechanical loading has increased the loss factor significantly at all measurement points, by between 4.8 and 8.1%, with a 5.6% increase observed at central point 1. These changes relate to an absolute change in compressive hysteretic loss factor of between 0.008 and 0.012.

Table 4 – Compressive Hysteretic loss factor values and changes before and after mechanical loading

	1	2	3	4	5
Initial	0.124	0.144	0.146	0.107	0.105
post static	0.131	0.153	0.158	0.115	0.111
Change	+0.007	+0.008	+0.012	+0.008	+0.005
% change	+5.62	+5.86	+8.13	+7.77	+4.79

Figure 31 shows transmissibilities calculated using the complex stiffness model with Young's modulus and loss factor values from the two rounds of testing (Table 3 and Table 4). The generated transmissibilities contain no response at the coupled rocking modes and no noise, allowing a clearer interpretation of changes occurring. Figure 31 clearly shows some of the changes described earlier, including the gain reduction at all points (increase in loss) and the reduced natural frequency (reduced modulus), as well as the greater overall spread in gain (greater rocking). Figure 31 also indicates a change in the direction of rocking or an increase in the rocking component, θ_2. For the pre-static loading

results, it was found that die edges 4-5 and 2-3 had similar gains, indicating the rocking axis was approximately parallel to y and the motion dominated by θ_1. However, post-static loading results show that the measurement points on these edges now have a larger gain difference between them, indicating a larger component of θ_2. This suggests the resultant rocking axis direction has changed and the imperfection has been changed significantly by the mechanical loading. It will be seen later that there are other factors that alter the observed response, such as environmental temperature and aging/further cure. However, it is seen that their effects on response differs to that observed here, i.e. the reduction in modulus and increased loss. The compared tests were also conducted within a short time interval and within the same environment, minimising any time dependent effects and any temperature variation experienced are too small to have the effects observed.

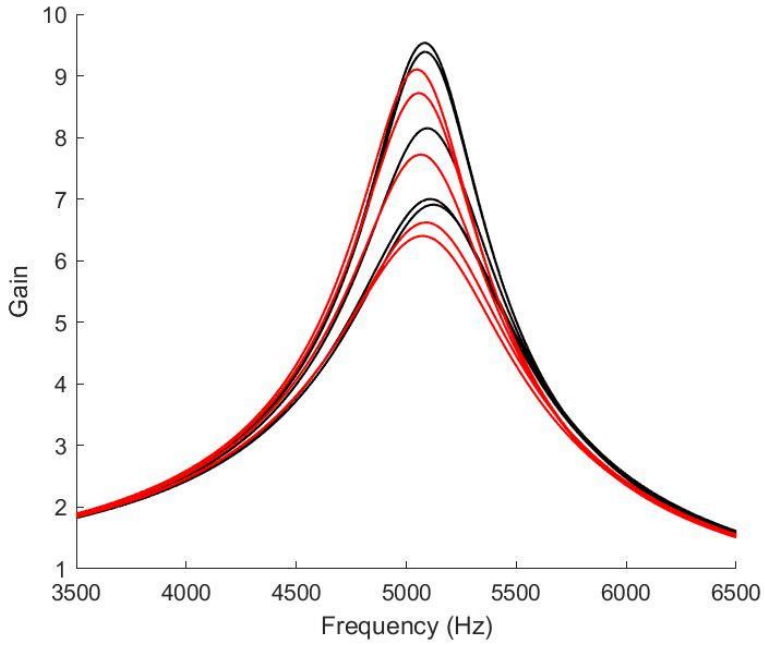


Figure 31 – Comparison of Transmissibility Functions generated with measured properties before (black) and after (red) mechanical loading

2.6.2.2. Shear

Figure 32 compares the experimentally measured shear transmissibility and phase plots, before (black) and after (red) mechanical loading has been applied, at the three measurement points on the die edge for both shear directions. It can be seen clearly that changes have occurred in both shear responses. For the translation dominated shear peak, it can be seen that the peak gain amplitude reduces and the peak shifts to a lower frequency with mechanical loading, similar to the bounce results.

The frequency shift is also observed in the phase plot. For shear direction 1 the magnitude of the contaminating rotation does not appear to change significantly. For shear direction 2, the contaminating rotation is greater, indicating greater coupling to the rotation mode. This coupling is observed in both transmissibility and phase plots at approximately 1.5-1.6KHz. Despite the greater contamination in shear direction 2 induced by mechanical loading, the rotation magnitude is still greater in shear direction 1. These changes agree with those observed for bounce tests, indicating that the imperfection has changed significantly and now causes greater coupling between shear direction 2 and rotation, as well as bounce and rocking about the y_2 axis.

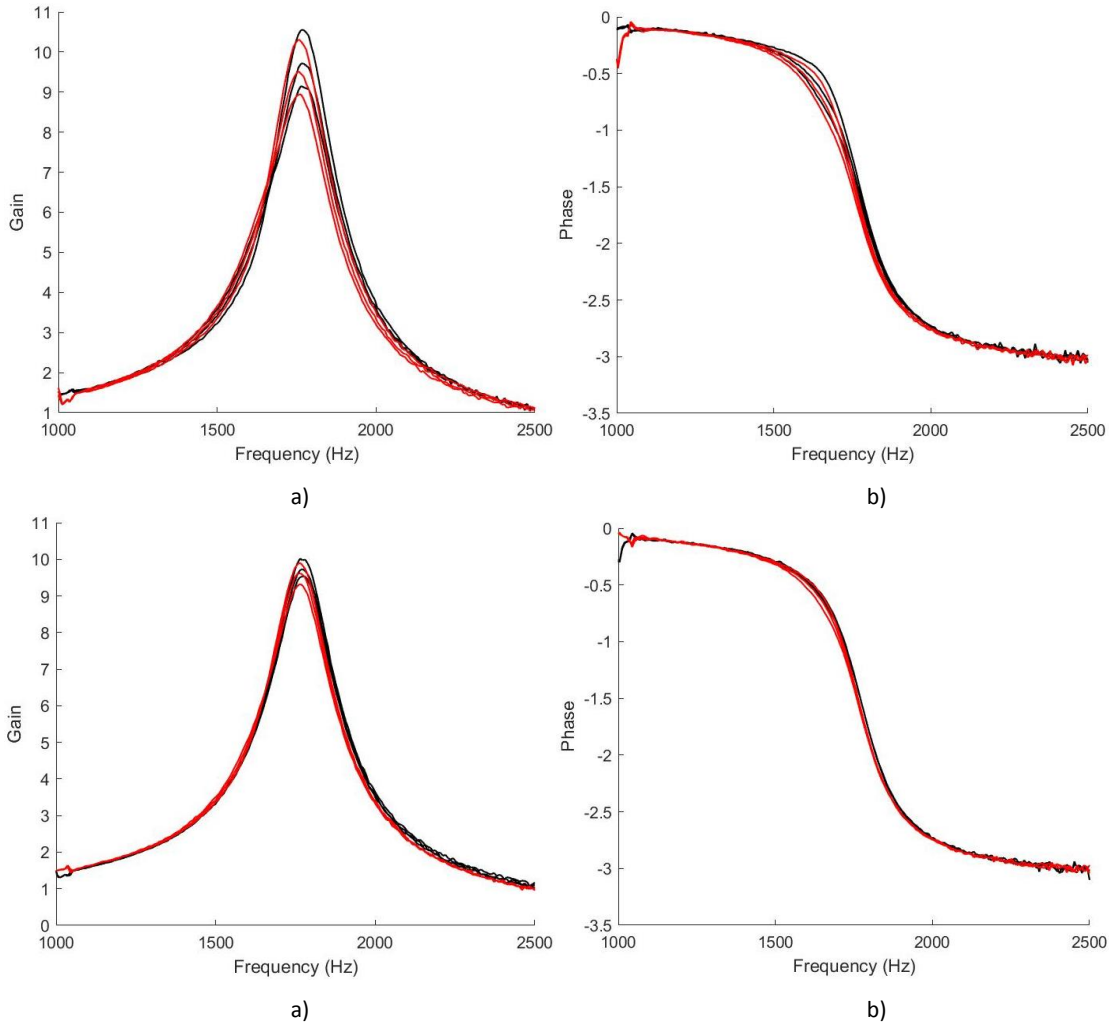


Figure 32 – Comparison of Transmissibility functions and Phase Diagrams before and after mechanical loading in shear direction y_1 (a+b) and y_2 (c+d)

The post static testing results were analysed using the same methods as the previous section to calculate the material properties. Table 5 and Table 6 show the apparent shear modulus and hysteretic loss factors, respectively, for each measurement point, including the absolute and

percentage changes in bond properties. Table 5 indicates that the mechanical loading reduces the apparent shear modulus by a small amount.

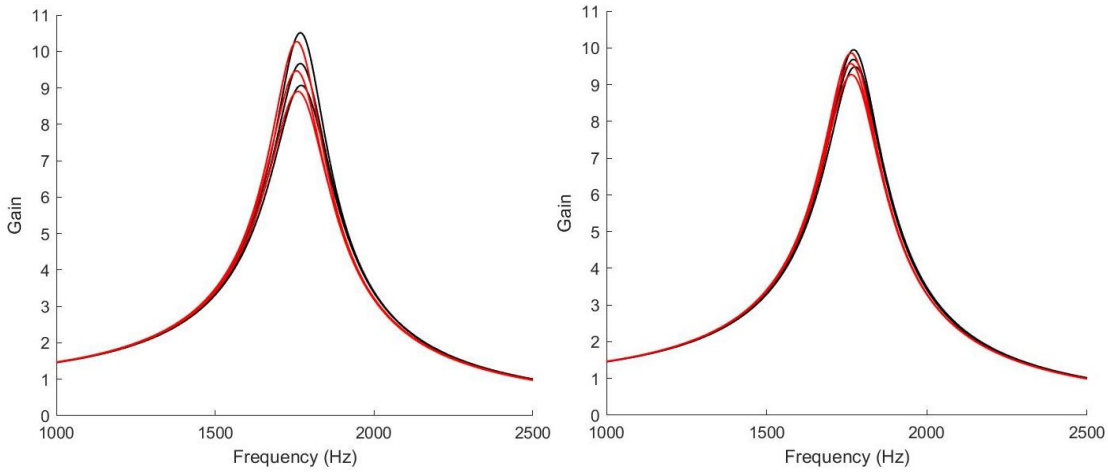
Table 5 – Apparent shear modulus values and changes before and after mechanical loading

	1		2		3	
Shear Direction	y_1	y_2	y_1	y_2	y_1	y_2
Initial	1.424	1.429	1.428	1.436	1.424	1.430
post static	1.405	1.415	1.412	1.419	1.406	1.416
Change	-0.019	-0.014	-0.016	-0.018	-0.018	-0.013
% change	-1.36	-0.95	-1.13	-1.22	-1.28	-0.95

Table 6 indicates that the mechanical loading increases the loss factor at all measurement points. The changes at the central point relate to absolute changes in shear hysteretic loss factor of 0.0022 and 0.0012. As observed for shear modulus, shear direction 1 experiences greater changes on average as well as at the central point. The greater effect in this direction is likely to be because this is the direction that underwent mechanical loading (quasi-static force deflection testing was only conducted in a single shear direction). However, a different effect is seen when observing the change in loss factor across the die measurement points in each shear direction. With shear direction 1 now varying by -7.92 and +6.41 (previously +8.11 and +6.67%), and shear direction 2 now varying by -2.95 and +3.24% (previously -2.68 and +2.11%). Therefore, the magnitude of contaminating twist at the translation mode has increased in shear direction 1, but reduced in direction 2, although shear direction still has a greater magnitude of contamination. These quantitative comparisons confirm the assertions made earlier by visual inspection of the testing results. All of the behaviour changes described can be observed in the TFs generated using the hysteretic SDOF model and measured material properties shown in Figure 33.

Table 6 – Shear Hysteretic loss factor values and changes before and after mechanical loading

	1		2		3	
Shear Direction	y_1	y_2	y_1	y_2	y_1	y_2
Initial	0.104	0.104	0.111	0.106	0.096	0.101
post static	0.106	0.105	0.113	0.108	0.098	0.102
Change	0.0022	0.0012	0.0021	0.0024	0.0023	0.0009
% change	2.17	1.19	1.91	2.31	2.37	0.91



a) b)

Figure 33 – Comparison of Transmissibility Function generated with SDOF model before (black) and after (red) mechanical loading in shear direction y_1 (a) and y_2 (b)

2.6.3. Environmental Temperature

Changing the environmental temperature can have a significant effect on the performance of MEMS sensors because the bond properties change and stress and deformation effects on the MEMS die. In this section, the dynamic behaviour of the bond will be assessed over temperature. This is achieved by observing the measured bond properties (moduli and loss factors) change over a typical operating temperature range of -70 to 150°C in both compression and shear. The bond properties will be calculated by analysing the transmissibility functions measured at various temperatures using the methods described earlier. Unlike previous sections, measurements are only made at a single central point on the die surface and edges in compression and shear tests respectively. The selected measurement point was shown earlier to be least affected by any contaminating motions and is the most appropriate location to analyse the translational modes and hence bond properties. The main aim of this section is to quantify the magnitude of the changes to bond properties over the specified temperature range. The findings will inform changes to the testing procedure when using bonds with different design parameters.

To perform vibration tests as the temperature is varied, the previous test setup must be altered from previous tests. The test samples are enclosed in a temperature chamber which contains an internal heating element to increase the environmental temperature and allows liquid nitrogen to be injected from an attached Dewar to decrease the temperature. A thermo-couple is placed within the chamber, close to the specimen, to measure the air temperature within the chamber. Before

performing measurements at a new temperature, the test sample is left for 15-20 minutes to acclimatise and allow the bond to reach the desired temperature. To assess the level of thermal equilibrium in the chamber the temperature fluctuations are observed via the thermo-couple output, with measurements only recorded when these fluctuations are ±1°C about the desired temperature. Temperature fluctuations are unavoidable due to the presence of holes at the top and bottom of the chamber to allow the sample to be attached to the shaker and access for the laser. The holes were covered as much as possible to reduce heat transfer without compromising the measurements. The fluctuations were worse for temperatures below ambient due to the sudden release of nitrogen through the solenoid valve.

Figure 34 shows a schematic diagram and photographs of the temperature test setup. The chamber is raised from the floor to allow room for the shaker to be placed underneath. A steel connection rod is then used, with M4 threads at either end, to attach the trial sample to the shaker armature, while raising the sample well into the chamber through the hole in the base of the oven. The laser vibrometer is extended and placed above the chamber, pointing vertically down with the laser access through the hole in the top of the chamber.

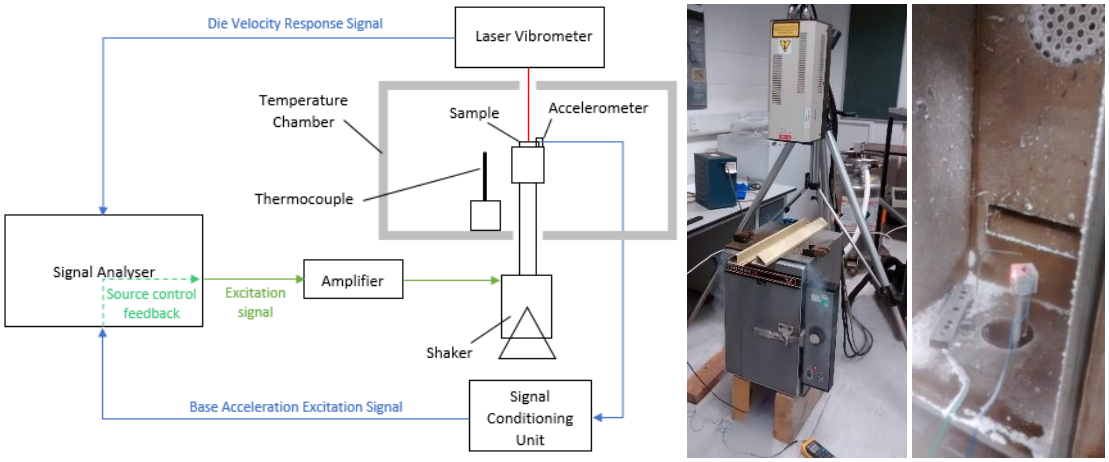


Figure 34 - Diagram and photographs of chamber setup

2.6.3.1. Bounce

Figure 35 shows the bounce transmissibility functions measured at the centre of the die and at 10°C intervals over the range -40 to 150°C, lower temperatures have been omitted due to suppressed and noisy responses. For each measured temperature, a dominant resonant peak is present. At 20°C the resonant peak is at approximately 5.1KHz, corresponding to the translational dominated bounce

mode observed in the multipoint tests. The peak gain and peak frequency vary greatly over the temperature range. As the temperature increases the modal frequency reduces and the peak gain increases. The modal frequency changes from approximately 6.7KHz at -40°C to 4.2KHz at +120°C, and peak gain from 3 to over 20 at the same temperatures.

The transmissibility functions contain significant levels of noise which affect the accuracy of the analysis. The noise increases as the temperature moves away from ambient conditions, with very high levels of noise observed at the extremes of the temperature range. The noise depends on the signal level/ focus of the laser (which is a measure of the intensity of the reflection off the die surface) the temperature of the air in the chamber which causes density and laser refraction to change, altering the focus of the laser. The transmissibility functions also include distortions from the shaker (shaker artefacts). These artefacts appear as sharp sporadic responses at a single frequency and are often associated with the testing setup. They can appear at frequencies associated with moving components such as the fan in the chamber, or resonance of the shaker armature, and have been seen due to cross-axis coupling of measurement transducers [59]. These artefacts were present in earlier multipoint tests but were small and occurred at frequencies away the modal peak and so had no detrimental effect on the results or analysis. The magnitude of the artefacts is much larger at ~4kHz. As the temperature increases it is observed that this artefact does not shift as significantly as the translation peak does, with their proximity increasing such that at 120°C the artefact and peak are less than 500Hz apart. Another artefact appears at approximately 6-6.5KHz and has a similar effect at the lowest temperatures, and actually coincides directly with the modal peak at certain temperatures.

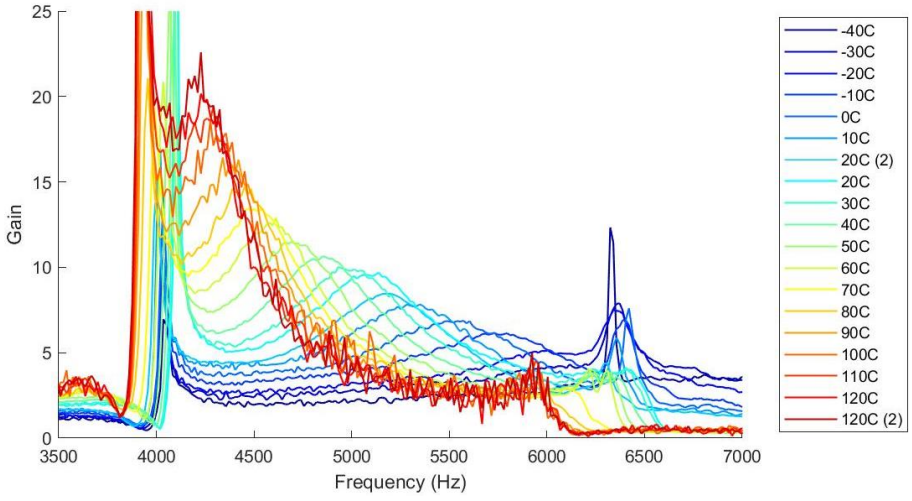


Figure 35 – Measured Bounce Transmissibility Functions for varying Environmental Temperature

Despite the presence of noise and artefacts in the transmissibility function the bond properties (Young's modulus and loss factor) have been calculated over temperature using the analysis procedures described in Section 2.5.3. Figure 36 summarises the results obtained for the apparent Young's modulus and loss factor with temperature. The figure indicates that Young's modulus decreases with temperature, and at a temperature of 120°C the apparent modulus is ~8MPa. There are two values plotted at a temperature of 20°C because the temperature variation was conducted in two stages: the first was a heating test from +20°C to +120°C, and the second was a cooling test from +20°C to -70°C. The initial ambient temperature measurement for the first stage has a lower apparent modulus than for the second stage, indicating that some stiffening has occurred due to the time testing at elevated temperatures. This stiffening may be attributed to changes in the material properties of the silicone due to aging/ further curing or viscoelastic mechanisms changing the stress/strain state of the bond.

Figure 36 also indicates that the compressive hysteretic loss factor also decreases with temperature, and at a temperature of -40°C the loss factor is approximately 0.3. The measurements at 20°C indicate there is a significant change between the two ambient temperature tests, and this is attributed due to the time testing at elevated temperatures which cause a ~10% change in loss factor.

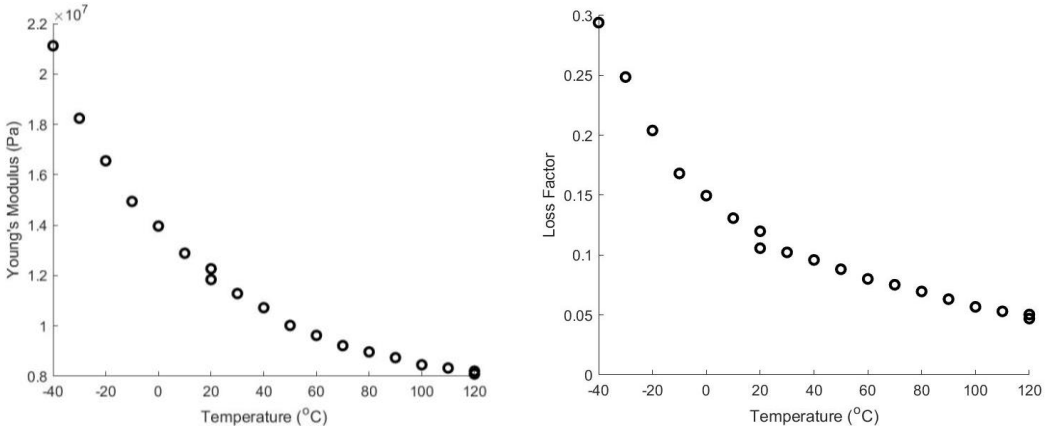


Figure 36 – Measured Bounce Properties over temperture

Figure 37 shows the transmissibility functions generated using a SDOF hysteretic damping model with the measured bond properties over temperature and comparison with test data. It can be seen that smooth changes over temperature occur and the general trends observed in the test data have been replicated, with generated data fitting well to the test data.

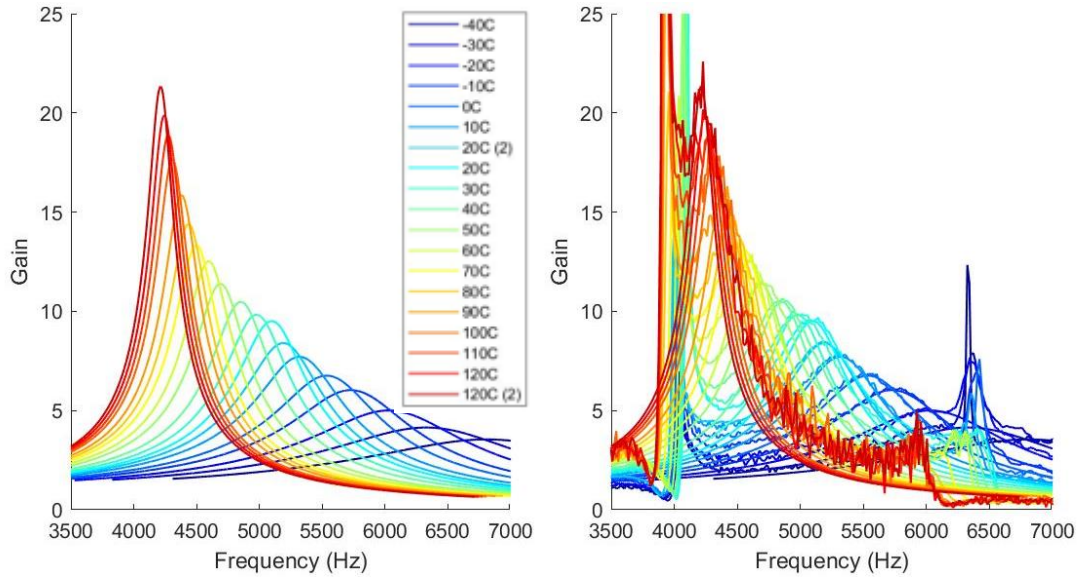


Figure 37 – Bounce Transmissibility functions generated using the complex stiffness model and comparison with Test data

2.6.3.2. Shear

Figure 38 shows shear transmissibility functions measured at the centre of the die edge and at 10°C intervals over the range -40 to 150°C, lower temperatures have been omitted due to supressed and noisy responses. Modal peaks can be seen for all temperatures shown. These are clear for the temperature increase tests, but noise and artefact issues obscure the peaks in the cooling tests. At 20°C the peak is observed at approximately 1.8KHz, confirming the results shown in Section 2.6.1.2. for the translation dominated shear mode observed in multipoint tests. The peak follows a similar trend as bounce over temperature, with its peak gain increasing and frequency reducing as temperature is increased. The frequency change is not as great as in bounce.

In the bounce results noise was found to increases at the limits of the temperature range considered. However, in the shear tests the noise levels are much greater for all cooling temperatures. In the heating test an artefact is found at approximately 1.5KHz which shifts with the modal peak but does not interfere with it. In the cooling tests, an artefact or signal issue causes a splitting of the peak is found which almost completely obscures the peak, particularly the gain. These issues will significantly affect the accuracy of bond property estimation later at the low temperatures considered.

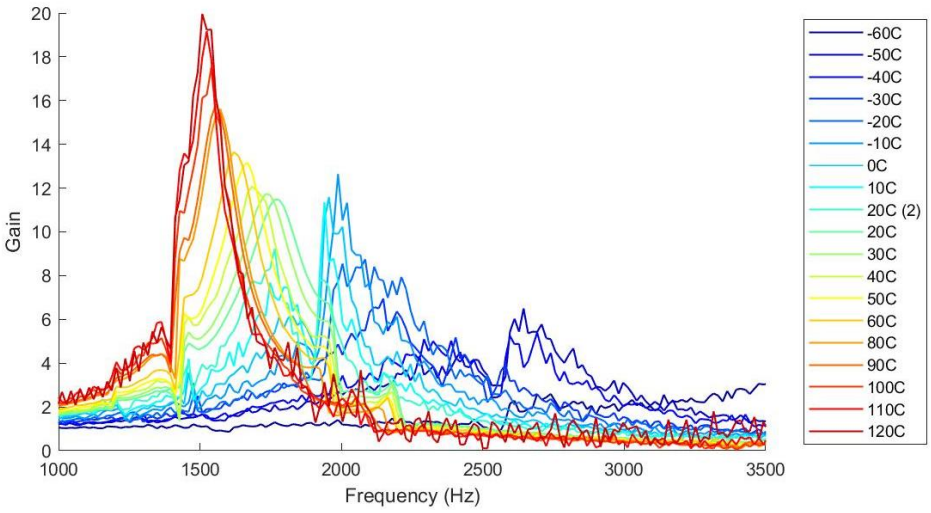


Figure 38 – Measured Shear Transmissibility Functions for varying Environmental Temperature

Using the analysis methods developed earlier, the material properties are determined from the transmissibility functions shown. Figure 39 summarises the results obtained for the apparent Young's modulus and loss factor with temperature.

Figure 39 indicates that the apparent shear modulus reduces with temperature. Despite the noise issues experienced during the cooling tests, the trend observed appears consistent and sensible. Unlike the compression results there is no significant shift in modulus between the two ambient tests - although this could be a consequence of the signal issues obscuring the peak.

Figure 39 also indicates that the loss factor generally reduces with temperature, but the signal issues discussed earlier are likely to have adversely affected the results for the cooling tests, due to inaccurate peak gain values. The heating tests show a decreasing trend in loss factor. A large increase in loss factor is seen between the two ambient tests, although due to the accuracy problems with the second measurement this cannot be relied upon.

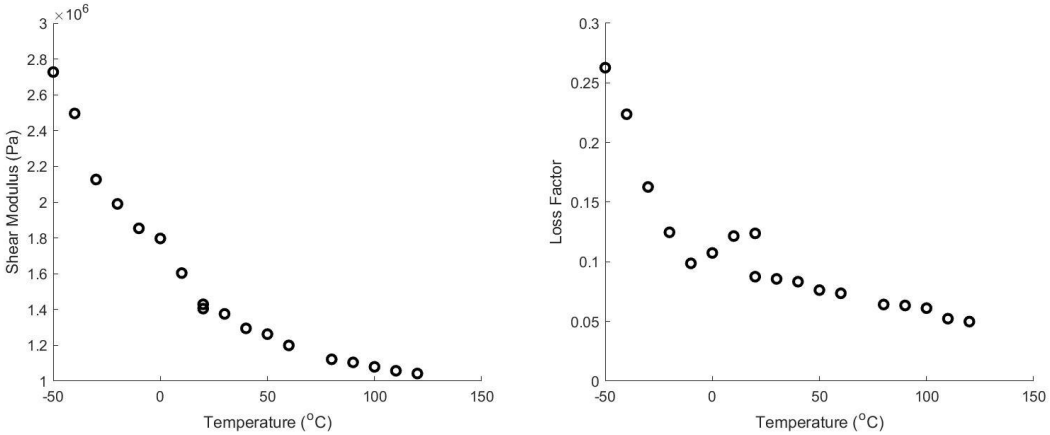


Figure 39 – Measured Bond Shear Properties over Temperature

Figure 40 shows the transmissibility functions generated using a SDOF hysteretic damping model with the measured bond properties over temperature, and comparison with test data. While the higher temperature data shows smooth trends and replicate the test results well. The noise issues experienced in the cooling tests, particularly loss factor, are clearly observable with quite sporadic changes in peak gain seen for temperatures between 20 and -20°C.

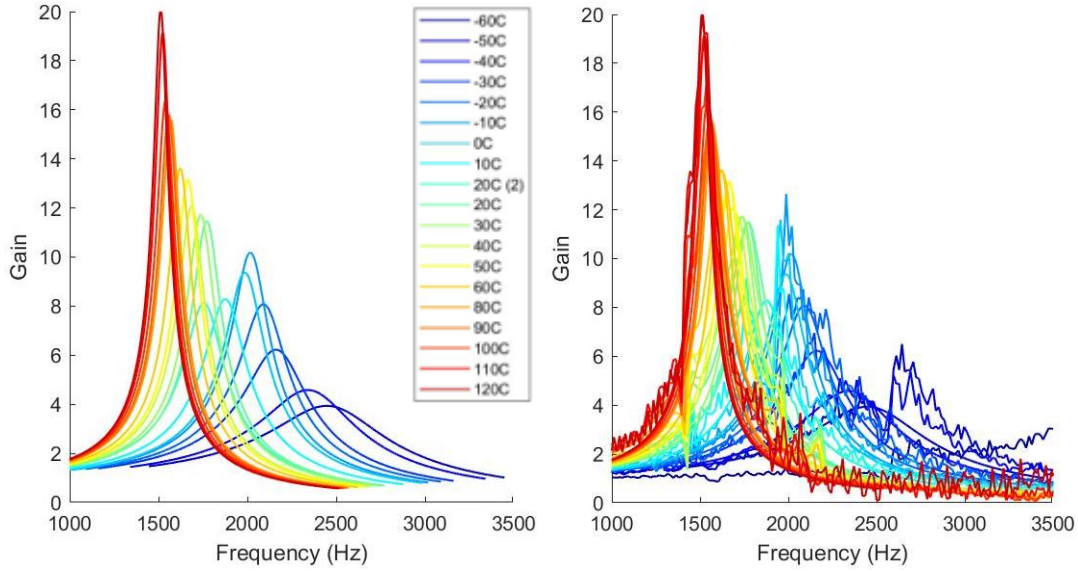


Figure 40 – Shear Transmissibility Functions Generated using the Complex Stiffness model and comparison with Test data

2.6.4. Response Linearity with Excitation Magnitude

In this section, the linearity of the die response is assessed to ensure future test are conducted at appropriate excitation levels and provide insight into behaviour changes in bonds because of design variations or over time due to exposure to differing temperature environments. Bond samples are analysed using sine sweep vibration tests for a range of different base accelerations and estimates made for bond properties. The tests use the same simple test setup used in the multipoint test (Figure 19), with no chamber or connection rod. Sine sweep vibration tests allow the magnitude of the base acceleration to be controlled (±0.1dB) over the whole frequency range and are well suited to linearity tests [59]. In the following sections, transmissibility functions and phase diagrams are measured and analysed for different base accelerations in bounce and shear directions.

2.6.4.1. Bounce

Figure 41 compares the measured transmissibility and generated transmissibility using the SDOF hysteretic damping model for various excitation magnitudes. The excitation level varies from

1mV-500mV, with a conversion factor of 1.014mV/ms^{-2}, and correspond to base accelerations of 0.986-493ms^{-2}. The response amplitude changes as the excitation is increased. As the excitation magnitude is increased the signal to noise ratio improves initially, but once over a limiting threshold the peak gain drops and the modal frequency reduces, indicating the presence of non-linearity. Comparing the measured and SDOF model generated data, a change in the peak shape is observed that is typical of non-linear behaviour. For the 500 and 250mV (and 100mV to a lesser degree) tests the peak appears skewed, particularly in comparison to the SDOF model generated transmissibility, indicating the presence of non-linearity which is not included in the analytical model. The lowest excitation tests appear to have larger gains at the peak, however, this is likely to be caused by noise issues experienced in the output signals.

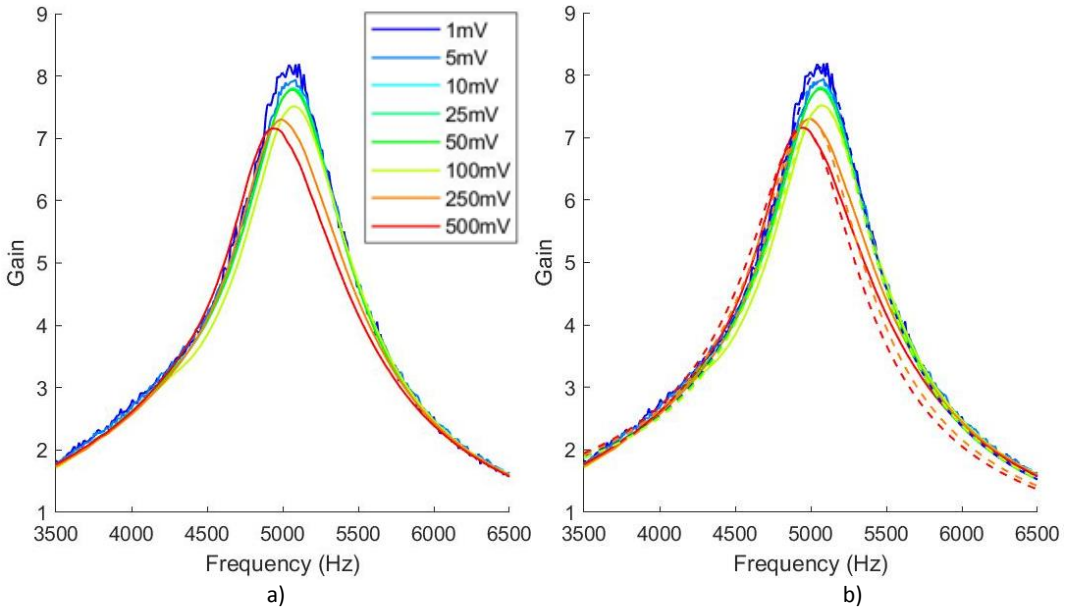


Figure 41 – Comparison of Bounce Transmissibility Functions measured and generated using the complex stiffness model, a) test data only, b) comparison with generated (dashed)

Figure 42 shows the apparent Young's modulus and compressive hysteretic loss factor, against base acceleration magnitude respectively. This figure indicates that the modulus is relatively stable at approximately 11.7MPa for accelerations up to ~10g, but reduces as the level of acceleration is increased further. Showing the linear response region and onset on non-linear behaviour.

Figure 42 also indicates a similar behaviour for the loss factor as the excitation level is increased. For excitations levels less than 50 mV (~5g) the loss factor is reasonably constant, but for higher levels of excitation the loss factor increases significantly. For low level excitations (1 and 5mV) noise is likely to cause inaccuracy in the calculated loss factor values. At larger excitation levels (10-

25mV, 1-2.5g), the noise reduces and the loss factor is relatively stable. However, the loss factor increases as the excitation level is increased further, for base accelerations 5g, 25g and 50g respectively.

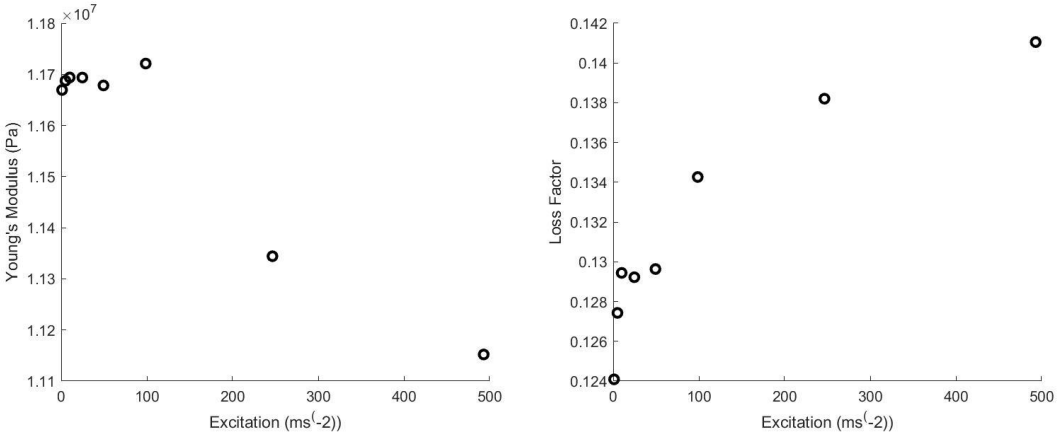


Figure 42 – Measured Bounce Bond Properties over excitation acceleration

It is concluded that the bond behaves linearly for base excitations up to 5g, and above this level the response becomes nonlinear. The non-linearity at first only affects the loss factor, and therefore the gain of the peak, with little change in the modulus observed at an acceleration of 10g. For excitations above 10g both the modulus and loss factor are significantly affected, this can be observed in Figure 43, a backbone-like graph of modulus against loss factor. The cause of this non-linear behaviour is associated with the strain dependence of the silicone bond, as at higher base excitation levels the bond experiences greater strains. A reducing storage modulus with increasing strains similar to those experienced in the experiments was observed by Warley et al. for a silicone rubber [66].

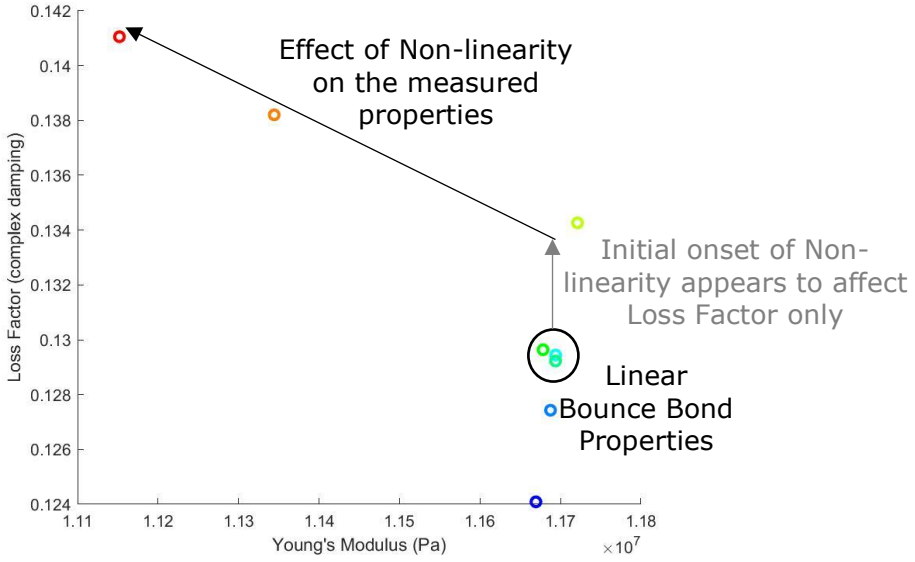


Figure 43 – Backbone-like plot showing linear bond bounce properties and their change with the onset of non-linear behaviour, Marker colour denotes increasing accelerations (blue-red)

2.6.4.2. Shear

Figure 44 compares the measured transmissibility and generated transmissibility functions calculated using the SDOF hysteretic damping model for various excitation magnitudes. The transmissibilities are similar for low levels of base acceleration (up to 25mV,24.7ms^{-2},2.5g), but agreement deteriorates for higher levels of acceleration as both the peak gain and frequency peak reduce and the peak becomes skewed, indicating the onset of non-linear behaviour. Unlike the bounce tests, noise is not an issue in the low excitation tests.

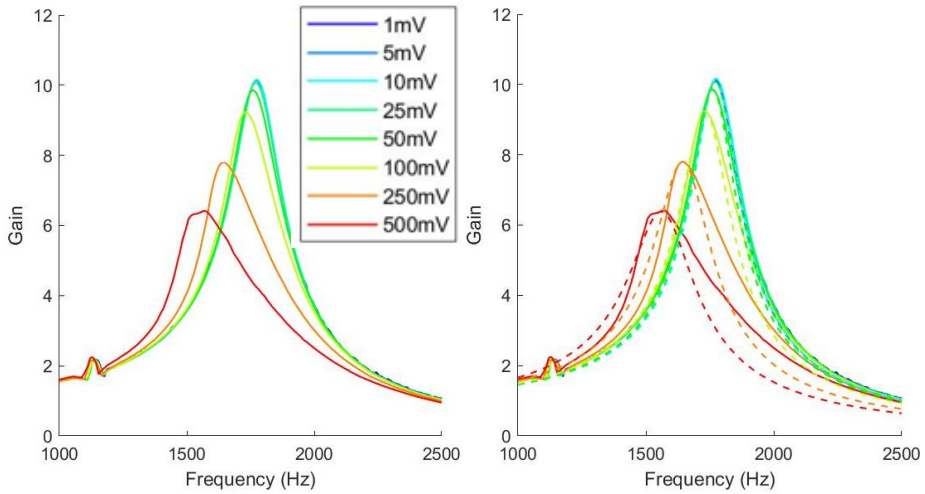


Figure 44 – Comparison of Shear Transmissibility Functions measured and generated using the complex stiffness model, a) test data only, b) comparison with generated (dashed)

Figure 45 shows plots of the apparent shear modulus and loss factor against base acceleration magnitude. It can be seen that for excitations up to 25mV (2.5g) the modulus is relatively stable at approximately 1.43MPa. Above this level the modulus reduces, indicating the onset of non-linear behaviour. Similarly for acceleration levels up to 2.5g, the loss factor is about constant at 0.1, but for larger excitation levels the loss factor increases.

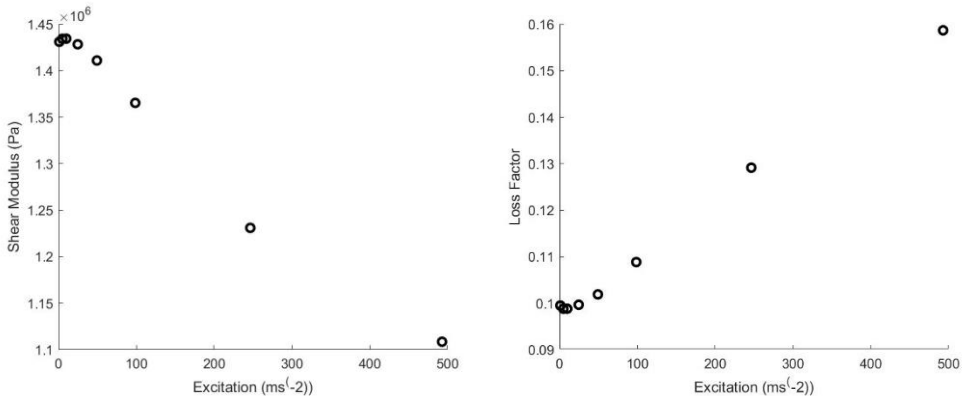


Figure 45 – Measured Shear Bond Properties over excitation acceleration

It is concluded that the bond behaves linearly for base accelerations up to 2.5g, and above this level the response becomes nonlinear. When this linear region is exceeded the modulus is seen to decrease significantly and loss factor increase, this can be further observed in the backbone-like graph shown in Figure 46. Unlike in the compressive tests the non-linearity of response has affected the modulus and loss factor at the same excitation level. Also, it can be seen that here in the shear tests, the lack of noise issues has produced an improved grouping of the excitations considered to be in the linear region of response.

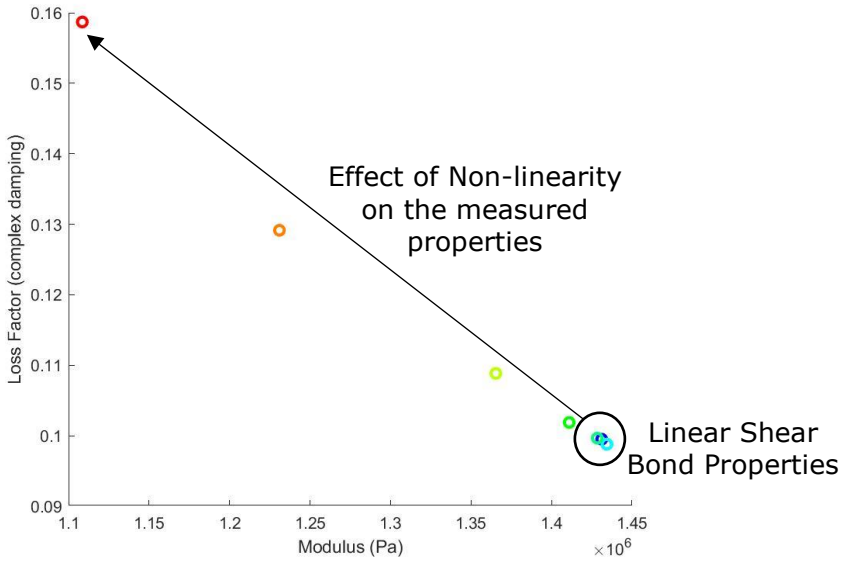


Figure 46 – Backbone-like plot showing linear bond shear properties and their change with the onset of non-linear behaviour, Marker colour denotes increasing accelerations (blue-red)

2.6.5. Surface Profile Measurement

To assess changes in the bond and die stress/strain state over time and to help identify any possible viscoelastic mechanisms occurring, it is important to be able to characterise the curvature and any change in curvature of the die under different conditions, such as the effect of temperature cycling and long term high temperature storage. This section focuses on experimentally measuring the surface profile of the die. The measurements made will also be used to validate and make comparisons with FE modelling results in a later chapter.

Numerous methods are available for measuring the shape of a surface. These typically use mechanical contact methods involving a stylus measuring displacement either as a line measurement (stylus moved across surface) or as discrete point measurements (grid like point measurements across

surface). For MEMS devices, the test assembly is small and the deformations of the die are expected to be small (sub-micron), which potentially limits the application of contact methods. For this reason, optical methods which are typically used to assess surface roughness and quality are assessed as an alternative to contact methods, as they are capable of sub- nanometre resolution of depth measurement (0.3nm). In this section, potential contact and optical methods are used to measure the surface profile of the die before and after bonding to assess the curvature induced in the die.

The Zeiss O-Inspect measuring machine was used to measure the surface profile initially. It uses a mechanical contact method based on a stylus to measure the surface profile and has a stylus resolution of 1.8µm. The height and location at each corner of the die was measured and then point measurements were taken across the die in a grid-like pattern, as shown in Figure 47. The initial flatness was measured to be 18.7µm and post bonding flatness was then measured to be 18.1µm. Given that the change in flatness (0.6µm) is less than the stylus resolution (1.8µm), it was concluded that the available contact method was not sufficiently accurate, and it is necessary to consider an alternative method offering a higher resolution.

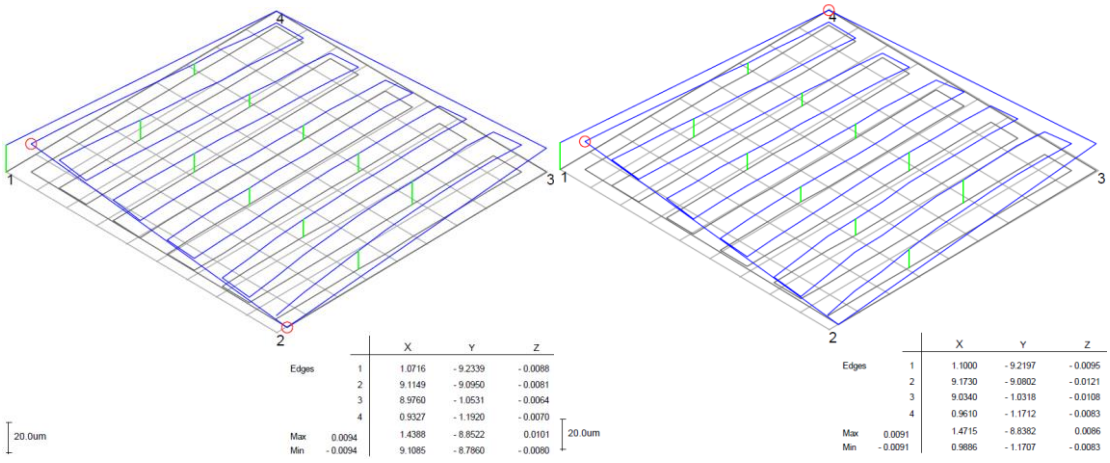


Figure 47 - Surface profile of the copper die before (left) and after (right) bonding measured using mechanical stylus Zeiss O-Inspect

The Bruker NP Flex 3D optical profiler was used to measure the surface profile. It is an optical instrument which uses white light interferometry to achieve sub-nanometre resolution in height (0.3nm). Figure 48 shows the measured surface profile scan. The measurement profile is similar to that obtained using the contact method described earlier, but with slight changes in deformation magnitude. It is difficult to assess and quantify the difference between scans, because there are no

referencing features to align the two scans. However, the results indicate that the central region appears to be flatter than at the edges, where most curvature is located. It is evident from the scans that the die surface initially (pre-bonding) exhibits a large saddle shape and bevelled edges caused by the guillotine cutting process used in the manufacture the sample. It is desirable to remove these effects in future tests.

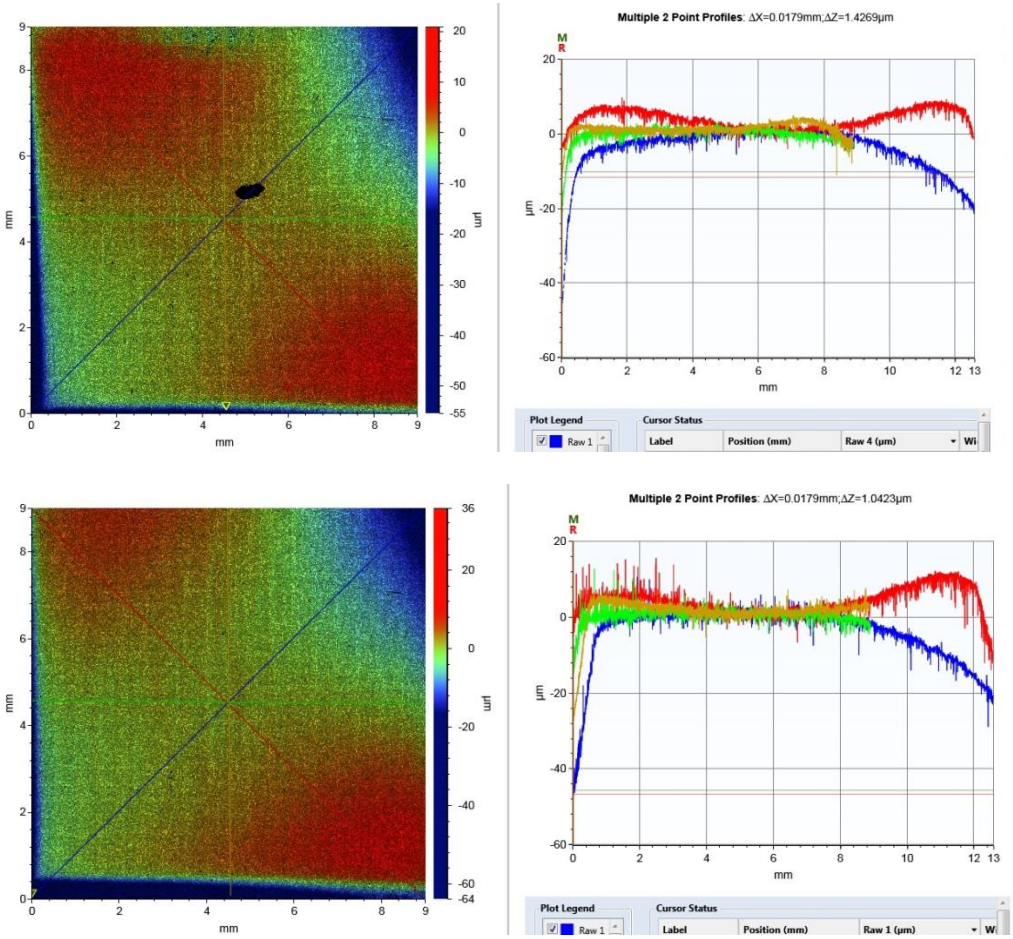


Figure 48 - Surface profile scan of the copper die before (top) and after (bottom) bonding using white light interferometry

In conclusion, trial surface scans have shown that the deformation occurring due to bonding is sufficiently large to justify further investigation. However, the measured deformations are too small to be measured reliably using the Zeiss O-Inspect measuring machine based on mechanical contact methods but can be measured accurately using the Bruker NP Flex 3D optical profiler. It was noted that if optical methods are used then referencing features must be added to the die to enable alignment of the scans and allow quantitative analysis. The method used to manufacture the die must also be changed to improve the initial flatness and remove the induced saddle shape and bevelled edges caused

by a guillotine like cut. In later tests the die will be manufactured by using an oil immersed EDM process to part off cross sections of a bar including grooves to act as a partial cross-hair, see Figure 49. Also, to reduce the output file sizes from the Bruker to assist in the processing and analysis of the data, the number of x-y points and stitching level (area of overlap between scans – multiple scans are required to measure the full surface) will be reduced. This will lose the resolution of the surface texture, but the z-axis resolution will be maintained at sub-nm level, and no data on the shape of the die will be lost.

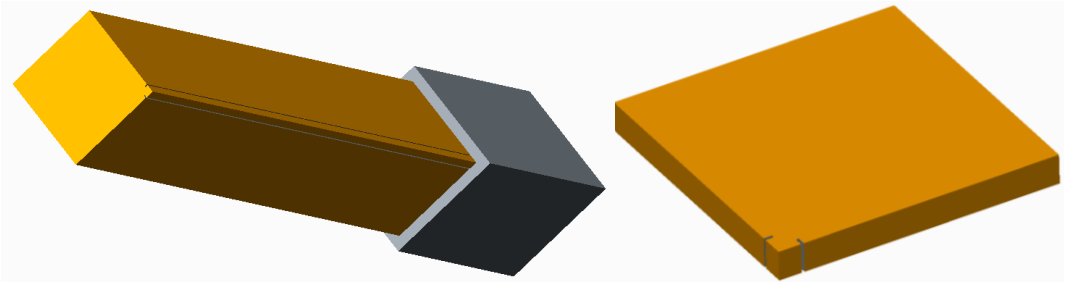


Figure 49 - Improved die design and manufacture, with reference features and greater flatness

2.7. Summary and Conclusions

A single bonded sample was tested experimentally to determine the material properties (modulus and loss factor) and stress/strain state under different environmental and loading conditions. Vibration test arrangements and procedures have been developed and applied in the bounce and shear directions to achieve these aims, including: interpreting the die mode shapes, evaluating changes to the die behaviour caused by short term mechanical loading, changes in environmental temperature and base excitation magnitude.

The motion of the die at modal frequencies was investigated by measuring the die response at different multipoint positions on the die surface or edge. By comparing the responses at different locations it was possible to analyse the overall die motion. The predominantly bounce and shear modal frequencies were identified and found to be contaminated by rocking/torsional components. It is believed that the resulting coupling between the translational and rotational coordinates was caused by imperfections in the bond and/or die manufacture and assembly processes. This hypothesis will be investigated further in the next chapter with derivation of an analytical model of an imperfect inclined bond, and by using relatively simple FE models to assess the influence of imperfections on transmissibility functions measured at different points on the die surface, similar to those used in the

multipoint experiments. The imperfections to be modelled include sloped bonds, offset of the die from its central position on the bond, and combinations of these. A qualitative analysis of the effects of imperfection on the transmissibility functions will be conducted. As well as a quantitative analysis investigating the implications on the accuracy of the obtained material properties.

The effects of short-term loading were assessed by subjecting the test sample to quasi-static force deflection tests in both compression and shear up to a maximum 25% strain. Although the results contained significant levels of noise, comparisons before and after the static tests showed that the response and bond properties (modulus and loss factor) changed significantly. In future tests, no mechanical loading will be applied to the die.

The effect of environmental temperature was assessed by conducting vibration testing in a temperature chamber. Significant changes to the response were observed over the temperature range tested, with approximate identification of the glass transition temperature at sub -50°C, due to the suppression of the modal peak observed. In these tests noise levels were increased, particularly in shear, which resulted in significant errors in determined mechanical bond properties. In future tests, several changes will be made to reduce/eliminate these issues. In particular, it is important to excite the sample at acceleration levels that remain within the linear region but improve the signal to noise ratio of the measurements. It was observed that using the chamber increased the noise levels because of condensation and vapour caused by using liquid nitrogen to cool the system. The chamber also caused spurious vibrations, due to its fan leading to artefacts in the transmissibility functions and in future tests this will be turned off momentarily while measurements are conducted.

The influence of using different levels of base acceleration to excite the sample investigated. Sine sweep tests were used to ensure a constant base acceleration was applied over the frequency range tested. The results showed a linear regions and non-linearity experienced were observed and identified in both tested directions and the differences between them and implications on the material properties were discussed.

A key objective within this chapter was to develop a Single-Degree-of-Freedom model under base excitation to represent the system being tested to determine the apparent material properties (modulus and loss factor) of the bond from experimentally measured transmissibility functions.

Although the method developed and used worked reasonably well several issues particularly with the loss factor were experienced during testing. Its accuracy is dependent on the quality of the measured transmissibility functions. The developed model uses only 3 points - the maximum gain point and the neighbouring points when quadratic interpolation is applied. The accuracy of this approach is affected by noise and the presence of artefacts near the peak. For low levels of noise, smoothing was used to improve accuracy, but this was limited to a moving average using only a small number of averaging points, and so cannot deal with larger levels of noise without artificially damping the response. Artefacts are difficult to remove, and if they affect the peak it is inevitable that the approach used will be inaccurate. It was also seen that the peak gain varies across the die due to the coupled rotation, and therefore unless measuring precisely at the centre of the coupled rotation the measured loss factor will be contaminated. An alternative method for determining the loss factor that is not based on the peak transmissibility value is to use the half-power method, based on the frequency bandwidth at the half-power points. In later chapters attempts will be made to determine an accurate and reliable method for calculating the loss factor in the presence of signal issues and coupling contamination based on a multi-power-bandwidth method.

Minimising the coupling observed in the experiments will be a priority. The hypothesis that this coupling was caused by manufacturing imperfections in the bonded sample will be investigated in chapter 3, using analytical models. While FE models will be created to investigate the errors induced by various imperfections in the calculated material properties.

3. Enhanced Loss Factor Analysis and Characterising Bond Imperfections

3.1. Introduction

In chapter 2, it was shown that the loss factor of the bond sample can be calculated from the peak gain of the transmissibility function, even when the damping is large. However, the accuracy of this method was found to be highly dependent on the quality of the transmissibility function measurement, with inaccuracies observed when significant levels of noise and artefacts are present, and the translation motion being measured is corrupted by coupled rotational components of motion. In this chapter, alternative methods of calculating the loss factor are investigated based on transmissibility functions, including the commonly used half-power bandwidth method and a derived, less well known, multi-power bandwidth method. These methods analyse the shape of the transmissibility, as opposed to the peak value, using the frequency bandwidth at different power levels to calculate the loss factor. Results obtained using these methods will be compared with the model used in Chapter 2 when analysing perfect and imperfect transmissibility functions. The single-degree-of-freedom hysteretic damping model described in Chapter 2 is used as the basis for generating transmissibility functions, with noise artificially added to these signals to simulate the effect noise has on loss factor error. Further improvements to the bandwidth models will be investigated, including removal of small damping assumptions and use of interpolation models to calculate bandwidth frequencies.

Coupling between translational and rotational motions of the die was observed in trial tests, causing errors in loss factor calculations and inconsistent results at differing measurement points on the die, and it was hypothesised that this coupling was caused by manufacturing or assembly imperfections in the bond. This hypothesis will be validated in this chapter by investigating the effect of sloped bonds using an analytical model. Simple FE models are used to investigate the effects of bond imperfections and die placement errors on transmissibilities under bounce and shear base excitations,

and the results are analysed to observe changes caused to the transmissibility functions measured at different locations on the die and quantify the loss factor and modulus errors caused by imperfections of different types and magnitudes.

3.2. Loss Factor Analysis Using Bandwidth Methods

In this section the underlying analysis for bandwidth methods is developed. The half-power bandwidth method is often used in modal analysis to estimate the damping in a system from transfer function (Frequency response or transmissibility) measurements [58] [61] [59] [67]. This method is presented first and its limitations for the current application explained. Alternative bandwidth-based methods based on the multi-power bandwidth method are then developed as a means to improve loss factor estimates.

3.2.1. Half-Power Bandwidth method

The half-power bandwidth is the difference between the two frequencies at which the response is half the power of the maximum response, i.e. difference between the frequencies ω_1, ω_2, when the transmissibility magnitude is equal to $\frac{T_{max}}{\sqrt{2}}$, as shown in Figure 50.

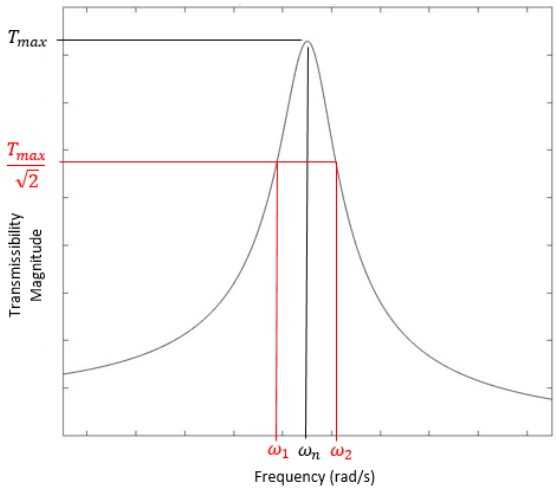


Figure 50 – Illustration of the Half power bandwidth on a modal peak

It is common for the loss factor to be expressed as the half-power bandwidth divided by the natural frequency i.e.

$$\eta = \frac{\omega_2 - \omega_1}{\omega_n} \tag{3.1}$$

The half-power method is well suited to determining loss factor estimates when the transfer function is dominated by a single mode. However, the accuracy of the estimate depends on the quality of the test data to calculate ω_1, ω_2 and ω_{n}. Any errors in these frequencies, for example caused by the resolution of the test data, or an error in the transmissibility magnitude due to, for example noise, resolution or artefacts, can induce significant errors in the loss factor estimate. To reduce these errors, it is proposed that the loss factors are calculated at different power levels and the results then averaged.

3.2.2. Multi-Power Bandwidth method

To determine the loss at the fractional power level p, the bandwidth is calculated by evaluating the frequencies when the transmissibility power is equal to p times the maximum transmissibility power. This is equivalent to:

$$(|T(\omega)|)^2 = p(|T|_{max})^2, \qquad \text{where } 0 < p < 1$$

Using equation (2.1) for the transmissibility and recalling that maximum transmissibility $|T|_{max}$ occurs when $\omega = \omega_n$ gives:

$$\frac{{\omega_n}^4 + {\omega_n}^4\eta^2}{({\omega_n}^2 - \omega^2)^2 + {\omega_n}^4\eta^2} = p\frac{1+\eta^2}{\eta^2}$$

Re-arranging this equation as a quadratic in ω^2 and solving, the frequencies defining the bandwidth $\omega_1 \text{and } \omega_2$ are:

$${\omega_1}^2 = {\omega_n}^2\left(1 - \eta\sqrt{\frac{1-p}{p}}\right), \qquad and, \qquad {\omega_2}^2 = {\omega_n}^2\left(1 + \eta\sqrt{\frac{1-p}{p}}\right)$$

Combining these equations, it can be shown that the loss factor is given by:

$$\eta = \frac{{\omega_2}^2 - {\omega_1}^2}{2{\omega_n}^2} \cdot \frac{1}{\sqrt{\frac{1-p}{p}}} \tag{3.2}$$

Equation (3.2) can be used to determine the loss factor based on the p'th power level. If the system being measured is a perfect single degree of freedom system, then the estimated loss factor will be independent of the level p used. However, if the measured transmissibility is affected by noise then different estimates would be obtained for different power levels. In what follows, to reduce the

effects of noise the loss factor is estimated for a range of p values between p=0.25 and p=0.9 and then the average value calculated. This method will be referred to as the averaged multi-power bandwidth method.

For cases when $\omega_1 \text{and } \omega_2$ are close and the damping is small, equation (3.2) for the loss factor can be approximated to

$$\eta \approx \frac{\omega_2 - \omega_1}{\omega_n} \cdot \frac{1}{\sqrt{\frac{1-p}{p}}} \tag{3.3}$$

When p=0.5, equation (3.3) reduces the standard half-power result given by equation (3.1).

3.3. Comparison of Loss Factor Analysis Methods

In this section, the performance of the loss factor calculation methods described in Sections 2.5.3. and Section 3.2. are assessed and compared for transmissibility functions generated using the Kelvin-Voigt single-degree-of-freedom hysteretic damping model with different loss factor values, frequency resolution and noise present. The effectiveness of smoothing functions to reduce the effects of noise is also assessed, together with improvements to the bandwidth methods and the use of interpolation models.

For the ideal case (no noise) the transmissibility function is generated using:

$$T^*(\omega) = \frac{X^*}{X_0{}^*} = \frac{k(1+i\eta)}{-\omega^2 m + k(1+i\eta)} = \frac{{\omega_n}^2 + {\omega_n}^2 \eta i}{{\omega_n}^2 - \omega^2 + {\omega_n}^2 \eta i}$$

To observe and quantify errors induced by the magnitude of the system loss factor and frequency resolution of the data, the loss factor, η and frequency resolution are varied from 0.01-0.5 and 0.01-10Hz respectively.

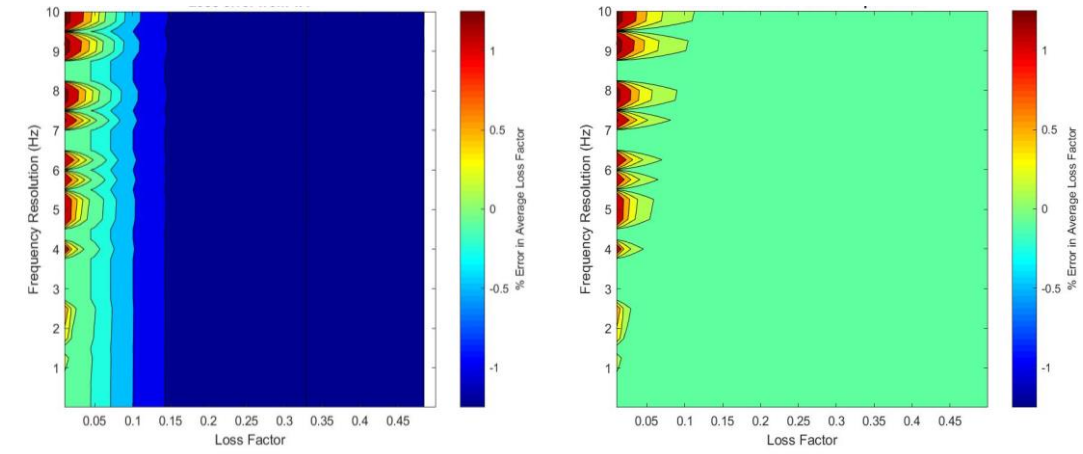
3.3.1. Inverse Maximum Transmissibility Methods and Improvements

In this section, the loss factor is calculated using the methods described in Section 2.5.3.2. based on the maximum transmissibility. i.e. eq's 2.4 and 2.3,

$$\eta \approx \frac{1}{|T^*{}_{max}|}, \qquad and, \qquad \eta = \frac{1}{|T^*{}_{max}| \sqrt{1 - \left(\frac{1}{|T^*{}_{max}|}\right)^2}}$$

It was shown in chapter 2, that the exact loss factor calculation provided a much-improved estimate for the loss factor, particularly at higher loss factors. Similar findings are observed here, together with a study into the effect of varying the frequency resolution of the test data.

Figure 51 plots the loss factor errors obtained using the two inverse maximum transmissibility methods of first order and the exact solution, for different loss factor values and frequency resolutions. It can be seen clearly that the exact solution has improved the accuracy for larger loss factor values. However, this method does contain areas of high error. These areas are associated with very low loss factors (<0.05) coupled with poor frequency resolution. This is caused by reduced peak width when damping is very low, which can lead to large changes in the gain over small frequency shifts, which may be missed if the frequency resolution is poor.



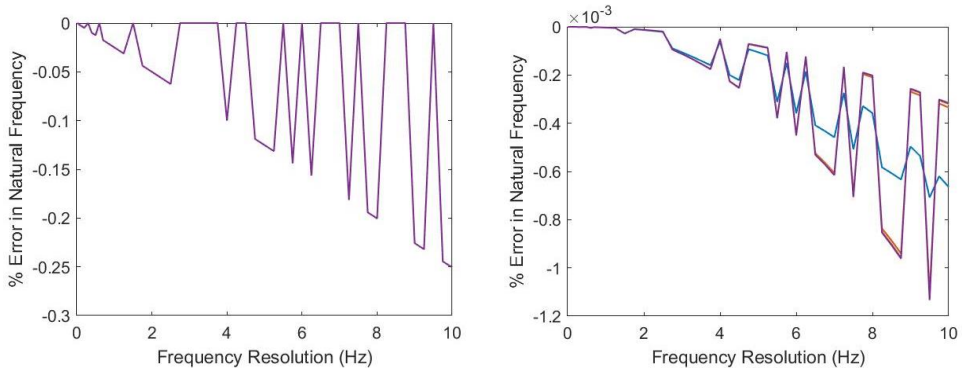
a) b)

Figure 51 - Loss Error for Inverse Transmissibility Methods, 1st order (a) and exact (b), for raw 'test' data of varying loss factor and frequency resolution

3.3.1.1. Quadratic Interpolation of Natural Frequency and Maximum Transmissibility

To improve the accuracy of natural frequency and maximum transmissibility measurements used in loss factor calculations an interpolation method is developed. Quadratic interpolation is performed at the modal peak, utilising the identified maximum point and its direct neighbours assuming a parabolic peak shape, to achieve improved accuracy values for peak gain and natural frequency, which can occur between measured frequency points. Figure 52 plots the calculated percentage error in the natural frequency found from the analysis for different frequency resolutions and loss factors. The results in b) were obtained using quadratic interpolation, whilst those in a) were obtained without. The use of interpolation reduces the error significantly (note scale change), although the error still increases

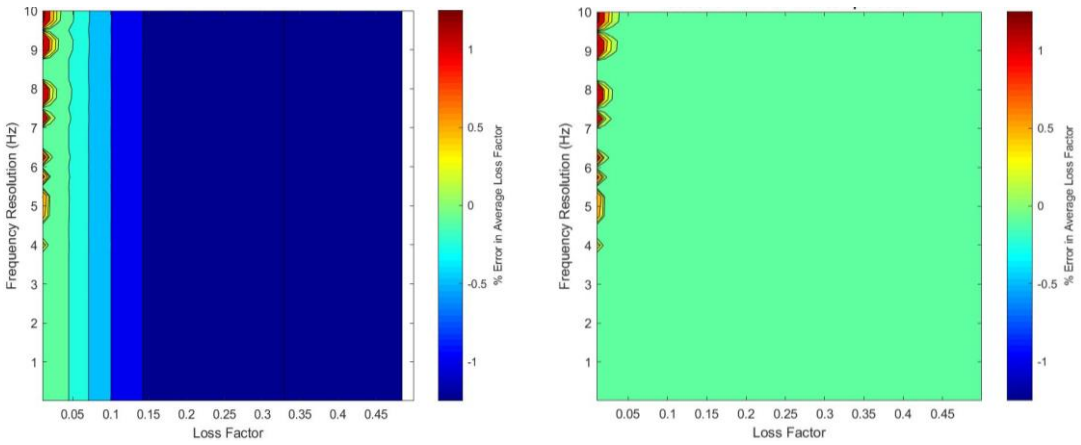
as the frequency resolution reduces. The interpolation does incur some dependency on the system loss factor, shown by the differing lines in b), however they follow the same general trend.



a) b)

Figure 52 - Natural Frequency Error over frequency resolution for various loss factors, from raw 'test' data (a) and 'test' data incorporating quadratic interpolation of frequency and transmissibility (b)

Figure 53 plots the loss factor errors obtained using the two inverse maximum transmissibility methods for different loss factor values and frequency resolutions. In contrast to Figure 51 quadratic interpolation methods have been used to improve natural frequency and maximum transmissibility estimates. Firstly, it can be seen that the high error areas occur in Figure 51 for low loss factor and poor resolution (<0.05 and >5Hz respectively) have been reduced. They have not been eliminated totally but have been reduced such that higher errors do not occur until loss factors are reduced to ~0.01, where modal peaks are so narrow that using a quadratic interpolation is no longer appropriate, due to the divergence from the assumed parabolic shape of the peak. Further improvements can also be seen in Figure 53, with more consistency over frequency resolution for a given loss factor (observed as vertical error boundaries for increasing loss factor).



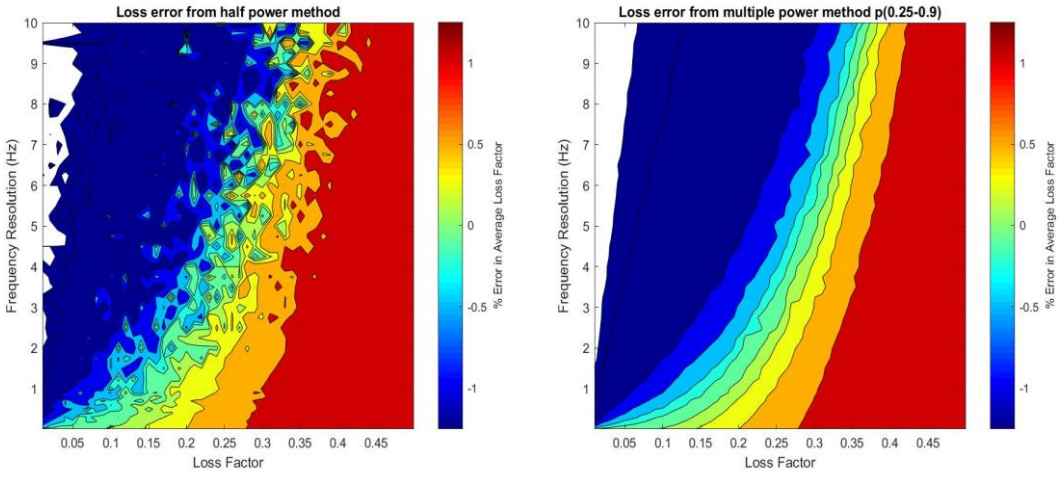
a) b)

Figure 53 - Loss Error for Inverse Transmissibility Methods, 1st order (a) and exact (b), for 'test' data with quadratic interpolation of natural frequency and maximum transmissibility, over varying loss factor and frequency resolution

3.3.2. Frequency Bandwidth Methods and Improvements

In this section, the same transmissibility functions as considered in Section 3.2.1 are analysed using the bandwidth methods described in Section 3.2. Figure 54 shows the percentage errors for the calculated loss factors using the half power method (equation (3.1)) and the averaged multi-power bandwidth method based on equation (3.3), where quadratic interpolation has been used to identify the peak transmissibility. The results indicate that the errors obtained using the bandwidth methods are much larger than those obtained using the exact inverse transmissibility method. For the bandwidth methods, there is only a relatively thin region representing ±1% loss error (dark blue and red show errors greater than -/+1% respectively).

Figure 54 indicates that the accuracy of the half-power method is sensitive to frequency resolution as calculations are performed at a single level as opposed to a range of levels in the averaged multi-power bandwidth method.



a) b)

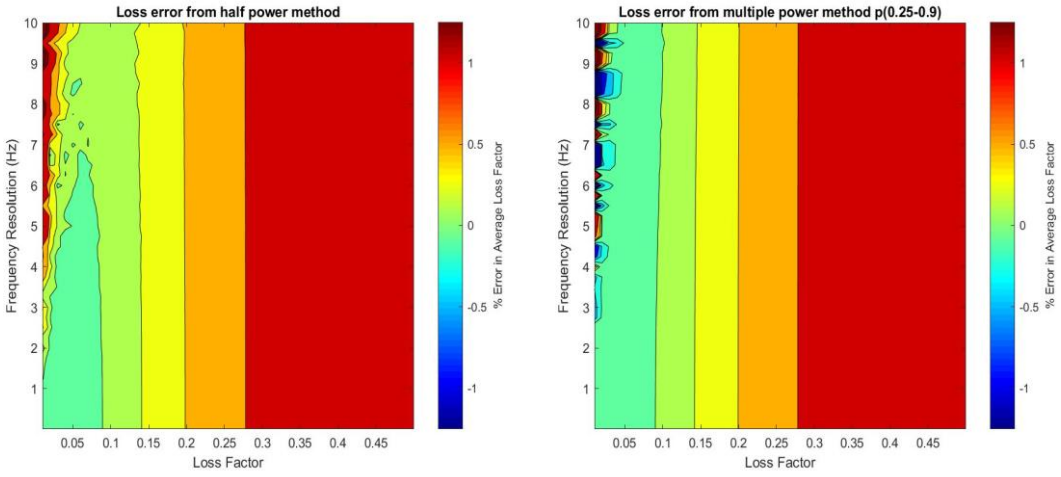
Figure 54 - Loss Error Frequency Bandwidth Methods, half-power (a) and multi-power (b), for 'test' data with quadratic interpolation of natural frequency and maximum transmissibility, over varying loss factor and frequency resolution

3.3.2.1. Linear Interpolation of Power Bandwidth Frequencies

Similar to the higher error regions observed in the inverse transmissibility methods, poor frequency resolution is a major cause. In those methods, it was seen that artificially increasing resolution through interpolation models greatly reduced the errors, and therefore interpolation of the power bandwidth frequency is now considered. Unlike the natural frequency location, the power bandwidth frequencies do not occur at a maximum, they occur in regions of the peak likely to be only

undergoing low changes in gradient over the frequency range between measurement points. Therefore, a simple linear interpolation model, using the neighbouring data point closest to the appropriate power level, is applied to improve the bandwidth frequency estimation.

Figure 55 shows the loss factor error maps for the two bandwidth methods after linear interpolation of the power bandwidth frequencies has been implemented. It can be seen that improvements in error have been attained, with <1% error for loss factors up to ~0.28, except for small regions as already mentioned due to very low loss and poor resolution. Once again it is observed that the averaged multi-power method improves upon the half-power method, with an increased ±0.1% error region at poorer frequency resolutions, due to its averaging over many power levels. In the averaged multi-power method error map, it can be observed that the dependence on frequency resolution has been significantly reduced and almost eliminated. Despite the improvements employed, it is still clear that the exact inverse transmissibility method provides better performance at increasing loss factors.



a) b)

Figure 55 - Loss Error for Frequency Bandwidth Methods, half-power (left) and multi-power (right), for 'test' data with quadratic interpolation of natural frequency and maximum transmissibility and linear interpolation of the power bandwidth frequencies, over varying loss factor and frequency resolution

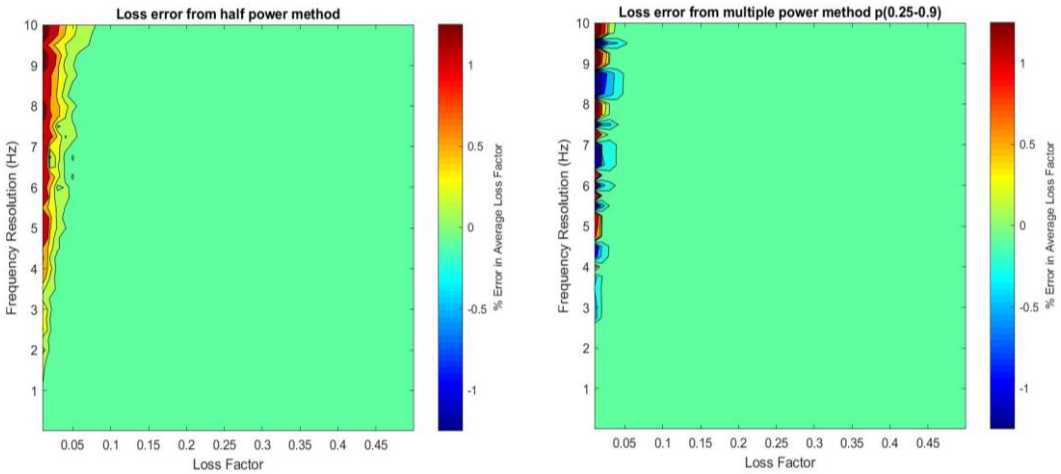
3.3.2.2. Bandwidth of Squared Frequency (removal of small loss assumption)

It has been found that the exact inverse transmissibility function provides lower errors than the bandwidth methods. The improvement in errors observed between the first order and exact solutions, particularly at high loss factors, was removal of the low loss assumption that was made during its derivation. A similar assumption was made in the derivation of the bandwidth methods, as was

explained in section 3.2.2. Through removal of this assumption and the use of the bandwidth of squared frequency (equation (3.2)) as opposed to the bandwidth of frequency (equation (3.3)), improvements in the errors at increased loss factors can be attained. Setting p=0.5 in equation (3.2) gives the improved half-power method as.

$$\eta = \frac{{\omega_2}^2 - {\omega_1}^2}{2{\omega_n}^2} \cdot \frac{1}{\sqrt{\frac{1-p}{p}}} \tag{3.4}$$

The differing methods will be defined as first and second order when using frequency bandwidth (low loss) and squared frequency bandwidth respectively. Figure 56 shows the percentage errors in the calculated loss factors, for the bandwidth methods using the bandwidth of squared frequency. Vast improvements can be seen at increased loss factors. Both methods (half power and multi-power) now show ±0.1% error for any system loss factor or frequency resolution, with the exception of the small region associated with low loss and poor resolution. In fact, if the contours of the maps were changed, a large majority would show errors of ±0.01%. Therefore, when applied to perfect data, i.e. without noise, artefacts or rotational contamination, and when using interpolation methods and removing low loss assumptions the bandwidth methods can provide similar errors in loss factor analysis than the exact inverse transmissibility method at any system loss factor and signal frequency resolution.



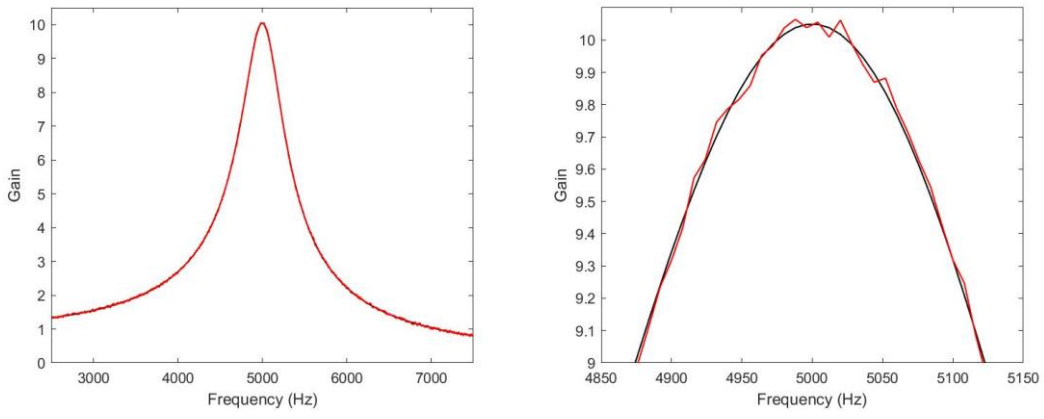
a) b)

Figure 56 - Loss Error for Frequency Bandwidth Methods, half-power (a) and multi-power (b), for 'test' data with quadratic interpolation of natural frequency and maximum transmissibility, linear interpolation of power bandwidth frequencies, and using the squared frequency bandwidth, over varying loss factor and frequency resolution

It was investigated whether the second order methods would induce these improvements without the use of the linear interpolation of the power bandwidth frequencies. It was observed that the loss errors were greater than those observed in Figure 54, unless the frequency resolution was very high (<<0.5Hz). Therefore, for the second order solution to be effective at reducing loss factor errors, highly accurate power bandwidth frequencies must be used.

3.3.3. Effect of Noisy Transmissibility Function on Loss Factor Errors

In this section the effect of low level noise, typical of a measured transmissibility function, on the accuracy of various loss factor calculation methods will be assessed. To create the noisy signal, a noise vector of random numbers between the values of ± a given noise magnitude is added to the perfect transmissibility function generated using the SDOF model. Due to the variation of frequency resolution and loss factor in analysing the accuracy of the loss factor calculations, the noise signal vector to be added varies in length and magnitude. The length of the noise vector is controlled by the frequency resolution, while the noise magnitude is calculated as a chosen percentage of the approximate maximum gain for a given loss factor (i.e. percentage.1/loss). In this section for low level typical experimental noise, the noise magnitude is 1% of the approximate maximum gain (±0.5%). An example of this noisy TF is shown in Figure 57, this has resolution and loss factor properties typical of those observed in the trial experiments (black – perfect TF, red – with 1% noise).



a) b)

Figure 57 - Noisy FRF using the frequency resolution and loss factor typically found in the experiments, a) full frequency range, b) detailed view at peak

As the noise vector must be varied for each change in loss factor and resolution, the shape of each noise signal is different on each Transmissibility function analysed. This changing shape of the

noise will affect the loss calculations, leading to sporadic errors and difficult comparisons. Therefore, in order to observe trends and enhance the comparability of differing calculation methods, the average error magnitude due to noise is calculated. To achieve this, the loss factor error is calculated 100 times for each loss factor and frequency resolution combination and the averages of their magnitudes (absolute) calculated. The errors are averaged using the absolute values so that positive and negative errors do not cancel one another out, producing average ± error magnitude over resolution and loss factor.

Figure 58 shows the average error maps for natural frequency and loss, when 1% noise is present. The maps shown include average loss errors calculated using the exact inverse transmissibility magnitude, half-power and averaged multi-power bandwidth methods. These methods utilise quadratic interpolation of natural frequency and maximum gain, and the bandwidth methods use linear interpolation of the power bandwidth frequencies and the second order solution.

It can be seen that the presence of noise has caused larger errors in both the calculated natural frequencies and loss factors. The natural frequency error increases for poorer resolution and greater loss factor, however is observed to be less than ±0.5% error for loss factors up to 0.35, and for typical room temperature properties less than ±0.2%.

The differing calculation methods have varying errors when noise is present. The exact inverse transmissibility magnitude method provides the lowest with greater errors seen for increasing loss and increasing resolution. This method achieves ±0.5% and ±0.25% errors, for loss factors below 0.5 and 0.2 respectively, and ±0.25% for RT typical test properties (~0.1 loss and 8-10Hz resolution). The bandwidth methods trends are similar, but with greater errors observed. For low loss factors it is beneficial to have test data with poorer frequency resolution, with errors of ±1% possible for loss factors less than 0.2 when resolution is higher than 7Hz. A possible reason for this unexpected trend is the greater number of oscillations, caused by the noise, present in the higher resolution signals. The half-power method can be seen to be slightly better than the multiple power method, with a larger ±1% error region, and significantly less higher error regions (5%+). This is contrary to the prediction that averaging over multiple points would improve errors when noise is present, the original purpose of deriving the multiple power method, in fact averaging has exaggerated the noise effects.

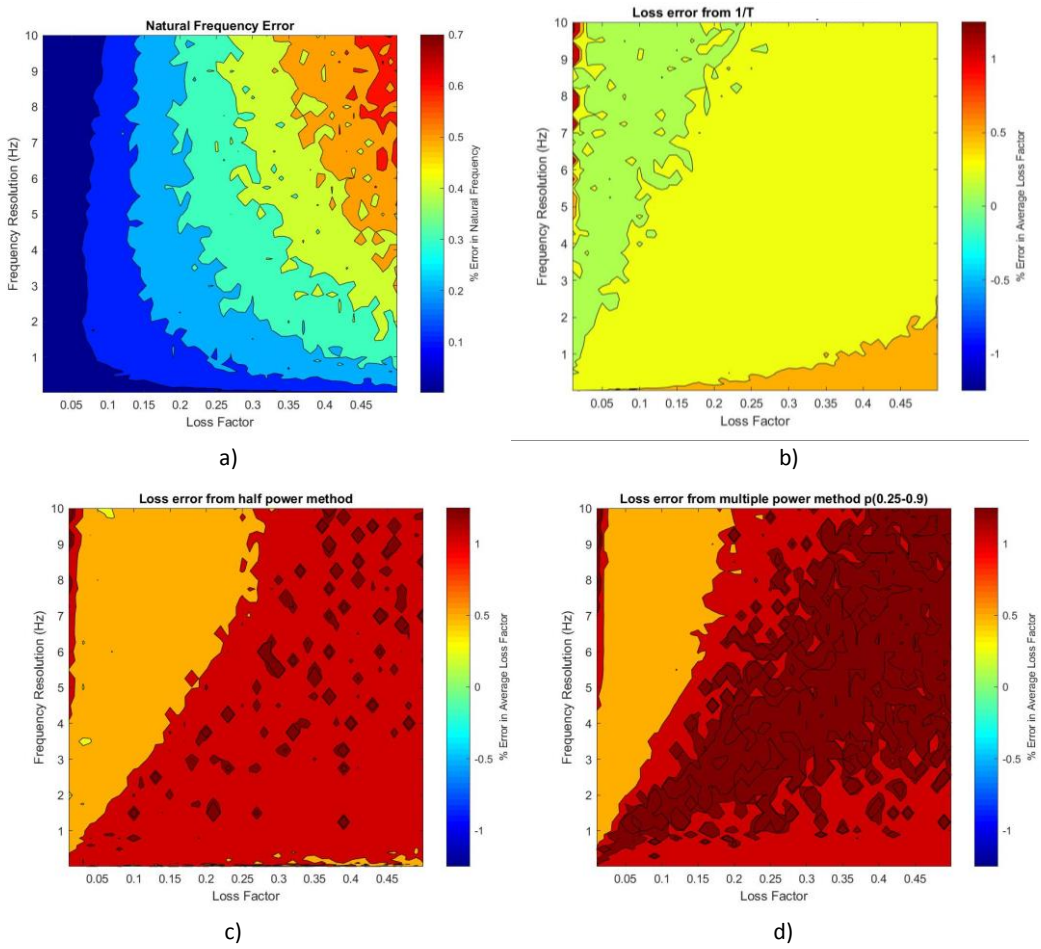


Figure 58 – Average natural frequency error (a), and Average loss factor error using exact inverse (b), second order half power (c) and multipower (d) calculation methods for noisy transmissibility functions (with quadratic interpolation of natural frequency and maximum transmissibility, and linear interpolation of power bandwidth frequencies)

The cause of the higher errors observed for the averaged multi-power bandwidth method was investigated by analysing the noisy transmissibility functions using differing combinations of the interpolations with first and second order solutions. It was observed that the use of quadratic interpolation of the natural frequency and maximum gain causes the same improvements at poor frequency resolutions. However, use of the second order solution leads to increased errors. It was seen in Section 3.3.2.2. that poor power bandwidth frequencies led to increased errors in the second order solution. Therefore, the noise is causing errors in the power bandwidth frequencies. In section 3.3.2.2. this was overcome using linear interpolation to improve the power bandwidth frequency estimates, however, when noise is present the same consistent improvements are not seen. Improvements were seen for low frequency resolutions and low loss, but significant error increases were observed for higher resolutions and system loss factors. Showing that the linear interpolation is unstable in these regions leading to greater power bandwidth frequency errors.

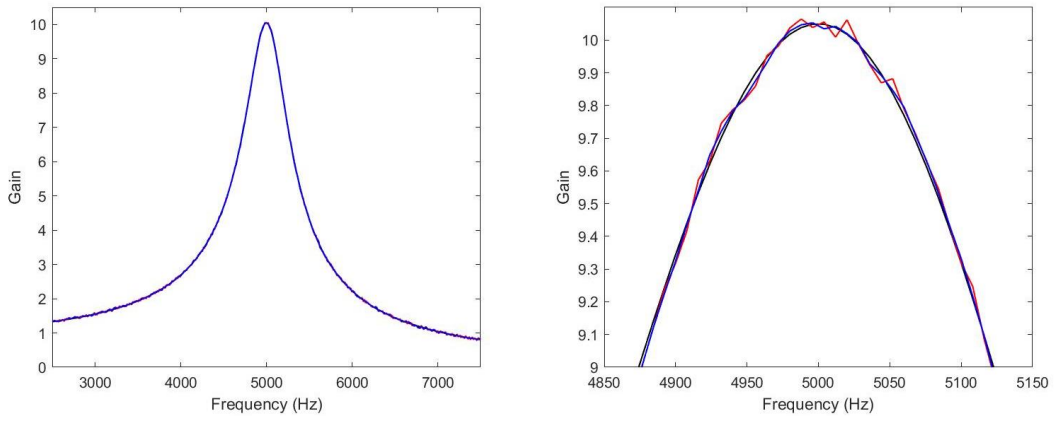
3.3.3.1. Noise Reduction – Transmissibility Function Smoothing

It was found in Chapter 2 that the noise can be reduced through smoothing of the signal using a small span moving average. In this section, smoothing will be used in order to reduce the noise and its effects on the accuracy of the natural frequency and loss factors assessed. Figure 59 shows the same perfect and noisy transmissibility functions (black and red respectively) as shown in Figure 57, as well as a smoothed version of the noisy signal (blue). It can be seen that the smoothing has reduced the noise, removing the oscillations at the peak.

The smoothing used is a moving average over a small span of frequency points. The size of the span is dependent on the frequency resolution of the signal, with higher resolution data requiring a greater span width. In order to automatically apply smoothing to data of varying resolution, an empirical relation between the span, *s* and resolution, *r* has been produced. This empirical function is dependent on the concerned absolute frequencies and range, and is created manually to ensure that at any given resolution the span is large enough to be effective while not too large to artificially add damping to the response, and is given (for this case) by.

$$s = 12 * r^{-1.1} + 2$$

As with the noisy data case discussed in the previous section, the smoothed noise signal is different for each transmissibility function analysed, as the resolution and loss are varied. Therefore, the same averaging process is applied, resulting in average error magnitude maps over loss and resolution.



a) b)

Figure 59 – Perfect (black), Noisy (red) and Smoothed (blue) Transmissbility Functions, noise applied is 1% of the maximum transmissibility magnitude, a) full frequency range, b) detailed view of peak

Figure 60 shows the average error maps for natural frequency and loss, using the same calculation methods as shown in the previous section. It can be seen that the natural frequency error trends are simialr to those observed when noise (unsmoothed) is present, however their magnitudes have been reduced. Reducing from ±0.5% to ±0.4% for loss factors up to 0.35, and at typical room temperature properties from ±0.2% to 0.1%.

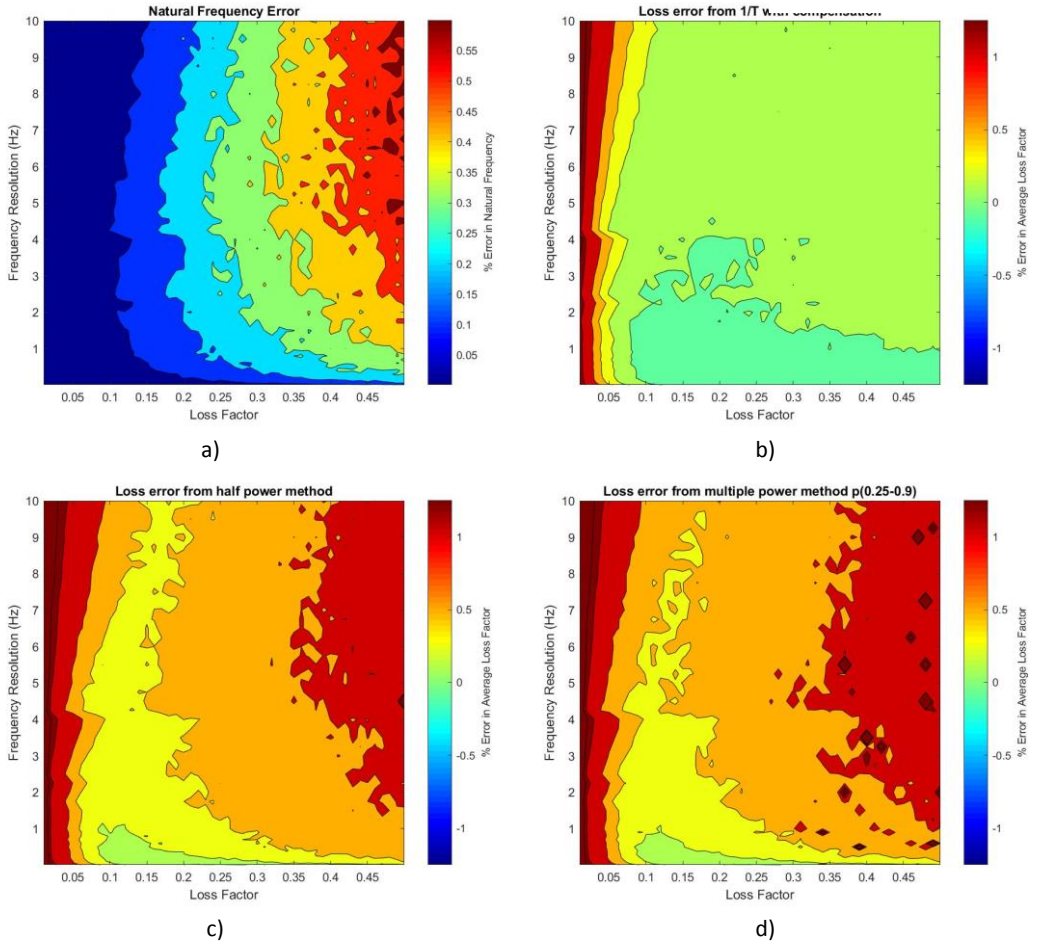


Figure 60 – Average natural frequency error (a), and Average loss factor error using exact inverse (b), second order half power (c) and multipower (d) calculation methods for smoothed noisy transmissibility functions (with quadratic interpolation of natural frequency and maximum transmissibility, and linear interpolation of power bandwidth frequencies)

The average loss error maps have also been significantly improved through use of smoothing for all calculation methods investigated. For the exact inverse transmissibility method, with low error regions expanding to higher losses, now with ±0.25% errors for loss factors up to 0.5. However, the smoothing has had some detrimental effect for low loss factors (<0.1). The use of smoothing has enabled errors of less than 0.1% for loss factors between 0.1-0.5 and resolutions better than 2Hz. The loss errors experienced in the bandwidth methods have been significantly as well, with expansion of the ±1% region to much greater loss factors (0.4 rather than 0.2), as well as a large region of ±0.5% error

unattainable previously. Once again however, smoothing has induced greater errors in the low loss region (<0.1). The smoothing has also lessened the difference between the half-power and multi- power methods, the halfpower can still be seen to be better, but to a much lesser extent.

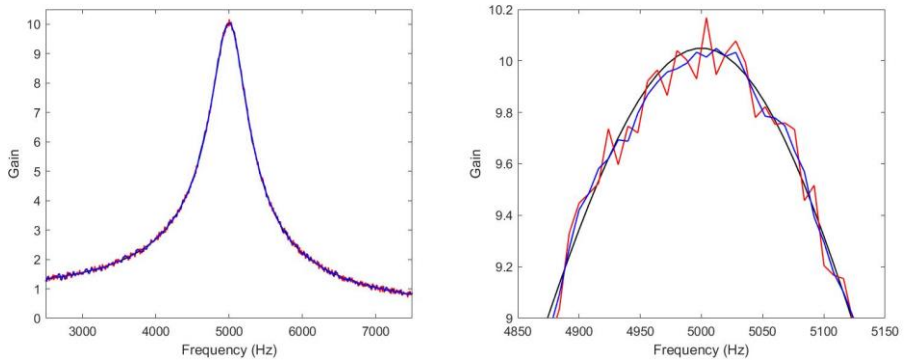
As investigated in the previous section, the use of linear interpolation and the second order solution for the averaged multi-power method are investigated to assess the smoothing effect on the instabilities observed for noise. It was seen that the smoothing applied has overcome the instabilities, with consistent improvements in loss factor errors observed when using the second order solution with linear interpolation of the power bandwidth frequencies for all frequency resolutions and system loss factors investigated.

3.3.3.2. Excessive Noise

The effect of low-level noise on the accuracy of natural frequency and loss factor calculations over frequency resolution and loss factor has been assessed, however, In the experiments higher levels of noise can be experienced. This higher level of noise was seen during temperature tests, due to changes in the laser-air interaction at elevated temperatures, or water vapour due to nitrogen release, and condensation of this water vapour on the die's surface. It was also seen in other tests, caused by low excitement levels (in linearity experiments), or generally poor laser signal due to focussing or reflection problems on the die's surface. In this section. The effect of higher noise levels on the accuracy of analysis is investigated. The methods and models used for this are the same as the previous section, only the magnitude of the noise will be increased to values of 2.5% and 5% of the maximum gain.

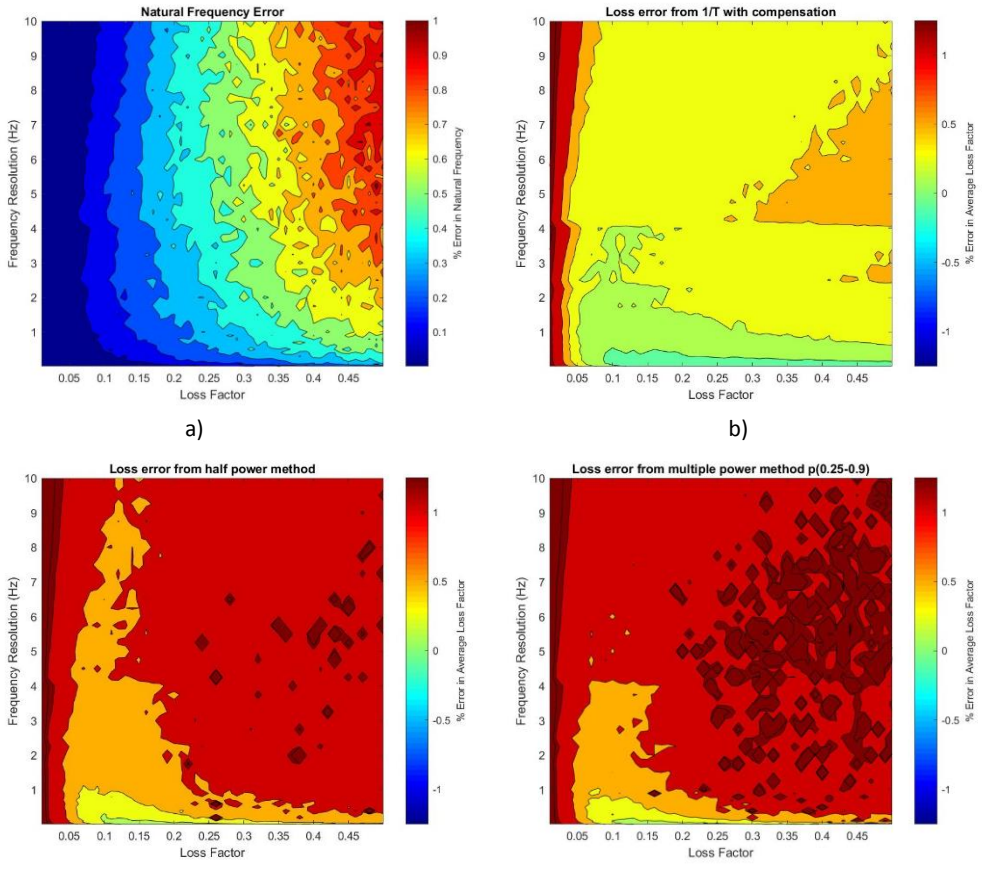
3.3.3.2.1. 2.5% Noise (peak gain)

Figure 61 shows the transmissibility functions with raw, smoothed and without 2.5% noise for typical loss and frequency resolution values, while Figure 62 shows the error maps for natural frequency and loss factor using various calculation methods. It can be seen that the inverse transmissibility method can achieve the lowest errors with ±0.5% for loss factors between 0.05-0.3 (or greater depending upon the frequency resolution), while the bandwidth methods can suffer from up to 5% error over the same range. The multiple-power can be seen to be worse than the half power, particularly at increasing loss factors, indicating that when high levels of noise are present, averaging the calculation over multiple powers exaggerates the noise effect as opposed to reducing it.



a) b)

Figure 61 – Perfect (black), Noisy (red) and Smoothed (blue) Transmissbility Functions, noise applied is 2.5% of the maximum transmissibility magnitude, a) full frequency range, b) detailed view of peak



a) b)

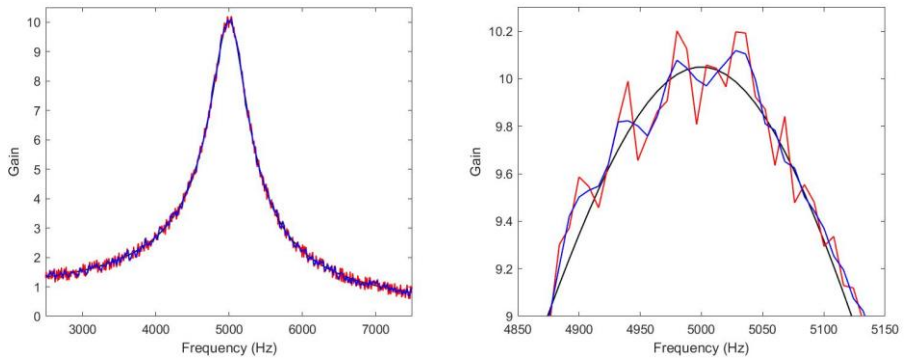
c) d)

Figure 62 – Average natural frequency error (a), and Average loss factor error using exact inverse (b), second order half power (c) and multipower (d) calculation methods for smoothed noisy (2.5%) transmissibility functions (with quadratic interpolation of natural frequency and maximum transmissibility, and linear interpolation of power bandwidth frequencies)

3.3.3.2.2. 5% Noise (peak gain)

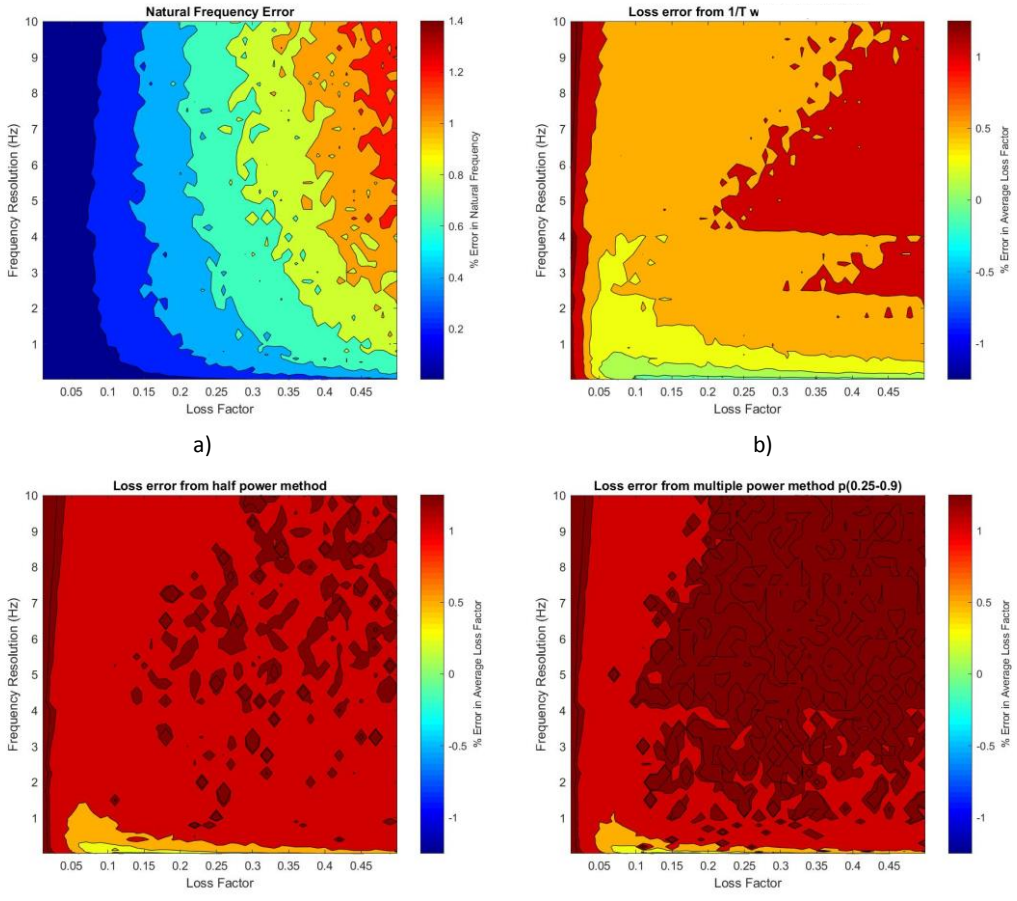
Figure 63 shows the transmissibility functions with raw, smoothed and without 5% noise for typical loss and frequency resolution values, while Figure 64 shows the error maps for natural frequency and loss factor using various calculation methods. As observed for the other noise levels, the inverse transmissibility method can achieve the lowest errors with ±1% for loss factors between 0.05-0.25,

increasing from ±0.5% seen for 2.5% noise, while the bandwidth methods still have accuracies up to 5% error but over a reduced range of loss factors. As seen for the lower noise levels the multi-power has greater errors that the half power, the difference between the two methods can be seen to increase with greater noise magnitudes



a) b)

Figure 63 – Perfect (black), Noisy (red) and Smoothed (blue) Transmissbility Functions, noise applied is 5% of the maximum transmissibility magnitude, a) full frequency range, b) detailed view of peak



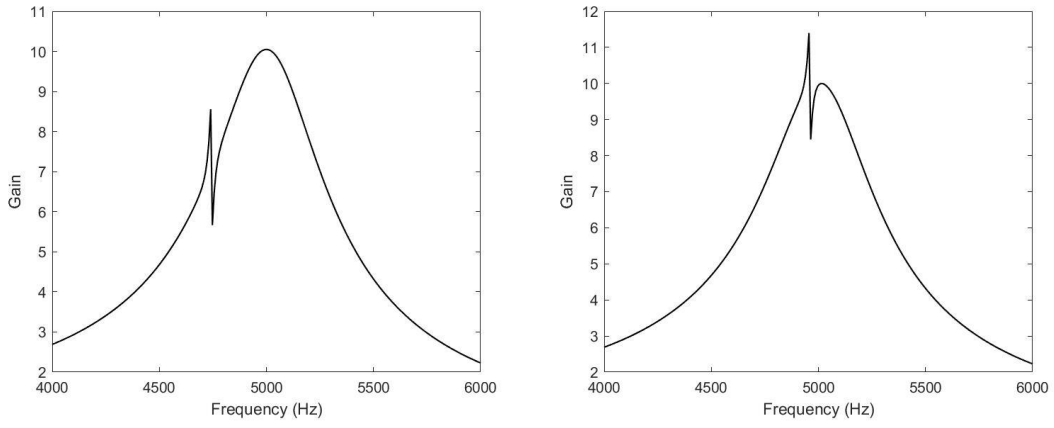
a) b)

a) b)

Figure 64 – Average natural frequency error (a), and Average loss factor error using exact inverse (b), second order half power (c) and multipower (d) calculation methods for smoothed noisy (5%) transmissibility functions (with quadratic interpolation of natural frequency and maximum transmissibility, and linear interpolation of power bandwidth frequencies)

3.3.4. Other Signal Issues – Artefacts

In the experimental tests, there are signal issues present other than noise that could affect the loss factor and natural frequency calculated using the analysis algorithm, such as artefacts. An artefact here is considered as a sporadic or erroneous sharp peak in the frequency response. These artefacts can be associated with resonances in the test setup or environment, in the experiments being analysed these could be related to components such as the shaker armature or the fan in the oven. For the artefact to cause errors in the loss factor calculations, it must be located close to or at the peak in the transmissibility function. Figure 65 shows examples of artefact locations that could affect the analysis of the peak, to the side of and at the centre of the resonance peak. The artefacts shown have been idealised by the addition of an exponential curve, with a maximum amplitude at a given frequency, and subtraction of the same reflected curve after that frequency location. From the equations governing the loss calculations, it can be deduced that, if the artefact exceeds the peak magnitude, the inverse peak magnitude methods will be affected, as well as the natural frequency. While the bandwidth methods will be affected if any part of the artefact has a magnitude associated with the power bandwidth frequencies for any power level included in the loss calculation. The two cases shown in Figure 65 will be analysed and the artefacts effects on each loss calculation method discussed, as well as methods for reducing the induced errors.



a) b)

Figure 65 – Transmissibility functions with artefacts likely to affect the analysis, a) side and b) central artefacts

3.3.4.1. Side of Peak Artefact

Figure 66 shows the fit of transmissibility functions generated using the SDOF Kelvin-Voigt model with hysteretic damping to the 'test' data with side artefact, using loss factors values calculated

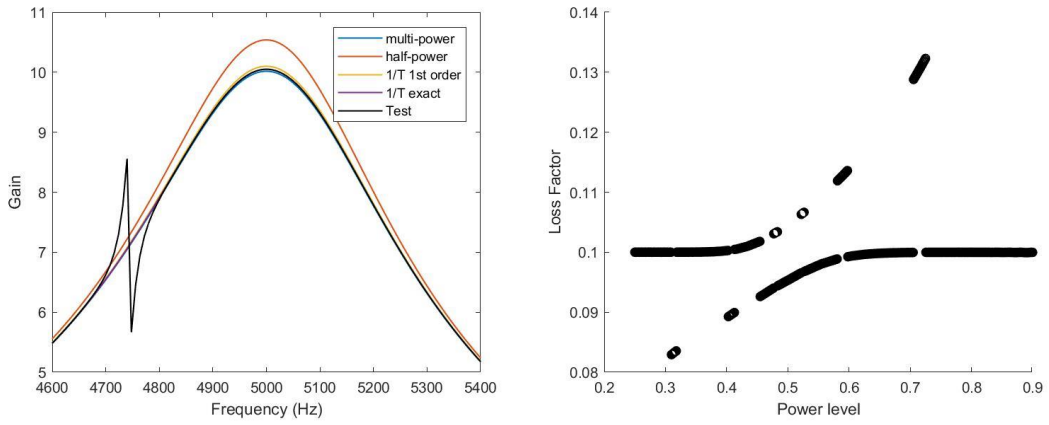
from various methods (a), as well as a plot (b) showing the loss factors calculated across the full power range (0.25-0.9). It can be seen that all the generated responses appear to fit the 'test' data well, with the exception of the half-power method, which has a much greater peak magnitude.

The inverse transmissibility magnitude methods fit well, as was to be expected given that the artefact does not interfere with the maximum gain of the peak, also because of this the natural frequency found is also accurate. The exact solution has an improved loss estimate due to the removal of the low loss assumption, that has a small detrimental effect on the first order loss estimate.

The half-power bandwidth method suffers from a large error of -4.7%, as can be seen in Table 7, which summarises the errors in natural frequency and loss from the various methods. The reason for this large loss error in the half-power method can be observed in the loss factor against power level, p plot in Figure 66b), where a lower loss value is experienced at 0.5 power. This lower loss is caused by the artefact, which is effectively narrowing the peak at the half-power magnitude.

From the power-loss plot it can be seen that the artefact has disrupted much of the power range (0.3-0.7), however despite this, the multi-power method has produced a relatively accurate loss estimate. In the power-loss plot it can be seen that there are both over and underestimates or the loss in this disrupted region, this is due to the peak and trough regions of the artefact respectively. These regions cause a lower/higher first power bandwidth frequency, therefore making the peak appear wider/thinner, causing the errors in loss factor.

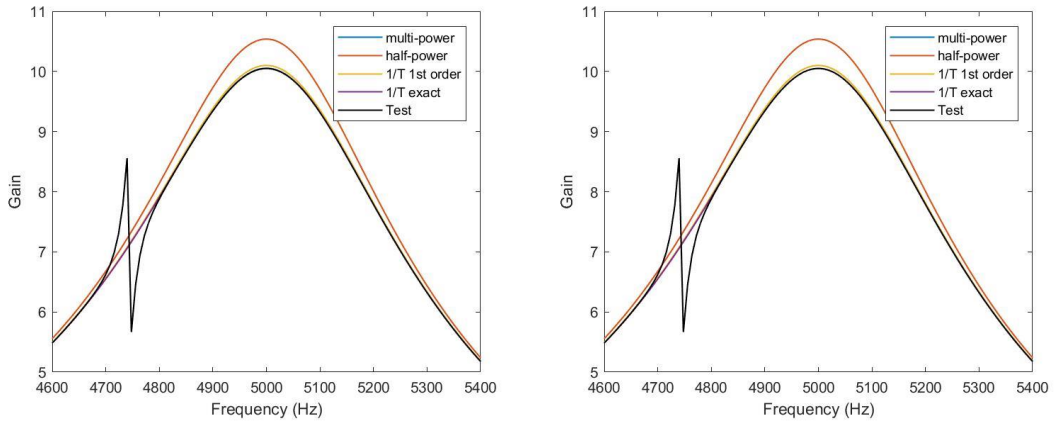
For a given power magnitude within this disrupted region there are three intersection points when there should be only one (due to the oscillation of the artefact), the analysis model chooses one of these points as the first power bandwidth frequency, whichever has the closest magnitude to the power magnitude. In this case, it has coincidently chosen such that when averaged the errors from over and underestimates have almost cancelled each other out, resulting in the low error of just 0.34%. However, the analysis could have selected all of the narrowed region (artefact trough), or all of the widened region (artefact peak), resulting in large underestimation or overestimation of the loss respectively.



a) b)

Figure 66 – Fit using various loss calculation methods (a) and loss factors calculated across power range for side artefact (b)

In order to avoid the possible errors in the multi-power method, the power range used in the calculation can be altered so that none of the disrupted region is used. Therefore, a power range of 0.25-0.3 can be selected, which only analyses the region below the artefact or 0.7-0.9, analysing the region above the artefact. The fit of these can be seen in Figure 67, and their errors in loss estimate can be seen in Table 7 as 0.004% (below) and -0.025% (above).



a) b)

Figure 67 – Fit of TFs using various loss calculation methods, a) using points above artefact, b) using points below

Table 7 shows the errors in the derived properties found from the analysis model using various loss calculation methods. Firstly, as expected the natural frequency selection has been unaffected by the artefact as it does not exceed the gain of the resonance peak. Also because of this an accurate maximum gain value can be selected, leading to an accurate loss estimate using the exact inverse transmissibility method. The half-power bandwidth has been greatly affected, with an error in its loss estimate of almost 5%. For any artefact of significant magnitude that is close to the peak, the half-

power method is likely to be detrimentally affected, and due to the single point measurement nature of this calculation the effect will likely be significant. When using the full power range, the multi-power bandwidth method has coincidently, in this case, averaged out errors, although could be significantly affected by the presence of a side artefact. However, because it can be used over any region, of any size, of the peak through alteration of the power range used, highly accurate loss estimates can still be attained.

Table 7 - Percentage errors in natural frequency and loss from various calculation methods, for an artefact to the side of the peak

	Error (%)
Natural Frequency	-3.22e-05
Loss – first order 1/T	-0.496
Loss – exact 1/T	5.3e-5
Loss – half-power	-4.68
Loss – multi-power (full range)	0.339
Loss – multi-power (above)	-0.025
Loss – multi-power (below)	0.004

3.3.4.2. Centre of Peak Artefact

Figure 68 shows the fit of generated transmissibility functions, using properties derived from differing calculation methods, to 'test' data with an artefact at the centre of the resonance peak. It can be immediately seen that the fit of all generated transmissibility functions is very poor. The poor fits are caused by large errors in the analysis models selection of natural frequency and maximum gain, which are chosen as the frequency at which the highest gain is observed and the highest gain observed in the 'test' transmissibility function respectively. As the artefact has the highest gain in the signal, its peak location and magnitude are erroneously selected as the natural frequency and peak gain respectively. All of the calculation methods use the wrongly selected natural frequency in the SDOF model to generate TFs centred about this location. The bandwidth methods also use the natural frequency in their calculation of loss factor, and the inverse transmissibility magnitude methods use the maximum gain in their loss estimation. Therefore, all methods are subject to highly significant errors, seen in Table 8 to vary from 13-27%, and predict vastly different frequency response compared to the 'test' data.

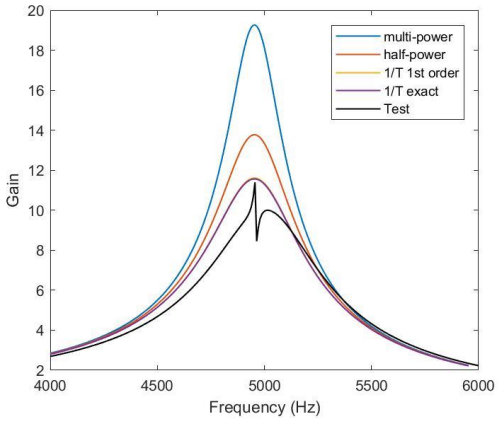
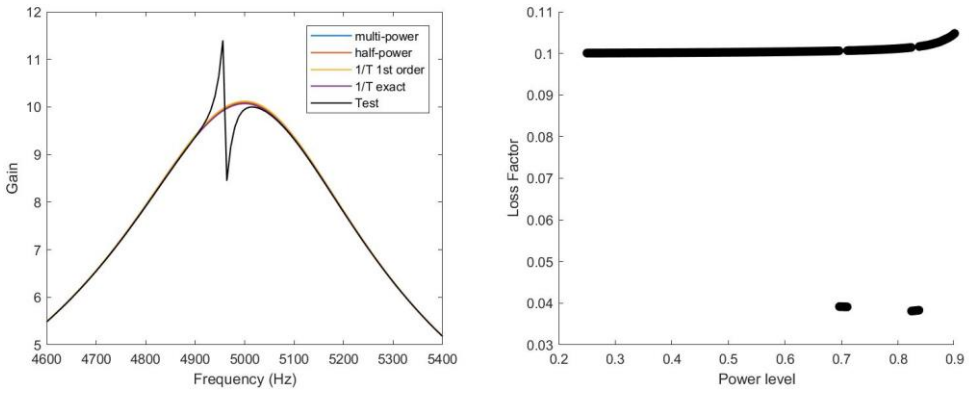


Figure 68 - Fit of TF using various loss calculation methods for a central artefact

It has been discussed that all loss calculations methods use one or both of the natural frequency and maximum gain found by the analysis model, and therefore for any of the methods to be accurate, a reasonable estimate of these quantities is required. The centrally located artefact is seen to obscure the location of the natural frequency and maximum gain from the analysis algorithm, if the artefact was offset from the peak (but still exceeded its maximum gain) it would be possible to exclude the artefact location from the search for the natural frequency, allowing for accurate selection. However, the only method to provide a decent estimate for the natural frequency and maximum gain for a central artefact, is to manually select them by interpretation and interpolation of the peaks shape.

Figure 69 shows the fit of the generated transmissibility functions using the various loss calculations and utilising a manually selected estimate for the natural frequency and maximum gain, as well as the power-loss plot for the shown transmissibility function with central artefact. It can be seen that the fits are significantly better than previous, and all replicate the frequency response well. They are however reliant on an accurate estimate of natural frequency and maximum gain being chosen. The half-power method is unaffected by the central artefact shown, as its trough is above the half-power magnitude, however it would be affected if the artefact magnitude was larger. The multi-power method using the full range would be affected due to the trough of the artefact. The power-loss plot in Figure 69 shows that the artefact is disrupting powers from approximately 0.7. Therefore, through selection of an appropriate power range (0.25-0.68) the multiple power method is unaffected.



a) b)

Figure 69 – a) Fit of TF for various loss calculations, using manual estimate of natural frequency and maximum gain, b) loss factors calculated across power range for central artefact

Table 8 shows the errors in natural frequency and loss from various calculation methods for the 'test' data containing a central artefact, with and without manual selection of natural frequency and maximum gain. It can be seen that the errors are large for all calculation methods when erroneous values of natural frequency and gain are selected by the algorithm, however, through manual estimation of these quantities the errors can be greatly reduced. The bandwidth methods both provide loss estimates with an error of 0.144%, however despite its calculation being solely reliant on the manually estimated maximum gain value the exact inverse transmissibility method has the lowest loss error of 0.02%.

Table 8 - Percentage errors for natural frequency and loss from various calculations for a centrally located artefact

	Error (%)	Error (%) with chosen fn and gain
Natural Frequency	-0.929	-0.086
Loss – first order 1/T	-13.53	0.512
Loss – exact 1/T	-13.21	0.016
Loss – half-power	-27.21	-0.028
Loss – multi-power (0.25-0.68)	-21.45	-0.027

3.4. Imperfect Samples – Coupled Motion

In Chapter 2, vibration tests using multiple measurement points on the dies surface/edge were conducted, and it was found that the frequency response varied at differing locations on the die. This included different peak gains at the modes of interest and responses at other frequencies, and indicates that the modes observed and analysed are not purely translational, because they are contaminated by a rotational component. It was hypothesised that this coupling of the translational and rotational coordinates was caused by imperfection in the bond and/or die manufacture and assembly. In this

section, analytical models for a perfect and sloped bond are derived and compared, to observe the influence of imperfection on the stiffness matrix for a bond imperfection. Simple FE models are created incorporating small and large manufacturing imperfections and used to evaluate their effect on frequency response functions (TF) at varying points on the die surface, similar to those used in the multipoint experiments. The imperfections modelled include a sloped bond with varying slope magnitude and direction, and offset of the die from its position centrally on the bond, as well as combinations of these. Qualitative analysis of bond imperfection on transmissibility functions is conducted, as well as quantitative analysis of the errors induced in the derived material properties for differing calculation methods.

3.4.1. Analytical Model

A 6 degree of freedom undamped analytical model is developed initially for a perfect constant thickness bond geometry which is then modified to consider a bond with a linearly varying (inclined) thickness. The aim is to identify the presence of coupling terms between the translational and rotational coordinates in the stiffness matrices, either inherent to the bond design or induced by the sloped bond imperfection. This work will help validate the hypothesis that bond imperfections cause rotational motions which contaminate the pure translational modes with rotational components when excited in bounce and shear directions.

3.4.1.1. Perfect Bond Geometry

Initially the stiffness matrix for a perfect bond is derived to observe any couplings for the uniform bond design. Figure 70 shows the perfect bond geometry together with the coordinate system used to analyse the mechanical response. It is worth noting that the rounded corners have been removed to simplify the model.

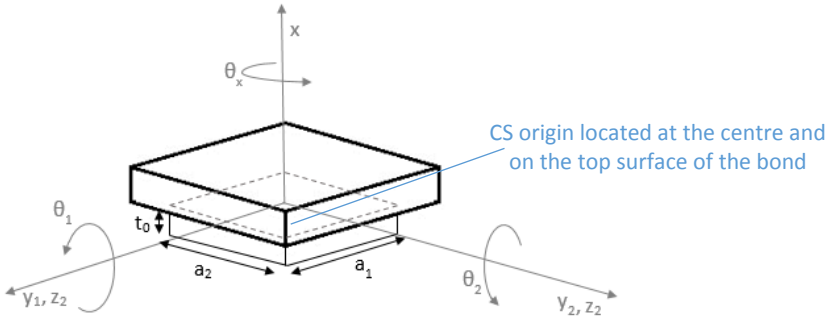


Figure 70 – Diagram – asm and plan of bond showing dz elements

For the perfect bond, the bond thickness is uniform across the bond area, so the thickness at any location z_1, z_2 across the bond can be expressed as:

$$t(z_1, z_2) = t_0$$

When the rigid die is subjected to displacements x (bounce), y_1 (shear), y_2 (shear) and rotations θ_1 (rock), θ_2 (rock), θ_x (twist), the compressive normal strain and stress at location (z_1, z_2) are given by

$$\varepsilon_{xx}(z_1, z_2) = \frac{x - z_1 sin\theta_2 + z_2 sin\theta_1}{t_0}, \quad and, \quad \sigma_{xx}(z_1, z_2) = \frac{E(x - z_1 sin\theta_2 + z_2 sin\theta_1)}{t_0}$$

and the shear strains and stresses at location (z_1, z_2) are given by

$$\gamma_{xy_1}(z_1, z_2) = \frac{y_1 - h_G sin\theta_2 - z_2 sin\theta_x}{t_0}, \quad and, \quad \tau_{xy_1}(z_1, z_2) = \frac{G(y_1 - h_G sin\theta_2 - z_2 sin\theta_x)}{t_0}$$

$$\gamma_{xy_2}(z_1, z_2) = \frac{y_2 + h_G sin\theta_1 + z_1 sin\theta_x}{t_0}, \quad and, \quad \tau_{xy_2}(z_1, z_2) = \frac{G(y_2 + h_G sin\theta_1 + z_1 sin\theta_x)}{t_0}$$

These equations can be simplified when assuming the rock and twist rotations θ_1, θ_2 and θ_x of the die are small, such that $sin\theta_1 \approx \theta_1$, $sin\theta_2 \approx \theta_2$ and $sin\theta_x \approx \theta_x$. The resultant forces and moments acting upon the die are found by integrating these elemental forces over the cross-sectional area of the bond, such that.

$$F_{xx} = \int_{\frac{-a_2}{2}}^{\frac{a_2}{2}} \int_{\frac{-a_1}{2}}^{\frac{a_1}{2}} \sigma_{xx}(z_1, z_2) dz_1 dz_2 = \frac{E x a_1 a_2}{t_0}$$

$$F_{y_1 y_1} = \int_{\frac{-a_2}{2}}^{\frac{a_2}{2}} \int_{\frac{-a_1}{2}}^{\frac{a_1}{2}} \tau_{xy_1}(z_1, z_2) dz_1 dz_2 = \frac{G a_1 a_2 (y_1 - h_G \theta_2)}{t_0}$$

$$F_{y_2 y_2} = \int_{\frac{-a_2}{2}}^{\frac{a_2}{2}} \int_{\frac{-a_1}{2}}^{\frac{a_1}{2}} \tau_{xy_2}(z_1, z_2) dz_1 dz_2 = \frac{G a_1 a_2 (y_2 + h_G \theta_1)}{t_0}$$

$$M_{\theta_1 \theta_1} = \int_{\frac{-a_2}{2}}^{\frac{a_2}{2}} \int_{\frac{-a_1}{2}}^{\frac{a_1}{2}} z_2 \sigma_{xx}(z_1, z_2) + h_G \tau_{xy_2}(z_1, z_2)\, dz_1 dz_2 = \frac{E a_1 {a_2}^3 \theta_1}{12 t_0} + \frac{G h_G a_1 a_2 (y_2 + h_G \theta_1)}{t_0}$$

$$M_{\theta_2 \theta_2} = \int_{\frac{-a_2}{2}}^{\frac{a_2}{2}} \int_{\frac{-a_1}{2}}^{\frac{a_1}{2}} -z_1 \sigma_{xx}(z_1, z_2) - h_G \tau_{xy_1}(z_1, z_2)\, dz_1 dz_2 = \frac{E {a_1}^3 a_2 \theta_2}{12 t_0} + \frac{G h_G a_1 a_2 (y_1 - h_G \theta_2)}{t_0}$$

$$M_{\theta_x \theta_x} = \int_{\frac{-a_2}{2}}^{\frac{a_2}{2}} \int_{\frac{-a_1}{2}}^{\frac{a_1}{2}} z_1 \tau_{xy_2}(z_1, z_2) - z_2 \tau_{xy_1}(z_1, z_2)\, dz_1 dz_2 = \frac{G \theta_x}{t_0} \frac{({a_1}^3 a_2 + a_1 {a_2}^3)}{12}$$

The force and moment equations can be used to determine the stiffness matrix of the perfect bond, such that:

$$K = \frac{1}{t_0}\begin{bmatrix} Ea_1a_2 & 0 & 0 & 0 & 0 & 0 \\ 0 & Ga_1a_2 & 0 & 0 & -h_G Ga_1a_2 & 0 \\ 0 & 0 & Ga_1a_2 & h_G Ga_1a_2 & 0 & 0 \\ 0 & 0 & h_G Ga_1a_2 & \frac{Ea_1{a_2}^3}{12} + {h_G}^2 Ga_1a_2 & 0 & 0 \\ 0 & -h_G Ga_1a_2 & 0 & 0 & \frac{E{a_1}^3a_2}{12} + {h_G}^2 Ga_1a_2 & 0 \\ 0 & 0 & 0 & 0 & 0 & G\left(\frac{a_1{a_2}^3}{12} + \frac{{a_1}^3a_2}{12}\right) \end{bmatrix}, \quad \begin{Bmatrix} x \\ y_1 \\ y_2 \\ \theta_1 \\ \theta_2 \\ \theta_x \end{Bmatrix}$$

Although the stiffness matrix indicates that the bounce force and twist moment are solely dependent on the bounce, *x* and twist, θ_x motions respectively, all other coordinates involve some form of coupling. In particular, shear and rocking coordinates are coupled. For example, coupling exists between y_1 *and* θ_2, and between y_2 *and* θ_1. The coupling arises because the bond is single-sided and would be eliminated if an identical bond was present on the other side of the die, i.e. two bonds, one on the bottom die surface and another on the top die surface. This style of 'sandwiched' bond is often used in material testing to determine shear properties by constraining the rotational components. Sandwiched bonds were not considered in this work because they would have interfered with measurements of bounce and curvature of the die, and single-sided die bonds are used extensively in MEMS devices.

The magnitude of the coupled rocking term depends on the height of the die centre of mass h_G, above the top surface of the bond. The coupling reduces as h_G, reduces and in principle disappears if h_G=0. For the bonds tested h_G is relatively small (<5x10^{-4} m) and because the die is thin the coupled rocking is unlikely to affect the measurements taken at different measurement locations. In trial tests, measurements were taken along a horizontal line through the centre of the sample which remained aligned and perpendicular to the measurement direction. If the die was thicker, it is likely that measurements taken along a vertical line (thickness dimension) would show the presence of a contaminating rocking contribution due to an increased h_G value.

3.4.1.2. Sloped Bond Geometry

To validate the hypothesis that manufacturing imperfections in the bond can cause coupling of translational and rotational motions, the stiffness matrix for a sloped bond is derived next. The bond is assumed to have nominal thickness t_0 at the centre of the die and a slope defined in terms of

magnitude, φ and slope direction β. Figure 71 shows a plan view of the bond indicating the direction of the slope.

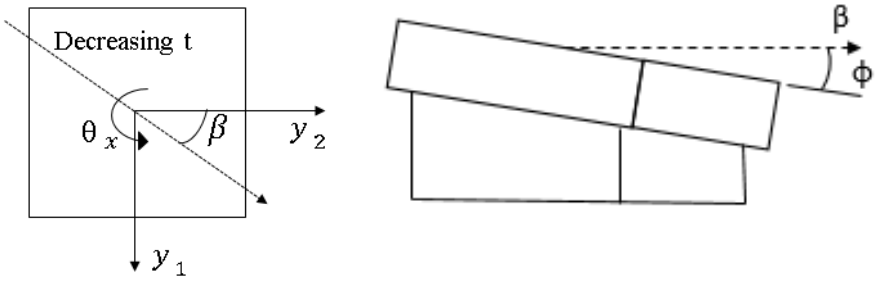


Figure 71 – Plan and side (perpendicular to incline direction β) view defining bond incline

Figure 72 defines slope angles α_1 and α_2 of the bond along the y_1 and y_2 axes respectively, which can be expressed in terms of slope magnitude, ϕ and direction, β as follows:

$$\alpha_1 = \phi sin\beta, \;\; \alpha_2 = \phi cos\beta$$

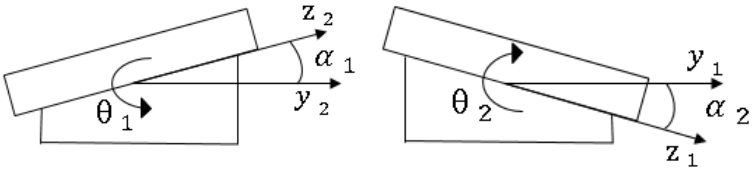


Figure 72 – side views of the sloped bond in y_1 and y_y directions, showing definition of the tilt angles α_1 and α_2

For the sloped bond, the thickness varies linearly across the bond, and so the bond thickness at location (z_1, z_2) can be expressed as

$$t(z_1, z_2) = t_0(1 - \frac{z_1}{t_0} sin\alpha_2 + \frac{z_2}{t_0} sin\alpha_1)$$

This equation is simplified by assuming tilt angles α_1 *and* α_2 are small, such that $sin\alpha_1 \approx \alpha_1$ and $sin\alpha_2 \approx \alpha_2$, which ensures the bounce and shear motions predominantly occur in the vertical and horizontal directions respectively. The following equations also assume that the rock and twist rotations θ_1, θ_2 and θ_x of the die are small, such that $sin\theta_1 \approx \theta_1, sin\theta_2 \approx \theta_2$ *and* $sin\theta_x \approx \theta_x$.

When the rigid die is subjected to displacements x (bounce), y_1 (shear), y_2 (shear) and rotations θ_1 (rock), θ_2 (rock), θ_x (twist), the compressive normal strain at any location (z_1, z_2) can be expressed as

$$\varepsilon_{xx}(z_1, z_2) = \frac{x - z_1\theta_2 + z_2\theta_1}{t_0(1 - \frac{z_1}{t_0}\alpha_2 + \frac{z_2}{t_0}\alpha_1)}$$

If the variation in thickness across the bond is small, then the strain can be approximated to

$$\varepsilon_{xx}(z_1, z_2) \approx \frac{1}{t_0}(x - z_1\theta_2 + z_2\theta_1)(1 + \frac{z_1}{t_0}\alpha_2 - \frac{z_2}{t_0}\alpha_1)$$

Using this result, the compressive normal stress at location (z_1, z_2) can be expressed

$$\sigma_{xx}(z_1, z_2) \approx \frac{E}{t_0}(x - z_1\theta_2 + z_2\theta_1)(1 + \frac{z_1}{t_0}\alpha_2 - \frac{z_2}{t_0}\alpha_1)$$

Similarly, the shear strains at location (z_1, z_2) can be expressed as:

$$\gamma_{xy_1}(z_1, z_2) = \frac{y_1 - h_G\theta_2 - z_2\theta_x}{t_0(1 - \frac{z_1}{t_0}\alpha_2 + \frac{z_2}{t_0}\alpha_1)} \approx \frac{1}{t_0}(y_1 - h_G\theta_2 - z_2\theta_x)(1 + \frac{z_1}{t_0}\alpha_2 - \frac{z_2}{t_0}\alpha_1)$$

$$\gamma_{xy_2}(z_1, z_2) = \frac{y_2 + h_G\theta_1 + z_1\theta_x}{t_0(1 - \frac{z_1}{t_0}\alpha_2 + \frac{z_2}{t_0}\alpha_1)} \approx \frac{1}{t_0}(y_2 + h_G\theta_1 + z_1\theta_x)(1 + \frac{z_1}{t_0}\alpha_2 - \frac{z_2}{t_0}\alpha_1)$$

and the resulting shear stress is

$$\tau_{xy_1}(z_1, z_2) \approx \frac{G}{t_0}(y_1 - h_G\theta_2 - z_2\theta_x)(1 + \frac{z_1}{t_0}\alpha_2 - \frac{z_2}{t_0}\alpha_1)$$

$$\tau_{xy_2}(z_1, z_2) \approx \frac{G}{t_0}(y_2 + h_G\theta_1 + z_1\theta_x)(1 + \frac{z_1}{t_0}\alpha_2 - \frac{z_2}{t_0}\alpha_1)$$

The resultant forces and moments acting upon the rigid die are found by integrating these elemental forces over the cross-sectional area of the bond to give

$$F_{xx} = \int_{\frac{-a_2}{2}}^{\frac{a_2}{2}}\int_{\frac{-a_1}{2}}^{\frac{a_1}{2}} \sigma_{xx}(z_1, z_2)dz_1dz_2 = \frac{E}{t_0}\left(xa_1a_2 - \frac{\theta_1\alpha_2a_1a_2^3}{12t_0} - \frac{\theta_2\alpha_1a_1^3a_2}{12t_0}\right)$$

$$F_{y_1y_1} = \int_{\frac{-a_2}{2}}^{\frac{a_2}{2}}\int_{\frac{-a_1}{2}}^{\frac{a_1}{2}} \tau_{xy_1}(z_1, z_2)dz_1dz_2 = \frac{G}{t_0}\left((y_1 - h_G\theta_2)a_1a_2 + \frac{\theta_x\alpha_1a_1a_2^3}{12t_0}\right)$$

$$F_{y_2y_2} = \int_{\frac{-a_2}{2}}^{\frac{a_2}{2}}\int_{\frac{-a_1}{2}}^{\frac{a_1}{2}} \tau_{xy_2}(z_1, z_2)dz_1dz_2 = \frac{G}{t_0}\left((y_2 + h_G\theta_1)a_1a_2 + \frac{\theta_x\alpha_2a_1^3a_2}{12t_0}\right)$$

$$M_{\theta_1\theta_1} = \int_{\frac{-a_2}{2}}^{\frac{a_2}{2}}\int_{\frac{-a_1}{2}}^{\frac{a_1}{2}} z_2\sigma_{xx}(z_1, z_2) + h_G\tau_{xy_2}(z_1, z_2)\, dz_1dz_2 = \frac{E}{t_0}\left(\frac{\theta_1a_1a_2^3}{12} - \frac{x\alpha_1a_1a_2^3}{12t_0}\right)$$

$$+ \frac{Gh_G}{t_0}\left((y_2 + h_G\theta_1)a_1a_2 + \frac{\theta_x\alpha_2a_1^3a_2}{12t_0}\right)$$

$$M_{\theta_2\theta_2} = \int_{\frac{-a_2}{2}}^{\frac{a_2}{2}}\int_{\frac{-a_1}{2}}^{\frac{a_1}{2}} -z_1\sigma_{xx}(z_1, z_2) - h_G\tau_{xy_1}(z_1, z_2)\, dz_1dz_2$$

$$= \frac{E}{t_0}\left(\frac{\theta_2a_1^3a_2}{12} - \frac{x\alpha_2a_1^3a_2}{12t_0}\right) - \frac{Gh_G}{t_0}\left((y_1 - h_G\theta_2)a_1a_2 + \frac{\theta_x\alpha_1a_1a_2^3}{12t_0}\right)$$

$$M_{\theta_x\theta_x} = \int_{\frac{-a_2}{2}}^{\frac{a_2}{2}} \int_{\frac{-a_1}{2}}^{\frac{a_1}{2}} z_1 \tau_{xy_2}(z_1, z_2) - z_2 \tau_{xy_1}(z_1, z_2)\, dz_1 dz_2$$

$$= \frac{G}{t_0}\left((y_2 + h_G\theta_1)\frac{\alpha_2 {a_1}^3 a_2}{12t_0} + (y_1 - h_G\theta_2)\frac{\alpha_1 a_1 {a_2}^3}{12t_0} + \theta_x \frac{({a_1}^3 a_2 + a_1 {a_2}^3)}{12} \right)$$

The force and moment equations can be used to determine the stiffness matrix of the sloped bond, such that:

$$K = \frac{1}{t_0}\begin{bmatrix} Ea_1a_2 & 0 & 0 & \frac{-Ea_1{a_2}^3\alpha_1}{12t_0} & \frac{-E{a_1}^3a_2\alpha_2}{12t_0} & 0 \\ 0 & Ga_1a_2 & 0 & 0 & -h_GGa_1a_2 & \frac{Ga_1{a_2}^3\alpha_1}{12t_0} \\ 0 & 0 & Ga_1a_2 & h_GGa_1a_2 & 0 & \frac{G{a_1}^3a_2\alpha_2}{12t_0} \\ \frac{-Ea_1{a_2}^3\alpha_1}{12t_0} & 0 & h_GGa_1a_2 & \frac{Ea_1{a_2}^3}{12} + {h_G}^2Ga_1a_2 & 0 & \frac{h_GG{a_1}^3a_2\alpha_2}{12t_0} \\ \frac{-E{a_1}^3a_2\alpha_2}{12t_0} & -h_GGa_1a_2 & 0 & 0 & \frac{E{a_1}^3a_2}{12} + {h_G}^2Ga_1a_2 & -\frac{h_GGa_1{a_2}^3\alpha_1}{12t_0} \\ 0 & \frac{Ga_1{a_2}^3\alpha_1}{12t_0} & \frac{G{a_1}^3a_2\alpha_2}{12t_0} & \frac{h_GG{a_1}^3a_2\alpha_2}{12t_0} & -\frac{h_GGa_1{a_2}^3\alpha_1}{12t_0} & G\left(\frac{a_1{a_2}^3}{12} + \frac{{a_1}^3a_2}{12}\right) \end{bmatrix}, \quad \begin{Bmatrix} x \\ y_1 \\ y_2 \\ \theta_1 \\ \theta_2 \\ \theta_x \end{Bmatrix}$$

Inspection of the derived stiffness matrix reveals coupling between bounce and rocking components, *x,* θ_1 and θ_2, and shear and twist components, y_1, y_2 and θ_x. It can be seen that the sloped bond experiences extensive coupling of its translational and rotational coordinates, in addition to the inherent coupling observed in the shear directions for a perfect bond.

The bond thickness variation has induced coupling of the bounce coordinate *x* with rotational rocking coordinates, θ_1 and θ_2. Through inspection of the coupling terms in the stiffness matrix, it can be seen that bounce is coupled to θ_1 if tilt angle α_1 is non-zero, and similarly is coupled to θ_2 if tilt angle α_2 is non-zero. Therefore, if the bond is sloped, i.e. $\phi \neq 0$, then the bounce will be coupled to both rocking coordinates, unless the slope direction, β is parallel to a shear direction. In this case, bounce will only be coupled to a single rocking coordinate, such that if β is aligned with y_1 then coupling exists with θ_2 only ($\alpha_1 = 0$), or if aligned with y_2 then bounce is coupled with θ_1 only ($\alpha_2 = 0$). If this coupling is present then when the bond is excited in the bounce direction, the response will include *x,* θ_1 and θ_2 components. Therefore, when tested over frequency as is conducted in the experiments, the resonant peaks due to the rocking modes will be visible in the transmissibility function, as well as contamination of the bounce modal peak with rocking components, unless the measurements are taken at the intersection of the rocking axes. When considering the responses at differing points on the dies surface,

this would result in multiple observable peaks in the TFs and varying gains between differing measurement points, as observed in the trial experiments.

It can also be seen in the stiffness matrix that the shear coordinates, y_1 and y_2, have further coupling terms induced by the slope in addition to that associated with the inherent coupling from the single sided bond design. These terms couple each shear coordinate with the rotational twist coordinate, θ_x. unlike the inherent coupling described for the perfect bond, coupling to θ_x will cause motion that will rotate the measurement points so that they are not consistently perpendicular to the measurement direction, resulting in varying gains at the various measurement points. This coupling will also result in excitement of the twist mode when under shear excitation, leading to multiple peaks in the transmissibility functions, as was observed in the trial experiments. Inspecting the terms for each shear direction independently, it can be seen that y_1 is coupled to twist if α_1 is non-zero, and y_2 is coupled to twist if α_2 is non-zero. Therefore, if a slope exists the twist will be coupled to the shear excitement unless the bond direction is aligned with that same shear direction.

In summary, the stiffness matrix for a sloped bond has confirmed that bond slope couples the translational and rotational coordinates, and it has been reasoned that this coupling, together with other forms of manufacturing imperfection, is the root cause for the rotational contamination observed in the trial experiments when the sample is excited in bounce and shear.

3.4.2. Finite Element Modelling

In this section, the bond imperfection study is extended to use simple FE models in Creo Simulate to investigate the influence of different bond imperfections. The FE simulations replicate the trial experiments by calculating the damped response of the die at various locations (same as those used in multipoint experiments) for base excitations applied in bounce and shear directions. The resulting multipoint transmissibility functions are analysed and compared qualitatively with those observed in trial experiments. Perfect and imperfect bond cases are investigated, and the measured bond properties compared to assess the errors induced by various imperfections. Figure 73 shows the tetrahedral mesh used in these FE models, the elements are sized such that there are 2 elements across the thickness of the deforming bond. The model incorporates a 6% viscous damping coefficient and elastic material properties for silicone (bond) of 2300kg/m3, 0.49 and 1.7MPa (for density, Poisson's

ratio and Young's modulus respectively), for aluminium (base) of 2700kg/m3, 0.3 and 69GPa, and for steel (die) of 7800kg/m3, 0.27 and 200GPa.

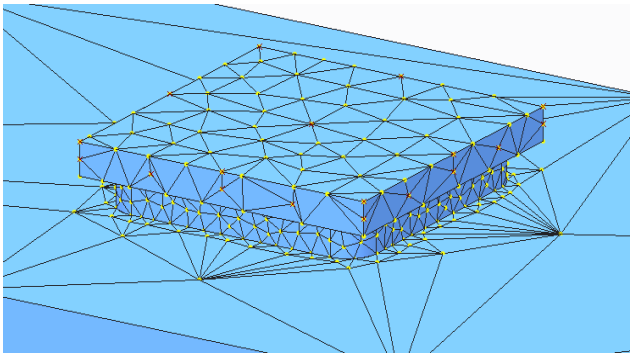


Figure 73 - Tetra mesh used for Creo Simulate FE models (shown is the perfect geometry case)

3.4.2.1. Perfect Bond

Figure 74 shows the transmissibility functions calculated at different points on the die for the perfect bond case simulated from the FE. The reproduced responses (omitted for clarity) are a relatively poor fit to the responses simulated from FE, particularly when excited in bounce (shear fits are better). These discrepancies in fit are due to the differing loss mechanisms used in the models (FE utilises viscous damping model). However, the absolute values for loss and modulus are not of concern and are only used as a benchmark for comparison with those derived for imperfect bonds. It can also be seen that the FE model responses are approximately equal at differing locations as would be expected for the perfect bond. Slight variations are observed showing the crudeness of the models used and are likely caused by asymmetric meshing of the bond.

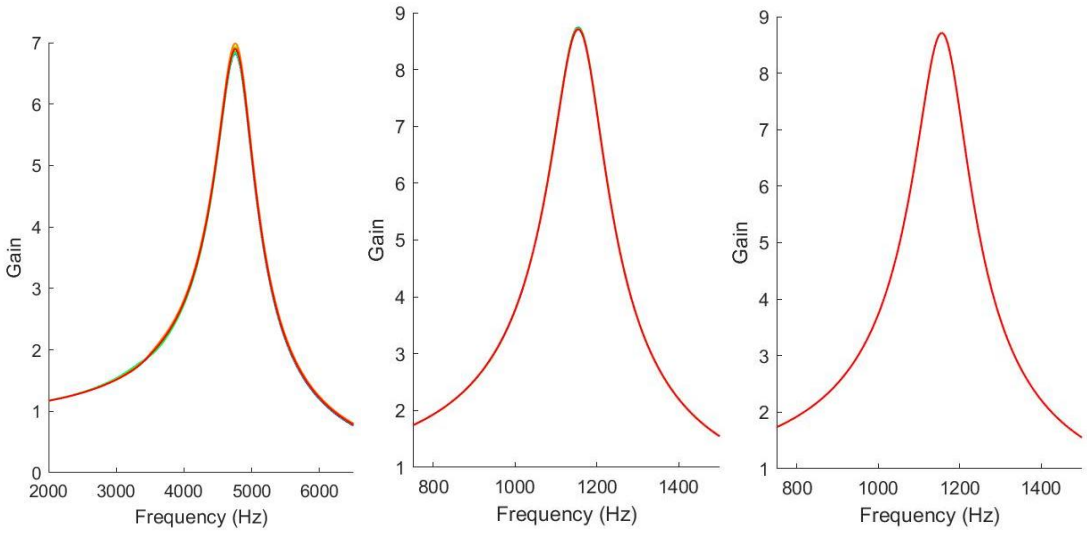


Figure 74 -Transmissibility functions simulated using Creo Simulate model of a perfect bond, a) bounce, b) shear y_1 and c) y_2

3.4.2.2. Sloped Bond

In this section the multipoint transmissibility functions are calculated for samples with sloped bond imperfections having different slope angles and direction, as defined in Figure 71. Small (ϕ~1°) and large (ϕ =5°) slope angles are considered together with slopes aligned and misaligned with the shear directions. The effects of these sloped bond variants on the transmissibility functions at different points will be investigated and discussed. A quantitative analysis of the errors will be discussed later.

Figure 75 shows the calculated multipoint transmissibility functions for a sloped bond aligned with shear direction y_2. The figure includes responses calculated for different excitation directions: bounce x (a), shear y_1 (b) and shear y_2 (c), as well as small (row 1) and large slope angles (row 2).

For small slope angles it can be seen that in bounce results occur in 3 distinct bands, with each band containing 3 point responses. This banded response is due to the presence of rocking about a single shear axis (y_1 (θ_1)), such that the points forming line measurements perpendicular to this axis experience the same response. In bounce a second modal peak is observed at approximately 3300Hz, which is associated with this coupled θ_1 mode. The shear results indicate that the slope couples the y_1 direction with die twist (θ_x), observed in the response as the variable gain between all points along the die edge and the secondary mode excitement visible at approximately 1050Hz, and associated with the twist mode. No coupling is observed for the y_2 shear direction, with all points experiencing a single and identical modal peak response. This coupling was predicted using the analytical sloped bond model described in Section 3.4.1.2. It was noted that when the imperfection is aligned with a shear direction, there is no coupling about that shear direction (other than the inherent), bounce couples to the rotation about that axis, while the other shear direction experiences coupling with twist.

For larger slope angles, the level of coupling increases. This causes the effects observed at smaller angles to be exaggerated, but no additional coupling effects are seen. The higher levels of coupling lead to greater variations in gain between the measurement points, as well as greater excitement at the secondary modes of rocking and twist for bounce and shear respectively. Despite the greater levels of coupling, shear direction y_2 remains uncoupled.

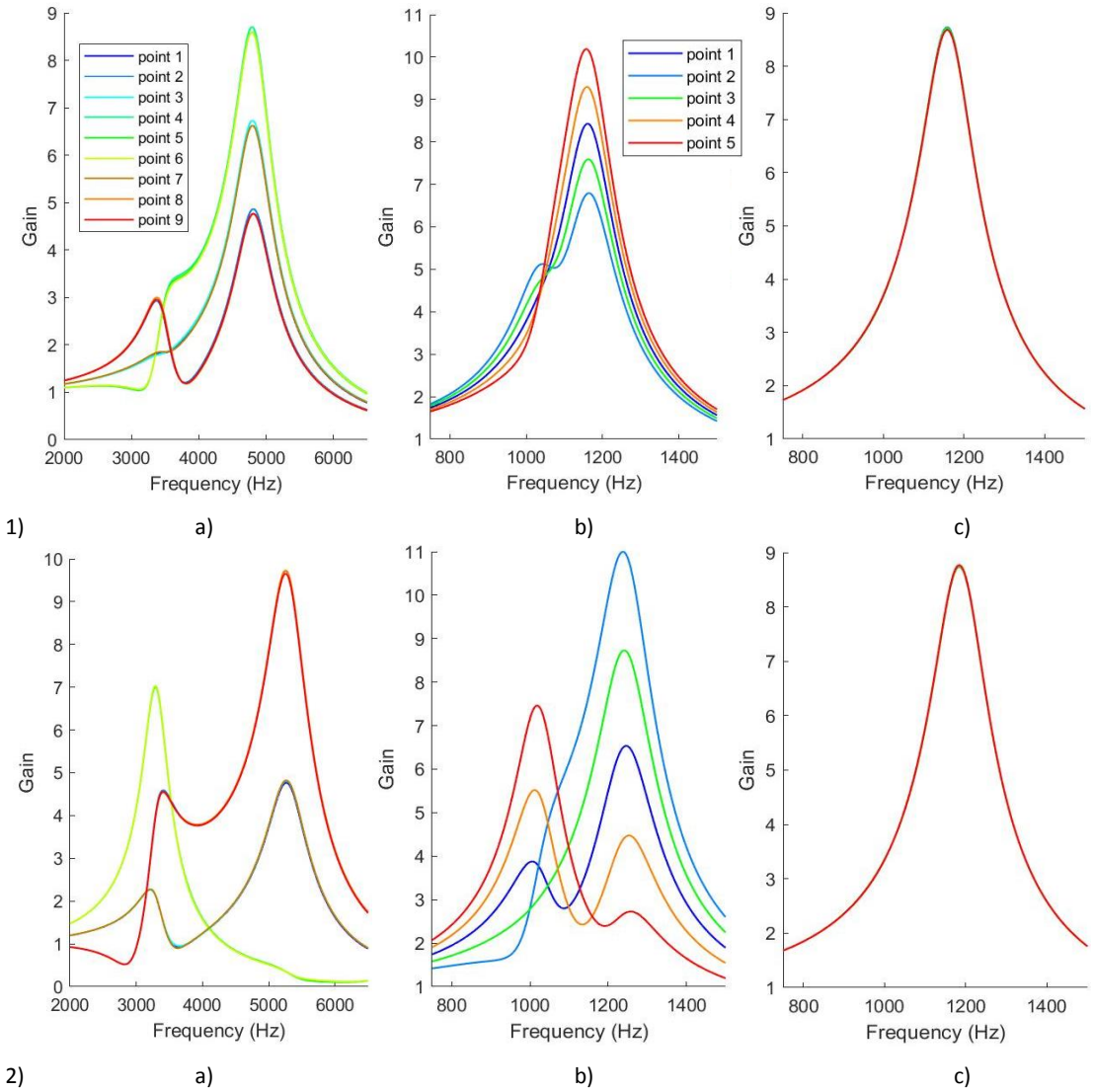


Figure 75 – Multipoint Transmissibility Functions for a sloped bond aligned with y_2 or β=0° excited in bounce x (a), shear y_1 (b) and shear y_2 (c), for ~1° (row 1) and 5° (row 2) slope angles

Figure 76 shows the calculated multipoint transmissibility functions for a sloped bond that is *not* aligned with a shear direction (2-dimensional slope). For small slope angles, the bounce response does not have a banded structure like Figure 75, indicating that bounce is coupled to both rocking coordinates. This coupling causes the gain for the bounce modal peak to vary and the rocking modes to be excited. The shear responses also suffer from varying peak gains and secondary mode excitement, indicating y_1 and y_2 are both coupled with θ_x, with the y_2 direction experiencing greater differences in gain and excitement of the twist mode because the slope direction is more closely aligned with the y_1 axis.

For larger slope angles, the coupling effects are exaggerated with greater contamination of the translation modes and excitement of the rotational modes than observed in Figure 75. However,

additional effects are also observed. In bounce the peak for the excited rotational mode changes with location, indicating that both of the rocking modes are excited significantly. However, as the frequency separation from the bounce peak remains large, this should not significant affect the accuracy of loss factor and modulus calculations. However, in shear the modal peak distorts and widens for larger slope angles because the shear responses couple and the frequencies split. It is anticipated that this peak widening will adversely affect the ability of the averaged multi-power bandwidth method to determine the loss factor.

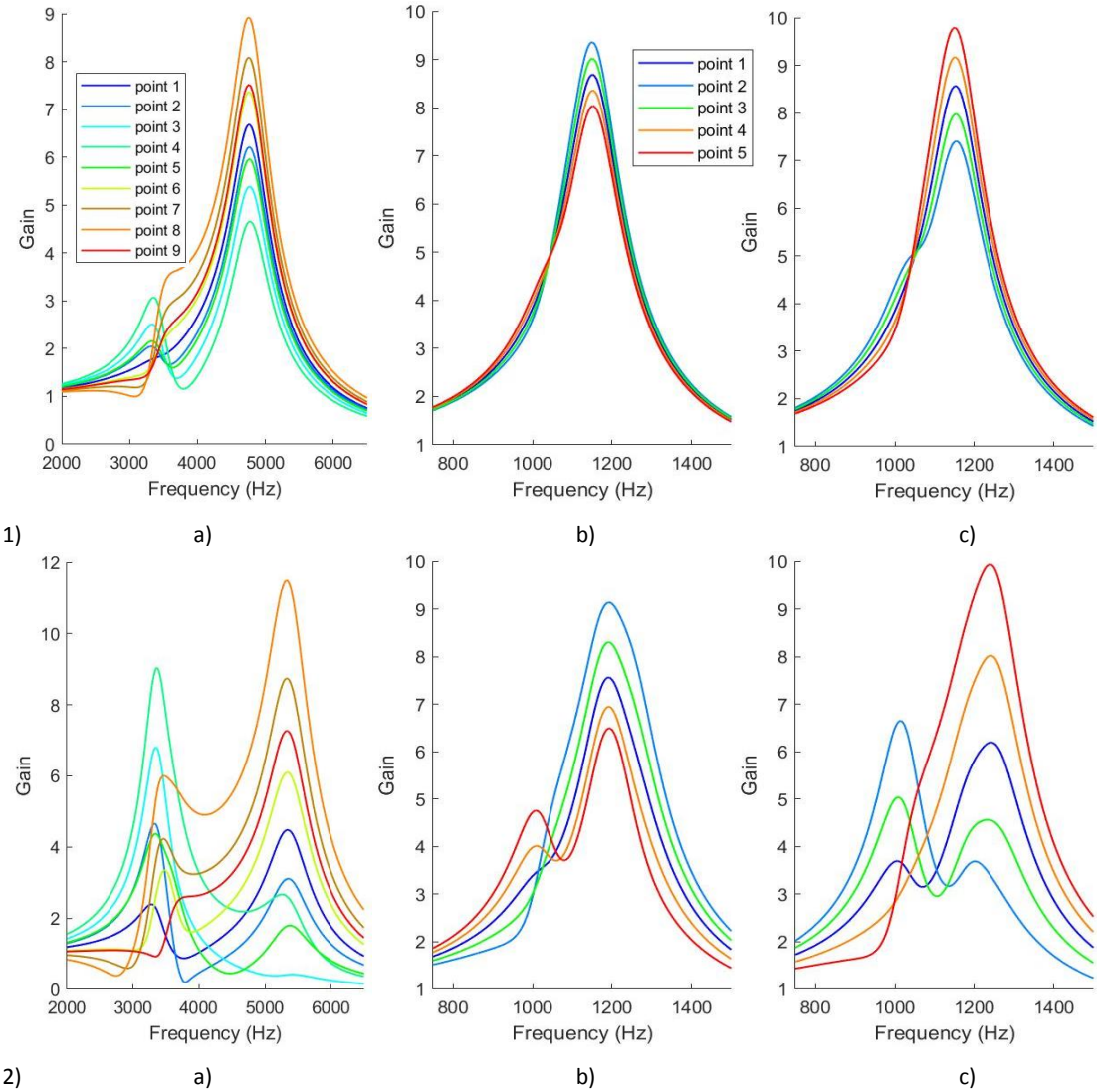


Figure 76 – Multipoint Transmissibility Functions for a misaligned sloped bond (β=60°) excited in bounce x (a), shear y_1 (b) and shear y_2 (c), for ~1° (row 1) and 5° (row 2) slope angles

3.4.2.3. Die Misplacement

In this section the multipoint transmissibility functions are calculated for bonds with a die misplacement or offset error, i.e. the centre of the die will be offset from the centre of the bond. Two

types of die misplacement are considered. These are when the die is misplaced along a particular shear direction and the more general case when the die is misplaced with components in both shear directions. Both cases are shown in Figure 77.

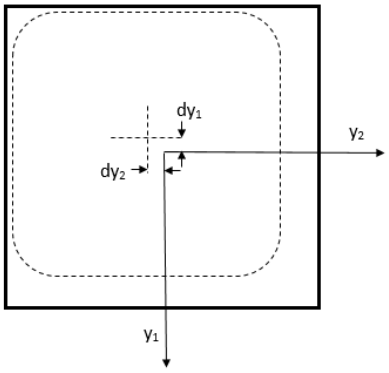
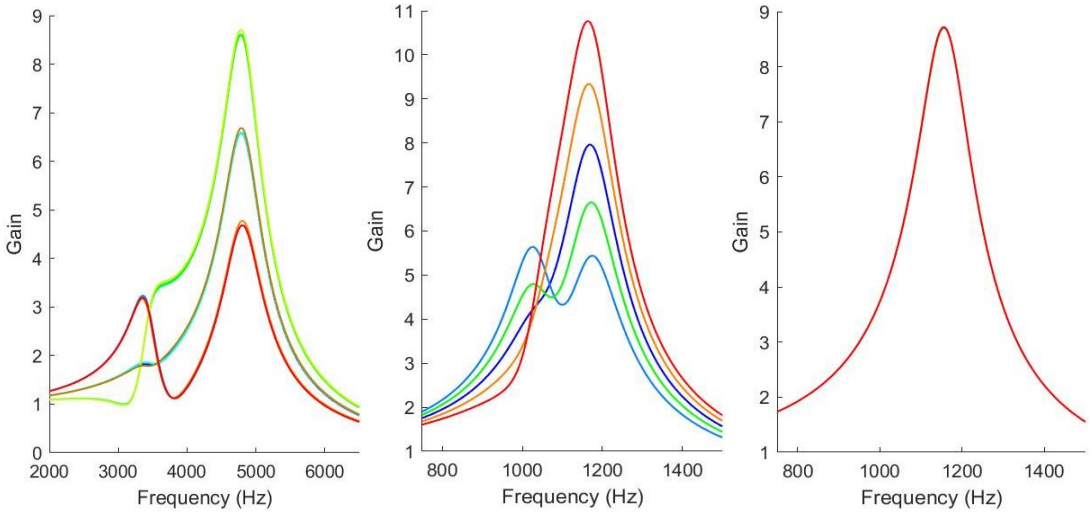


Figure 77 - Diagram of die offset definition

Figure 78 shows the calculated multipoint transmissibility functions when the die is misplaced a distance -0.3mm along the y_2 shear direction. The figure includes responses calculated for different excitation directions: bounce x (a), shear y_1 (b) and shear y_2 (c). It can be seen that the bounce response is very similar to that obtained in Figure 75 and has the same banded structure. Results in the y_1 shear direction indicate coupling with twist, θ_x. However, the y_2 shear direction has no coupling contamination, with identical responses obtained at all measurement points. Comparing Figure 75 and Figure 78 it can be deduced that the level of coupling for the given die misplacement is slightly larger than that observed for low angle (~1°) slope.



a) b) c)

Figure 78 – Multipoint Transmissibility Functions for a die misplaced -0.3mm in the y_2 direction excited in bounce x (a), shear y_1 (b) and shear y_2 (c)

Figure 79 shows the calculated multipoint transmissibility functions when the die is misplaced distanced -0.3mm along the y_2 direction and 0.4mm along the y_1 direction. The additional offset in the y_1 direction induces coupling between θ_x and y_2, as well as the existing y_1 coupling, and increases the level of coupling observed in bounce, including excitement of the second rocking mode as well. It is also observed that, despite maintaining the same offset in y_2, adding offset in y_1 reduces the level of coupling between y_1 and θ_x. Comparing Figure 76 and Figure 79 it can be deduced that die misplacement induced similar levels of coupling to those observed for the large slope angle case. Despite this high level of coupling, the shear mode peaks do not appear to distort. This issue will be discussed later when errors in estimated loss factors are considered in Section 3.4.2.4.

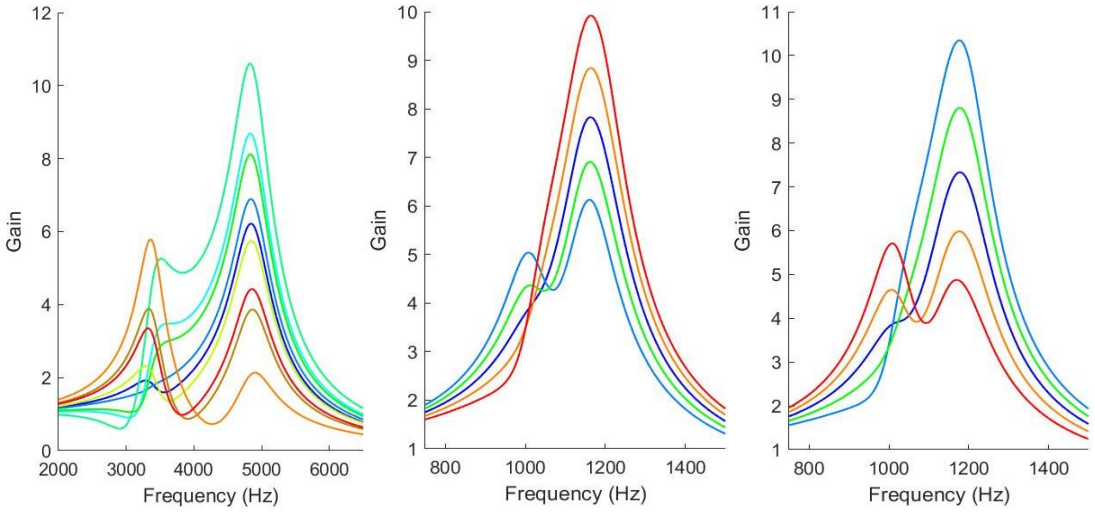


Figure 79 – Multipoint Transmissibility Functions for a die misplaced 0.4mm in the y_1 direction and -0.3mm in the y_2 direction excited in bounce x (a), shear y_1 (b) and shear y_2 (c)

3.4.2.4. Combined sloped bond and misplaced die imperfections

In this section the multipoint transmissibility functions are calculated for samples with sloped bond and misplaced die imperfections. As a part of this investigation the sign of one imperfection is varied in order to observe whether imperfections of differing types can counteract each other and reduce the level of coupling observed between translational and rotational coordinates. The two cases considered in this section are shown in Figure 80. Case 1 considers a large slope angle and die displacement, while Case 2 is the same as Case 1 except the offset in the y_2 direction has the opposite sign, allowing observations to be made how the two imperfection types interact.

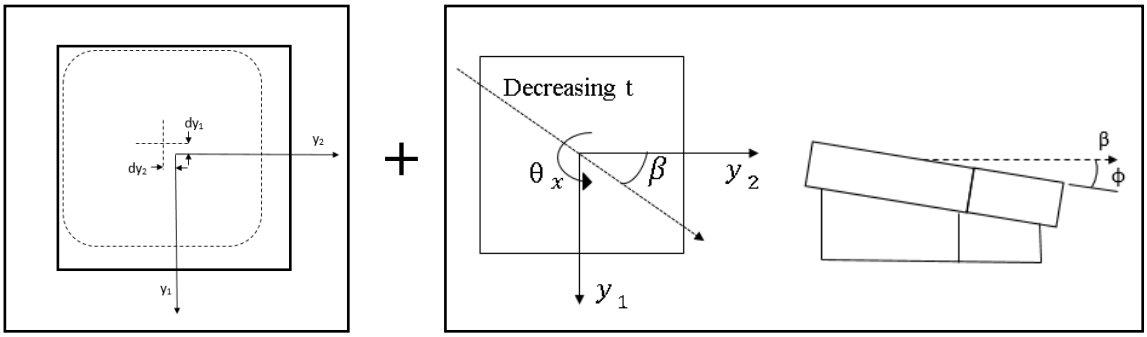
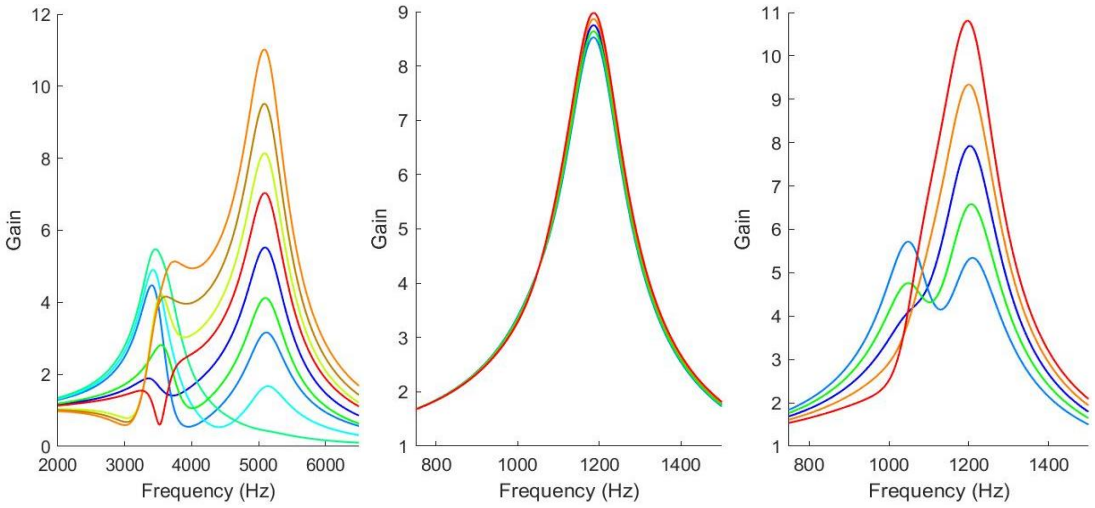


Figure 80 - Diagrams Defining Combined Imperfections

Figure 81 shows the calculated transmissibility functions for Case 1. Compared to responses observed earlier for the large angle slope, the coupling to bounce reduces with the additional die offset, with lower excitement of the rocking modes and less variation in gain at the bounce mode. In the shear y_2 direction, lower coupling is also experienced, with much less distortion of the shear peak as well. Further to this, the coupling between y_1 and twist, θ_x, has almost been eliminated, with almost no response at the twist mode frequency and only a low level of rotational contamination at the shear mode frequency. Therefore, the addition of the 2D offset has reduced the coupling in all 3 translational directions, strong coupling still exists in the responses to x and y_2, however in y_1 has almost been eliminated

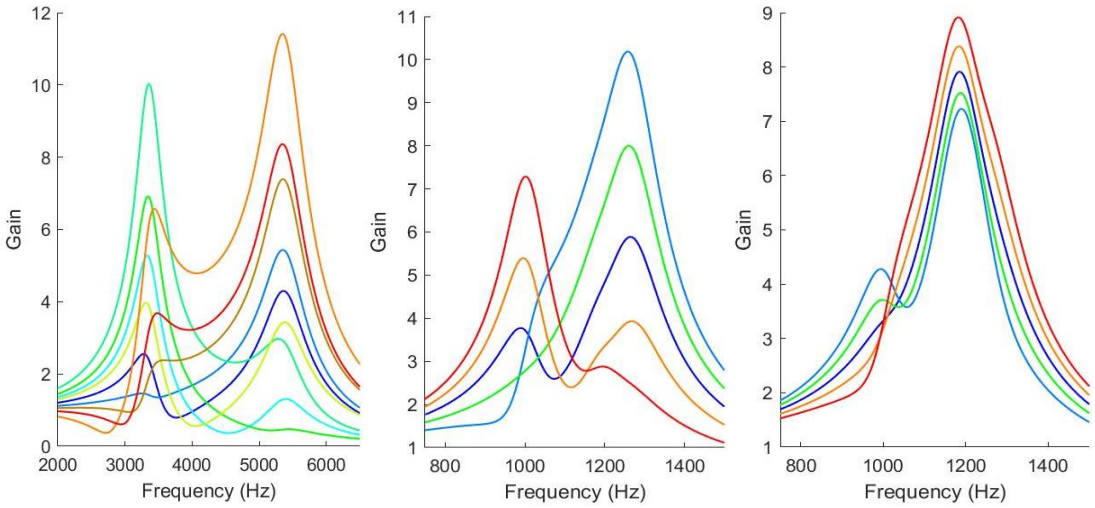


a) b) c)

Figure 81 - Multipoint Transmissibility Functions for case 1 of a combination of sloped bond and misplaced die excited in bounce x (a), shear y_1 (b) and shear y_2 (c)

Figure 82 shows the calculated transmissibility functions for Case 2. It can be seen that the results are significantly different to Case 1 due to the change in y_2 sign. The change has caused greater coupling between bounce and rocking than observed for the large angle slope alone, with greater excitement of the rocking modes under bounce excitation. The level of coupling observed in the y_1 shear

response has also been increased, with larger twist response at both the twist and shear mode frequencies. Distortion of the y_1 shear mode peak also indicates a large split has been induced in the shear modes, particularly evident when observing the difference in peak location between measurements at point 1 (cyan) and point 5 (red). The y_2 shear response also changes greatly, but its coupling with θ_x is reduced, with lower excitement of the twist mode, and less variation in the peak gains at the translational mode frequency. However, despite this reduced coupling between y_2 and θ_x, distortion of the shear mode peak is visible. This is likely to be caused by the large split induced by the relatively large imperfections and the high level of coupling observed between y_1 and θ_x. Therefore, while it has been observed that the two imperfection types can oppose one another and reduce the levels of coupling experienced between translational and rotational coordinates, it is sensitive to the directions of those imperfections, and can cause increases in coupling levels, as well as cause large frequency splits in the shear modes.



a) b) c)

Figure 82 - Multipoint Transmissibility Functions for case 2 of a combination of sloped bond and misplaced die excited in bounce x (a), shear y_1 (b) and shear y_2 (c)

3.4.2.5. Measured Bond Property Errors Induced by Imperfect Samples

In this section, the calculated transmissibility functions for samples with sloped bond and misplaced die imperfections are analysed using the methods described in Sections 3.2 and 3.3 to estimate the loss factor and modulus for the bond. The methods used are of the exact and second order forms (equations (2.3) and (3.2)) and include interpolation models.

Table 9 summarises the percentage errors obtained for the estimated loss factor and modulus based on frequency response calculations at the central point (point 1), for different imperfections. The percentage errors are calculated by comparing values obtained for the perfect and imperfect bonds.

For modulus calculations, the errors are relatively low when the imperfection level is small, i.e. ~1° slope angle. However, when the imperfection is larger, the errors are much greater (>5%) because the modal peak frequency increases, suggesting that the bond has stiffened.

The loss factor errors are dependent on the calculation method used and the results shown in Table 9 indicate the inverse transmissibility method is more sensitive to imperfections. The errors obtained using this method are >3% for low level imperfections, and are significantly higher for larger level imperfections, with some >50%. In comparison the averaged multi-power bandwidth method provides much improved loss estimates, with errors <1% for low level imperfections. However, for larger imperfections the shear loss factors are >~10%, due to the frequency splits between the two shear modes. In bounce, accurate loss factors are achieved with errors less than 1.5%, even when different combinations of imperfection are considered.

Table 9 – Percentage errors (compared to the FE perfect bond case) in modulus and loss, calculated using various methods, for the central measurement points in bounce and shear directions, yellow indicates <±1% error transitioning to red at >±10%

	Modulus Error (central point) %			Loss Factor Error (central point) – mp %			Loss Factor Error (central point) - 1/T %		
Imperfection Description	**X**	**y1**	**y2**	**X**	**y1**	**y2**	**x**	**y1**	**y2**
0° direction (1°)	1.73	1.21	0.44	-0.19	0.90	0.00	3.01	3.54	0.13
0° direction (5°)	22.56	16.58	4.95	-1.00	-2.42	-0.03	44.65	34.16	-0.48
60° direction (1°)	0.16	-0.50	-0.54	-0.11	0.24	0.60	2.13	0.49	1.73
60° direction (5°)	26.22	6.57	15.53	-1.04	14.89	28.02	54.29	15.65	41.53
1D offset	1.34	2.65	0.00	-0.28	-0.02	0.00	3.64	9.74	0.00
2D offset	3.72	1.55	3.89	-0.65	9.74	12.78	9.92	11.64	19.06
5° slope (60°) +offset	14.85	5.58	8.37	-0.53	0.04	-0.37	24.12	-0.31	10.07
5° slope (60°) +offset (y2 sign change)	27.13	20.06	5.19	-1.31	12.40	5.72	61.20	49.37	10.22

In experiments central measurement points are used to calculate the bonds material properties. However, this measurement location is only approximate and can vary slightly between tests, whether on the same or differing samples. Therefore, it is important to understand how the derived properties attained vary depending on the measurement location on the die surface or edge.

In the following sections the average (mean) and spread (max-min) in errors over the entire die surface/edge are shown and discussed. The values shown use the 9/5 extreme locations in bounce and shear directions respectively, representing the worst case. In reality, measurements will not be taken at the corners/edge, however this provides a metric for the variability of properties calculated over the entire measurement location range.

Table 10 shows the mean absolute percentage errors in modulus and loss factor, calculated over all measurement points, while Table 11 shows the spread in those averaged errors. For modulus calculations, as seen for the central measurement points, low level imperfections suffer from small average errors, particularly for low slopes (<2%), offset errors are higher but still <4%. These maximum average errors are seen in bounce, with shear modulus estimates observed to be less sensitive. Modulus estimates in both directions for large imperfections are subject to much greater average errors, with many over 10%. The spread in modulus error is relatively low, this is because the stiffness effect is consistent over the differing measurement points, and therefore experiencing the same peak frequency shift. For some large imperfections there is a significantly larger spread, this is due to low response at some or one measurement points where the translational motion is being counteracted by the rotational contributions. Therefore, the translational mode peak is not observed in the frequency response and the coupled mode is mistakenly selected as the peak to be analysed.

For loss factors, again the calculation method used is important, with the inverse transmissibility method showing excess average errors of over 10%, unless the imperfection is aligned with a shear direction, leaving a shear mode uncoupled and therefore able to be analysed accurately. The spread in errors over the measurement locations follow this same pattern. In the majority of cases the spread in error is greater than 70% and, in some cases, exceed 3000% (these are caused by the same subdued response cases discussed for modulus error spread). Therefore, the inverse transmissibility method is highly sensitive to measurement position if any level of imperfection is present in the bond.

The average loss errors observed for the multi-bandwidth method are significantly better, with <~2% average errors seen for low level imperfections. Larger magnitude imperfections have a more significant effect, particularly in shear. The spreads in the errors follow the same pattern, with spreads

of <6% observed for the low-level imperfections over the extreme measurement location range. Therefore, the multi-power bandwidth method is relatively position insensitive, especially considering that the values discussed are worst case, and the range of measurement locations in reality will be much smaller than investigated here.

Table 10 – Average of absolute errors across die surface/edge (all measurement points), for modulus and loss factor using various calculation methods, yellow - <1%, red - >10% average error

	Average Modulus Error %			Average Loss Factor Error – mp %			Average Loss Factor Error - 1/T %		
imperfection description	x	y1	y2	x	y1	y2	x	y1	y2
0° direction (1°)	1.80	1.20	0.44	1.64	1.47	0.05	23.19	13.81	0.25
0° direction (5°)	32.27	16.78	4.95	1.03	6.24	0.03	25.06	78.21	0.48
60° direction (1°)	0.24	0.50	0.54	1.29	1.05	0.80	17.39	4.65	9.03
60° direction (5°)	26.17	6.70	13.59	9.78	18.99	29.67	538.35	17.22	59.96
1D offset	1.42	2.66	0.01	1.77	2.06	0.04	24.32	26.02	0.04
2D offset	4.01	1.48	3.49	2.18	9.56	14.42	55.93	19.20	32.79
5° slope (60°) +offset	18.62	5.58	8.40	5.91	0.05	2.03	77.61	1.75	26.85
5° slope (60°) +offset (y2 sign change)	27.18	17.21	5.26	14.94	33.01	10.48	472.28	83.67	10.67

Table 11 – Spread in % errors across die surface/edge (all measurement points), for modulus and loss factor using various calculation methods, yellow - <1%, red - >10% error spread

	Modulus Error Spread %			Loss Factor Error Spread – mp %			Loss Factor Error Spread - 1/T %		
Imperfection Description	x	y1	y2	x	y1	y2	x	y1	y2
0° direction (1°)	0.84	1.19	0.02	4.98	4.54	0.16	70.02	43.93	0.67
0° direction (5°)	74.77	3.74	0.01	3.22	26.96	0.03	74.28	258.66	0.34
60° direction (1°)	0.84	0.35	0.75	5.01	2.97	2.42	71.11	15.17	29.03
60° direction (5°)	7.38	0.33	7.45	42.19	50.01	19.10	4116.53	39.18	155.35
1D offset	1.00	1.93	0.04	5.13	6.34	0.12	69.88	81.69	0.14
2D offset	3.18	0.64	1.43	7.33	16.47	4.32	293.46	56.01	97.17
5° slope (60°) +offset	63.90	0.04	2.23	37.09	0.08	5.72	408.12	5.64	84.35
5° slope (60°) +offset (y2 sign change)	7.36	13.58	1.36	94.20	95.92	29.07	3336.99	232.37	23.11

3.5. Concluding Remarks on Loss Factor Calculation Methods

In this chapter, methods have been developed to improve the accuracy of loss factor predictions from experimentally measured transmissibility functions. The methods used include the averaged multi-power bandwidth method, use of interpolation methods for peak frequency, maximum

gain and bandwidth frequencies, as well as removal of the low loss assumptions that is normally used. The effect of signal imperfections, such as noise and artefacts, and bond imperfections, such as sloped bonds and die misplacements were investigated and the errors they induce in the derived properties were quantified. An analytical undamped model was used to illustrate the potential for bond imperfections, such as a sloped bond, to couple translational and rotational coordinates. Through simple FE models it was also shown that the transmissibility functions measured in trial experiments are consistent with bonds containing manufacturing imperfections such as sloped bonds, die misplacement or a combination of the two.

Different methods for estimating the loss factor have been considered throughout the investigations, including inverse transmissibility, half-power bandwidth, and averaged multi-power bandwidth methods. For a perfect bond geometry and noise-less measurements all methods considered have potential to make accurate loss factor predictions (<0.1% error) for loss factors <0.5, provided the low loss assumption is removed. Noise was found to have a significant effect on errors, even for relatively low levels of noise, and for this reason methods were introduced to smooth the data. These methods greatly improved the loss factor estimates for all calculation methods when the noise was low. However, for increased levels of noise the errors increased, with smoothing less effective. For low levels of smoothed noise, the results indicated that the inverse transmissibility method produced errors of <0.25% for loss factors in the range 0.05-0.5, while the averaged multi-power method produced larger errors of ±1 for low frequency resolutions and losses between 0.05 and 0.35.

Artefacts, described here as a sporadic high response at a single frequency, located in the transmissibility function at the side and centre of the modal peak were also investigated. Side artefacts did not affect the inverse transmissibility method, but can affect the accuracy of bandwidth methods. Central artefacts were found to induce large errors (>10%) for all loss factor calculation methods due to its effect on the natural frequency and maximum gain. However, through manual estimation of the natural frequency and maximum gain, estimated loss factor errors can be reduced.

The impact of bond and manufacturing imperfections on the estimates for modulus and loss factors were studied. For loss factors it was found that the inverse transmissibility method was susceptible to errors, even for low levels of sloped bond, and were larger still for small die misplacement

imperfections. A further issue observed with this method is that it is highly sensitive to the measurement location and therefore in order to calculate accurate loss factors the response must be measured at the die centre. The averaged multi-power method provided improved accuracy <1% for small imperfections, and reasonable accuracy <2.5% for larger imperfections if aligned to a shear direction, while accurately estimating the loss for small die offset imperfections as well. This method was found to be relatively insensitive to measurement position, allowing accurate estimates even if only approximately located towards the centre of the die.

Modulus estimates were found to be accurate for small slopes and die misplacements. However, large imperfections were found to induce large stiffness changes that produced large errors in the modulus estimate. Hence, in order to achieve accurate estimates for both modulus and loss factor only low levels of imperfection can be tolerated. This includes small angle 1- and 2-dimensional sloped bonds and 1D offsets. If 2D offsets are present accurate bounce properties can be derived but shear values are greatly affected due to splitting of the two modes.

The two main loss factor calculation methods investigated, the exact inverse transmissibility magnitude method and the second order multi-power bandwidth method, have been seen to both have advantages and disadvantages in differing scenarios. Both methods are highly accurate for perfect frequency response data over a large range of system loss factors. However, the multi-power method was seen to be more susceptible to errors from noise present in the transmissibility function, particularly when the noise magnitude exceeded 1% of the maximum gain. In the noise investigations it was seen that the half-power method was superior to the multiple-power, and the averaging process increased errors as opposed to reducing them. The multi-power method overcomes the errors experienced in the half-power method when artefacts are present in the signal, although requires manual estimation of the natural frequency and maximum gain if the artefact is located such that it obscures the maximum point of the modal peak. The advantage of the multi-power method is pronounced when there are manufacturing imperfections in the bond or die assembly imperfections, being relatively insensitive to contaminating rotations and measurement position, giving greater confidence in comparison between tests on the same or differing samples. As the differing methods have varying advantages and disadvantages in differing scenarios, both methods will be considered for

use in the experimental analysis. Considering both results will not only provide a reasonable range for the desired outputs, but along with a description of the issues present for a given transmissibility function, i.e. noise magnitude, artefact, level of coupling, it should allow selection of the most appropriate/accurate for a given signal.

4. Chapter 4: Finite Element Model Development

4.1. Introduction

In chapter 2, vibration tests on a bonded 'dummy' MEMS die were conducted, and it was found that its dynamic response varied due to changes in environmental temperature. This temperature dependence is partly due to the changing stress and deformation state of the die. To investigate the changing stress/deformation state of the die over temperature and its resulting impact on the natural frequency of the die a Finite Element model is developed. The FE model provides a simpler means of varying bond properties such as bond geometries (shape and thickness) and adhesive material properties (modulus and coefficient of thermal expansion). The model also represents important knowledge transfer to the sponsoring company to aid the modelling of small die bonds. This chapter first describes how and why stresses and deformations are caused during the die attach process, and how they induce errors in the performance of inertial sensors (Section 4.2.). Section 4.3. gives a general overview of the FE model, with description of its three parts, followed by a detailed description of the model, including investigations and discussions into the effects of model parameters, and concluding with the parameters required to achieve convergence. Results for the converged model outputs as a function of temperature are shown in Section 4.4. including the effects of including bonding stress, varying bond properties and using temperature dependent material properties. Conclusions on the observations are made and how the developed model will be used further in later chapters.

4.2. Theory

The die bond considered is a small adhesive bond with a cross-sectional area in the order of 10-100mm^2 having a thickness as small as 50µm. In practical applications the bond attaches the MEMS die, containing the sensitive MEMS element, to the device package. Figure 83 shows a diagrammatic representation of the sensor structure.

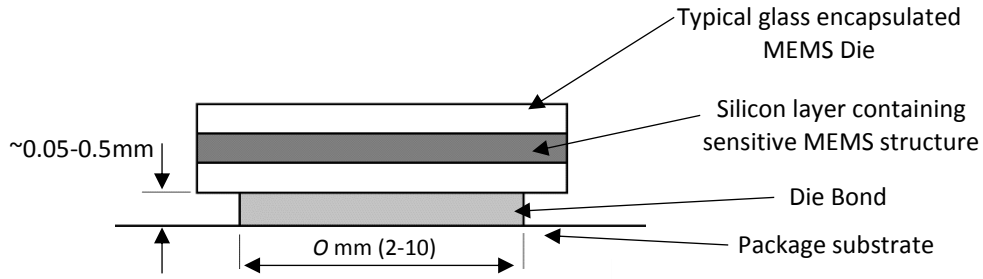


Figure 83 - Diagram of Die attachment via Die Bond, showing layers of the bonded structure

The device package, die bond adhesive and die each have different thermal expansion coefficients. Therefore after bonding, when cooling from the curing temperature each of the components contract at varying rates. This results in the bond becoming stressed and the die becomes curved, where the stress and curvature levels vary with temperature. A simple diagram of the expected deformations after bonding are shown in Figure 84.

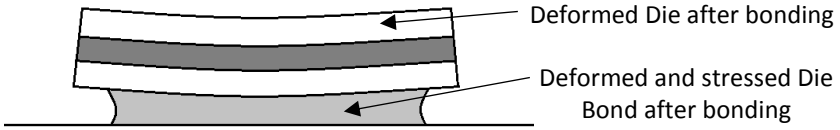


Figure 84 - Diagram showing typical deformations in the Die and Bond after bonding

The changing shape and stress in the die bond will cause the dynamic properties of the die to change and so affect device response to shock and vibration. The curvature of the die causes differing deformations of the MEMS structure, leading to bias offset effects. For example, within capacitive MEMS devices there are free and fixed electrodes and any stress induced deformations can change their relative position, resulting in misalignment and therefore unwanted capacitance changes, which causes sensing offsets. In accelerometers, this may produce a zero-g bias offset effect, where the capacitance change is interpreted as an acceleration when there is none applied. Figure 85 shows a simple diagram of the differing deformation and misalignment between the electrodes. The deformation can also induce stresses in the MEMS element at the free electrode anchoring, changing its dynamic characteristics and leading to scale factor changes. For example, if the anchors are stiffened by the stress the free electrode will deform less under a given acceleration, causing a lower capacitance change indicating a lower acceleration than actually applied. These performance errors vary with temperature.

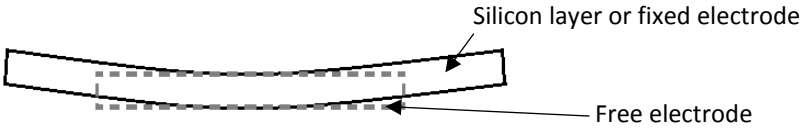


Figure 85 - Deformation and misalignment in capacitive electrodes due to induced curvature after bonding

The FE model developed here investigates the curvatures induced in the die and the changes in the dynamic behaviour of the die due to bonding and various trends over the operating temperature of a typical MEMS sensor. The performance effects considered are directly linked to the changes in die curvature and dynamics. The literature review also identified changes occurring over time, possibly due to stress relaxation within the bond [53] [44]. The magnitude of the die stress and curvature induced after bonding provides an indication of the potential changes over time due to possible viscoelastic mechanisms, i.e. a higher initial stress/curvature has a greater potential to change over time. However, any effect of permanent changes to the bond over time by viscoelastic mechanisms or through adhesive property changes due to further curing or aging, and their effects on temperature dependence are not investigated within the FE model.

4.3. Model description

4.3.1. Overview

The FE model developed includes simulations for: i) free expansion during temperature rise due to the curing temperature of the adhesive ii) constrained contraction as cooling takes place after bonding, and iii) dynamic response of the pre-stressed bond.

4.3.1.1. Free Expansion

The geometry of the modelled assembly includes the base, the bond and the die. The assembly is heated from room temperature (22^{o}C) to the curing temperature of the die bond adhesive (Dow Corning Q1-9225 silicone - 150^{o}C), resulting in an expanded assembly due to thermal expansion. Figure 86 shows a diagrammatic representation of this part of the process. The different parts of the assembly expand at different rates depending on their respective thermal expansion coefficients, and results in relative sliding between the different parts. The sliding is assumed to be frictionless, due to the unknown frictional behaviour between the surfaces, and so provides a worst-case solution for the stress

and curvature induced by the bond (i.e. maximum expansion). The use of a frictionless contact eliminates any changes to the shape of the contact interfaces, allowing full contact between interfaces to be maintained after expansion and mitigating the risk of any unbonded regions.

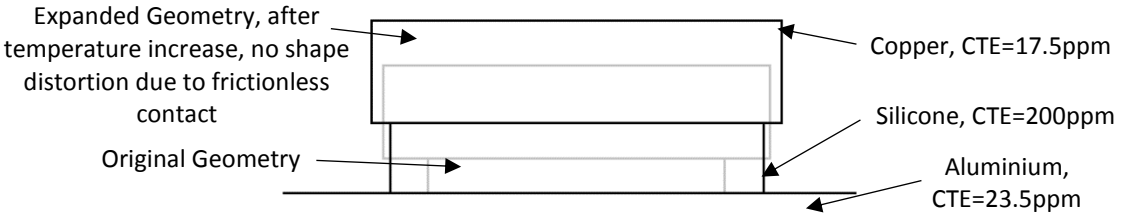


Figure 86 - Temperature increase stage of the modelling, showing original and expanded geometries

4.3.1.2. Constrained Contraction

The assembly is cooled back from the curing temperature to room temperature (or any temperature of interest). During this temperature change the different parts are rigidly constrained to each other at their contacting interfaces. During cooling, the parts contract at their respective rates, but because the bonded interfaces are constrained stresses and deformations are induced. The deformation induced are caused solely by the temperature change as the cure shrinkage is not included in the model, therefore the curvatures observed in the model are likely to be underestimated. Figure 87 shows a diagrammatic representation of the assembly showing the expanded and contracted geometries before and after cooling.

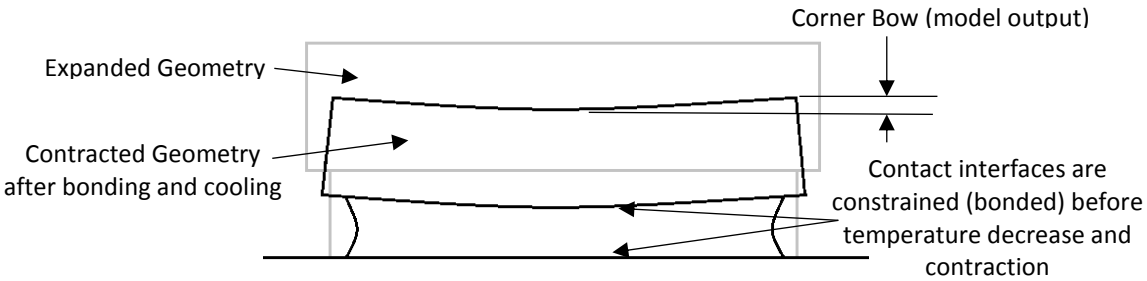


Figure 87 - Bonding and cooling stage of the modelling, showing expanded and deformed geometries, with definition of the output metric corner bow

4.3.1.3. Dynamic Response

The modal response of the stressed structure is investigated and the frequencies corresponding to bounce and shear translations are calculated. Figure 88 shows a diagrammatic representation of the die bond undergoing bounce and shear translations. The frequency changes caused by stress and curvature are calculated by comparing their values with same modal model but using the original unexpanded geometry (with constrained interfaces). The frequencies are calculated over a range of temperatures to establish the performance effects over temperature.

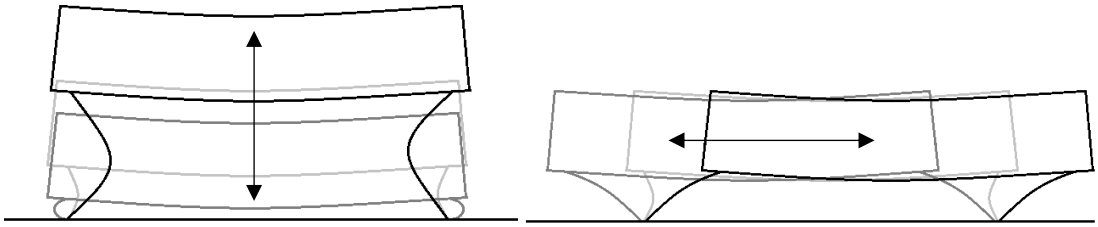


Figure 88 – Translational Die modes calculated during modal stage of the modelling, left, bounce, right, shear

4.3.2. Detailed Model Description

4.3.2.1. Finite Element Software Implementation

The FE model is developed using ANSYS Workbench v.15 to allow the sponsoring company to use its multiphysics capabilities in future work and allow knowledge and data transfer. Figure 89 shows the ANSYS model flowcharts used for the free expansion and constrained contraction stages.

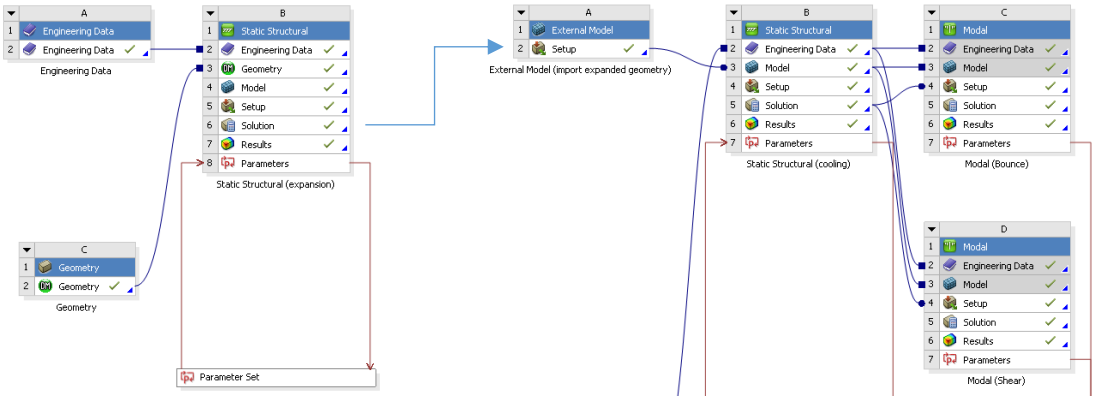


Figure 89 - ANSYS Workbench model flowcharts, left, expansion, right, contraction and modal

4.3.2.2. Assembly Geometry

The assembly is modelled in Creo as individual parts and then assembled, before being exported and then imported into ANSYS in the form of a Step file (.stp). Initially the geometry emulates that of the trial test sample, i.e. a copper 10x10x1mm die, 9x9x1mm silicone bond (rounded corners) and a 25x25x25mm aluminium base. The modelled geometries have 4 lines of symmetry and therefore a 1/8 model can be used, which greatly reduces the number of elements and time required to perform calculations. The symmetry conditions also provide the added benefit of constraining the entire assembly about its vertical centreline during the free expansion stage, maintaining the alignment of parts. Figure 90 shows the whole and 1/8 models used throughout the work.

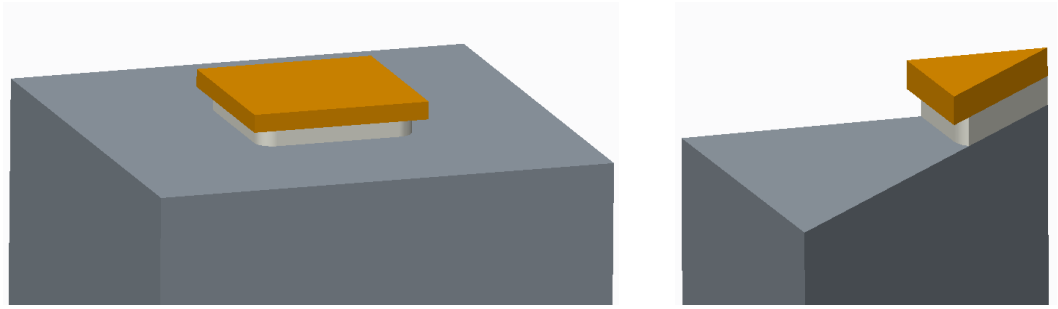


Figure 90 - Modelled geometries in Creo, left, whole, right, 1/8 model using 4 lines of symmetry

Table 12 summarises the material properties used. All materials are assumed to behave as linear elastic materials and it is assumed the values remain constant over the range of temperatures considered.

Table 12 - Material Properties used in FE models

Property	Copper	Silicone	Aluminium
Young's Modulus (MPa)	130000	2	70000
Coefficient of Thermal Expansion ($x10^{-6}$)	17.5	200	23.5
Density (kg/m^3)	8940	2500	2700
Poisson's Ratio	0.35	0.49	0.34

4.3.2.3. Contact Algorithm and Detection

ANSYS has multiple regimes for detecting and performing contact calculations. For the models developed here where there is surface to surface contact, there are 5 differing contact algorithms: i) penalty, ii) augmented Lagrange (iterative penalty), iii) Lagrange multiplier, iv) pure Lagrange multiplier and v) multipoint constraint [68] [69]. For free expansion model, the default options can be used with no loss of accuracy due to the simplicity of the model. However once bonded contact has been initiated, the contact algorithms used, and their governing parameters have a much greater impact on outputs. For this reason, the influence of using different contact parameters will be investigated.

The penalty method uses contact springs to model contact normal and tangential to the contact. The contact stiffnesses normal (FKN) and tangential (FKT) create a relationship between the pair of contact surfaces. Other contact parameters such as opening stiffness (FKOP), penetration tolerance (FTOLN) and elastic slip tolerance (SLTO) also inform the behaviour of the contact surfaces [68]. These contact parameters will be investigated in greater detail later in Section 4.3.2.4.

The augmented Lagrange method is controlled in a similar manner to the penalty method, being comprised of an iterative series of penalty methods, resulting in better conditioning and less

sensitivity to the contact stiffness and other contact parameters. However, this method may require additional iterations when the deformation leads to highly distorted meshes. Initial studies showed failure of the two multiplier methods due to over constraint of the contacting surfaces - this is a known issue with the algorithms. These algorithms also introduce a greater number of degrees of freedom which can cause spurious modes in modal analyses [68]. For this reason, these two contact algorithms are excluded from further convergence studies.

The multipoint constraint method (MPC) builds so-called MPC equations internally based on contact kinematics (found directly from the definition of the contact pairs) and overcomes issues of traditional contact algorithms by eliminating DOFs of the contact nodes. Also, there is no requirement to input contact stiffnesses and shape functions are considered automatically. The MPC method also overcomes the small-strain restriction of traditional contact methods by automatically updating the MPC equations at each iteration when performing large deformation problems [68]. It is anticipated that this could be significant for the models considered here due to the pre-stressing and slenderness of the bonds.

As well as the various algorithms ANSYS offers, there are multiple contact detection methods, including gauss point and nodal detection schemes. These define the contact detection points on the contacting surfaces. At these points the contact elements are constrained against penetration through the target surface. For gauss point detection, the detection points are at the gauss integration points of each contact element generally provide more accurate results than the nodal detection scheme which use the contact surface nodes themselves as the detection points [68]. The use of nodal detection is usually reserved for edge or corner contact with a surface, as gauss point detection can lead to erroneous penetration in these cases – this issue can be visualised in Figure 91. Nodal detection is not recommended for surface to surface contact due to the requirement of smoothing the contact surfaces leading to longer computation times. A further surface projection based method is available, which uses contact nodes as detection points. However, it enforces constraint on the overlapping surfaces as opposed to individual nodes. This method brings advantages in accuracy for stress of the underlying elements and results are less sensitive to the assignment of contact and target surfaces. However, the

disadvantage is higher computational effort and possible errors in gap and penetration results at edge and corner contact due to averaging over the surface [68].

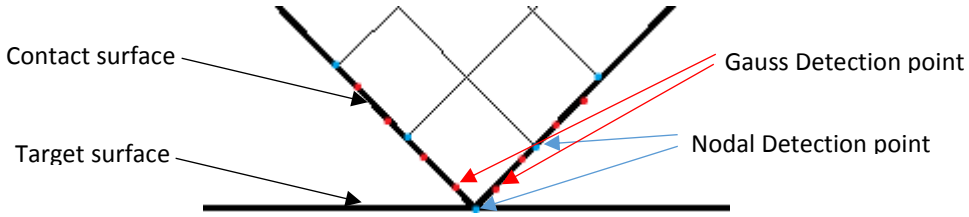
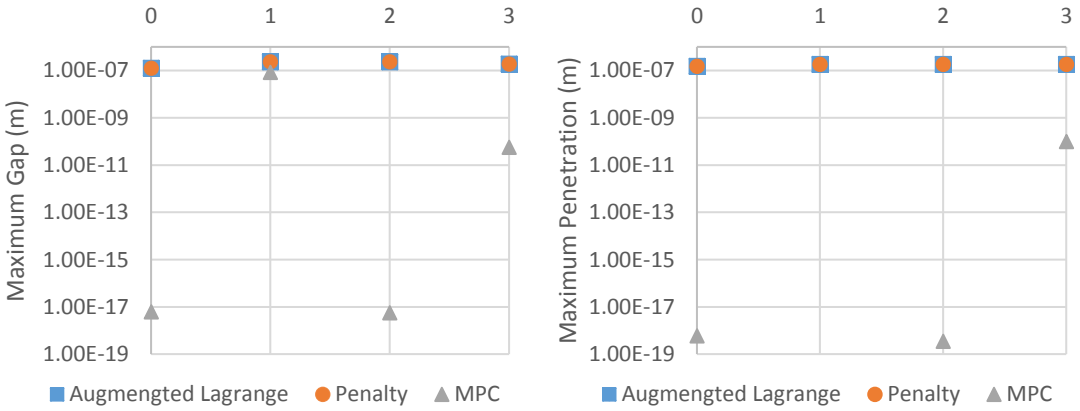


Figure 91 - Contacting bodies showing contact detection points, blue, nodal detection, red, gauss point detection

Figure 92 displays the 'quality' metrics gap and penetration present in the contact interfaces for various contact algorithms and detection schemes. It can be seen there is no difference between the penalty and augmented Lagrange contact algorithms and very little difference between the various contact detection methods. The MPC contact algorithm is seen to enforce greater constraint on gap and penetration in the contact with lower values seen across all detection methods investigated, inferring a better quality of modelled contact. Unlike the other algorithms there is a large variation in metrics between detection methods.

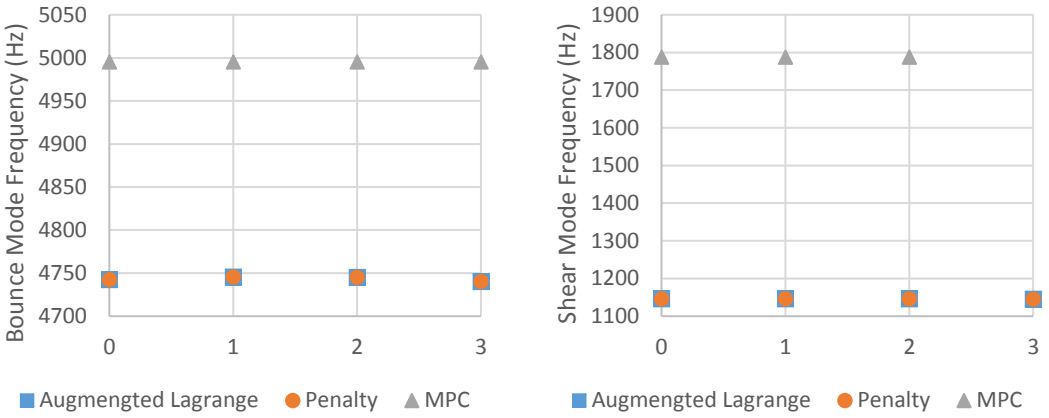


a) b)

Figure 92 - Model Quality metrics Gap (a) and Penetration (b) for various contact algorithms and detection schemes, 0 – gauss point, 1 – nodal (contact), 2 – nodal (target), 3 – surface projection

Figure 93 shows the calculated frequencies for the bounce and shear modes of the die. As with the quality metrics, the penalty and augmented Lagrange algorithms produce identical results with very little variation between the detection methods used (max 5Hz). The MPC method also displays low variation between detection methods, indicating the variation in the quality metrics do not affect the outputs. This method produces results with a large difference from the other algorithms, almost 250Hz greater in the bounce mode and over 600Hz higher in the shear mode. This may be because the shape

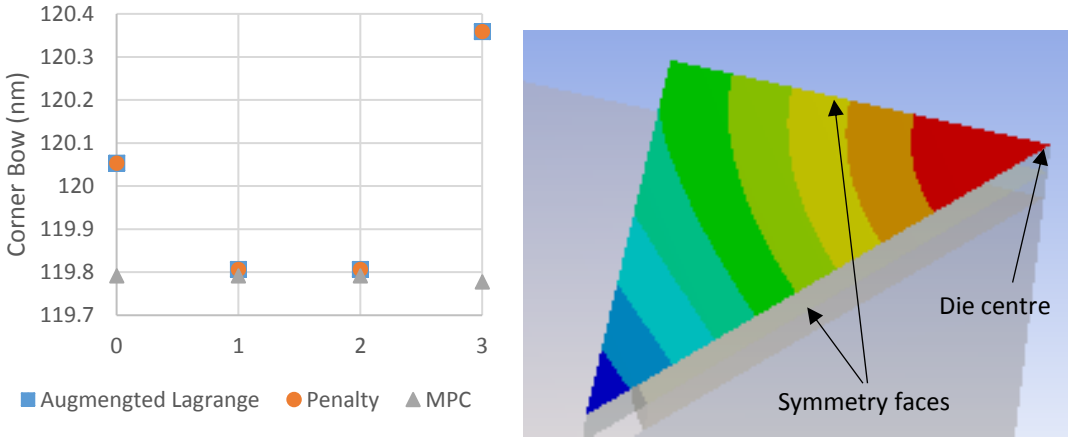
functions are considered automatically in the MPC method, and so capture the stiffening effect expected from a slender bond shape. More information about these higher modal frequencies is gained when convergence studies with mesh refinement are considered later in Section 4.3.2.5.



a) b)

Figure 93 – Bounce (a) and Shear (b) Mode Frequencies of the Die for various contact algorithms and detection schemes, 0 – gauss point, 1 – nodal (contact), 2 – nodal (target), 3 – surface projection

Figure 94 shows the bow (corner to centre) induced in the top surface of the die. There is only a small level of variation between all investigated contact algorithms and detection methods (<0.6nm). This variation occurs for the penalty and augmented Lagrange algorithms for differing detection methods, indicating these algorithms produce identical responses to each other. The MPC algorithm is consistent across all detection methods, showing that variations in the quality metrics have not influenced the results of interest.



a) b)

Figure 94 – a) Bow in Die's top surface (centre to corner height differential) using various contact algorithms and detection schemes, 0 – gauss point, 1 – nodal (contact), 2 – nodal (target), 3 – surface projection, and FE image of distribution (b)

Investigations using various contact algorithms has shown that the penalty and augmented Lagrange methods produce identical results for all metrics, and therefore only the augmented Lagrange will be considered in further model studies, such as mesh and contact parameter variation, based on the claim by ANSYS that it provides better conditioning and accuracy [68]. The MPC algorithm showed better enforcement of gap and penetration, with significantly lower values experienced indicating a better quality of modelled contact. Although it produced vastly different modal frequencies for both shear and bounce modes, which could be the effect of the automatic consideration on shape factors, MPC will be considered in further convergence studies. The investigation of various contact detection methods saw significant variations in the quality metrics for the MPC algorithm, although it was observed that this had no significant effect on the frequency and bow results. Relatively low variation (0.6nm) was seen in the die's bow for penalty and augmented Lagrange methods. Therefore due to the insignificant differences seen between the methods, the disadvantages experienced in terms of convergence issues and computation times of the nodal schemes and ANSYS' claim of generally more accurate results, only the Gauss point detection method will be considered in further modelling [68].

4.3.2.4. Contact Parameters

As mentioned in Section 4.3.2.3, the contact algorithm Augmented Lagrange (and Penalty) uses contact parameters to control the relative behaviour of the pair of contact surfaces. These contact parameters can have a highly significant effect on the outputs of the model. In this section, an appropriate selection of parameters are varied both individually and as a collective to assess the sensitivity of the model's outputs, and how they compare to the outputs using the MPC algorithm, which will be seen to be completely insensitive to these parameters. The parameters investigated includes normal, tangential and opening stiffnesses (FKN, FKT and FKOP), and penetration and elastic slip tolerances (FTOLN and SLTO). A contact sized mesh, using 250um elements at the contact interface, is used to investigate the effects of the control parameters. The effect of differing mesh regimes and sizes are evaluated in the next section.

4.3.2.4.1. Individual Effects

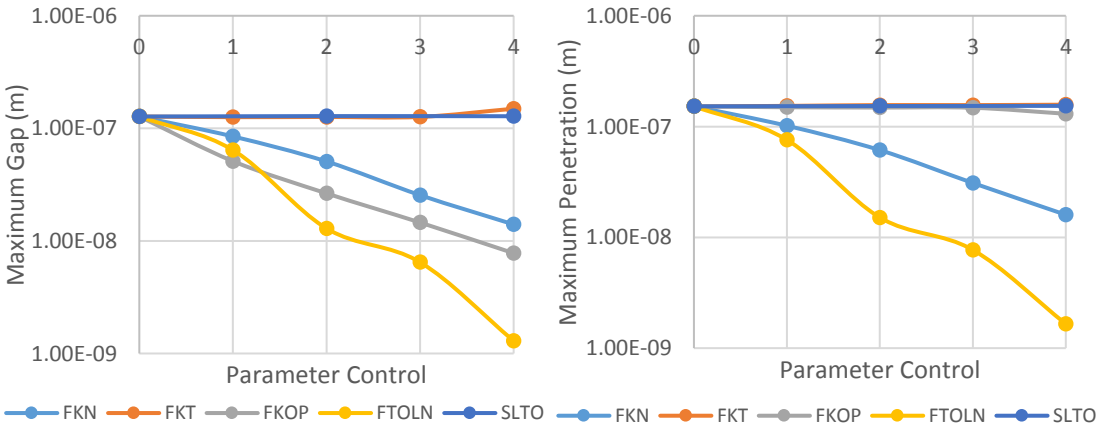
In this section the individual contributions of the chosen contact parameters are assessed. The parameters are varied individually (one at a time – OAAT) from their default values with an increasing

level of constraint and control and the effect on the model metrics observed. This process identifies the parameters with the most significant effect on the model outputs, allowing for an initial set of parameter values to be chosen and then varied together as a set in the next section. Table 13 shows the values tested for each parameter.

Table 13 - Table containing the various parameters varied and the values tested, FKN – normal contact stiffness, FKT – tangential contact stiffness, FKOP – contact opening stiffness, FTOLN – penetration tolerance, SLTO – elastic slip tolerance

Parameter Control	FKN	FKT	FKOP	FTOLN	SLTO
0 (Default)	10	1	1	0.1	0.01
1	15	2.5	2.5	0.05	-
2	25	5	5	0.01	0.005
3	50	10	10	0.005	-
4	100	25	20	0.001	0.001

Figure 95 shows the effect of each contact parameter on the model quality metrics, gap and penetration. The penetration tolerance (FTOLN) is seen to have the most significant effect on both outputs, reducing them by two orders of magnitude, as the parameter is varied by the same factor. The normal stiffness is also highly significant for both outputs, because it is the main parameter used to control the augmented Lagrange algorithm. The contact opening stiffness (FKOP) is significant when reducing the maximum gap. However, the penetration is insensitive to its variation. For both metrics the tangential stiffness (FKT) and elastic slip tolerance (SLTO) are seen to have a detrimental but negligible effect.

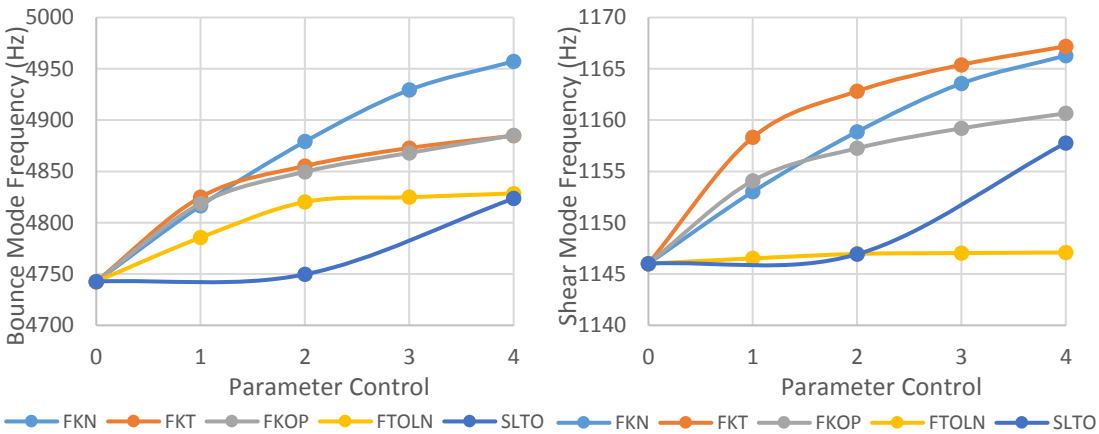


a) b)

Figure 95 - Model Quality metrics, Maximum Gap (a) and Penetration (b) when contact parameters are varied individually

Figure 96 shows the individual parameter effects on the die's two translational modal frequencies, bounce and shear. It can be observed that each mode is controlled most significantly by different parameters. For the bounce mode, increasing the normal stiffness provides the greatest change in frequency due to the die motion and bond deformation being in the normal direction. The tangential stiffness is also significant because of the Poisson's ratio effect coupling the normal deformation to the shear direction. The opening stiffness and penetration tolerance also lead to large changes in the bounce frequency, by reducing the gap when the bond is in tension (FKOP) and the penetration when the bond is compressed (FTOLN). The elastic slip tolerance appears at first to have little effect. However a large change is observed at its extreme value, indicating a level of instability when this parameter is varied too much.

For the shear mode, changes to the tangential contact stiffness give the largest changes in frequency, like in bounce due to the deformation direction of the bond and motion of the die. Normal stiffness again has a significant effect, as well as the opening stiffness because of the tension experienced in the bond at the extremes of the mode shape. In the shear case the penetration tolerance has negligible effect as there is no compression of the bond. The elastic slip tolerance again has little effect at the first increase of control and then looks unstable when increased further.



a) b)

Figure 96 - Die translational mode frequencies, Bounce (a) and Shear (b), when contact parameters are varied individually

Figure 97 shows the bow in the die after cooling (height difference between corner and centre of the die) and its variation when the contact parameters are varied. Different trends can be observed for this metric, with some causing increasing and others decreasing curves with greater control.

Penetration tolerance has the greatest effect for the tested values, increasing the bow with greater control. This is because the variation in penetration is reduced across the bond surface. A similar trend is observed for the opening stiffness because of the same effect but reducing the gap variation as opposed to the penetration. There appears to be an instability when FKOP is too large. Increasing the normal and tangential contact stiffnesses show similar but opposing trends for the bow, with normal increasing and tangential reducing the resulting bow. Again, as observed in both modal frequency trends for increasing control of elastic slip instability is indicated.

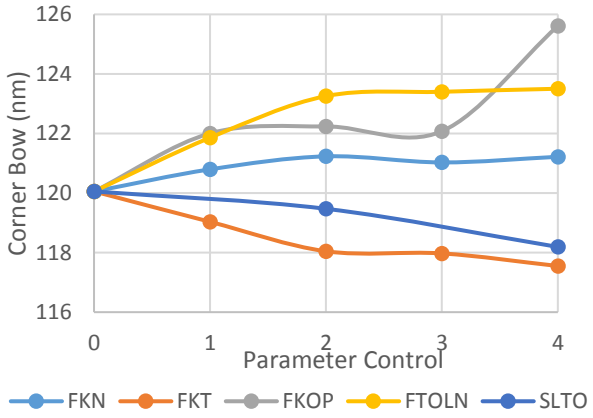


Figure 97 - Corner bow when contact parameters are varied individually

This section has identified the most significant parameters for each model metric considered, and it has been found that different metrics were dominated by different parameters. The elastic slip tolerance appeared to cause instability or have little effect on all metrics and so is maintained at its default value. The penetration tolerance had the most significant effect on the considered quality metrics, as well as the bounce mode and bow outputs and therefore will be subject to greater control than the default. The normal, tangential and opening stiffnesses have also been found to be significant for all or most metrics, particularly the outputs, and hence values greater than default control will be used. FKN will be controlled to the highest degree given its significance and converging trends for all metrics. FKT is controlled at a higher setting because of its influence on outputs, particularly for the shear modal frequency. FKOP is controlled to a lesser degree, due to the indication of instability at higher levels. However tighter control than the default will be used because of the importance shown due to the presence of tension in the bond. Table 14 shows the parameter values chosen initially. These values are varied as a set in the next section to confirm convergence is achieved.

Table 14 - Contact Parameter values for bonded contact default and those initially chosen from sensitivity analyses

Control	FKN	FKT	FKOP	FTOLN	SLTO
Bonded Default	10	1	1	0.1	0.01
Chosen	50	10	5	0.01	0.01

4.3.2.4.2. Combined Effects

In this section this initial set of parameters are varied together to confirm convergence has been attained or to determine whether a lower level of control would suffice. The variation ranges from 0% (default) to 200% of the set chosen from the previous individual parameter investigation, and the individual parameter values used are shown in Table 15. As part of this investigation, 1/4 models are considered as well as the 1/8 geometry models used in previous sections to further investigate the differences observed in the modal frequencies, particularly shear, when using the differing contact algorithms, Augmented Lagrange and MPC. The mesh used in these models is the same 250 μm contact sized mesh used in the previous sections.

Table 15 - Contact Parameter values used when parameters are varied together, from default values for bonded contact to 200% of the values chosen from individual parameter investigations

Control (%)	FKN	FKT	FKOP	FTOLN	SLTO
0 (Default)	10	1	1	0.1	0.01
10	15	2	1.5	0.09	0.01
25	20	3	2	0.075	0.01
50	30	6	3	0.05	0.01
100	50	10	5	0.01	0.01
200	100	20	10	0.005	0.01

Figure 98 shows the quality metrics when the parameter set for the differing models is varied. It is seen that the augmented Lagrange algorithm is sensitive to the changes in parameters varying by 3 and 2 orders of magnitude in maximum gap and penetration respectively. The MPC algorithm is insensitive to the changes in parameters used. There is no significant difference between the 1/8 and 1/4 models, but there is a difference of over 1 order of magnitude for gap when using the MPC algorithm. However, both are below $1x10^{-17}$m and so assumed to be insignificant.

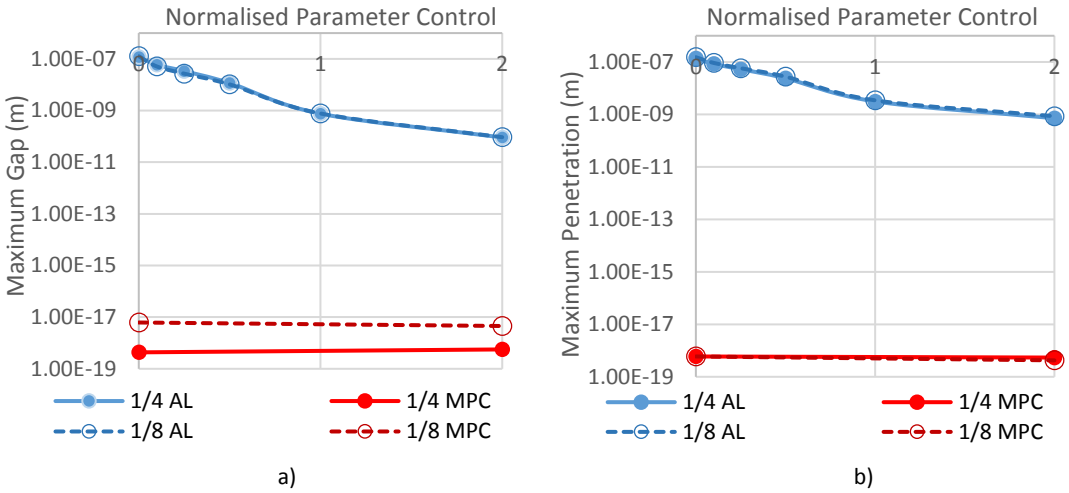


Figure 98 – Variation of model quality metrics, Maximum gap (a) and penetration (b), with parameter control level, using contact algorithms Augmented Lagrange (blue) and Multipoint Constraint (red), for both 1/8 (dotted) and 1/4 (solid) models

Figure 99 shows the effect of the varied parameter set on the bounce mode frequency. It can be seen clearly that the Augmented Lagrange algorithm converges to the MPC result with greater control of the contact parameters, which is insensitive to the parameter changes. There is a negligible difference between the 1/8 and 1/4 geometries.

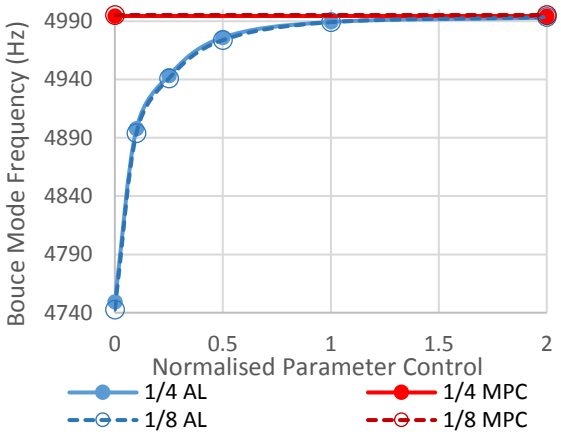
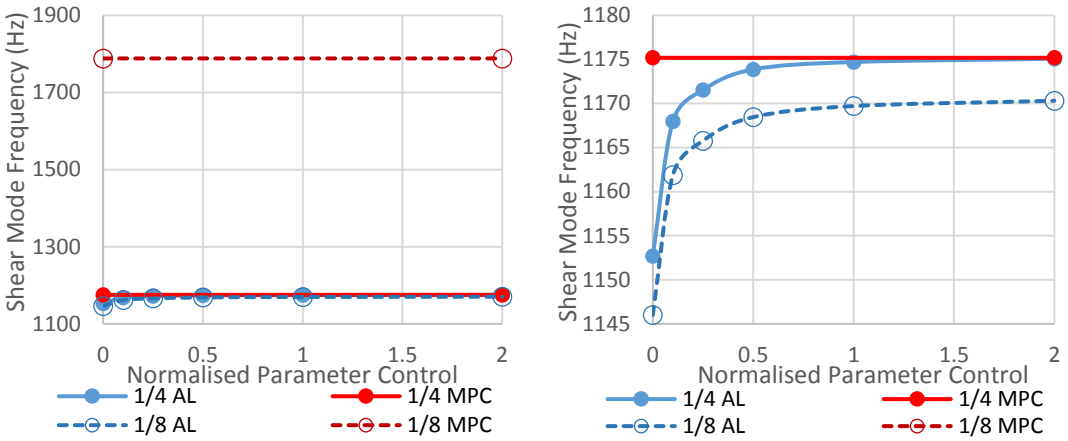


Figure 99 - Variation of Die Bounce mode frequency with parameter control level, using contact algorithms Augmented Lagrange (blue) and Multipoint Constraint (red), for both 1/8 (dotted) and 1/4 (solid) models

The difference in the shear mode between the different contact algorithms observed earlier for the 1/8 model in Section 4.3.2.3 is seen in Figure 100 (a). Unlike the bounce mode, increasing control does not cause the augmented Lagrange result to converge to the MPC value. However, for the 1/4 geometry the MPC and augmented Lagrange results are in much closer agreement, ~22Hz as opposed to ~650Hz, at default parameter values, and with increasing parameter control converge at the MPC result. This difference between the two geometries for the MPC algorithm indicates that there is an

error occurring when using MPC with the 1/8 model. This error appears not to affect the 1/8 model using the augmented Lagrange algorithm. Therefore, the extra constraint enforced by the extra symmetry condition causes issue with the MPC result, indicating an over constraint within the model. This is confirmed in the ANSYS documentation which states the multipoint constraint algorithm is susceptible to overconstraint [68]. The agreement and convergence within the 1/4 models indicates that there is no problem for this geometry. Further problems with shear results for the 1/8 model are discussed in the next section, when the mesh regimes and element sizes are considered.



a) b)

Figure 100 - Variation of Die Shear mode frequency with parameter control level, using contact algorithms Augmented Lagrange (blue) and Multipoint Constraint (red), for both 1/8 (dotted) and 1/4 (solid) models, a) wide frequency range, b) detailed view of convergence trend with smaller frequency range

Figure 101 displays the height difference between the corner and centre of the die (bow) for the varying parameter set, contact algorithm and geometry, and for this output a different trend is observed. In the modal frequencies, the augmented Lagrange model converges to the MPC result, with the expected shape of a curve with an ever-decreasing gradient. However, for the bow the initial change from default parameter values causes a sharp drift away from the MPC value (which like the other metrics is unaffected by the contact parameters) to a maximum, which then reduces with greater control, but never converges with the MPC result. The difference between the contact algorithms at maximum is only ~1nm (<1%), and at 200% of the chosen parameters this reduces to ~0.5nm. Like the shear mode frequency, a difference is seen between the two geometries, in both the MPC and augmented Lagrange results. These differences are only relatively small, 0.1 and 0.1-0.2nm respectively, and this could be an indication that the over constraint that effects the shear mode also causes error in the bow results.

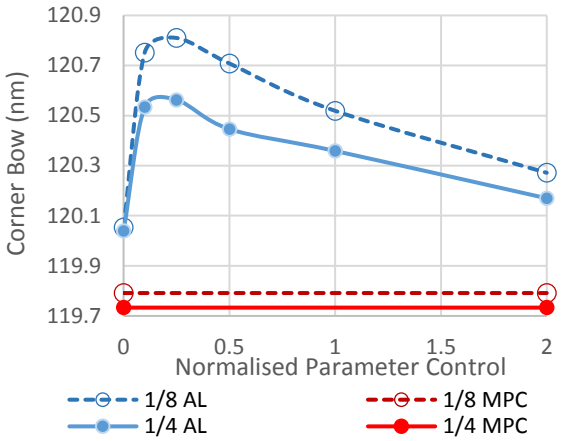


Figure 101 - Variation of Corner Bow with parameter control level, using contact algorithms Augmented Lagrange (blue) and Multipoint Constraint (red), for both 1/8 (dotted) and 1/4 (solid) models

4.3.2.5. Mesh

Initial studies showed that convergence required high mesh densities in the bond, which is to be expected given that this flexible part undergoes significant deformation as the die vibrates. The die mesh size is also important, to ensure the curvature induced after bonding is predicted accurately. The base mesh is less important because only low levels of deformation occur, due to its high modulus and thickness. However, the bond and base are in contact and therefore similar mesh sizes at the interface may be required in both parts to achieve converged results for the model outputs, particularly for the modal frequencies.

4.3.2.5.1. Regime

Multiple mesh regimes could be employed to achieve the above requirements. However due to the use of an 1/8th model, resulting in triangular geometries only tetrahedral elements are considered. Different sizing methods have been considered, including part sized, allowing for consistent element sizes within each part, and contact sized, which provides consistent and matched element sizes on each side of a contact interface. It was found in the previous section however that a 1/4 model overcame the convergence issues observed in the shear mode frequency. This geometry is modelled using the same two mesh regimes as the 1/8 model as well as a part sized mesh using quadrilateral elements, resulting in a uniform structured mesh due to the square part geometries. Figure 102(a-e) shows the differing mesh regimes using the coarse 250um element size.

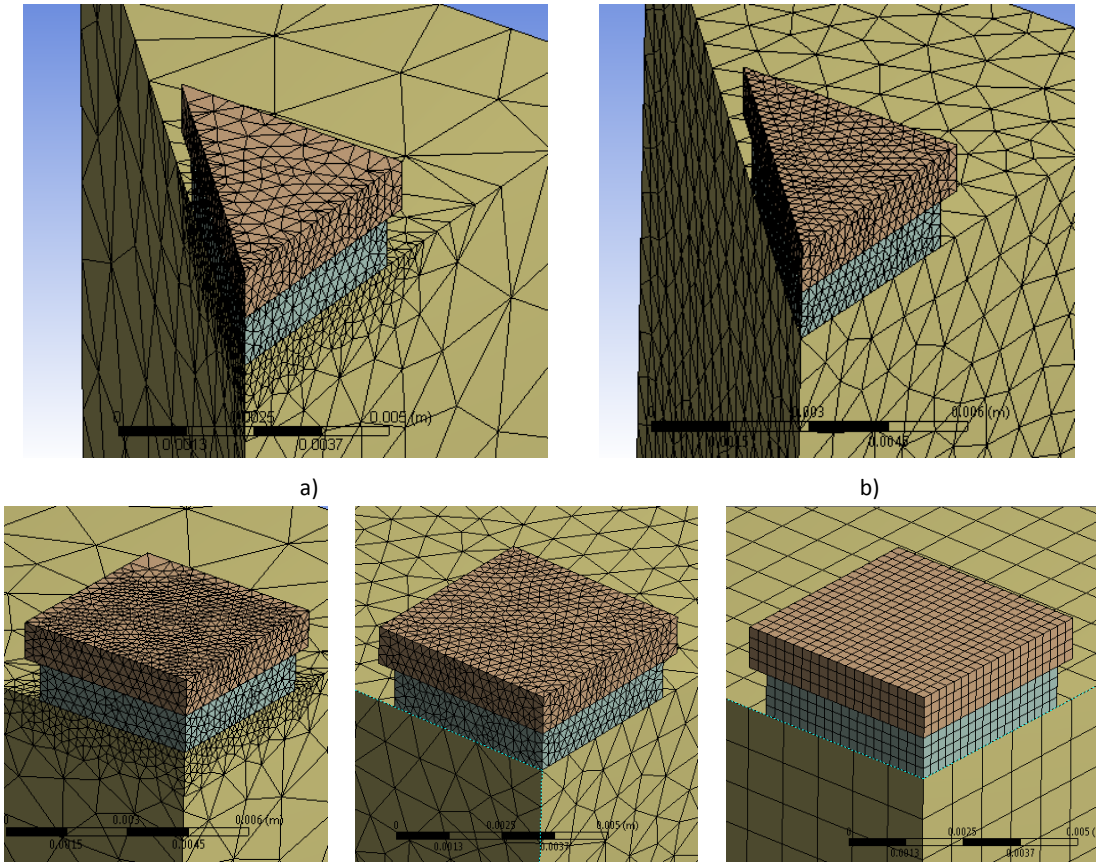


Figure 102 - Various mesh regimes investigated for 1/8 and 1/4 models, a) 1/8 contact sized tetra elements, b) 1/8 part sized tetra elements, c) 1/4 contact sized tetra elements, d) 1/4 part sized tetra elements, e) 1/4 part sized quad elements

A comparison of the mesh quality metrics, gap and penetration, show good agreement between the different mesh regimes. A significant reduction in both metrics is observed when using the MPC algorithm, which was discussed previously in Section 4.3.2.3.

Figure 103 shows the variation in bounce and shear mode frequencies for the varying mesh regimes investigated. It can be seen that there is some variation in the bounce mode frequency for differing regimes, with a difference of approximately 20Hz between contact and part sized tetrahedral meshes. Less variation is seen between the contact algorithms (~5Hz, larger for quadrilateral mesh), while the 1/8 and 1/4 geometries are in close agreement for a given mesh regime. However, the shear mode shows a significant difference between the 1/8 and 1/4 models using the MPC contact algorithm. This offset was observed in Section 4.3.2.3, the MPC result using the 1/8th geometry is erroneous, and the much higher shear mode frequency is caused by over constraint of the bond [68]. When using a 1/4 geometry, the shear mode frequency is in agreement between the different contact algorithms and mesh regimes(<0.5Hz).

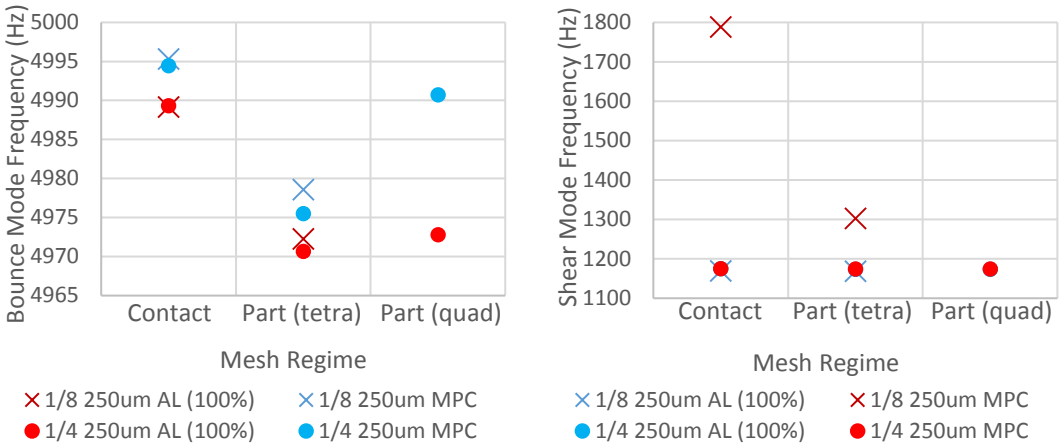


Figure 103 - Variation in Die bounce and shear mode frequencies for various mesh regimes and contact algorithms

Figure 104 shows the variation in the bow observed using the various geometries and mesh regimes. It is seen that there is a difference of approximately 2-3nm between mesh regimes and 1nm between the differing geometries. However, it is likely that the mesh sizes used in the differing regimes will have a significant effect, and the different regimes may have different convergence trends with reducing mesh sizes. Therefore, all the considered geometries and mesh regimes are investigated with reducing mesh sizes to observe these convergence trends for the most important model outputs. These results are shown and discussed in the following section.

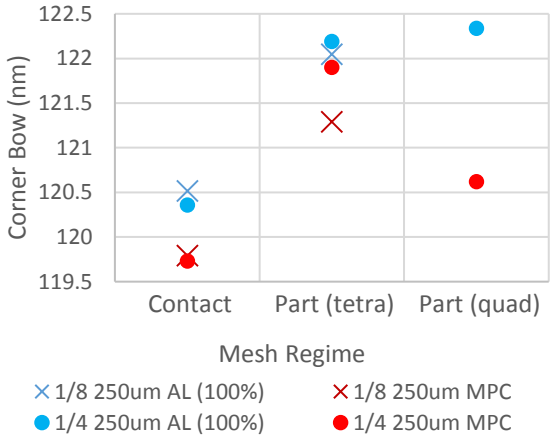


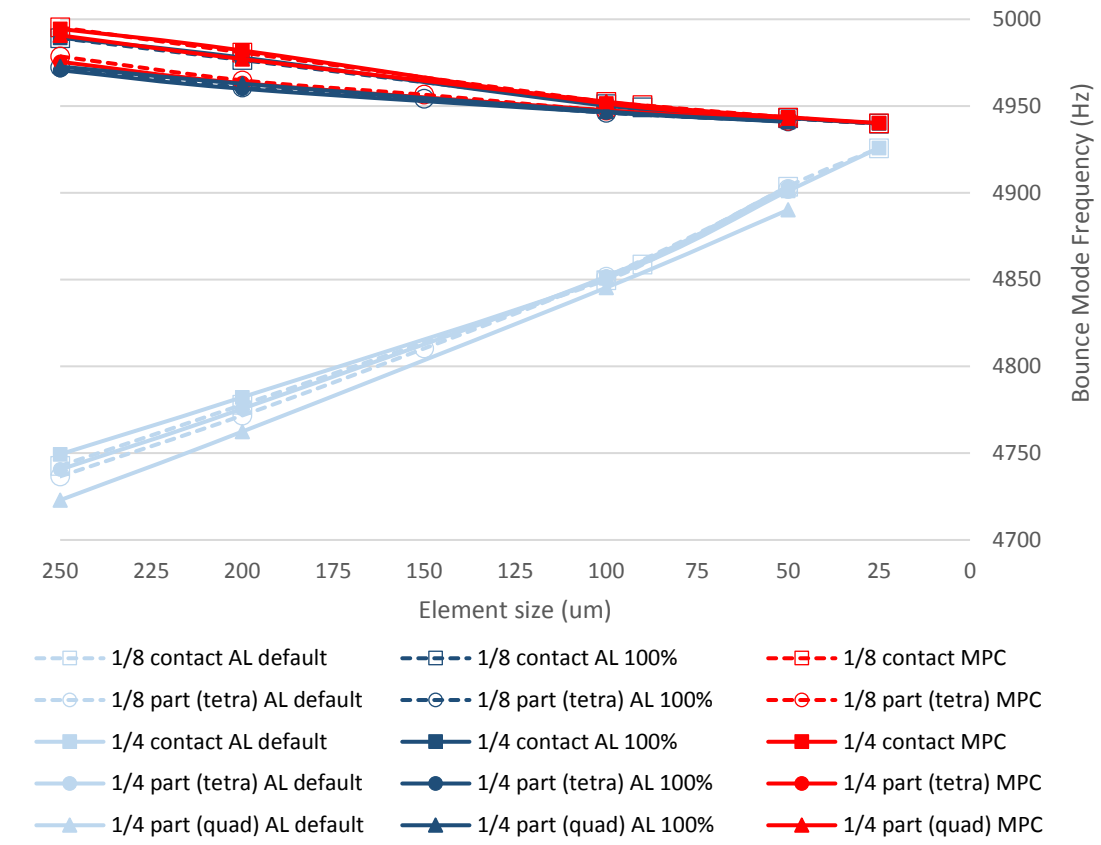
Figure 104 - Variation in corner bow for various mesh regimes and contact algorithms

4.3.2.6.2. Size

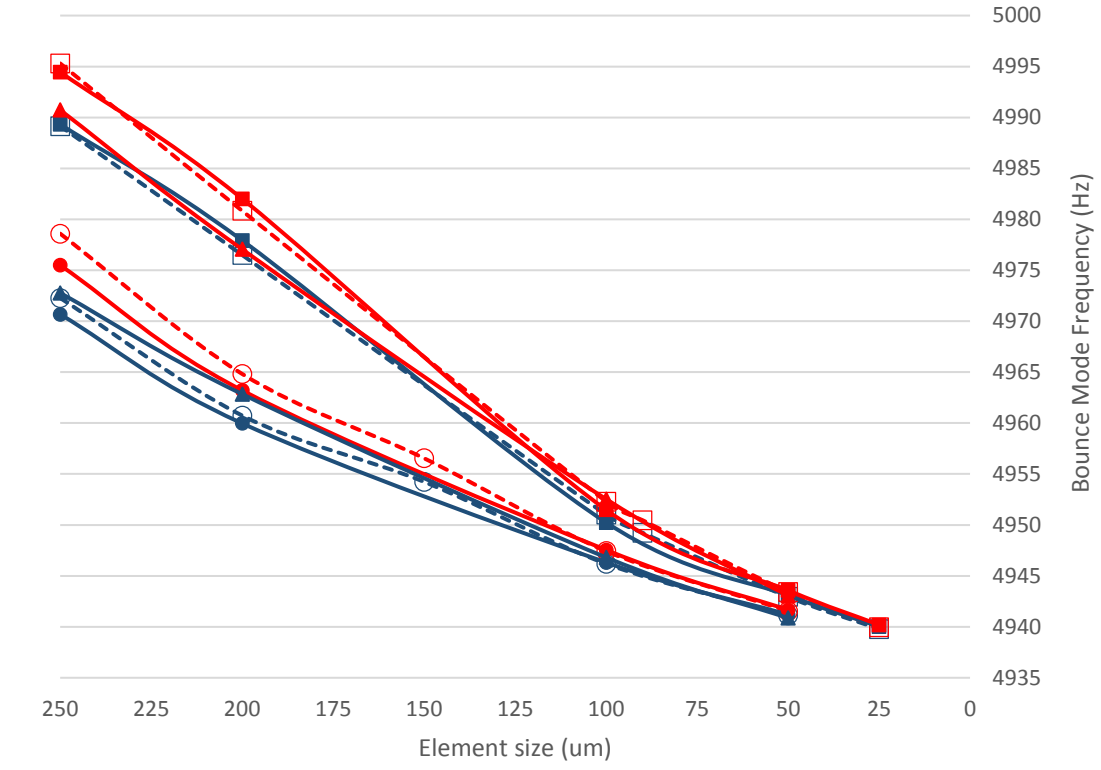
In this section the element sizes for each mesh regime are varied to establish their convergence trends, using both the augmented Lagrange (using default and controlled parameters) and MPC contact algorithms. Also displayed in the graphs are the results using the 1/8 model. This model

has already been shown (Section 4.3.2.3.) to experience erroneous results for the shear mode when used with the MPC contact algorithm, as well as a small (~5Hz) frequency difference compared to the 1/4 model when using the augmented Lagrange algorithm, which was seen to be present despite tighter control with the contact parameters. Despite this known error the 1/8 models are included here to ascertain whether a finer mesh will provide convergence/ reduce these differences between the differing geometries and to identify any other issues that may occur due to the use of the extra symmetry condition. As well as the problems identified with the shear frequency, it is currently unclear whether the bow is affected adversely and therefore inclusion of these models in this study should clarify any possible accuracy issues for this output.

Figure 105 shows the convergence trends for the bounce mode frequency with reducing element sizes for various models. It can be seen that there is close agreement between the 1/8 and 1/4 models when using the same contact algorithms and mesh regimes, indicating the bounce mode is unaffected by the symmetry issues affecting the shear mode frequency. There is a large change in the default augmented Lagrange models with reducing mesh sizes, which converge to values similar to the controlled augmented Lagrange and MPC values at elements below 25µm. Although convergence can be achieved here without controlling the parameters, reducing the element sizes to these values has a much greater effect on CPU times, with 25µm models taking several hours to run. A lower change is seen in the controlled augmented Lagrange and MPC values when mesh sizes are varied, with a maximum change of 10Hz observed between 100 µm and 25 µm models. At coarse mesh sizes there is a small difference (20Hz) between the part sized and contact sized tetra meshes, which reduces with mesh refinement to ~5Hz at 100 µm element sizes. For these meshes there is close agreement between the controlled AL and MPC algorithms (max ~5Hz), whereas the part sized quad mesh has a larger difference between contact algorithms (max ~20Hz), with its augmented Lagrange outputs close to part sized tetra values and its MPC values in closer agreement with the contact sized tetra values. However once again these offsets reduce with mesh refinement, with a maximum difference of 5Hz between mesh regimes at element sizes of 100 µm.



a)



b)

Figure 105 - Bounce mode frequency convergence with element size refinement, including 1/8th (dotted) and 1/4 (solid) models, AL default (light blue), controlled AL (dark blue) and MPC (red) contact algorithms, for contact sized tetra mesh (square), part sized tetra mesh (circle) and part sized quad mesh (triangle – ¼ only), a) wide frequency range, b) fine frequency range showing detail in AL controlled and mpc results

Figure 106 shows the convergence trends for the shear mode frequency with reducing element sizes for various models. As previously observed there is a large difference in the 1/8 models between the AL and MPC algorithms, which can be seen clearly in the top graph, along with a further observation that this difference is unaffected by mesh refinement. This difference does not exist within the models using the 1/4 geometry, and therefore this error has been assessed to be caused by over constraint from the extra symmetry condition imposed. When observing the trends over a smaller frequency range (see Figure 106 (b)), it can also be seen that there are differences between the different geometries for both the default and controlled augmented Lagrange models, indicating the extra symmetry condition also induces an error in this contact algorithm, albeit to a much lower degree (5-10Hz as opposed to 150-650Hz). Once again, this frequency offset is unaffected by the element size.

A further issue with the 1/8 model is that the shear modal model fails when the element sizes drop below a certain limit. This limiting element size is different for various mesh regimes. Contact sized models (tetra elements) fail for elements below 90 µm and for part sized tetra models below 150 µm, the models fail at the same value regardless of contact algorithm. The modal model fails because a single element becomes too distorted during the contraction stage of the modelling. Considering that the 1/4 models do not exhibit this behaviour for any of the tested mesh regimes, this issue is again caused by the extra symmetry condition, and logically it can be determined that the distorted element must lie on this symmetry face. It could be that this distorted element is the cause of the frequency differences as well as the failure, but the distortion has a varying significance on the two algorithms.

Within the 1/4 models the convergence behaviour is similar to the bounce mode. The default augmented Lagrange models converge to the controlled augmented Lagrange and MPC models at sub 25 µm elements, with a large change in frequency seen over the mesh refinement (20Hz). Low change to convergence for the controlled augmented Lagrange and MPC models is observed, reducing by 2-3Hz over the mesh refinement. Once again for these 2 models there are 2 bands of values, the contact sized and part sized, which are seen to converge within 1Hz at element sizes of 100 µm. For the shear mode there is better agreement between the controlled AL and MPC models for the quadrilateral mesh than seen in for the bounce mode.

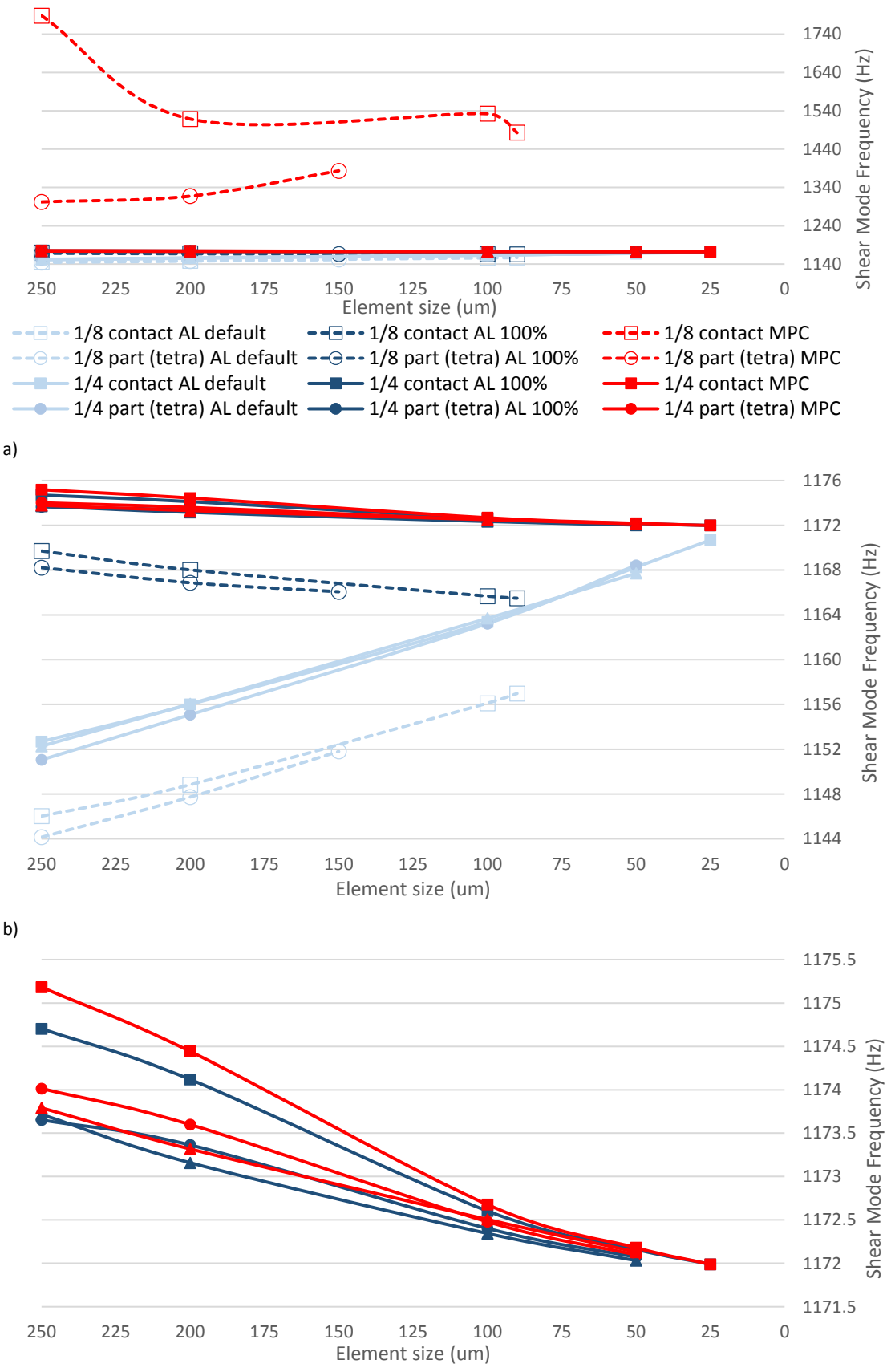


Figure 106 - Shear mode frequency convergence with element size refinement, including 1/8th (dotted) and 1/4 (solid) models, AL default (light blue), controlled AL (dark blue) and MPC (red) contact algorithms, for contact sized tetra mesh (square), part sized tetra mesh (circle) and part sized quad mesh (triangle – ¼ only)

Figure 107 shows the corner bow for various models when the mesh size is refined. It can be seen that all models exhibit the same behaviour with results increasing with reducing mesh size, approaching convergence towards element sizes of 25 µm. There are two distinct bands of results as seen in the other model outputs, contact sized and part sized, with part sized experiencing slightly higher levels of bow. This difference reduces with mesh refinement (2nm at 250 µm to ~0.5nm at 50 µm) and there is good agreement between respective augmented Lagrange and MPC models (~1nm at 250 µm, reducing to 0.5nm at 100 µm), except for the part sized quad mesh regime where a larger difference is present (2nm at 250 µm) as seen in the bounce mode. Good agreement is also seen between respective 1/8 and 1/4 models (negligible at 100 µm), indicating that the issues affecting the shear mode frequency does not affect the corner bow. The most significant model parameter for achieving corner bow convergence is observed to be the mesh size, with contact parameters having much less affect for this output when compared to the trends seen for the modal frequency metrics.

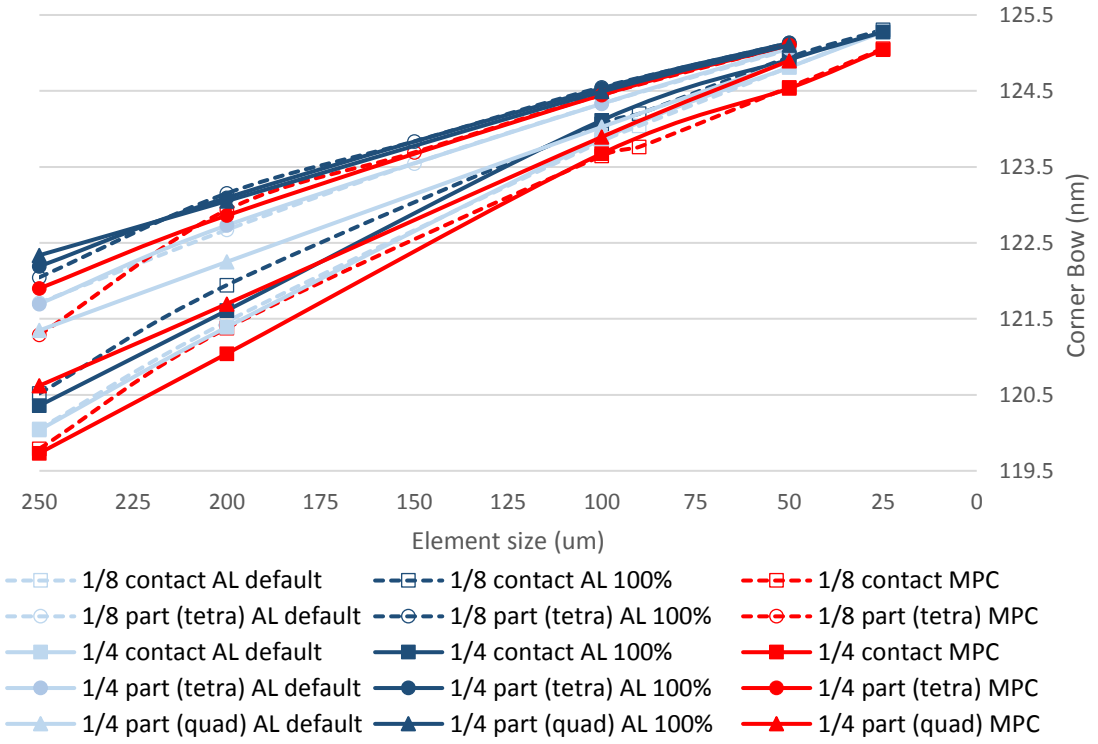


Figure 107 - Corner Bow convergence with element size refinement, including 1/8th (dotted) and 1/4 (solid) models, AL default (light blue), controlled AL (dark blue) and MPC (red) contact algorithms, for contact sized tetra mesh (square), part sized tetra mesh (circle) and part sized quad mesh (triangle – ¼ only)

In summary, the above studies indicate that good convergence of model outputs is achieved for mesh sizes below 100µm. While using the contact sized meshes provides high mesh densities at the important contact interfaces, and the die and bond parts, they expand quickly in the base greatly

reducing the number of elements and therefore computation time, ensuring a time efficient model. The MPC algorithm is found to converge quickly. However a 1/4 geometry model is required, as over constraint in the 1/8 geometry causes erroneous shear mode frequencies.

4.3.2.6. Requirements due to Bonding stress

This section observes the trends in the modal frequencies for a case where the bond is unstressed at room temperature (here considered to be 22^{o}C) and compares them to trends already seen for the pre-stressed case - bow is not considered here because no curvature is induced without the stressing the bond. This study is conducted to assess any difference in the model requirements, such as contact parameters, mesh regime and mesh size due to the presence or lack of stress in the bond. Within these studies only 1/4 geometry models are used, using only the controlled augmented Lagrange and MPC contact algorithms, considering all mesh regimes.

4.3.2.6.1. Contact Parameters

In this section the contact parameters are varied as a set, using the parameter set chosen in the earlier study for the pre-stressed case. Figure 108 shows that the pre-stress induced in the bond due to the contraction after bonding causes an increase in the converged bounce and shear modal frequencies of over 150Hz and 5Hz respectively. The unstressed case exhibits the same convergence behaviour as that seen for the pre-stressed case, with the augmented Lagrange results converging to the MPC result with increasing control of the contact parameters. However, for the unstressed case a larger level of change in the results is seen over the same parameter variation, and convergence with the MPC result requires a higher level of parameter control compared with the pre-stressed bond. Therefore, the presence of stress in the bond improves the convergence trends. This could be the effect of the stress encouraging the closing of gaps and stiffening the contact interfaces. It is seen in both models that the contact sized mesh regime (tetrahedral elements) provides the quickest convergence with parameter control.

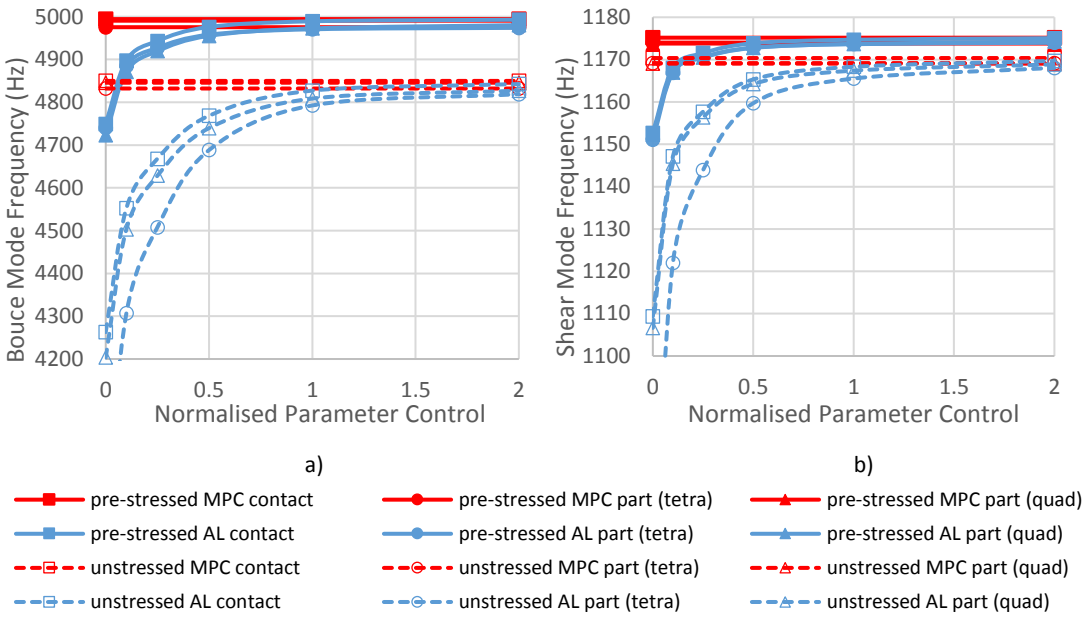


Figure 108 - Modal Frequencies, a) bounce and b) shear, as the contact parameter set is varied for 1/4 geometry models using 250um elements, for the pre-stressed (solid) and unstressed (dotted) cases, using the MPC (red) and AL (blue) contact algorithms and for contact sized tetra (square), part sized tetra (circle) and part sized quad (triangle) mesh regimes

4.3.2.6.2. Element Size

In this section the mesh size is reduced to observe the effect on the modal frequencies. Figure 109 shows results for the bounce and shear frequencies. There is a clear frequency offset between the pre-stressed and unstressed cases for both modes, and at convergence the offsets are approximately 150 and 5 Hz respectively. As seen in the previous mesh refinement section (Section 4.3.2.5.2.) for the pre-stressed case, the contact and part sized results differ but converge with a finer mesh, with good agreement between the contact algorithms for each respective mesh regime. However in Figure 109, it can be seen that the unstressed case does not follow this same behaviour. Firstly, there is a greater variation between the results for differing mesh regimes, this is seen to reduce with mesh size. There is also less agreement between the augmented Lagrange and MPC contact algorithms. This offset does not reduce with the mesh refinement, ~15 and 2Hz for bounce and shear respectively. This consistent difference between the contact algorithms is due to the lower level of convergence achieved with the same contact parameters, and was described in the Section 4.3.2.6.1. (unstressed case requires tighter control). If a higher level of parameter control was used in the unstressed case, these offsets would be expected to reduce, with closer agreement between the different contact algorithms (augmented Lagrange will converge with the MPC results). When only observing the MPC results it can be seen that significant convergence between differing meshes and to a final result occurs at 100 µm.

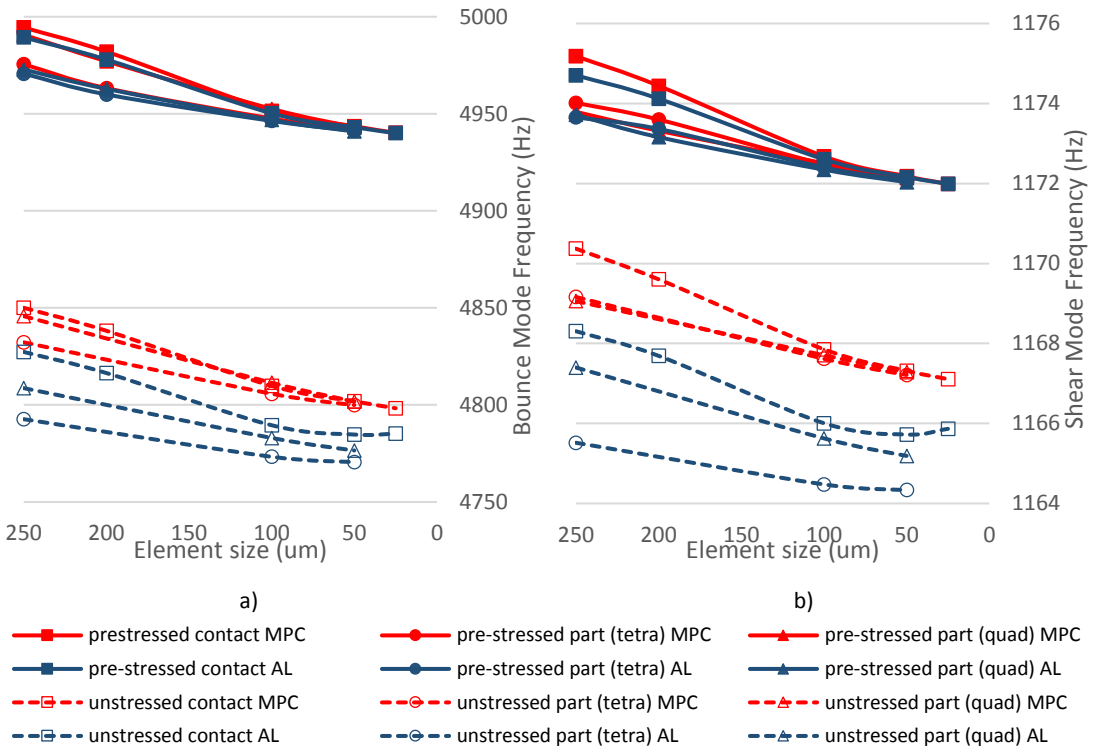


Figure 109 – a) Bounce and b) Shear Modal Frequencies as the mesh size is varied for 1/4 geometry models, for pre-stressed (solid) and unstressed (dotted) cases, using MPC (red) and controlled AL (blue) contact algorithms and for contact sized tetra (square), part sized tetra (circle) and part sized quad (triangle) mesh regimes

4.3.2.7. Summary of Model Requirements

The studies within this chapter were conducted to investigate the individual and combined effects of the model features and parameters possible in ANSYS, and assessing the convergence of the model outputs, including modal frequencies and die deformation, as well as minimising contact quality metrics, gap and penetration. The outcomes of these investigations can then be used to a develop a Finite Element model capable of accurately determining the die mode and bow for various bond designs. The model options studied included contact algorithms and detection methods, contact parameters, symmetry effects, mesh regime and sizing as well as the effects of bonding stress on both results and model requirements.

The contact algorithms multipoint constraint (MPC), augmented Lagrange (AL) and penalty methods were investigated along with the contact detection methods, using gauss point and differing nodal schemes. It was seen that the MPC algorithm produced converged results for modal frequencies without the need for contact parameter control. However, it was also subject to issues of overconstraint leading to large errors in the shear mode when an 1/8 geometry is used. Alternatively, the AL algorithm can be used, but this requires tight control of the contact parameters to achieve convergence of

frequency metrics, most significantly the stiffness' FKN, FKT and FKOP and penetration tolerance FTOLN (chosen set, 50, 10, 5, 0.01 respectively). However, issues with the 1/8 model were observed when mesh sizes were reduced below certain lengths, with the shear modal model failing due to highly distorted elements. The differing contact detection methods produced relatively consistent results, likely due to the flat surface-surface contact, the results were particularly consistent for the MPC algorithm. The default option of gauss point detection was chosen, due to ANSYS' claim of faster CPU times and better accuracy, as well as it recommendation for use with surface-surface contact [65].

Reducing the number of symmetry conditions within the model overcomes the issues mentioned for the shear mode frequency convergence. Using a 1/4 model it was found that the AL algorithm frequency results converge to the MPC values with control of contact parameters for both modes, with no limiting mesh size observed. These converged outputs were not significantly changed when using differing element types or sizing methods, particularly when element sizes were reduced to 100µm or smaller. However, the convergence trends were slightly different with the contact sized mesh observed to converge quickest with respect to the contact parameters (using AL). The contact sized mesh also had significantly lower CPU times due to the reduced number of elements. This was achieved by maintaining high mesh densities at the bond and die but reducing significantly the mesh in base.

The bow was affected by the element sizing significantly compared to all other factors, as opposed to the frequency metrics which depended more on the contact algorithm and parameters used. As a compromise between speed and accuracy an element size of 100µm is chosen - at this value the most significant change has already occurred and reducing the size further causes CPU times to increase significantly, although it is key to mention that this value will vary for bonds with differing thickness. However, the element size to thickness ratio will be kept constant (10 elements across thickness).

The change in requirements due to the level of stress in the bond was also investigated. To assess this, two cases were used: one which was bonded at the bonding temperature and is therefore pre-stressed at room temperature and the other bonded at room temperature and hence unstressed. It was seen that the unstressed bond required greater control of the contact parameters (when using

AL algorithm) to achieve convergence with the MPC result. This indicates that the stress enhances the convergence. It can be similarly concluded that this is the same at higher temperatures for the pre-stressed case (as there is lower stress and deformation) and that at lower temperatures convergence requires lower control. These conclusions only apply to the augmented Lagrange contact algorithm, when using MPC there is no convergence trend with the contact parameters and the convergence with element size, for differing regimes, is very similar for both cases.

Table 16 - Table showing chosen model features and parameters

Geometry	Mesh Regime	Element Size	Contact Algorithm	Contact Detection	Contact Parameters			
					FKN	FKT	FKOP	FTOLN
1/4	Contact Sized Tetrahedral	100µm (1/10 bond t)	MPC	Gauss Point	50	10	5	0.01

4.4. Results

This section presents the results obtained for the final FE model using the features and parameters chosen from the individual and combined investigations conducted earlier. The model is tested at various environmental temperatures so that the modal frequencies and bow trends with temperature can be investigated.

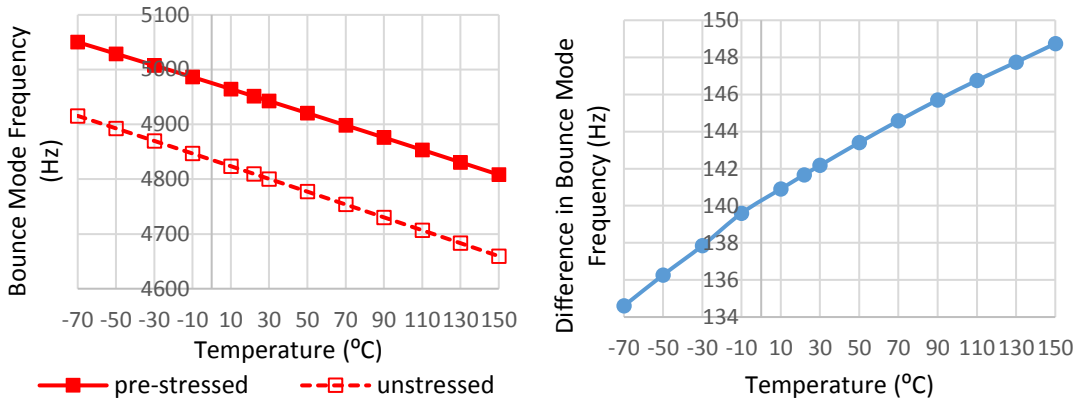
4.4.1. Temperature Effects

4.4.1.1. Geometrical Effects only

The temperature trends showed here are caused by geometrical effects only because the material properties are kept constant over the temperature range considered. Constant properties are used because of the unavailability of reliable T-dependent properties for silicone and the difficulty in testing due to the extraneous variables experienced (further curing, aging, mechanical stiffening). To show the effect of bonding stress over temperature, the results presented include cases emulating temperature cured and room temperature cured bonds.

Figure 110 shows the variation in the bounce mode frequency over temperature for both the high temperature and room temperature cured bonds. In both cases the bounce mode frequency reduces approximately linearly with increasing temperature. However, it can be seen that there is a clear offset between the bounce mode frequencies for the two cases, suggesting the change in the

cure/bonding temperature affects the dynamics of the bond, with the pre-stressed case experiencing the bounce mode at a frequency approximately 140Hz higher. Figure 110 (b) shows how the frequency difference varies over temperature. It is observed that the offset increases with increasing temperature, with an offset change of over 10% for the temperature range. Given that the bounce frequency reduces with temperature the significance of the offset with respect to the absolute modal frequency increases with temperature. This results in the pre-stress causing a bounce mode frequency increase of 2.74% at -70°C raising to 3.2% at 150°C.

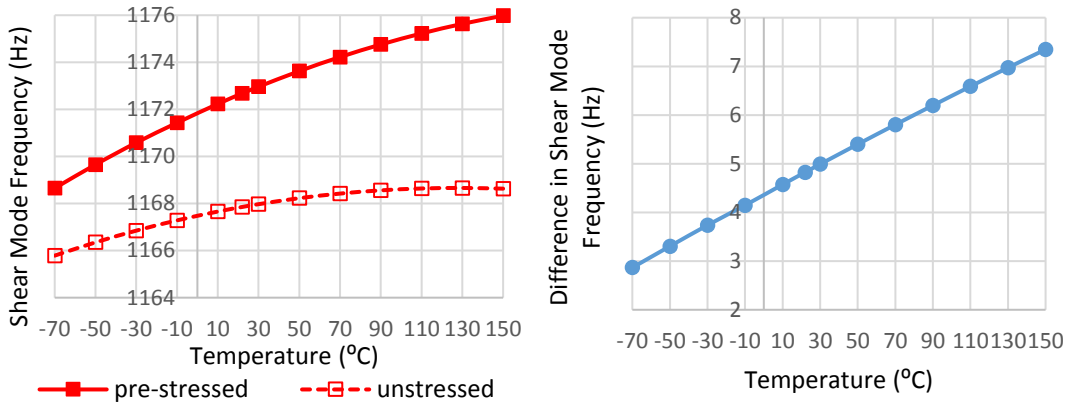


a) b)

Figure 110 – a) Variation in Bounce mode frequency over temperature for the pre-stressed and unstressed cases, and b) difference in the bounce mode frequencies over temperature

Figure 111 shows the shear mode frequency variation and difference between the two stress cases considered. Once again it can be seen that the pre-stress causes an increase in the modal frequency, and this offset increases with increasing temperature. The offset between the stress cases is less constant than seen in the bounce mode, with the offset at 150°C being greater than double the offset at -70°C. The magnitude of the offset however is significantly lower in the shear mode, increasing from 2.87Hz to 7.35Hz over the temperature range. This large percentage variation in offset is due to a differing trend over temperature between the two cases, which significantly differ from the approximately linear trends observed in the bounce mode. In the shear cases the frequencies increase with increasing temperature, the opposite effect occurs in bounce. The increasing frequency is also non-linear, with the gradient reducing at higher temperatures. The gradient change (frequency/temperature) is seen to be different due to the stress state, with the unstressed bond (room temperature cure) experiencing almost zero change when the temperature is increased to 150C,

whereas the pre-stressed case still sees an increasing shear mode frequency at this temperature (although this increase is slowing).



a) b)

Figure 111 – a) Variation in Shear mode frequency over temperature for the pre-stressed and unstressed cases, and b) difference in the shear mode frequencies over temperature

Figure 112 shows the variation over temperature and the difference in the die bow for the two differing stress cases. Firstly, in this figure the definitions of the two cases can be seen by observing the temperature at which there is zero bow, i.e. the pre-stressed case has zero bow at its cure temperature of 150°C, and in the same way the unstressed case at 22°C. This is because at these temperatures, the respective bonds are unstressed as it is at these temperatures that the bonded contact is initialised. In reality, there would be a small level of stress at these temperatures due to the cure shrinkage. However, this has not been included in the models. The bow trends with temperature are approximately linear, with the bow reducing with increasing temperature. For the pre-stressed case, the bonding temperature is at the maximum of the temperature range and therefore only experiences positive bow (die top surface is concave, centre lowest point), which reduces to zero at 150°C. For the unstressed case, the bow reduces to zero at 22°C and then continues to negative bow values, representing a convex top die surface (centre highest point) as the temperature is increased further. The bow difference between the two cases also varies over temperature approximately linearly, ranging from 135nm at -70°C to 110nm at 150°C. This linear trend results from the difference between the bow/temperature gradients of the two cases, which arises because of the slightly different geometries when bonding is initiated, because of the thermal expansion effects when heated to the bonding temperature.

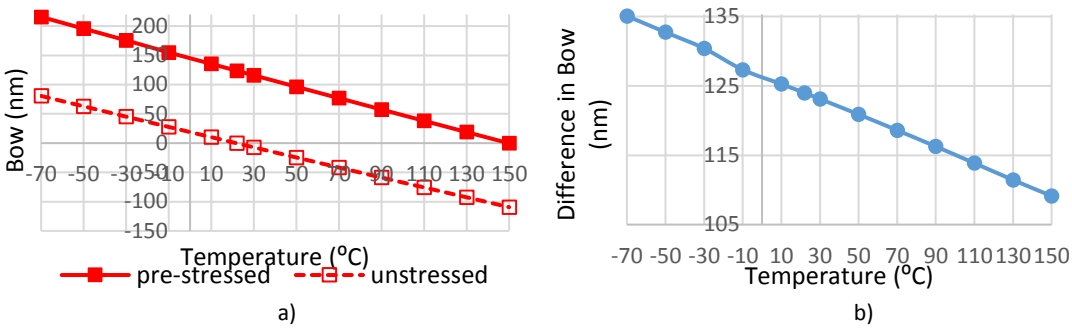


Figure 112 – a) Variation in Die Bow over temperature for the pre-stressed and unstressed (at RT) cases, and b) difference in the deiffering bows over temperature

4.4.1.2. Effect of Material Properties

In this section the key material properties identified in the literature are varied. The effect of these property variations on the temperature trends of the model outputs are shown and discussed. This includes how the absolute and normalised outputs vary over temperature, as well as the differences experienced due to including bonding stress (comparison of high temperature and room temperature curing). The properties of the silicone bond varied include: Young's modulus, thermal expansion coefficient and Poisson's ratio.

4.4.1.2.1. Young's Modulus

The Young's modulus is varied between 1 and 4MPa (initially 2MPa). Figure 113 shows the effect of this modulus change on the variation of the bounce mode and stress effects (difference in bounce mode between pre-stressed and unstressed cases) over temperature. It is observed that increasing the modulus causes the expected stiffening of the bond leading to greater absolute bounce mode frequencies and greater absolute changes over temperature. The bounce mode's normalised behaviour over temperature, not shown here, is identical. It is also seen that the effect of bonding stress increases with increased modulus values, with greater frequency differences observed. This increased stress effect is proportional to the increase in bounce mode frequency.

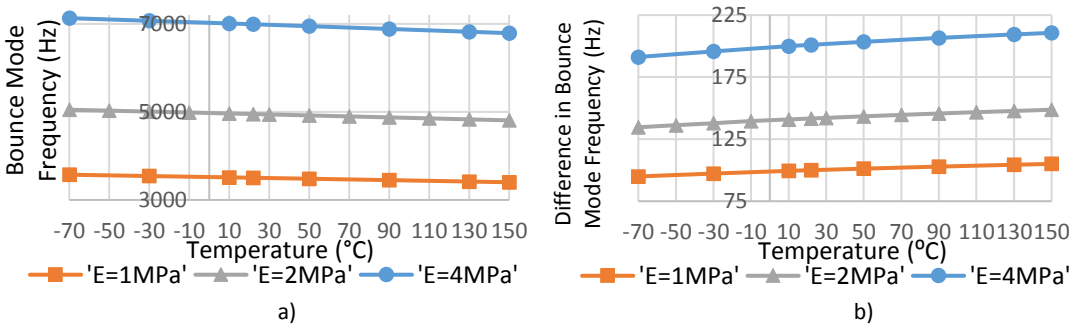
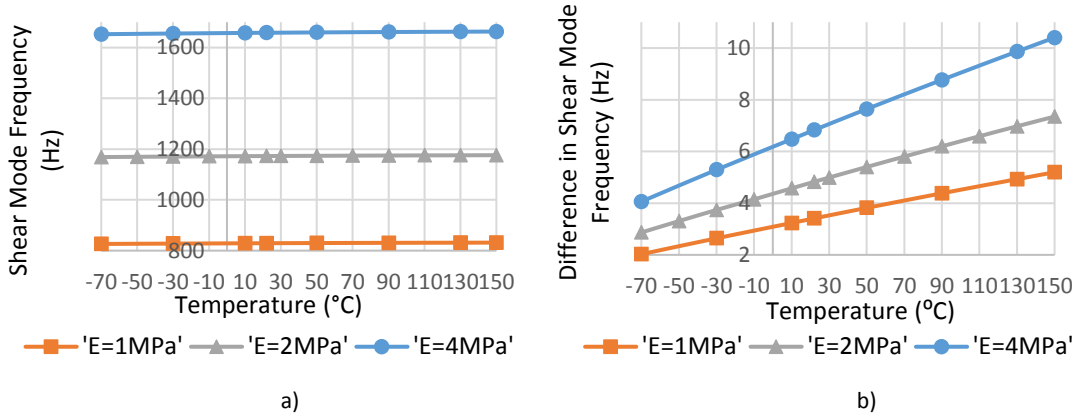


Figure 113 – a) Bounce Mode Frequency b) Pre-stress Effect over temperature when Young's Modulus is varied

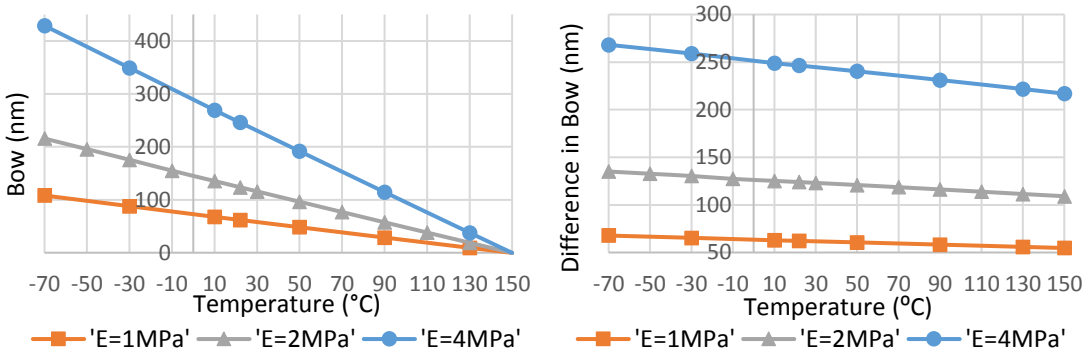
Figure 114 shows the effect of modulus variation on the shear modes temperature behaviour and pre-stress effects. The modulus change has a very similar effect as described for the bounce mode. With the absolute shear mode frequency increasing for greater modulus values, and identical normalised temperature trends. While again, the frequency difference, between pre-stressed and unstressed cases, increases with an increase in modulus. Like in the bounce direction this increased stress effect is proportional to the modal frequency change.



a) b)

Figure 114 – a) Shear Mode Frequency and b) Pre-stress effect over temperature when Young's Modulus is varied

Figure 115 shows the die bow variation and stress effects over temperature for the varying modulus values used. It can be seen that the bow change is directly proportional to the Young's modulus change, with double the bow at any given temperature when the modulus is doubled. This direct proportionality of the induced bow is echoed in the stress effects over temperature. With the bow difference, between the stress cases, increasing in line with the modulus change.



a) b)

Figure 115 – a) Die Curvature and b) Pre-stress effect over temperature when Young's Modulus is varied

4.4.1.2.2. Thermal Expansion Coefficient

The thermal expansion coefficient of the bond material is varied between 100-400ppm. Figure 116 shows the effect of this variation on the absolute and normalised bounce mode temperature trends and the effect of the bonding stress. The bounce frequencies for the various expansion coefficients are similar at the bonding temperature, with a very small offset caused only by the slight difference in the expanded geometry after the temperature increase to the bonding temperature. However, as the temperature is reduced away from the stress-free temperature, the curves diverge, with the higher expansion coefficients inducing greater increases in the bounce frequency. Unlike Young's modulus variation, changing the thermal expansion coefficient alters the bonds normalised changes over temperature, with larger expansion causing greater percentage changes over temperature. The change in the normalised rate of change over temperature appears proportional to the thermal expansion coefficient change imposed. The change in thermal expansion behaviour also has a significant effect on the bounce mode frequency differences between the stress cases. With increased expansion rates causing greater bond stress effects, while also causing greater variation in stress effects over the temperature range.

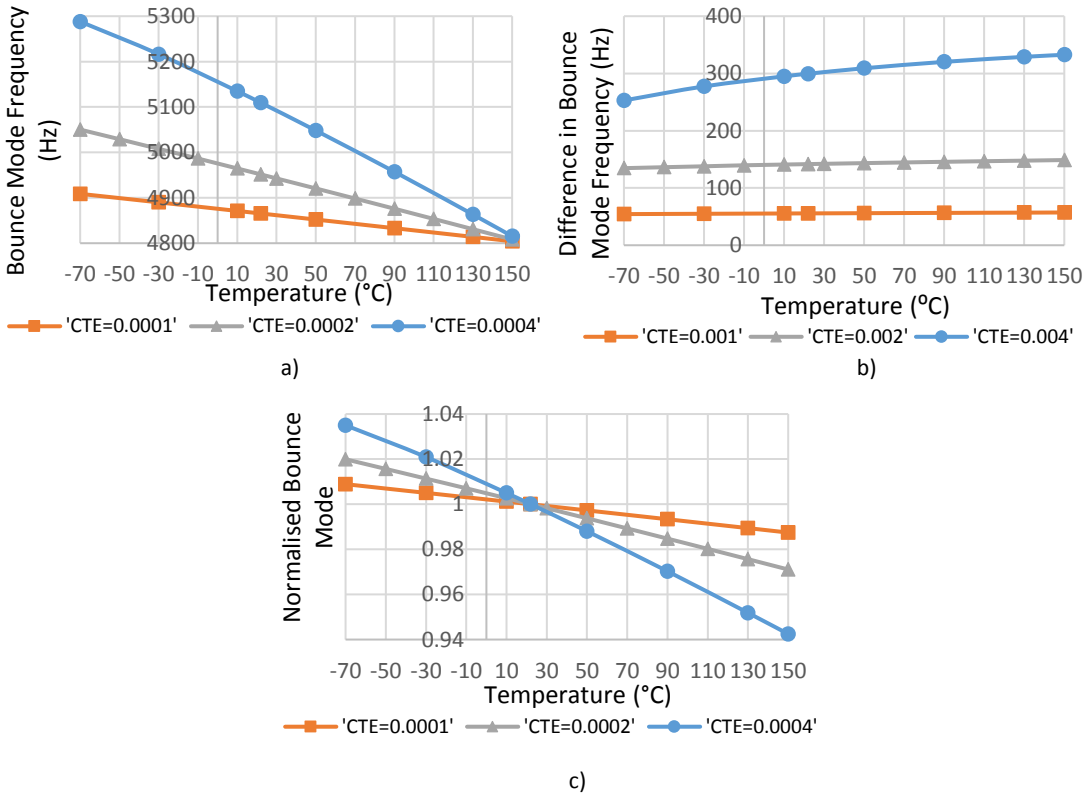


Figure 116 – a) Bounce Mode Frequency, b) Pre-stress Effect and c) normalised Bounce Frequency over temperature when Thermal Expansion Coefficient is varied

Figure 117 shows the effect of varying the bond's thermal expansion coefficient on the shear modes temperature behaviour and the effect of bonding stress. It is seen that changes to the expansion behaviour causes significant changes in the shear mode frequency and its trend over temperature. Similar to the bounce mode, the differing expanded geometries cause differing shear mode frequencies at the bonding temperature. However, as the temperature is reduced the increased thermal expansion rates cause greater reductions in the modal frequency, with a far greater level of non-linearity. These are particularly clear in the normalised plot, which shows the higher expansion coefficients induce significantly larger percentage changes over temperature, with greater increases in the rate of change as temperature is reduced. In general, the higher thermal expansion also causes greater pre-stress effects, with larger frequency differences observed. However, because of the greater non-linearity induced in the shear mode temperature trend for higher expansion rates, the pre-stress effects behaviour over temperature is greatly changed.

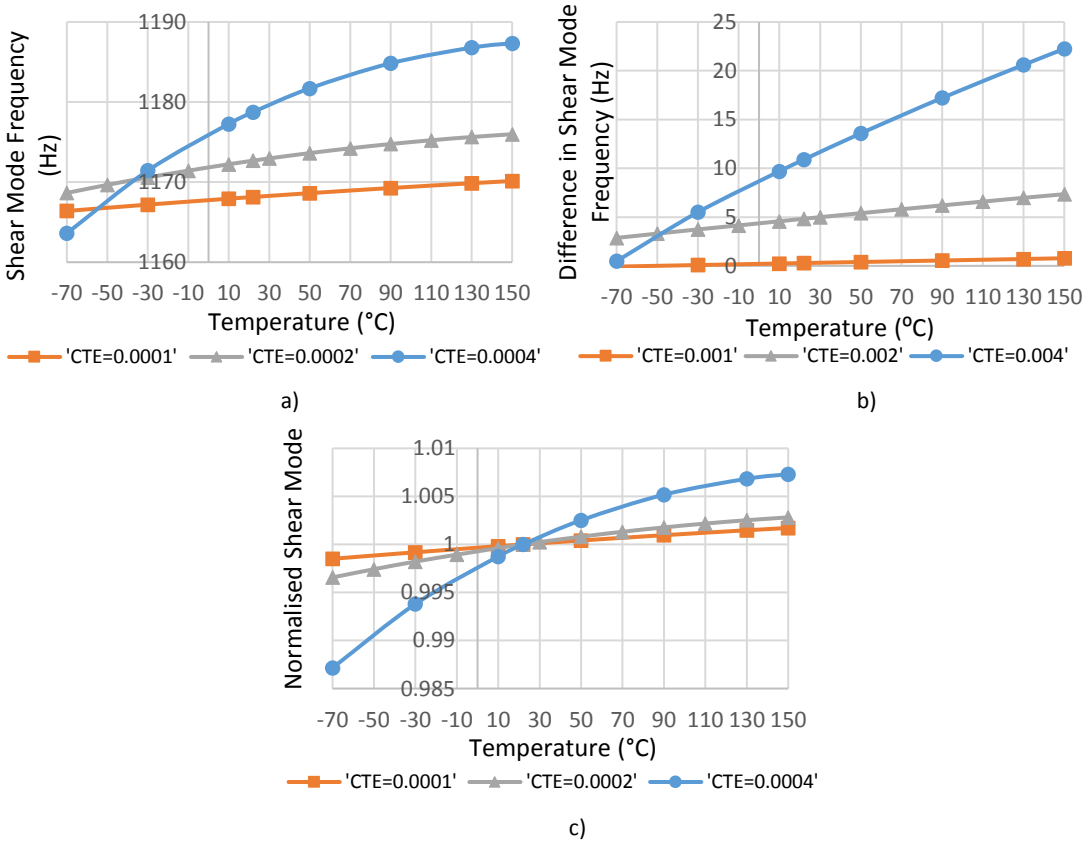
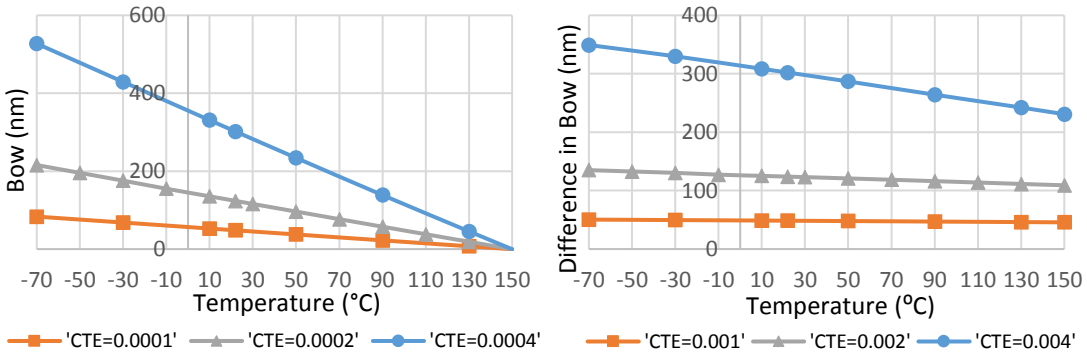


Figure 117 – a) Shear Mode Frequency, b) Pre-stress Effect and c) normalised Shear Frequency over temperature when Thermal Expansion Coefficient is varied

Figure 118 shows how the bonding stress effect and die bow temperature trends are affected by changes to the bond's thermal expansion coefficient. It is seen that higher expansion rates cause

greater curvature of the die. The curvature increases observed are greater than the change to the thermal expansion coefficient. This supports Rusanen and Torkkeli's assertion that the thermal expansion mismatch of the bond can be more significant in inducing curvature than the bond's modulus [44]. The significance of the thermal expansion coefficient is also shown when comparing the bonding stress effects for various values. With significant increases in the curvature differences between the stress cases seen for higher expansion rates, and therefore greater bonding stress effect. Similarly, to absolute bow, the stress effect varies more than the change made to the variable.



a) b)

Figure 118 – a) Die curvature and b) Pre-stress Effect over temperature when Thermal Expansion Coefficient is varied

4.4.1.2.3. Poisson's Ratio

In this section the Poisson's Ratio value for the silicone bond has been varied between 0.49 and 0.499, to observe its effect on the model outputs and their trends over temperature, and the effects of bonding stress. Figure 119 shows the effect of Poisson's ratio variation on the absolute and normalised bounce mode temperature trends and the effect of the bonding stress. It can be seen that an increased Poisson's ratio causes a significant increase in bounce mode due to the stiffening associated with the volume changes occurring during the bounce mode motions. Despite this increased bounce frequency, the frequency changes observed over temperature do not change greatly, leading to a reduction in the bounce modes normalised behaviour over temperature. The increased Poisson's ratio also causes a lower bonding stress effect on the bounce mode, with lower frequency differences observed between the pre-stressed and unstressed cases.

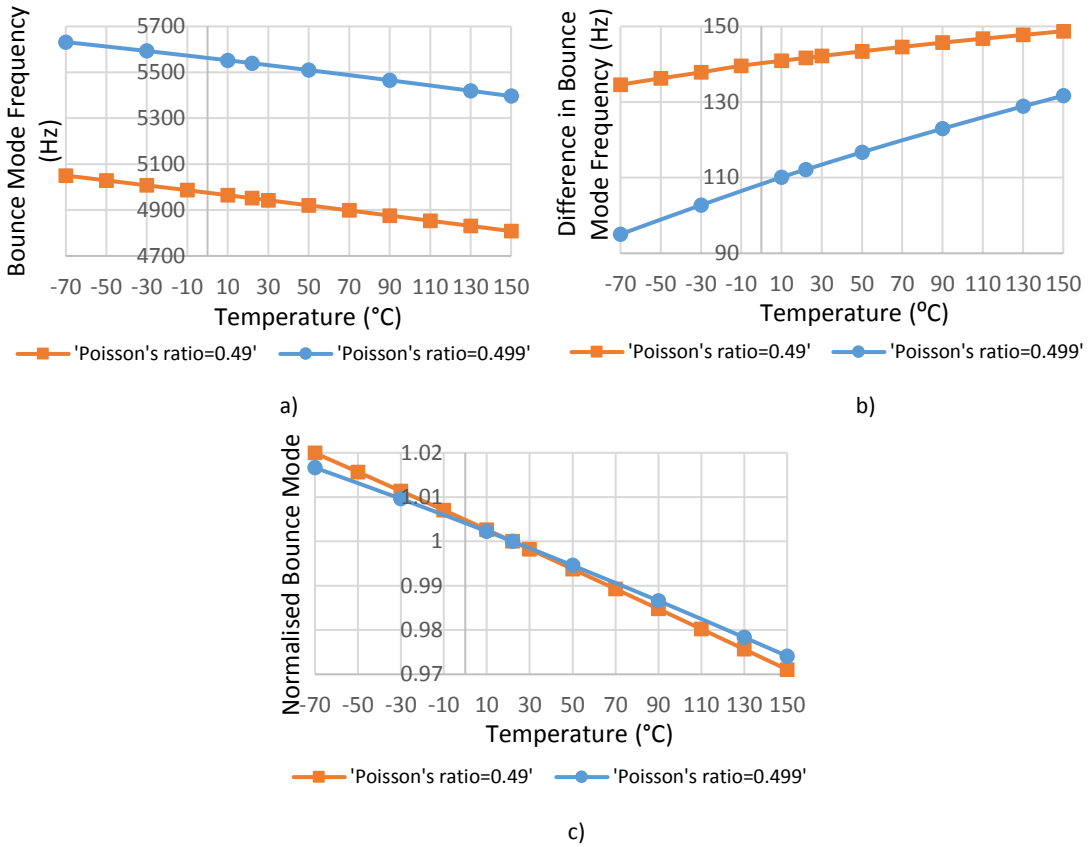


Figure 119 – a) Bounce Mode Frequency, b) Pre-stress Effect and c) normalised Bounce Frequency over temperature when Poisson's Ratio is varied

Figure 120 shows the effect of varying the bond's Poisson's ratio on the shear modes absolute and normalised temperature behaviours and the effect of bonding stress. The increased Poisson's ratio has a lower effect on the shear mode, with only a small reduction in the modal frequency (<2Hz). Similar to the bounce mode, there is little observed change in the shear mode frequency's temperature behaviour due to the property change, leading to a slight increase in the normalised rate of change of the modal frequency over temperature. The non-linear behaviour of this trend appears unchanged. It is also observed that the effect of the bonding stress is reduced with the increase in Poisson's ratio, however this reduction is only small, given that the pre-stress effects on the shear mode are relatively insignificant (maximum difference of ~7Hz).

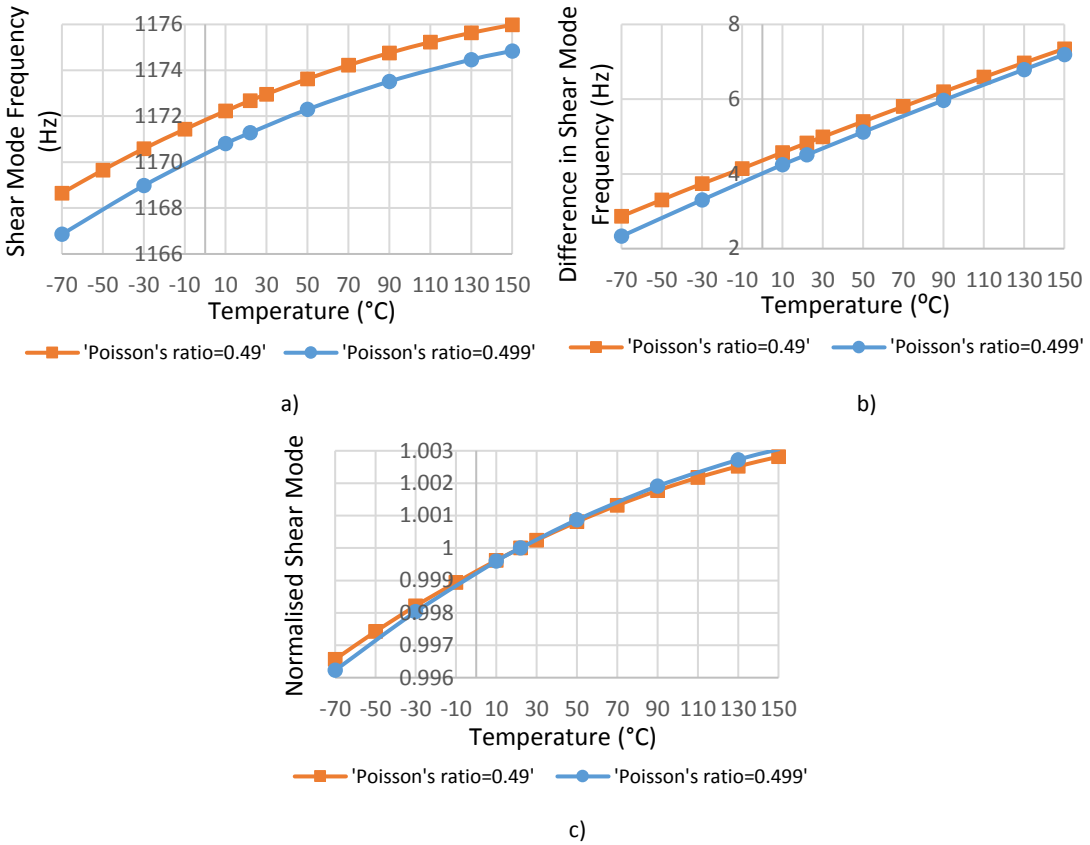


Figure 120 – a) Shear Mode Frequency, b) Pre-stress Effect and c) normalised Shear Frequency over temperature when Thermal Poisson's Ratio is varied

Figure 121 shows the effect of varying the bond's Poisson's ratio on the die's bow observed over temperature and the effect of bonding stress. It can be seen that the increased Poisson's ratio induces a greater induced curvature rate as temperature is reduced from the stress-free bonding temperature, leading to greater die bow values at all temperatures. The increased Poisson's ratio is also seen to exaggerate the effects of bonding stress, with significant increases in the bow difference between the stressed and unstressed cases.

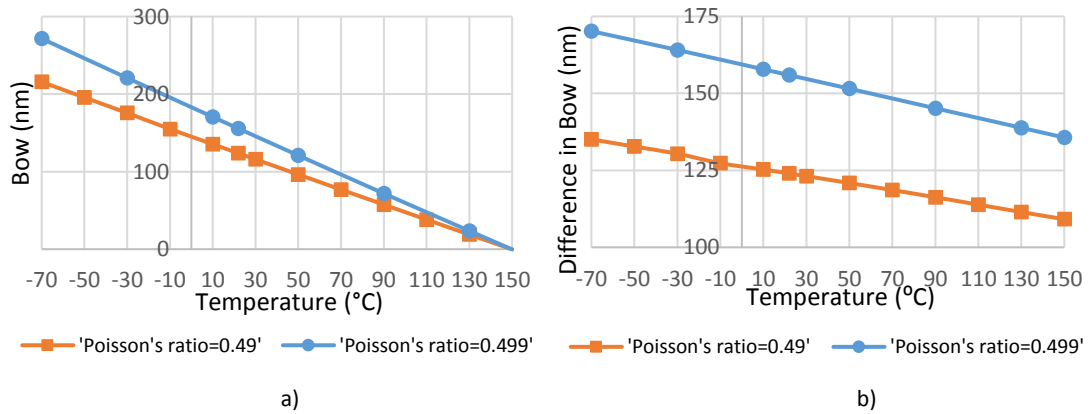


Figure 121 – a) Die curvature and b) Pre-stress Effect over temperature when Poisson's Ratio is varied

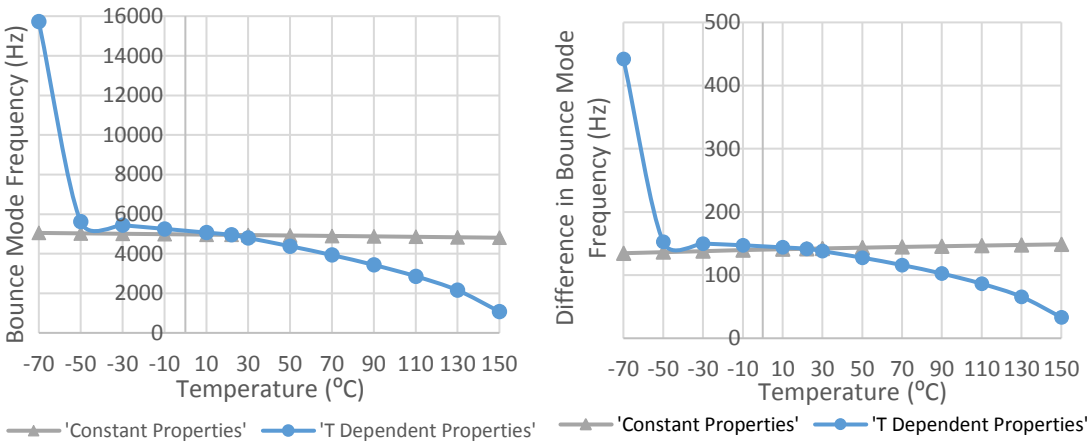
4.4.1.3. Estimated Young's Modulus Temperature Dependency

In this section, an estimated temperature dependent Young's modulus is used in the FE model and the resulting model outputs and pre-stress effects over temperature are compared to those found for a constant modulus. The Young's modulus estimates at different temperatures are shown in Table 17, the ambient property value is the same between the differing cases (2MPa at 22°C).

Table 17 - Estimated Temperature Dependent Young's Modulus used in FE Model

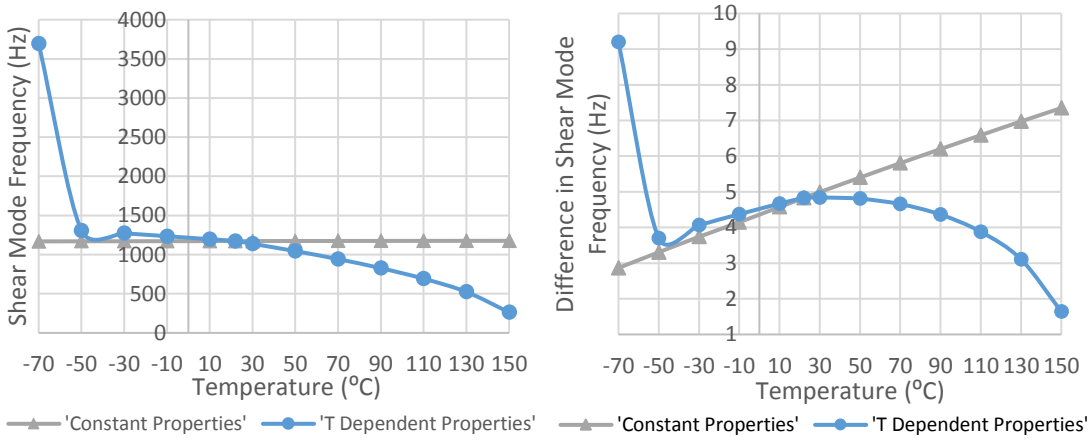
Temperature (°C)	Young's Modulus (MPa)
-70	20
-60	5
-50	2.5
22	2
150	1

Figure 122 and Figure 123 shows the effect of the temperature dependent Young's modulus on the modal frequency and associated pre-stress effect over temperature, for the bounce and shear mode respectively. The differences induced between the constant and temperature dependent are similar for the two modes and are strongly linked to the behaviour observed in Section 4.4.1.2.1. when the effect of varying Young's modulus was investigated. It is seen that for temperatures above ambient, when the T-dependent modulus is lower than the constant value used, the resulting modal frequencies are lower and vice versa when the T-dependent modulus is higher than the constant values at temperatures lower than ambient. The same effect is seen for the pre-stress effects over temperature, with greater frequency differences observed in the model with the greater Young's modulus at that given temperature. It can be seen that when constant properties are used, the modal frequencies and the pre-stress effects suffer from almost negligible change over the temperature range when compared to the change occurring when using the T-dependent Young's modulus. Therefore, if the bond's material properties have significant temperature dependency, this will dominate the temperature dependency of the modal frequencies.



a) b)

Figure 122 – a) Bounce Mode Frequency and b) Pre-stress Effect over temperature when Estimated temperature dependent Young's Modulus is used, with comparison to constant properties



a) b)

Figure 123 – a) Shear Mode Frequency and b) Pre-stress Effect over temperature when Estimated temperature dependent Young's Modulus is used, with comparison to constant properties

Figure 124 shows the effect of a temperature dependent Young's modulus on the bow induced in the die over temperature. Similar behaviour can be seen to that described for the modal frequencies, with lower bows experienced in the model with the lower Young's modulus at a given temperature. Therefore, the temperature dependent properties used induce greater bows at temperatures below ambient and lower bows above ambient. At 22°C, when the Young's modulus is the same in both models, the same die curvature is observed. Hence, the bow at a given temperature is only dependent on the modulus at that temperature, and is not affected by any modulus change occurring over temperature.

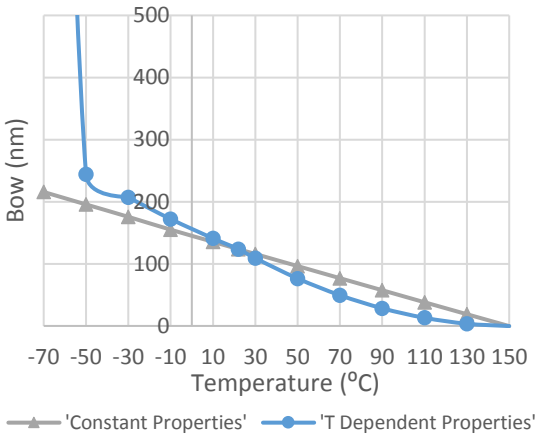
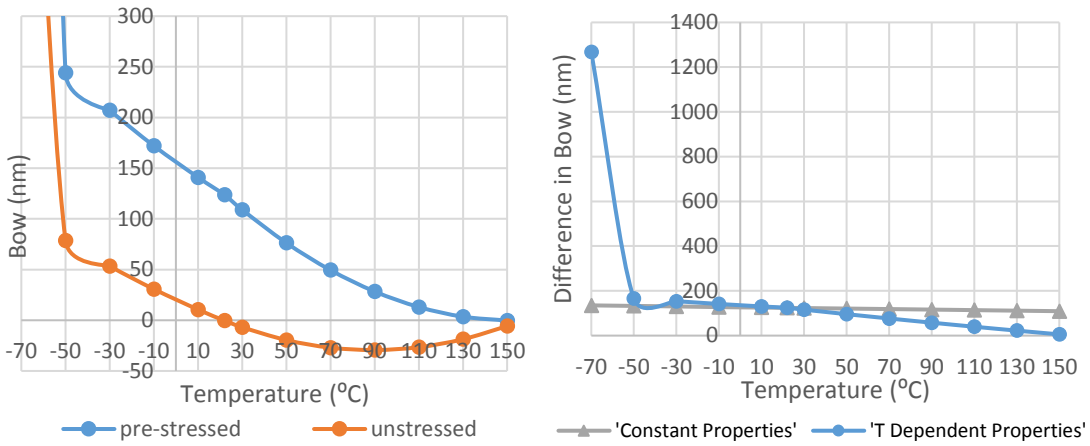


Figure 124 - Bow over temperature when Estimated temperature dependent Young's Modulus is used, with comparison to constant properties

Figure 125 shows the bow variation over temperature for the pre-stressed and unstressed cases when a temperature dependent Young's modulus is used and comparison of the effect of bonding stress on the bow with a constant modulus. It can be seen that the temperature dependent Young's modulus causes a differing bow behaviour over temperature, this is of particular interest for temperatures above ambient. As the temperature is increased from ambient, a convex die shape is induced, as was observed for a constant Young's modulus in Figure 112 in Section 4.4.1.1. However, as the temperature increases the modulus reduces causing a reduction in the rate of curvature to the point at which a maximum convex curvature is observed at approximately 90°C. For further temperature increases the bow reduces, showing that the reduction in modulus is overcoming the thermal expansion effects, such that it can accommodate the additional stresses as well as those already induced during the temperature increase to 90°C. This effect continues, and accelerates, until the bow approaches zero at 150°C. This behaviour causes there to be little pre-stress effect at 150°C for the temperature dependent model, which increases as the Young's modulus increases with reducing temperature. The pre-stress effect increase accelerates as the temperature is reduced and young's modulus increases. The temperature dependency of the bond material dominates the temperature trend of the pre-stress effects, with much greater differences observed between stress cases, than seen with a constant modulus.



a) b)

Figure 125 - Comparison of Die bow induced over temperature for Pre-stressed and Unstressed cases using temperature dependent Young's modulus and the comparison of Pre-stress effects between constant and temperature dependent

4.5. Conclusions

4.5.1. Model Parameters

The model parameter requirements are summarised in Section 4.3.2.7. The MPC contact algorithm provided improved quality metrics, gaps and penetrations, whilst also providing converged model outputs without the tight contact parameter control required when using the Augmented Lagrange contact algorithm. It was found that the MPC is susceptible to overconstraint, but this could be overcome by limiting symmetry to a 1/4 model geometry.

The converged outputs were found not to change greatly for differing mesh structures, but a contact-sized tetrahedral mesh appeared to provide improved convergence trends with reducing mesh size, achieving convergence with element sizes of 100µm in the bond. This regime provided the same high mesh densities in the bond, but reduced the total element numbers and ensured the model is efficient.

Some differing requirements were observed when bonding stress is omitted, requiring greater control of contact parameters to achieve convergence when using Augmented Lagrange. However, this is not required for use of the MPC algorithm, which provided similar convergence trends for the differing stress cases.

4.5.2. Model Outputs as a function of Temperature

4.5.2.1. Geometrical Effects

The model assumed the material properties are constant over temperature due to difficulty in measuring the temperature dependent properties because of extraneous variables experienced during testing. Therefore, any changes in the model outputs as temperature is varied are caused solely by geometrical changes. As temperature was reduced away from the bonding temperature, curvature was induced in the die, increasing linearly with temperature. It was seen that as temperature was increased it caused significant reductions in the bounce mode and relatively small but non-linear increases in the shear mode frequency. While the inclusion of bonding stresses caused significant stiffening of the bounce direction, its effect was less significant on the shear mode frequency, however it did significantly alter the temperature behaviour of the shear mode due to changes in the non-linearity observed.

4.5.2.2. Material Properties

In order to understand the effect of changes over temperature on the model outputs, the important material properties identified from literature were varied for the silicone bond, including Young's modulus, coefficient of thermal expansion and Poisson's ratio.

Increasing Young's modulus caused a proportional increase in the bow induced over a given temperature change, with the rate of curvature (with T change) doubling when the modulus is doubled. The increase in modulus caused significant increases in the modal frequencies because of the greater stiffness of the bond. The changes observed over temperature were proportional to the absolute frequency change, leading to identical normalised behaviour over temperature. The bonding stress effects were also proportional to the absolute changes in modal frequencies.

Varying the thermal expansion coefficient leads to more complex changes in the outputs. A greater expansion rate caused greater curvature to be induced, with the increase in bow larger than the increase imposed by the thermal expansion coefficient. This supported the assertion by Rusanen and Torkkeli that the bond's thermal expansion mismatch can dominate the induced curvature [44]. A change in the expansion coefficient does not greatly affect the modal frequencies at the bonding temperature (150°C), with only small offsets observed caused by the slight difference in geometry due

to varying expansion during the temperature increase. However, the change in thermal expansion coefficient causes significant changes in the temperature behaviour. The rate of change in bounce mode frequency greatly increases for larger expansion rates, leading to a proportional increase in the normalised changes over temperature. The shear mode also varies more over temperature when thermal expansion is increased. However, in this case the increase in normalised change increases more with each increase in thermal expansion. The non-linearity observed in the shear modes frequency change over temperature is increased significantly with increases to the expansion rate.

Poisson's ratio was increased from 0.49 to 0.499, and it was seen to induce greater curvatures in the die due to the bond's lowered ability to absorb stresses through a volume change. The bonding stress effect on the bow was significantly increased when Poisson's ratio was larger. The property change had a significant effect on the bounce mode, increasing greatly when Poisson's ratio was increased, due to the stiffening of the volume change associated with the bounce mode motion. Despite this large increase, the variation in frequency over temperature was similar, leading to a reduced normalised change over temperature. The Poisson's ratio change only had a small effect on the shear mode, with a slight increase in the normalised change due to a slight decrease in the shear mode frequency.

4.5.2.3. Temperature Dependent Young's Modulus

To observe the effect on the model outputs and their temperature trends, an estimated set of temperature dependent Young's modulus values were used in the model and compared to the results using a constant value. The same effect as varying the temperature constant modulus at a given temperature was observed. i.e. for temperatures above ambient, the modulus was higher and therefore led to increased modal frequencies and bow, and vice versa for temperatures below ambient. At ambient temperature, the modulus was the same and therefore all outputs were the same.

It was seen that the outputs of the temperature dependent model varied significantly more than the constant model, which was almost negligible in comparison. This shows that the temperature dependency of the bond's modulus dominates the changes in modal frequencies and bow over temperature. This was not investigated for other properties, however considering the significance of

the changes observed in varying thermal expansion and Poisson's ratio, any temperature dependence of these properties is likely to dominate over geometrical effects.

4.5.3. Concluding Remarks

In this chapter, modelling procedures have been developed to create an FE model for evaluating the curvature state and modal frequencies of a die, bonded to a substrate via a small-scale adhesive bond typical of a MEMS inertial sensor, and their change over temperature. This includes investigation and identification of the contact algorithm, detection method and parameters, as well as the geometries, mesh regimes and element sizes to be used to achieve convergence of the model outputs. The importance of modelling the bonding stresses, due to constrained contraction from the bonding temperature has been shown. With significant differences observed in the model outputs and their behaviour over temperature, between pre-stressed and unstressed cases. The stressing of the bond in the model is solely due to the constrained bond experiencing a temperature change and therefore varying contractions of the bond and adherends. Shrinkage likely to occur during curing of the bond is not modelled and therefore the stresses observed are likely underestimated in comparison to reality.

The modelling procedures developed in this chapter will be used to create further FE models to investigate bond design effects, in Chapter 5. In these models the bond's shape and thickness will be varied, and their effect on the die's modal frequencies and curvature, and their changes over temperature investigated. The aim of this investigation is to identify design parameters to reduce the bonding stress and curvature induced, as well as the change in curvature and modal properties over temperature.

Material property variation within this chapter has already shown bond material property considerations to achieve these aims. The greatest reduction in die curvature was achieved using a bond with a lower thermal expansion coefficient, and it is thought the curvature will be minimised by matching the thermal expansion of the bond material with that of the adherends (base and die). The curvature can also be significantly reduced with a material of lower modulus, with curvature reduction directly proportional to the modulus reduction. A lower Poisson's ratio was also seen to reduce curvature.

Curvature and modal frequency change over temperature was dominated by material property temperature dependence, therefore greater stability of the bond properties will be achieved through reduced temperature dependency of the bond's material properties. When using constant properties over temperature, the most significant reduction in modal frequency change was realised by reduction of the bond's thermal expansion coefficient. This was achieved without affecting the absolute frequency (bond stiffness), and therefore is more effective than a reduction in Young's modulus, which still exhibits the same normalised change over temperature. Similarly to curvature, it is thought that the modal changes will be minimised through matching of the bond and adherend's thermal expansion coefficients.

5. Chapter 5: Bond Design Variation- FEM

5.1. Introduction

The die attach is a significant process in inducing thermo-mechanical stresses and deformations in the die [33]. These stresses and deformations affect the sensor performance by changing the MEMS element dynamics, leading to scale factor changes, and by changing curvature causing bias offsets variations [41] [34]. The induced stresses and deformations are dependent on the environmental temperature and therefore sensor performance changes over temperature also [53]. Understanding and quantifying this temperature dependency allows for compensation to be applied to correct the sensor outputs for changing temperature. Die bonds have also been seen to change over time due to viscoelastic mechanisms occurring within the bond [53] [44]. This change changes the temperature dependency of performance metrics over time making temperature compensation more difficult, if not impossible. Similar issues are also caused due to the bond properties changing over time due to aging or further curing effects.

Temperature compensation cannot be relied upon solely to reduce performance changes over temperature. Elimination of the temperature dependency through design of a stress-free bond, consisting of no stress or deformation at any temperature would be the ideal solution. This would also tackle the issue of time dependency because if there is no stress or curvature there would be no stress relaxation or creep, and even changing material properties over time would have no direct effect on performance metrics. It should be noted that there are other temperature effects that can cause performance issues that would persist even with such a stress-free bond, for example susceptibility to shock and vibration. Of course, complete elimination is not a realistic aim given the differing thermal properties of the adhesive and adherends, so reduction of both the absolute and change over the operating temperature of die stress and curvature is the primary aim. It has been seen that stresses and deformations can be reduced through die bond design parameters such as a 4-dot bond shape as opposed to full coverage [42] [37] and the use of thicker bonds [46] [41]. The bond material is also key, with a low modulus material being advantageous [33] [44] [42]. However, it is also seen that if the

mismatch in thermal expansion coefficients is extreme between the die, bond and substrate, its effect dominates the curvature observed [44]. The deformation profile across the die's surface can also affect performance, particularly in MEMS gyroscopes using ring resonator geometries, where varying deformation around the ring circumference leads to quadrature bias.

In Chapter 4 an FE model was developed to assess changes in the dynamic and static behaviour of the die over temperature. No resonator geometry was included due to the extra complexity of the model, especially the extra meshing control required in the micro structures. It is therefore assumed that changes in the translational die modes, insinuates changing bond properties and die response to motion, and curvature, inferring changes to the element dynamics and statics, are directly linked to changes in device performance. Extensive modelling studies were conducted and reported in Chapter 4 to develop a converged and efficient model to evaluate the translational die mode frequencies and die curvature over typical operating temperature of sensors. This model has potential to be expanded at a later date (outside the scope of the current project) to include resonator geometries to observe performance changes directly.

In this Chapter, the design of the die bond will be varied in the FE model and the frequency and deformation outputs calculated over temperature. The primary objective of this chapter is to determine how bond design parameters can lead to improvements in device performance and performance stability over temperature and time (inferred), where an improved bond would exhibit:

- Lower sensitivity/change in outputs (frequencies and curvature) over temperature
- Lower sensitivity/change of outputs over time. Note: the developed FE model is not capable of determining this, so a lower level of absolute curvature will be considered better as there is less scope for change if viscoelastic mechanisms to occur. Changes over time are directly observed in Chapter 6 where various bond designs are tested over time, including before and after temperature cycling and high temperature storage.
- Lower levels of variation in deformation around a circular path on the dies surface, representing a possible ring geometry.

5.2. Design Variables

The key bond design parameters were identified in the literature review to reduce the stress within the bond, including bond thickness, shape and material.

5.2.1. Bond Thickness

Thicker bonds were observed to experience lower stress and induce less curvature in the die [33]. Bond thickness is also likely to affect the dynamic behaviour and physical properties of the bond. These behaviour changes are significant in MEMS sensors because the die bonds are extremely thin, with die bonds having thicknesses as small as 10 microns. The slenderness of the bond is a key term here and is a measure comparing the cross-sectional area to the thickness of the structure, with high slenderness describing a bond having a large area (A) to thickness (t) ratio. The slenderness is often described by the shape factor *S,* which is defined as the ratio of one bonded/loaded area, A (cross-sectional area) to the force free area, A_{FF} (area of free sides, perimeter multiplied by thickness) [64] [62] [63]. i.e. the shape factor S is given by:

$$S = \frac{A}{A_{FF}}$$

For a square bond, the shape factor is

$$S\ (Square) = \frac{w}{4t}$$

where t is the thichness and w is the width.

As the slenderness increases the constrained surfaces of the bond causes a stiffening effect when the bond is loaded in compression or tension. Gent and Meinecke [64], Gent and Lindley [62] and others [63] have used the classical theory of elasticity and superposition principle of deformations to derive expressions to describe the stiffened modulus, known as the apparent modulus E_a, in terms of the elastic modulus and shape factor. For a square cross-section, the apparent modulus can be written as:

$$E_a(Square) \cong E(1 + 2.25S^2)$$

In many applications rubbers are assumed to be incompressible due to the bulk modulus, K, being orders of magnitude higher than the Young's modulus [62]. However, due to the stiffening effect from the bonded surfaces, for bonds of high slenderness the Young's modulus is comparable to the

bulk modulus and therefore the incompressibility assumption breaks down and bulk deformation contributes to the total deformation. In this case, Gent and Lindley [62] provide an expression for the corrected modulus E'$_a$ such that:

$$\frac{1}{E'_a} = \frac{1}{E_a} + \frac{1}{K}$$

Figure 126 shows how the apparent modulus and corrected apparent modulus vary over thickness for a square bond (w=9mm), also shown is the basic Young's modulus. It can be seen that as the thickness is reduced, and therefore slenderness is increased the apparent modulus values quickly increase away from the standard Young's modulus value for silicone rubber. Then as the slenderness is increased further, the apparent modulus curves diverge. It is at this point that the incompressibility assumption breaks down and bulk deformation becomes significant. Beyond this slenderness value, the apparent modulus needs correction using the bulk modulus to be accurate, and as the thickness is reduced to zero (slenderness approaches infinity) the corrected apparent modulus tends to the bulk modulus of the material.

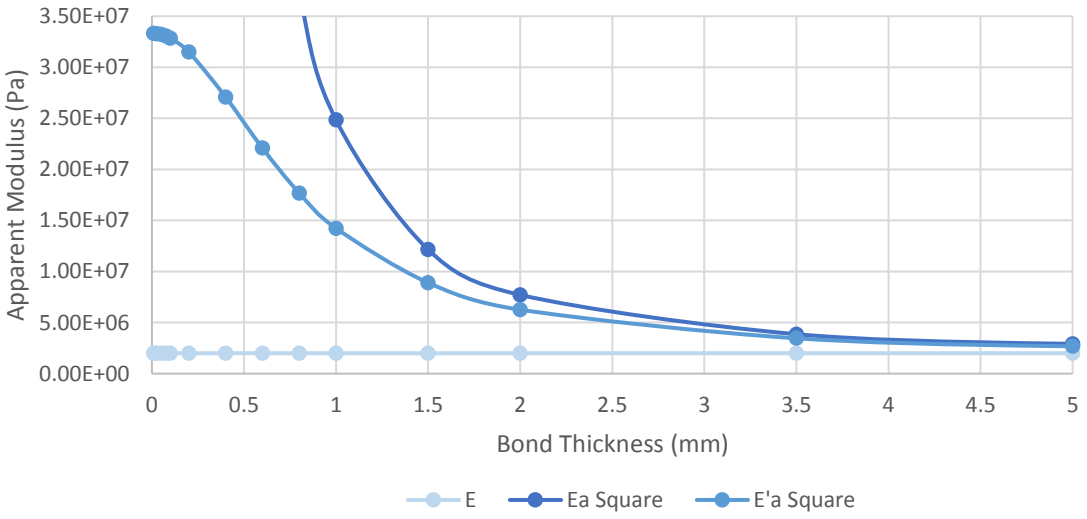


Figure 126 – Variation in Apparent Modulus and corrected Apparent Modulus over thickness for a square bond

This behaviour indicates that for bonds having high slenderness it is important to have an accurate value of the bulk modulus. The bulk modulus is often calculated from the Young's modulus and Poisson's ratio of a material using the relation:

$$K = \frac{E}{3(1-2\nu)}$$

Figure 127 below shows how the bulk modulus changes when Poisson's ratio is varied between 0.49 and 0.4999. The sensitivity of the bulk modulus to changes in Poisson's ratio is clear, and would have a significant effect on the apparent modulus for a typical bond in a MEMS device.

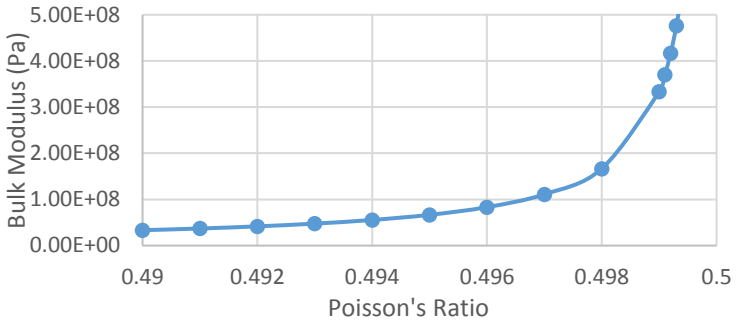


Figure 127 – Variation of Bulk Modulus with Poisson's Ratio for Silicone Adhesive

Figure 128 shows the effect of varying Poisson's ratio on the apparent modulus over thickness. It can be seen that for a typical MEMS die bond having thicknesses in the range 20-250µm, the difference between the apparent modulus values is significant.

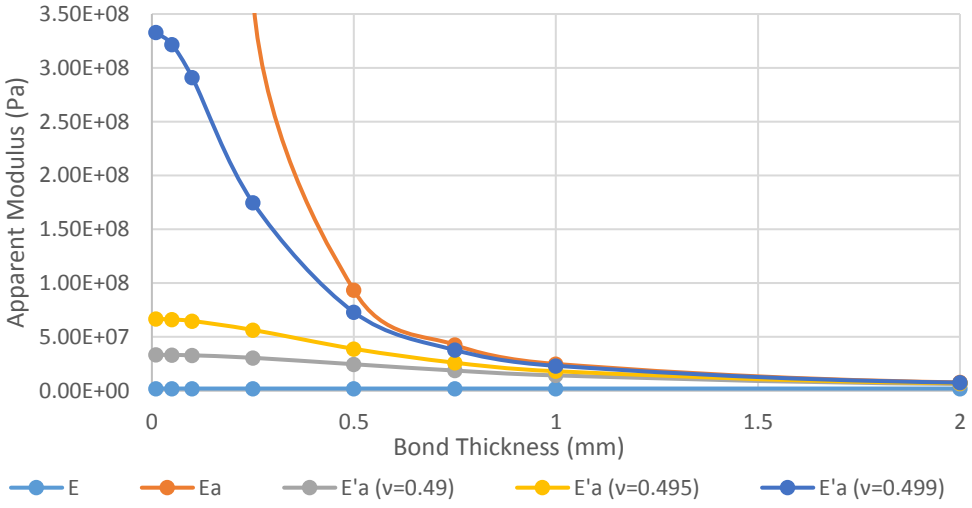


Figure 128 – Variation of Apparent Moduli over thickness for differing Poisson's Ratio values

5.2.2. Bond Shape

Within the literature, it was found that bonds based on a 4-dot arrangement experienced lower levels of stress and induced less die curvature than an equivalent sized full coverage square bond [37]. This conclusion is further investigated here and is expanded to include investigations over temperature and thickness, as well as investigation of a 9-dot bond arrangement. This is to determine whether further 'discretising' the bonds surface leads to further improvements in curvature reductions.

These dotted or discretised bond shapes are linked to the thickness and slenderness discussed in the previous section. By dotting the bond over the same area, it is effectively lowering the slenderness of the structure when considering each dot as a bond and the overall arrangement as a series of dot bonds connected in parallel. The slenderness is reduced because a single dot still has the same thickness but a greatly reduced cross sectional and increased force-free area. Due to this lowered slenderness the stiffened apparent modulus effect is greatly reduced despite the area and thickness not changing as significantly (some change in cross-sectional area due to the spaces between the dots).

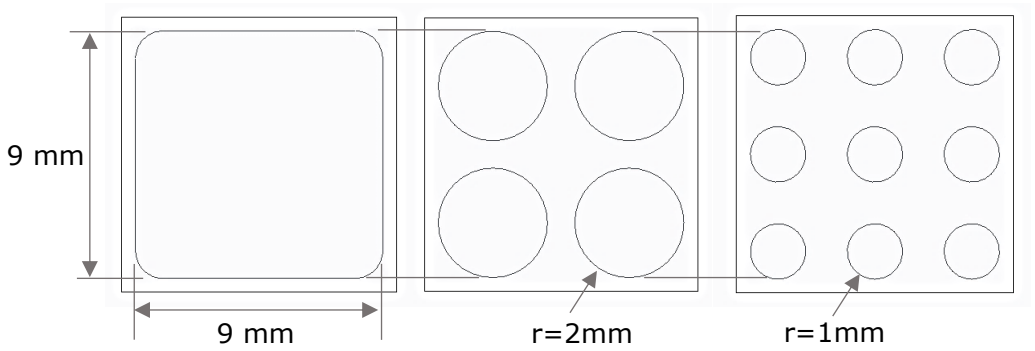


Figure 129 – Bond Shapes to be investigated in FE modelling study

The shape factor for a single circular dot is

$$S\ (circle) = \frac{r}{2h}$$

And the expression for apparent modulus from Gent and Lindley [61] is

$$E_a(Circle) = E(1 + 2S^2)$$

Figure 130 compares the shape factors of the various bond shapes over thickness. The square bond has the highest shape factor followed by the 4-dot bond and then the 9-dot bond, confirming as mentioned earlier that discretisation of the bond lowers the shape factor and therefore affects the resulting apparent modulus.

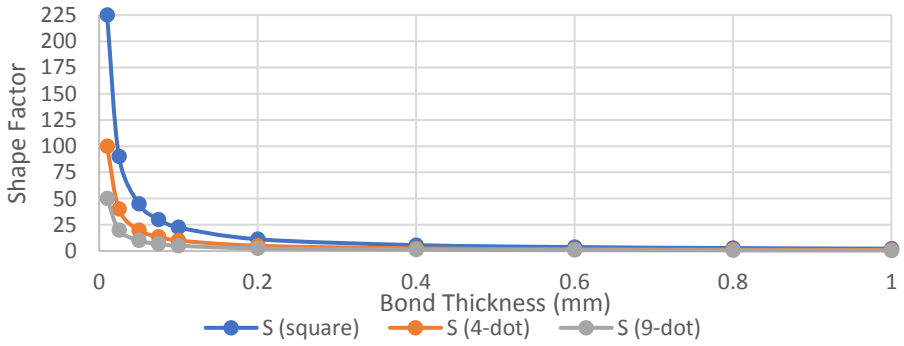


Figure 130 – Shape Factor variation over thickness for differing bond shapes

Figure 131 shows how the apparent moduli and corrected apparent moduli of the various bond shapes vary over thickness. It is observed that as thickness reduces to zero, all of the bond shapes experience their apparent modulus tend to the bulk modulus value despite their shape factor. The shape factor affects how the apparent modulus tends towards this value rather than affecting the limiting value of the apparent modulus, which is solely controlled by the bulk modulus. It can be seen that the higher the shape factor bond, the higher the thickness at which the apparent modulus stiffening effects occur, and the higher the thickness at which the incompressibility assumption breaks down. However, because the apparent moduli tend towards the same value for all bond shapes, the bonds with lower shape factor at a given thickness, i.e. the dotted bonds undergo a greater rate of change in their apparent moduli, as it increases from the standard Young's modulus value to the bulk modulus value over a smaller thickness change.

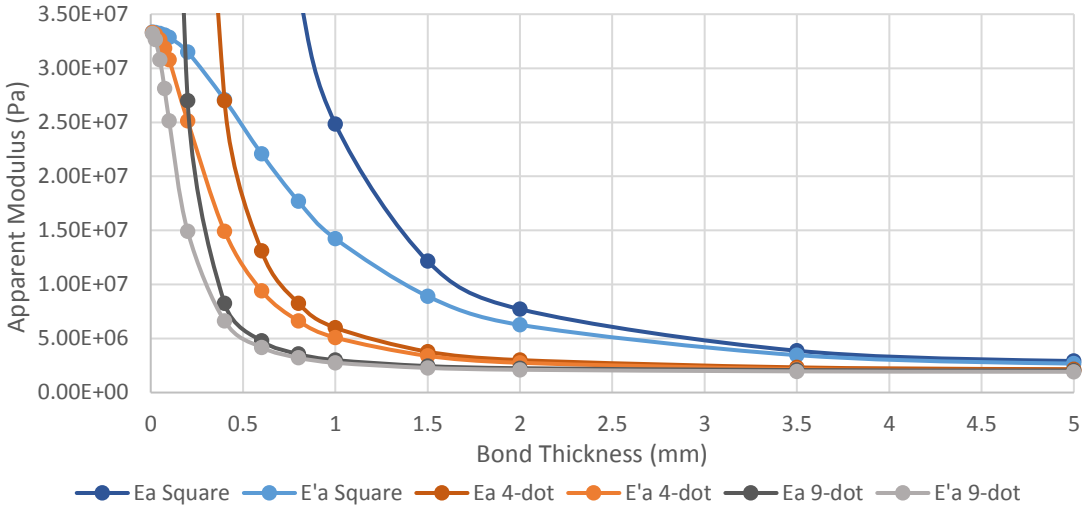


Figure 131 – Apparent Modulus variation over thickness for various bond shapes

5.2.3. Bond Material

The advantages of differing bond materials are discussed in the research literature. In particular the importance of low modulus adhesives in the production of a low stress bond, with development of adhesives specifically for MEMS packaging an area of high interest in industry. However due to the high number of other parameters being investigated and the low availability of new adhesives to allow experimental testing within this project only the currently used silicone adhesive is utilised in the investigations. This adhesive has been used for many years and is well suited for use with MEMS sensors due to its very low modulus, but does suffer from a high thermal expansion coefficient,

which is over an order of magnitude higher than that of the die and substrate. Due to the lack of material property data over temperature and the difficulties encountered in material testing due to the occurrence of extraneous variables such as aging and further curing, only approximate material properties (constant over temperature) are used in the FE investigations. The effect of temperature dependent Young's modulus, as well as variation of Young's modulus, thermal expansion coefficient and Poisson's ratio was investigated in Section 4.4.1.

5.2.4. Die Parameters

The die parameters investigated include the die thickness. This parameter was not mentioned in the literature review, and the purpose of its inclusion is to vary the relationship between the stress in the bond and the curvature induced in the die. This parameter is not investigated within the FE models, but will be included in experimental investigations in chapter 7.

This could also be achieved through changing the die material, however in reality changing the die material of a MEMS sensor is difficult. This difficulty is due to the use of silicon wafers to create MEMS structures, the main die material then encapsulates this wafer. This is often a borosilicate glass due to its similar thermal expansion properties to silicone. Therefore, changing the die material significantly will most likely just cause issues within other packaging processes, with greater curvature induced at wafer level packaging stages. This is not considered within the experiments or FE models, but could be an area of future investigation.

5.3. Model Descriptions

5.3.1. Overview

The model used in this chapter was developed in Chapter 4 but varies the bond shape and thickness, as well as some variation die design parameters. As discussed in Chapter 4 the FE model is split into two main parts: i) a temperature increase model, which provides an expanded assembly geometry at the curing temperature of the bond material (22^{o}C - 150^{o}C); and ii) a temperature decrease model, in which bond surfaces are constrained, at their expanded state, and produces a deformed and stress bond assembly, providing die bow/deformation outputs and translational die mode frequencies via a modal analysis. This second model is performed over the temperature range -70^{o}C to 120^{o}C.

5.3.2. Detailed

In Chapter 4 different modelling and control options were investigated to assess convergence of the model outputs, translational modal frequencies and die deformation, and to minimise the contact quality metrics gap and penetration. The model options investigated included contact algorithms and detection methods, contact parameters, including contact stiffness' and tolerances, symmetry effects, mesh regime and sizing. The outcomes of these investigations lead to the creation of the models used here.

The final model utilises the multipoint constraint (MPC) algorithm. This contact algorithm is beneficial due to it requiring no control of the contact parameters to achieve convergence for a given mesh. The use of MPC does limit the use of symmetry as it was seen in the development that 1/8 models suffered from overconstraint leading to erroneous outputs when using this algorithm. Figure 132 shows the quarter models used to ensure no overconstraint issues and accurate outputs. The lower number of symmetry conditions increase the CPU times. However, they are still comparable to those of a 1/8 model requiring high contact parameter control (using Augmented Lagrange).

The mesh regime used was found to have a negligible effect on the converged outputs, particularly at mesh sizes sub 100µm, with contact and part sized tetrahedral and quadrilateral mesh regimes investigated. However, it was seen that the contact sized tetra mesh converged quickest with respect to element size, as well as having the fastest CPU times due to its reduced number of elements. For the dotted bonds, Figure 132 shows that the mesh on the top surface of the die is much coarser than for the square bond. This is caused by gaps between the dots allowing the mesh to expand. A mesh regime with sizing control of the elements on this surface was investigated, to assess any change in the output, particularly the deformation outputs. However, no change was found.

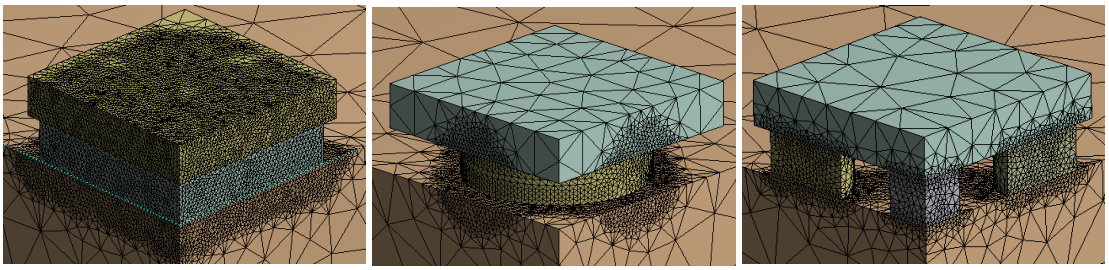


Figure 132 – Mesh regimes used for various bond shapes, 1mm thick bond examples shown

5.3.3. Mesh Convergence for Most Slender Bond Models

It was found in the development of the FE model that 100µm elements are required to reach a good level of convergence of model output metrics for a 1mm thick bond. It was intended that 10 elements would be used across the thickness of the bond when the bond dimensions were altered. However, for the thinnest bonds investigated, 250µm and 100µm, abiding by this rule is difficult because of the resulting excessive CPU times. Hence, fewer elements are used across the thickness, this section evaluates the convergence of these thinnest bonds with element size, to ensure accurate results are obtained. Due to the large differences observed between bond designs for the model outputs, shown here are the normalised change in output with changes to the element size. The results are normalised using the outputs from the proposed mesh size, 50µm.

Figure 133 shows the normalised bounce mode frequency against element size for the two differing bond thicknesses. Both thicknesses show convergence-like trends with the change reducing with each reduction in elements size, and show similar behaviour over the differing bond shapes. The 9-dot bonds experience the greatest change, followed by the 4-dot bond, with the square shape experiencing the lowest change with element size, which is likely to be due to their varying cross-sectional area. The dot radii in the 9-dot bond are 1mm and therefore require a smaller mesh size across its diameter as well as thickness compared to the 2mm radii of the dots comprising the 4-dot bond. A good level of convergence is reached at the proposed 50µm element size for both thicknesses for all bond shapes. The 250µm bond experiences a change of ~<±0.5% when element size is increased or decreased by 25µm, while the 100µm bond experiences <0.05% change for an increase from 50µm to 60µm elements.

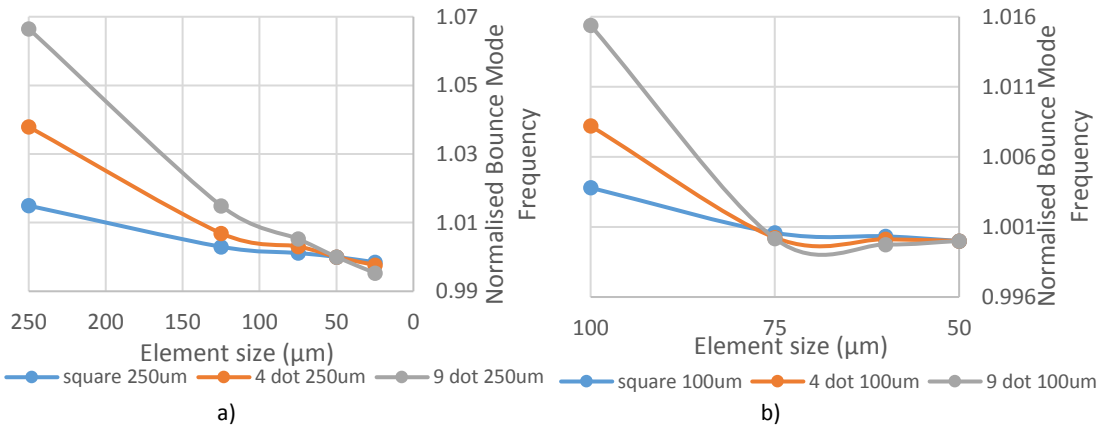
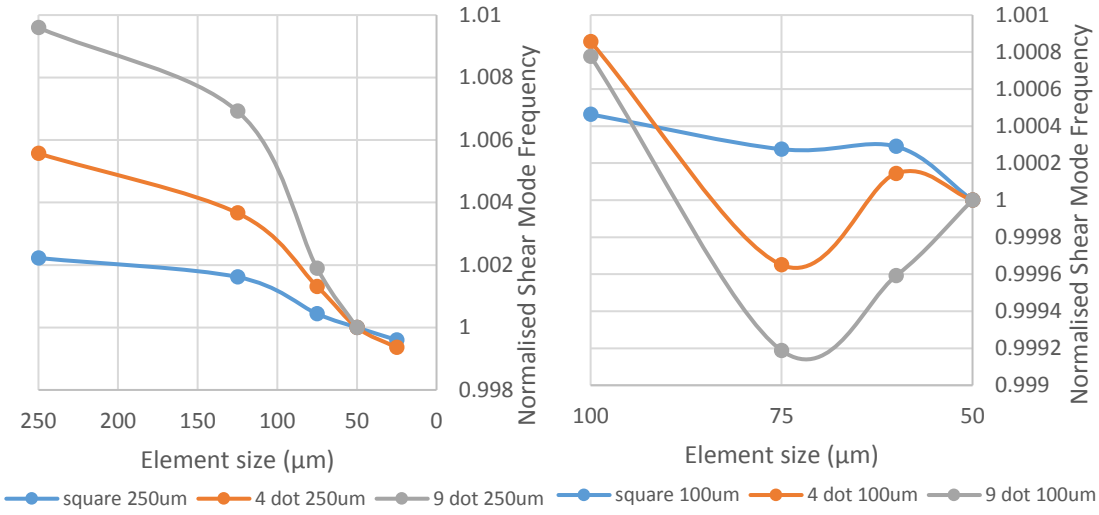


Figure 133 - Normalised Bounce Mode Frequencies for 250µm (a) and 100µm (b) thick bonds

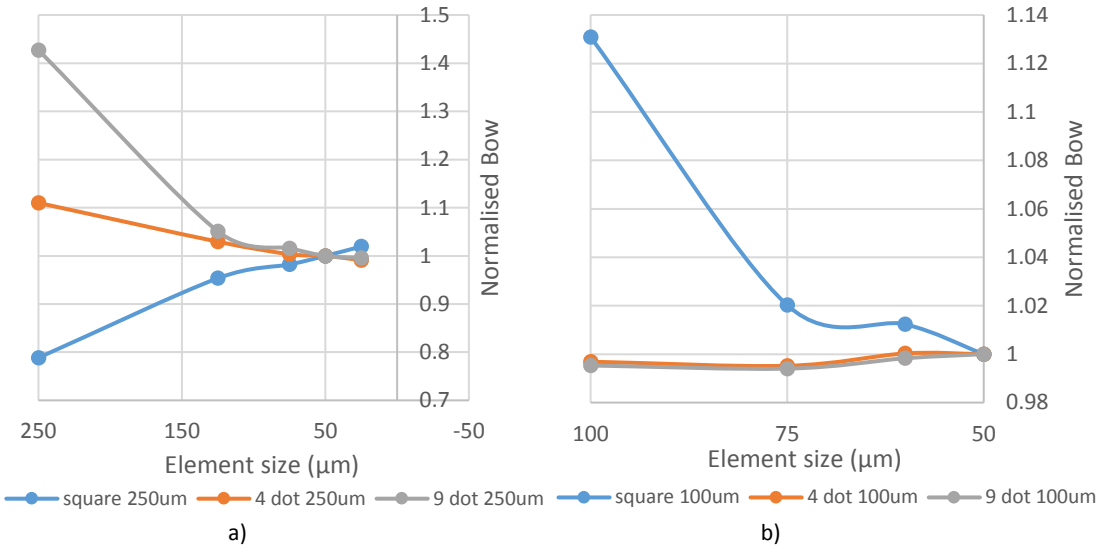
Figure 134 indicates that the shear mode frequency does not follow the same typical convergence-like trend, with larger changes in the outputs seen at lower element sizes and some oscillation in the results. Despite this, there is still only a small level of change present when the element size is changed. For the 250µm bond a maximum of 0.2% is observed when the element size is increased by 25µm, this is again experienced by the 9-dot bond, with the square shape again seeing the lowest change. For the 100µm bond a maximum change of 0.4% is seen for the 9-dot bond when the element size is increased to 60µm, and less than 0.9% when only a single element is used across the thickness (100µm element).



a) b)

Figure 134 - Normalised Shear Mode Frequencies for 250µm (a) and 100µm (b) thick bonds

Figure 135 shows the normalised bow against mesh size for the two bond thicknesses, and it is observed that this metric experiences the greatest level of change. This strong trend with element size was first identified in Chapter 4. Extremely large percentage changes are seen in the 250µm bond when only one element is used across the thickness, with a maximum of over 40% change for the 9-dot bond. This greatly reduces when more than two elements are used. However, a maximum change of ~2% is still experienced when the element size is reduced from 50µm to 25µm, this maximum occurs for the square bond. The dotted bonds experience a lower level of change, and this is seen across both bond thicknesses. For the 250µm thickness, the change is <1% (between 50 and 25µm elements) and <0.2% for the 100µm bond (60µm and 50µm elements), while the square bond experiences a change of ~1.25%. Due to the large changes seen in the bow for the thinnest bonds, possible errors need to be considered when comparisons are made later, particularly for the square bond shape.



a) b)

Figure 135 - Normalised Bow values for 250µm (a) and 100µm (b) thick bonds

5.4. Results

In this section the FE results, including die modal frequencies, die bow and the variation in die deformation are shown for various bond designs over temperature. With the effects of design parameters discussed.

5.4.1. Shape and Thickness effects at room temperature

The behaviour of the differing bond shapes over bond thickness is investigated. Figure 136 shows how the bounce mode frequency varies with thickness for the three differing bond shapes. It is observed that all the bond shapes experience similar behaviour over thickness, with the bounce mode increasing non-linearly with a decreasing thickness. This non-linear relationship is caused by three separate effects. Firstly, the bounce mode frequency equation (rearranging eq. 2.2) has a dependence of $\frac{1}{\sqrt{t}}$. Also, as the thickness is reduced the bond mass decreases, and finally, the stiffening effect due to the slenderness of the bond as described previously, where the apparent modulus tends towards the bulk modulus as the cross-sectional area to thickness ratio increases. For the most slender bonds, which are of most interest in MEMS devices, the apparent modulus effect dominates because for these bonds the bond mass becomes negligible compared to the mass of the die. As expected the square bond is the stiffest, and the 9-dot the most flexible. This is partly due to the greater area of the square bond, but is dominated by the differing relationships between thickness and shape factor, as shown in Figure 130. The 9-dot bond experiences the greatest relative change when the thickness is reduced from 1mm

to 0.1mm. This is because of the differing thickness to apparent modulus relationship. This causes the square bond to stiffen over a larger range of thicknesses, so the apparent modulus value at 1mm is already much greater than the basic elastic modulus value, whereas the 9 dot is not greatly stiffened at 1mm thick but then quickly increases to the bulk modulus as the thickness is reduced, see Figure 131.

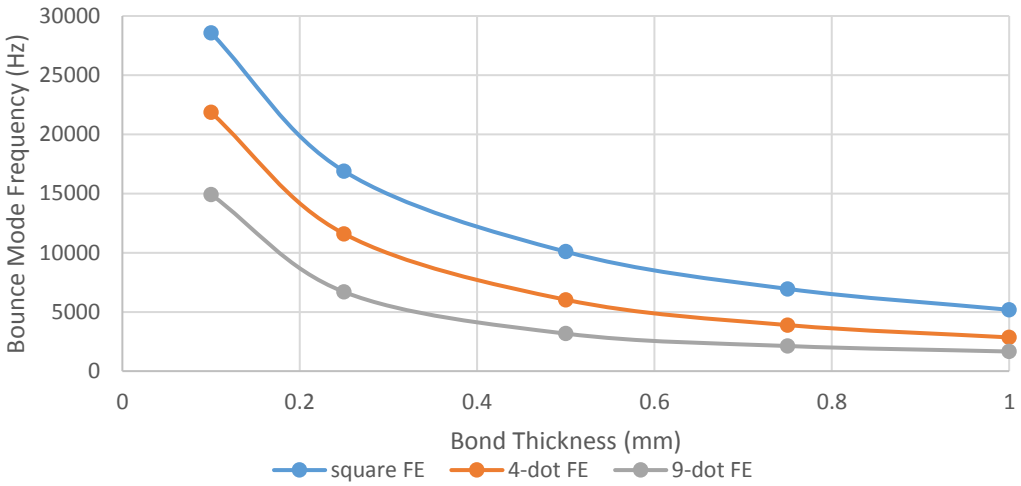


Figure 136 - Bounce Mode Frequency trends with frequency of the various bond shapes at room temperature

Figure 137 shows the change in the shear mode frequency with thickness. Like the trend described for the bounce mode, the modal frequency increases non-linearly with decreasing thickness. In this case, there is no stiffening effect due to the slenderness (shear modulus is constant) and therefore this non-linear relationship is solely due to the dependence on $\frac{1}{\sqrt{t}}$ and the effect of reducing bond mass with thickness. The lack of any stiffening effect means that, unlike the bounce mode, the percentage change of the modal frequency, for the thicknesses tested, is very similar across the different bonds from 1mm to 0.1mm.

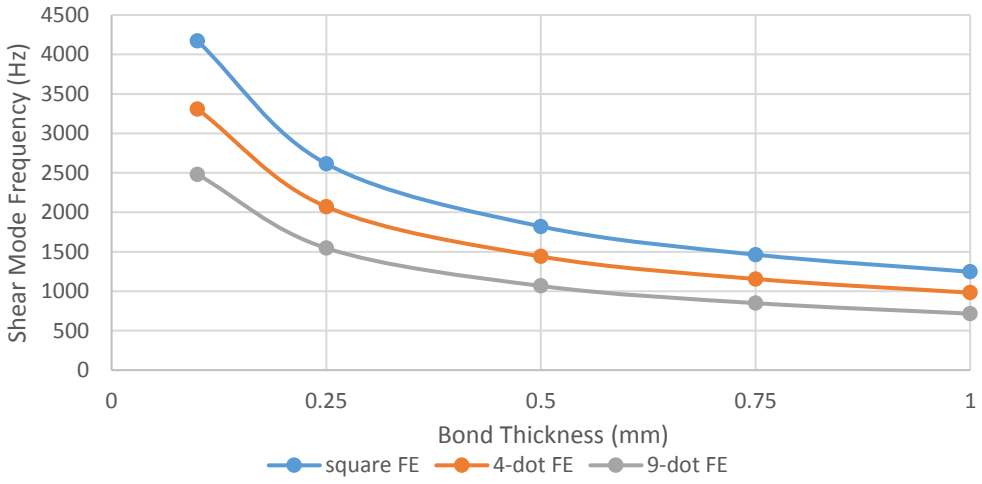


Figure 137 - Shear Mode Frequency trends with thickness of the various bond shapes at room temperature

Figure 138 shows the die bow, defined as the height difference between the centre and corner of the die, variation with bond thickness. It is clear that for the majority of thicknesses the dotted arrangements have significantly lower bow magnitudes than the square bond, and that these arrangements have much more consistent values across various thicknesses. The two dotted bonds have a negative bow value for all thicknesses. A negative bow value here represents a convex top surface of the die, and a positive value a concave shape. For the square bond the induced die curvature reduces with decreasing bond thickness, contrary to conclusions in the literature that thicker bonds reduce the stresses in the bond [46] [41]. This could be due to the large CTE mismatch with the adherends, as mentioned by Rusanen and Torkelli [44]. The square bond also undergoes a change in sign when the bond thickness is reduced from 0.25mm to 0.1mm, suggesting that there is a thickness at which there is zero curvature of the die. It should be noted here that there were some convergence difficulties for the 0.1mm bonds, particularly the square shape, as discussed previously. The 9-dot arrangement has a lower curvature magnitude than the 4-dot at all thicknesses, and it seems that further bond discretisation has led to further improvements in the stresses induced, although these are small when compared to the reductions from the square bond to 4-dot. The 9-dot bond also follows the expected trend of increasing curvature, due to larger bond stresses, with reductions in bond thickness. The 4-dot bond partly follows this trend but appears to reach an optimal bond thickness where minimal curvature is experienced, but then curvature increases when the thickness is increased or decreased away from this value.

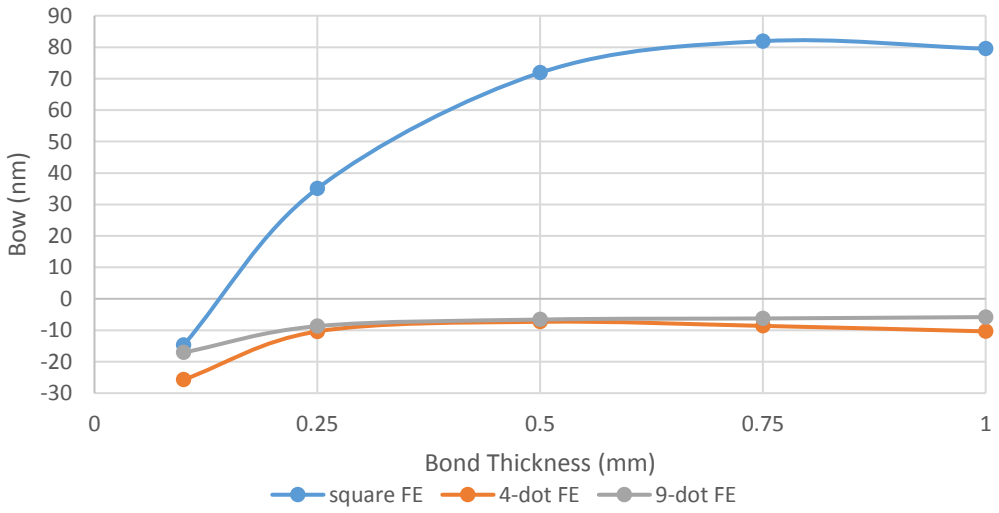


Figure 138 - Die Bow trends with thickness of the various bond shapes at room temperature

Figure 139 shows the location of deformation probes used to assess the deformation profile across the die surface around a circular path about the centre of the die. Results for each bond shape at differing thicknesses are shown in Figure 140 to Figure 142. Figure 143 compares the variations observed for the different bond shapes for typical die bond thicknesses of 100 and 250µm.

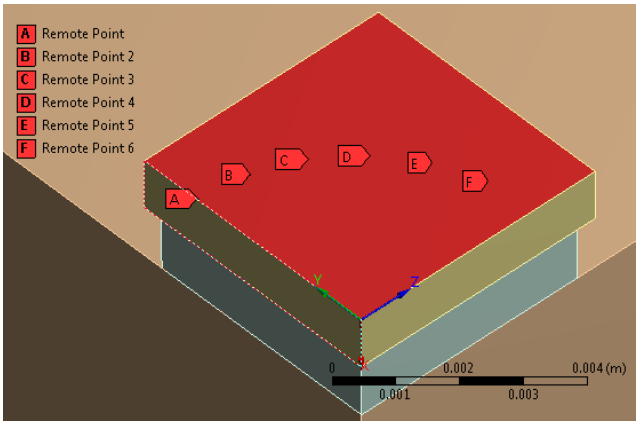


Figure 139 - Deformation probe locations used in curvature variation, follow a circular path with 7.5mm diameter about the centre of the die at 15° intervals

Figure 140 shows the deformation variation, around the path shown in Figure 139, for square bonds of various thicknesses at ambient temperature. It can be seen that the thickest bonds, 1mm and 0.75mm thick, experience the largest curvature, and that the curvature reduces with decreasing thickness values. It can also be seen that the magnitude of curvature is proportional to the level of deformation variation around the die, and that the deformation changed sign when the thickness is reduced from 0.25 to 0.1mm, representing a change from a concave to convex profile of the dies top surface.

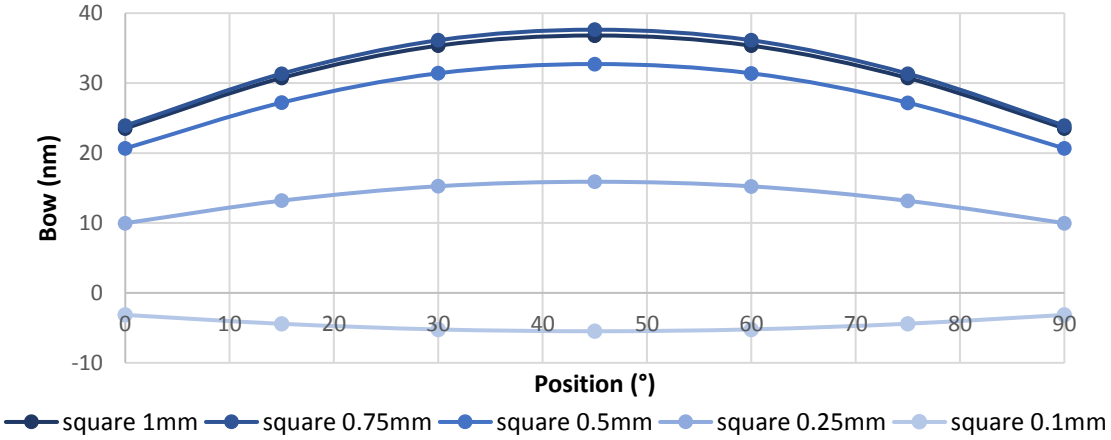


Figure 140 - Height Variation of die top surface (compared to die centre) 7.5mm circle around centre of die for square bond of various thicknesses

Figure 141 shows the deformation profiles for 4 dot bonds of various thicknesses. It is clear from these results that the variation around the die is proportional to the magnitude of curvature experienced. The 4-dot bond follows a more expected trend such that the curvature increases with bond thickness reductions. However, there is a limiting value where further increases above that thickness results in further curvature, although these increases are small. The 9-dot follows the trend more strictly with every decrease in thickness resulting in an increase in curvature. As with the other two bond shapes, a larger curvature results in a larger variation around the die.

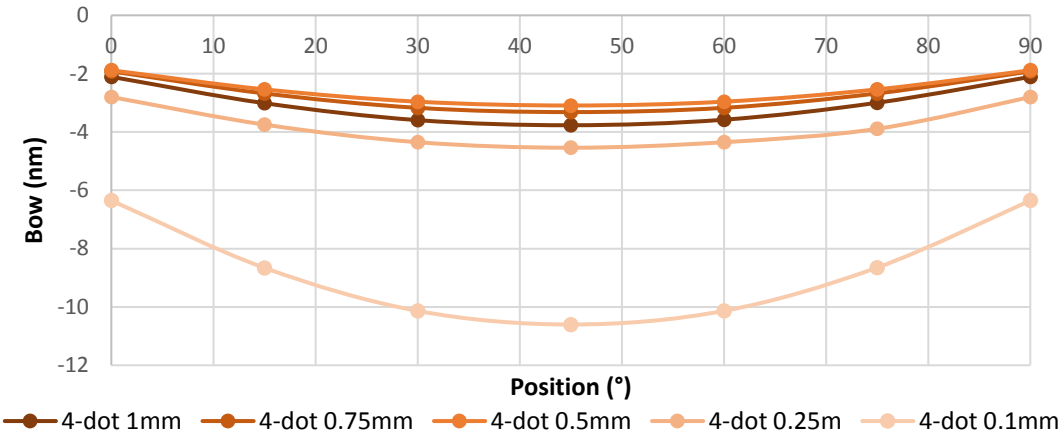


Figure 141 - Height Variation of die top surface (compared to die centre) 7.5mm circle around centre of die for 4-dot bond of various thicknesses

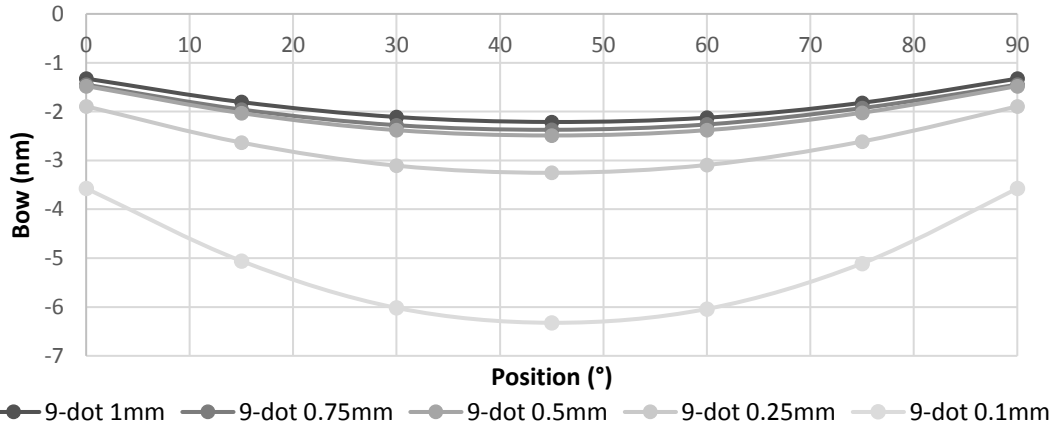


Figure 142 - Height Variation of die top surface (compared to die centre) 7.5mm circle around centre of die for 9-dot bond of various thicknesses

Figure 143 compares the deformation variation profiles of the thinnest bonds of each bond shape. These thicknesses are within the typical range used in MEMS devices. The bond shapes investigated do not seem to affect the level of variation occurring, and appear to be controlled by the magnitude of curvature experienced. For example, 4-dot and 9-dot bonds with the same curvature

magnitude are likely to have the same variation around the die, although they will have different thicknesses. The relative variation around the die is consistent across bond shapes, with 33.5-41.3% variation (of maximum curvature at 45°). The spread across bond shapes in relative variation reduces at lower thicknesses to 37.3-40.6% at the 0.1mm bond thicknesses. The 250µm thick square bond has the largest curvature and largest variation (and a different sign), followed by the 100µm 4-dot and 9-dot. The 100 µm square bond has improved curvature compared to the other bonds of the same thickness, but is worse than their thicker counterparts. The 9-dot 250µm bond has the lowest curvature and the lowest variation in deformation than any other bond investigated.

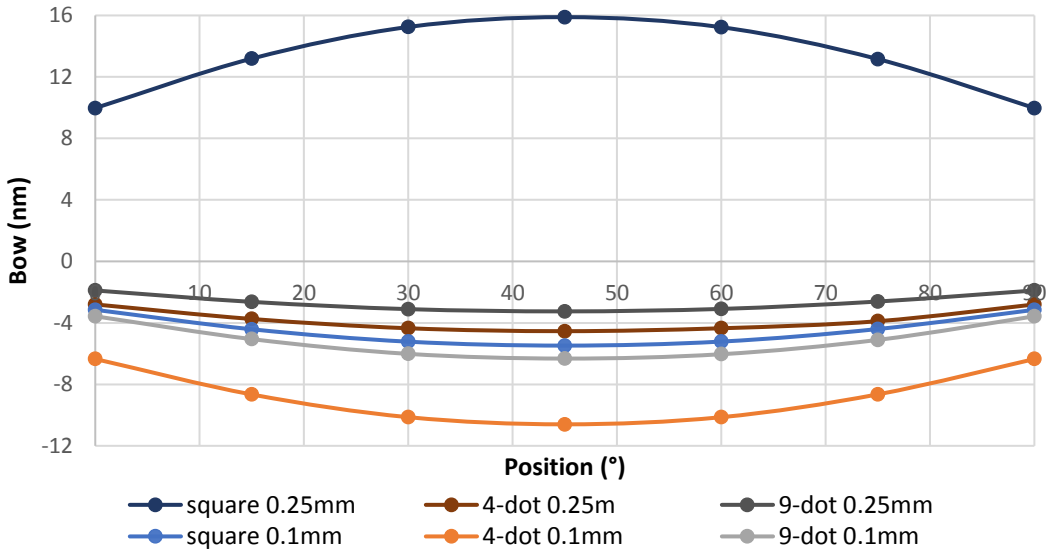


Figure 143 - Height Variation of die top surface (compared to die centre) 7.5mm circle around centre of die for various bond shapes of typical die bond thicknesses

5.4.1.1. Comparison with Empirical Slenderness Expressions

In this section the die modal frequency results from the FE modal are compared to the frequencies calculated using various moduli values, including the basic elastic modulus E (bond mass effects only), the apparent modulus E_a (bond mass and slenderness effects for incompressible bond), and the apparent modulus with compressibility correction E'_a (bond mass and slenderness effects for compressible bond). Figure 144 shows results for the various bounce mode frequencies for the three bond shapes and how they change with thickness. It is clear that there is a wide variation in the theoretical bounce mode frequencies when using the differing moduli values, highlighting the significance of the stiffening and the importance of an accurate modulus value. The significance of the stiffening is dependent on the shape factor. As mentioned previously the relationship between

thickness and shape factor varies for the differing bond shapes, but its effect is clear in Figure 144. This can be seen from the point at which the curves using E, E_a and E'_a diverge. With slenderness effects occurring when the E and E_a curves separate, in Figure 144 this point is only visible for the 9-dot arrangement, at ~1mm, as both the 4-dot and square bonds are already affected at 1mm thickness. When the E_a and E'_a curves diverge, the incompressibility assumption breaks down and to accurately predict the apparent modulus and therefore bounce mode frequency, correction using the bulk modulus is required. Once again this occurs above 1mm thicknesses for the square shape, at 1mm thickness for the 4-dot and at below 0.5mm thickness for the 9-dot bond. Considering that the maximum bond thickness used of interest is 250microns, to accurately predict the stiffness of the bond compressibility effects must be considered. When these effects are considered there is very good agreement with the FE results. There is a slight offset for the square bond, which could be due to the theoretical model using a perfectly square bond geometry, whereas the FE geometry has rounded corners, having radius 1mm. The other difference between the FE and theoretical models that could cause this offset, is the presence of the bonding stress, which was seen in chapter 4 to cause significant changes in the bounce mode frequency and is expected to be most significant in the square bond due to the greater curvatures observed.

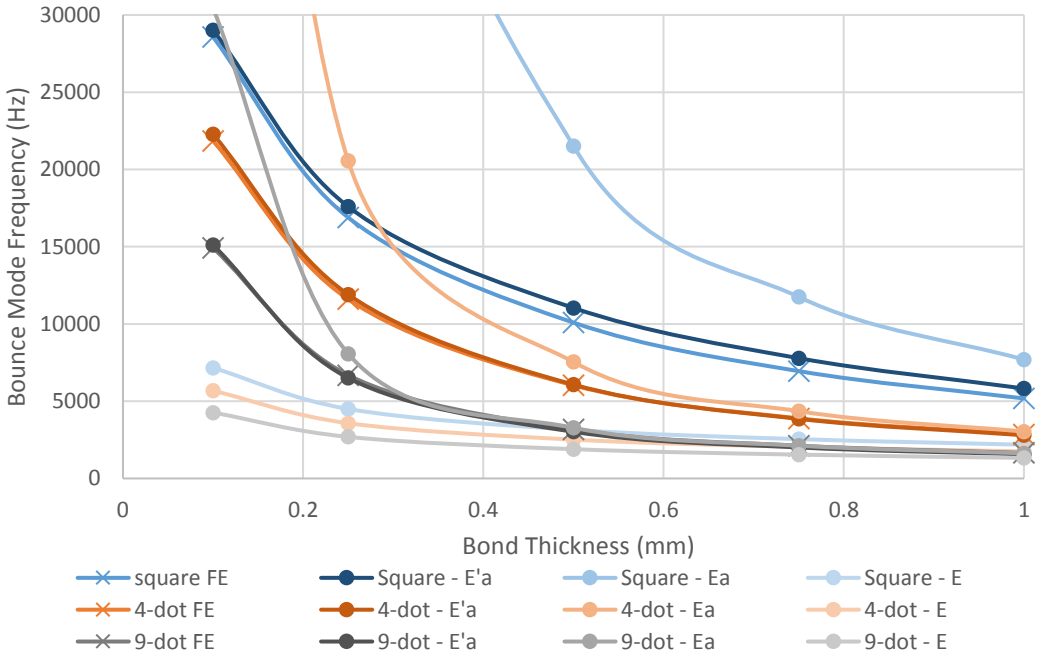


Figure 144 - Comparison of Bounce Mode Frequencies for various bond shapes over thickness, using various Modulus values, E – Elastic modulus, E_a – Apparent modulus, E'_a – Apparent modulus with compressibility correction

Figure 145 shows results for the shear mode frequencies calculated using FE and theoretically using a constant shear modulus value, with no stiffening effect due to the slenderness of the bond. It can be seen that there is very close agreement between the results. There is some disagreement at large thicknesses ~1mm which is likely to be present for larger thickness bonds. This is because of the single-sided bond which results in a non-perfect shear motion in which there is an element of rocking that will become more significant the thicker the bond becomes. This can be compensated for, however, for the thicknesses of bond used in MEMS devices, it is unnecessary because the rocking component is negligible.

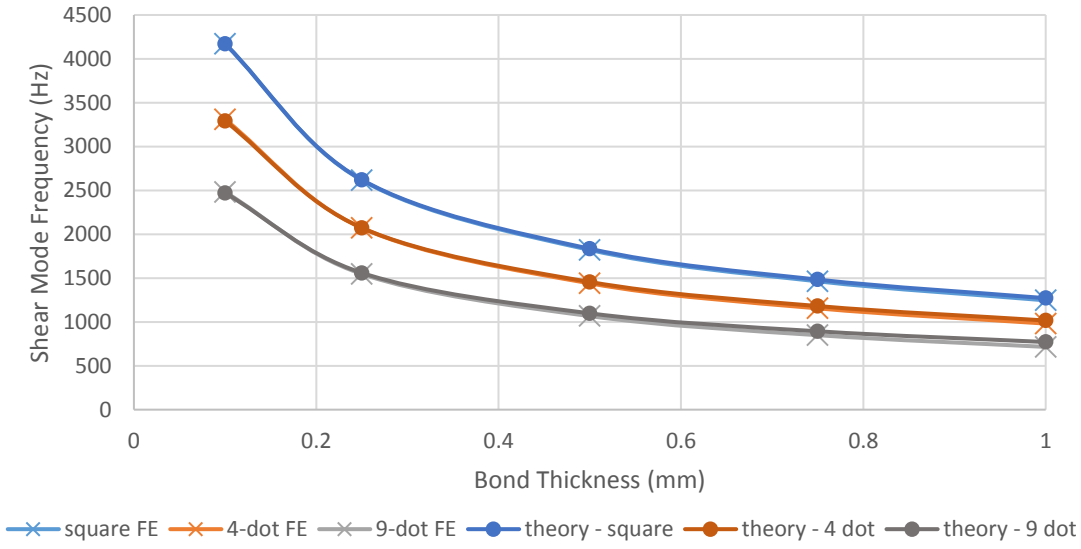


Figure 145 – Comparison between FE and theoretical Shear Mode Frequencies for various bond shapes over thickness

5.4.2. Thickness effects as a function temperature

In this section the thickness effects as a function of temperature are assessed for each bond shape individually. The die frequencies and bow are calculated over temperature, and their absolute values, change and normalised change over temperature are analysed. The normalised outputs are normalised using the output at ambient temperature. The trends identified are solely caused by geometrical effects given that the material properties are kept constant over the temperature range.

5.4.2.1. Bounce Mode

Figure 146, Figure 147 and Figure 148 show the bounce mode frequency, both absolute and normalised over temperature for a square, 4-dot and 9-dot bond of differing thicknesses respectively. It can be seen that similar trends occur with all bonds softening with increasing temperature, seen in

the graphs as a decreasing bounce mode frequency at increasing temperatures. Greater absolute frequency changes are seen for thinner bonds, showing that the thinnest bonds stiffen/soften more over temperature due to the higher stress levels experienced. For the normalised trends it can be seen that the thickest bonds undergo the lowest relative change, similar to that seen in the absolute trends, with the two thinnest bonds for all bond shapes experiencing over ±2% change in bounce mode frequency over the temperature range. This change is relatively linear with temperature, implying that the compressive/tensile stress effects induced in the bond are linearly proportional to temperature change. Temperature dependent material properties would change this relationship, but for the thinnest bond, 0.1mm thickness, it is seen that its relative change over temperature drops below that of the next thinnest, 0.25mm thick, for all bond shapes. This change in behaviour appears to be linked to the shape factor and apparent modulus effects. Firstly, the absolute modal frequency is much greater for the thinner bonds than for the thicker bonds given the stiffening effect discussed previously, and therefore the frequency change required to achieve the same relative change is much greater. Secondly, the different bonds experience different changes in their normalised trends when their thickness is varied, as well as experiencing this drop in relative change at differing thicknesses. The thickness at which this drop in rate of relative change occurs and the changes in this rate over thickness appear to be dependent on the relationship between shape factor and thickness for the bond shape.

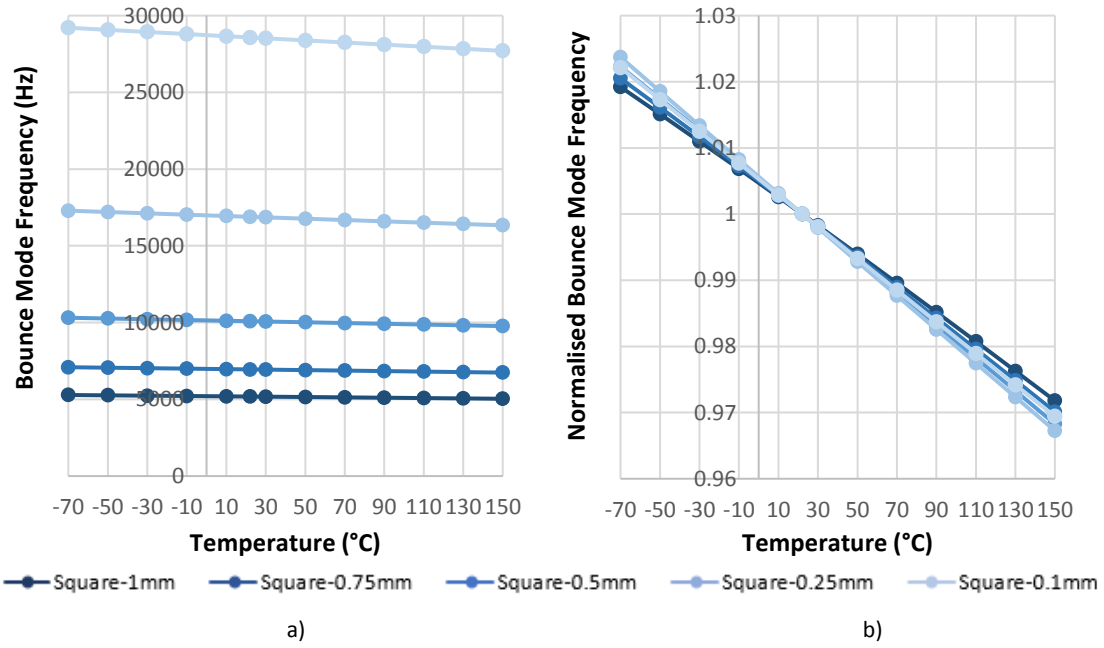
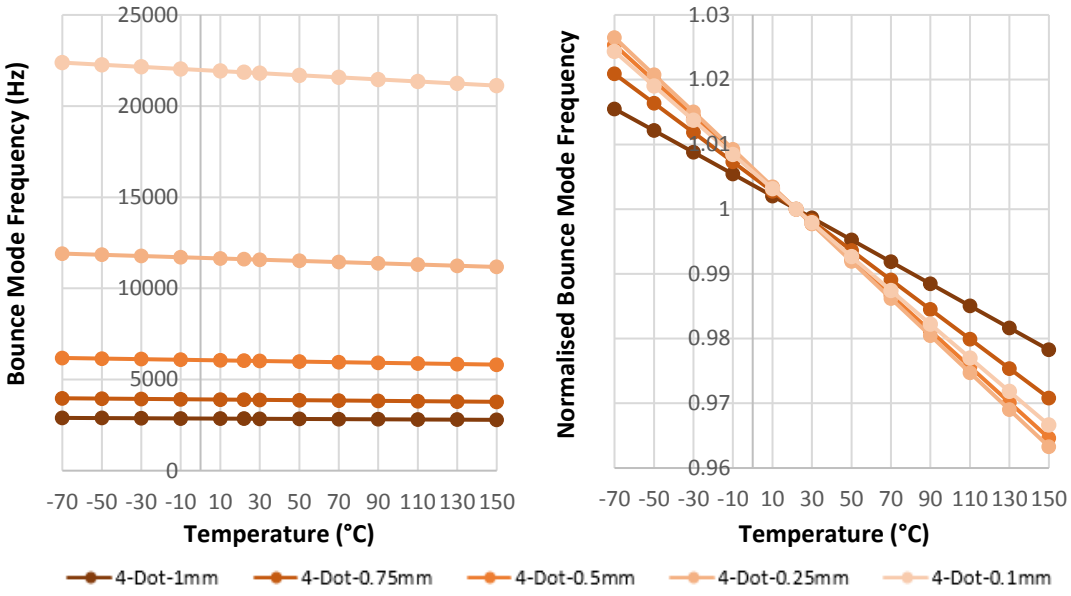
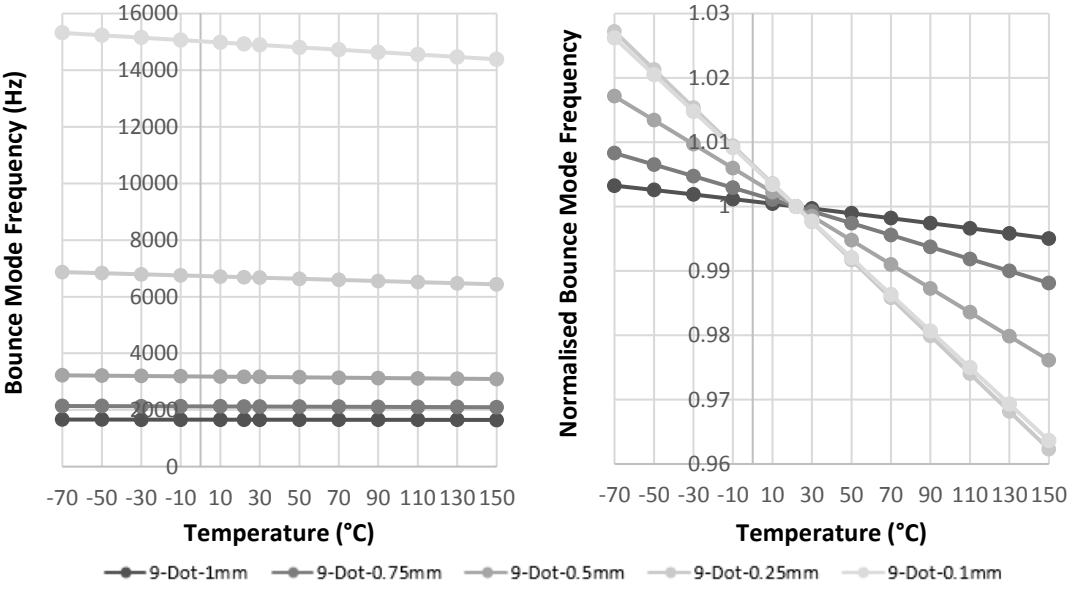


Figure 146 - Bounce mode frequency variation, a) magnitude and b) normalised, over temperature for a square bond of varying thickness



a) b)

Figure 147 - Bounce mode frequency variation, a) magnitude and b) normalised, over temperature for a 4-dot bond of varying thickness



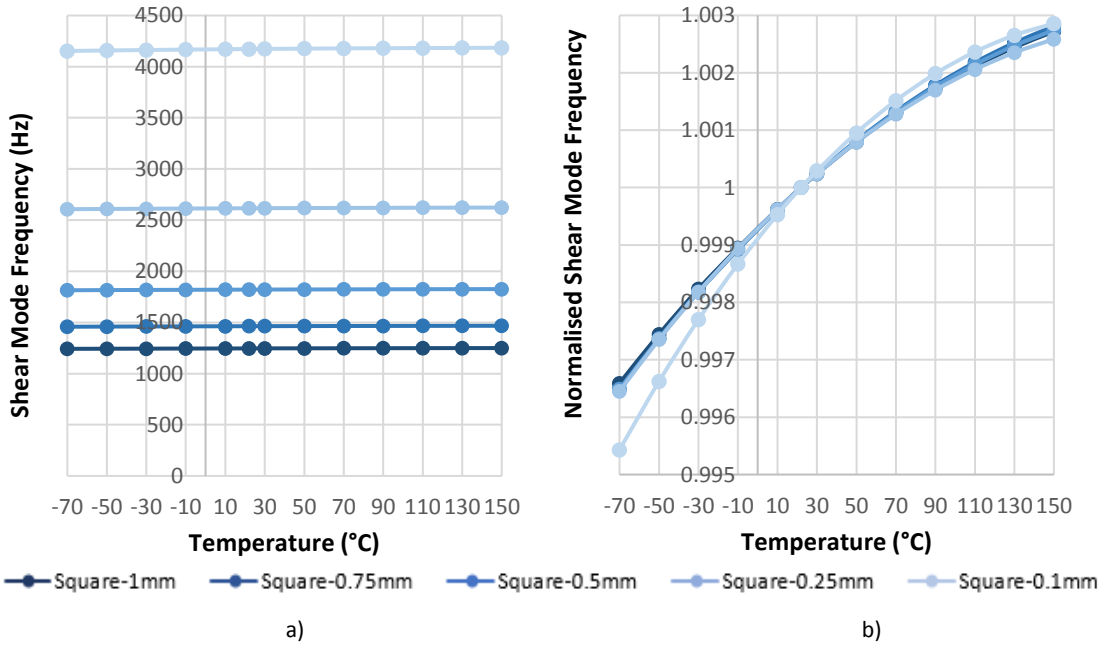
a) b)

Figure 148 - Bounce mode frequency variation, a) magnitude and b) normalised, over temperature for a 9-dot bond of varying thickness

5.4.2.2. Shear Mode

Figure 149, Figure 150 and Figure 151 show the shear mode frequencies, both absolute and normalised, over temperature for square, 4-dot and 9-dot bonds of varying thickness respectively. The changing stress has a different effect on the shear mode than observed for the bounce mode, with softening behaviour observed with decreasing temperature. The normalised behaviour is more complex than that seen for bounce, with a non-linear relationship observed, the level of non-linearity

varies with thickness and bond shape. Firstly, the level of change is much lower in the shear mode with the maximum normalised change less than ±0.5%. For a decrease in temperature away from the bonding/stress-free temperature, it is seen that the rate of relative change increases with greater temperature changes, and this rate of increase becomes greater for thinner bonds. However, in general, thickness reductions do not greatly change the magnitude of normalised change observed over temperature, with the square, 4-dot and 9-dot experiencing between 0.61-0.74%, 0.68-0.79% and 0.80-0.89% over the tested thicknesses respectively. The largest normalised change for the square bond occurs for the 0.1mm thickness. Omitting this data point the square bond only experiences a normalised change variation of between 0.61-0.63% over the remaining thicknesses. This sudden change in behaviour involving a significant increase in normalised change and non-linearity, indicates a differing thermal behaviour of concave and convex die curvature. The normalised change over temperature of a convex shaped die is greater than for concave, even for convex surfaces of significantly lower magnitudes of curvature. Thickness reductions increase the non-linearity observed and therefore the shape of the temperature dependence curve. These trends between shear mode frequency and temperature indicate that the induced shear stress effect becomes more significant the larger they are, i.e. the further the temperature is from the stress-free temperature of 150°C.



a) b)

Figure 149 - Shear mode frequency variation, a) magnitude and b) normalised, over temperature for a square bond of varying thickness

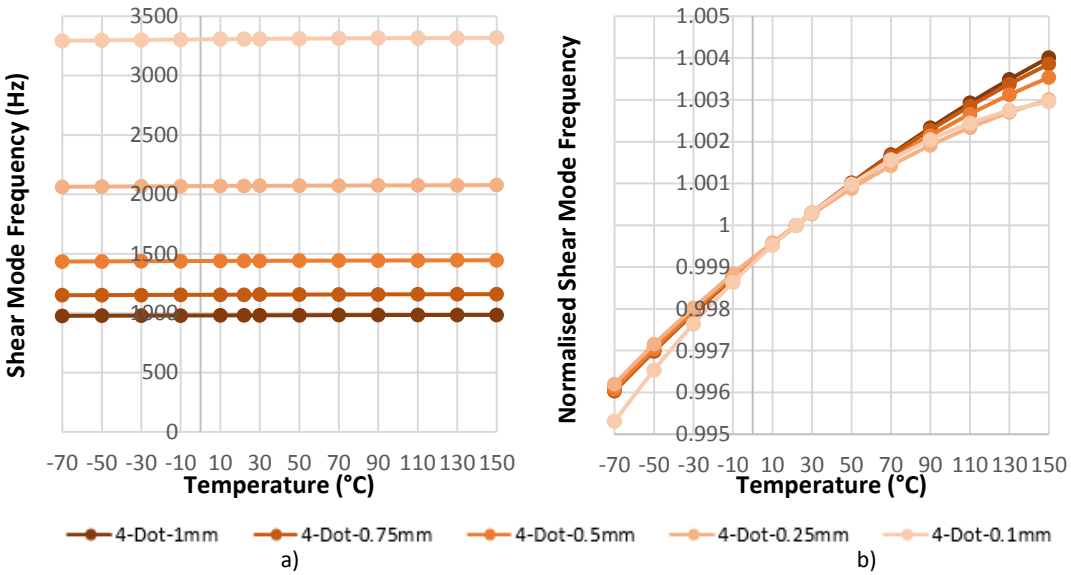


Figure 150 - Shear mode frequency variation, a) magnitude and b) normalised, over temperature for a 4-dot bond of varying thickness

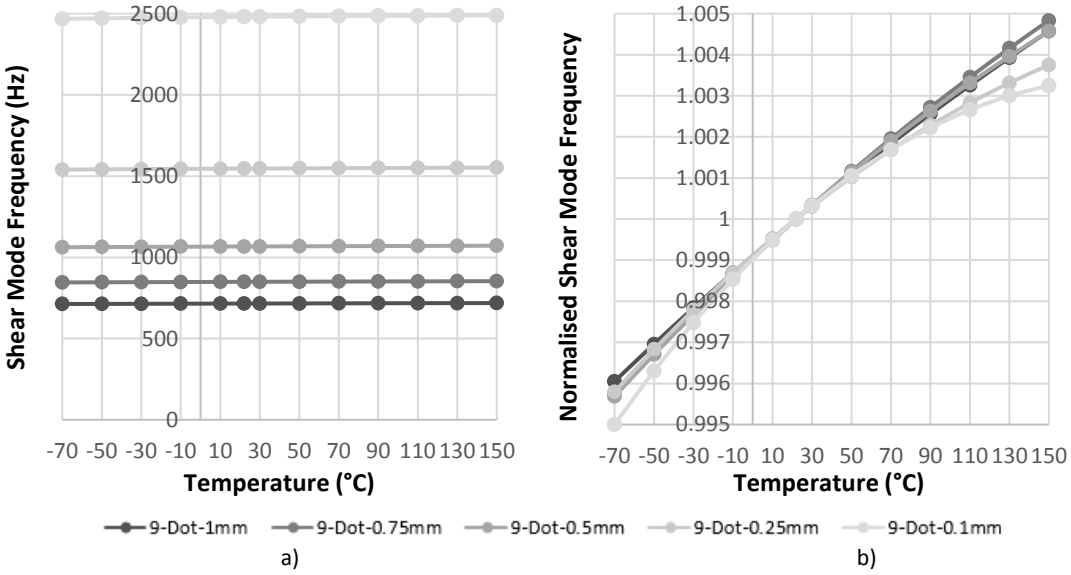


Figure 151 - Shear mode frequency variation, a) magnitude and b) normalised, over temperature for a 9-dot bond of varying thickness

5.4.2.3. Die Bow

Figure 152, Figure 153 and Figure 154 show the die bow variation and normalised variation over temperature for bonds of different thickness bonds for square, 4-dot and 9-dot bonds respectively. It is observed that all bonds have zero curvature at the stress-free temperature (bonding temperature) of 150°C, and that the bow increases in magnitude as the temperature decreases away from this value. The resulting bows and their change over temperature and thickness are highly dependent on the shape of the bond. Square bonds as mentioned earlier induce a concave top surface at larger thicknesses, and the magnitude reduces with thickness until experiencing a sign change at a thickness of approximately

0.15mm. Whereas the 4-dot bond induces a convex top surface, with the bow magnitude reducing with thickness down to a thickness of 0.5mm before increasing greatly with further thickness reductions. The 9-dot bond is more consistent with the bow magnitude continually increasing with thickness reductions, and these bow increases become greater with each drop in thickness. The normalised bow graphs do not show much difference in behaviour over temperature for the varying thicknesses, with similar rates of change observed for all thicknesses of the same bond shape and only slight changes in non-linearity. The exception to this is the 0.1mm square bond which experiences a more significant slowing of the rate of change towards the lowest temperatures. This again could be an effect of the convergence difficulties or showing the varying temperature behaviour of a concave die shape.

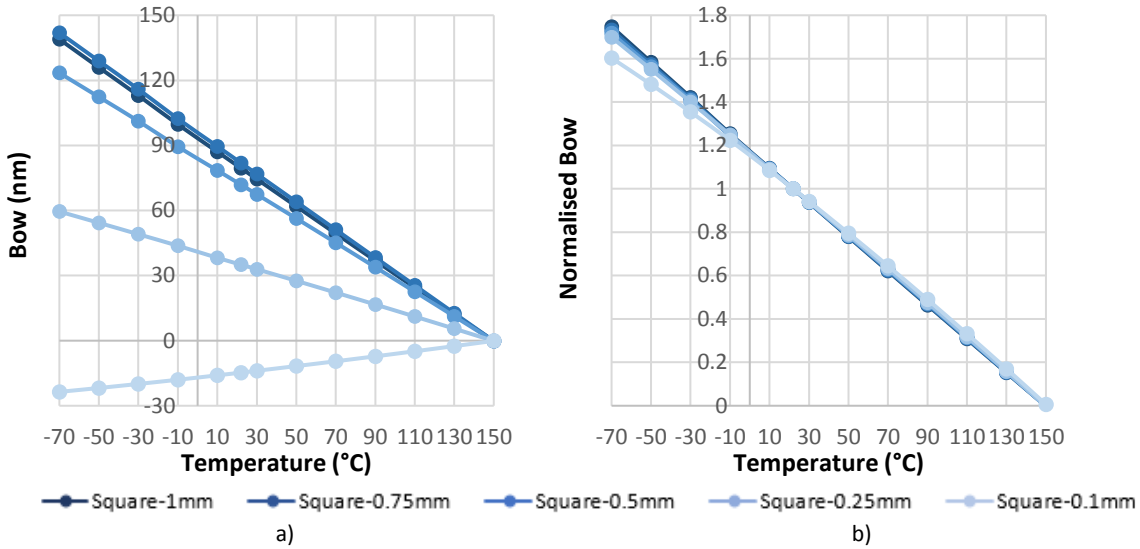


Figure 152 – Die bow variation, a) magnitude and b) normalised, over temperature for a square bond of varying thickness

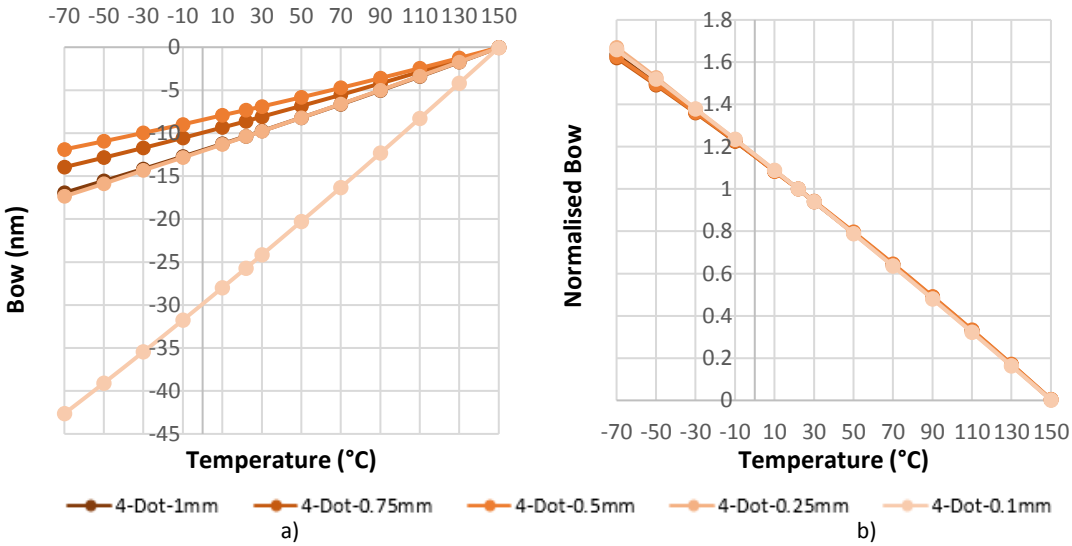


Figure 153 – Die bow variation, a) magnitude and b) normalised, over temperature for a 4-dot bond of varying thickness

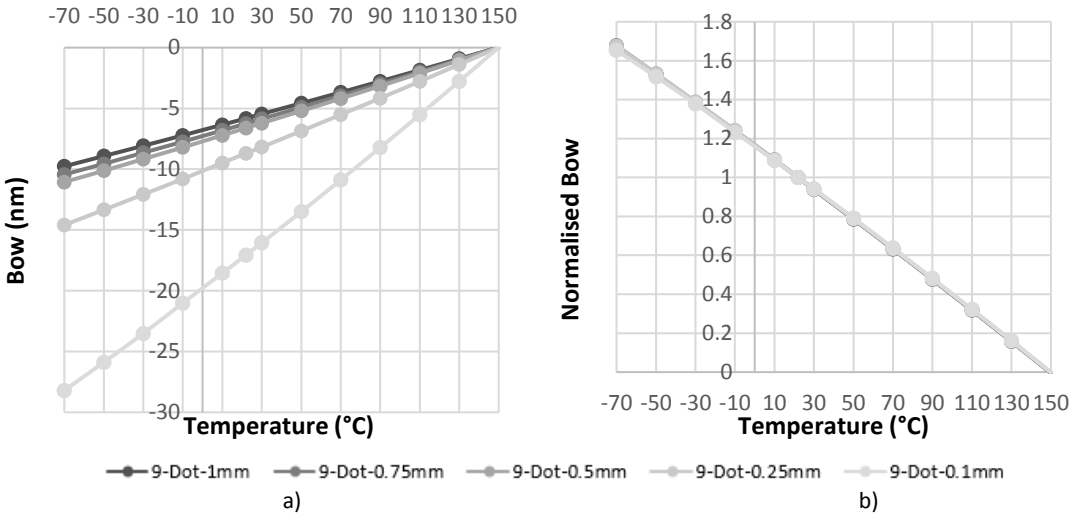


Figure 154 – Die bow variation, a) magnitude and b) normalised, over temperature for a 9-dot bond of varying thickness

5.4.3. Shape effects as a function of temperature

In this section the bond shape effects as a function of temperature are assessed for different bond thicknesses individually. The die frequencies and bow are observed over temperature, and their absolute values, change and normalised change over temperature are analysed. The outputs are normalised using the output at ambient temperature. The trends identified are solely caused by geometrical effects given that the material properties are kept constant over the temperature range.

5.4.3.1. Bounce Mode

Figure 155, Figure 156 and Figure 157 show the bounce mode frequency variation, both absolute and normalised over temperature for all bond shapes for 1mm, 0.5mm and 0.1mm bond thicknesses respectively. It can be seen that the absolute frequency changes occurring over the temperature range within each bond shape are proportional to their bounce mode frequency. For example, it has been shown that the square bonds have the highest bounce mode frequency and 9-dot bonds have the lowest due to the square bond's greater area and slenderness stiffening effects, and because of this undergo the greatest frequency changes over temperature for all thicknesses. However, in the normalised trends differing behaviour is observed. It can be seen that the bonds experiencing the greatest and lowest normalised changes over the temperature range vary for differing bond thicknesses. The order of largest to smallest normalised change for 1mm bonds is square, 4-dot, 9-dot. For 0.5mm bonds the order changes to 4-dot, square, 9-dot, and for 0.1mm bonds it changes again to 9-dot, 4-dot, square. The bounce mode frequency is dependent on the bond stiffness in

compression/tension, therefore Young's modulus, or in the case of slender bonds the apparent Young's modulus. It has been shown that the apparent Young's modulus is controlled by the bond material and geometry or shape factor. The material is consistent across differing bonds, but the shape factor varies, and it was seen that this causes differing apparent modulus trends over thickness for the different bond designs in Figure 131. Therefore, it is reasonable to assume that stiffening effects observed over temperature, which are associated with geometrical changes and stress within the bond, are also closely linked to the slenderness stiffening effects.

In Figure 131, it was seen that all bonds tend towards a limiting apparent modulus equal to the Bulk modulus of the bond material. However due to differences in their shape factors, they experience different stiffening rates. For example, the square bond begins stiffening at a larger thickness, but at a slower rate compared to the 9-dot bond which stiffens at a much lower thickness but at a much quicker rate. This effect can account for the changing relationships of normalised bounce frequency change between the bond shapes for different bond thicknesses. For a 1mm bond thickness, the rate of apparent modulus change with thickness is largest for a square bond and therefore the changing deformation state over temperature has the greatest effect on this bond shape. At 0.5mm bond thickness, the 4-dot bond is experiencing the greatest rate of E'_a change and likewise at 0.1mm thickness, the 9-dot bond experiences the highest rate of change, agreeing with the normalised trends observed over temperature for these thicknesses. The Bounce mode frequency trends for all bond shapes and thicknesses are relatively linear with temperature change.

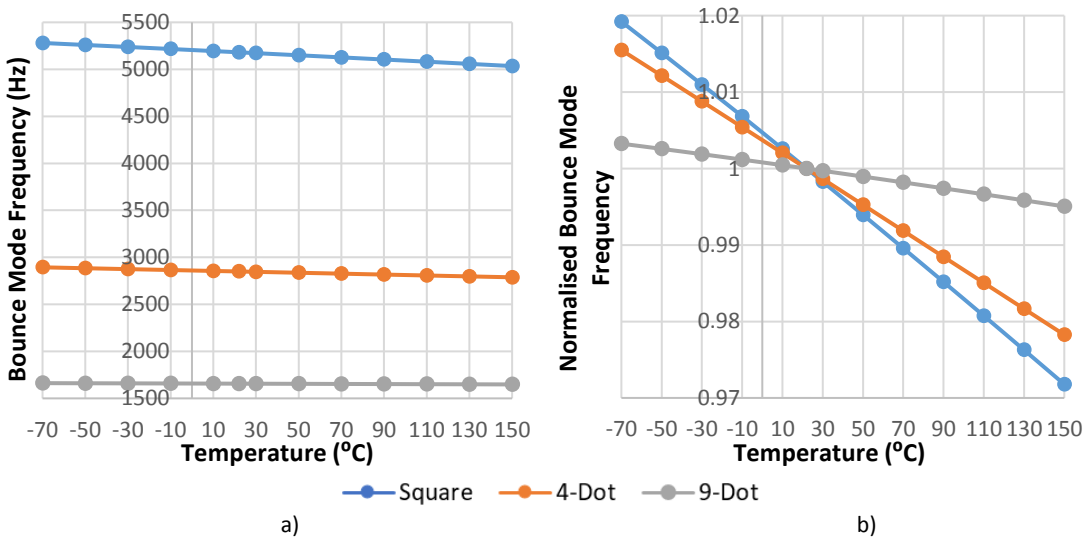
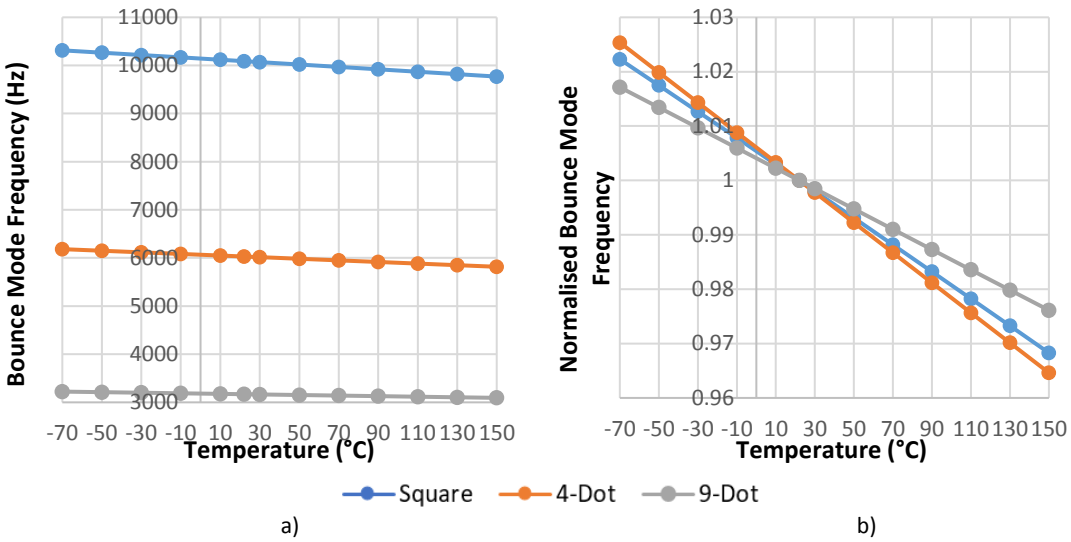
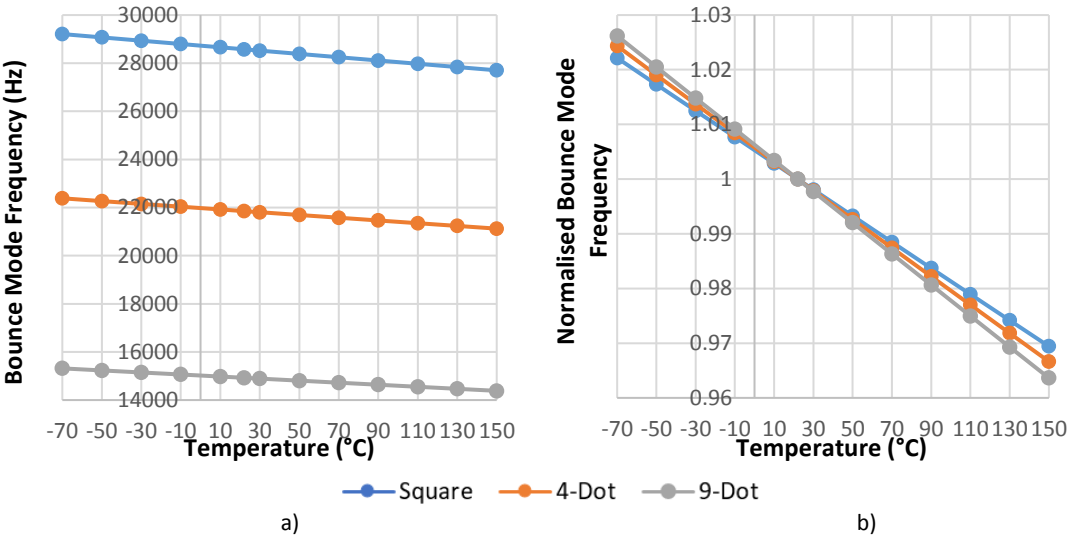


Figure 155 - Bounce mode frequency variation, a) magnitude and b) normalised, over temperature for a 1mm thick bond of varying shape



a) b)

Figure 156 - Bounce Mode Frequency variation, a) magnitude and b) normalised, over temperature for a 0.5mm thick bond of varying shape



a) b)

Figure 157 - Bounce mode frequency variation, a) magnitude and b) normalised, over temperature for a 0.1mm thick bond of varying shape

5.4.3.3. Shear Mode

Figure 158, Figure 159 and Figure 160 show the shear mode frequency, both absolute and normalised over temperature for all bond shapes for 1mm, 0.5mm and 0.1mm bond thicknesses respectively. It can be seen that the bond shapes have a consistent relationship with the normalised shear frequency changes occurring over the temperature range, with the 9-dot bond experiencing the greatest and the square bond the lowest change for all thicknesses of bond. It was shown earlier that the shear mode frequency changes with thickness are due to the reduced bond mass and $\frac{1}{\sqrt{t}}$ dependence, and are not dependent on the bond's shape factor, like the bounce mode. The consistency between the normalised change trends observed here could be a further indication that the varying

trends for bounce at differing thickness were caused by the dependence on the apparent modulus changes with thickness. The stiffening seen with increasing temperature, although relatively small, is non-linear, and it was already said that this non-linearity increases with reductions in bond thickness. However, it can be clearly seen in these figures that the level of non-linearity and the increase observed over thickness vary with bond shape. At thicker bonds, it is evident that the shear mode frequency trends for square bonds over temperature suffer from the greatest level of non-linearity while 9-dot the lowest. However, for the 0.1mm bond all bond shapes have a similar level of non-linearity in their shear mode frequency variation over temperature, showing that the 4-dot and, more so the 9-dot bonds suffer from greater increases in non-linearity compared to the square bond shape.

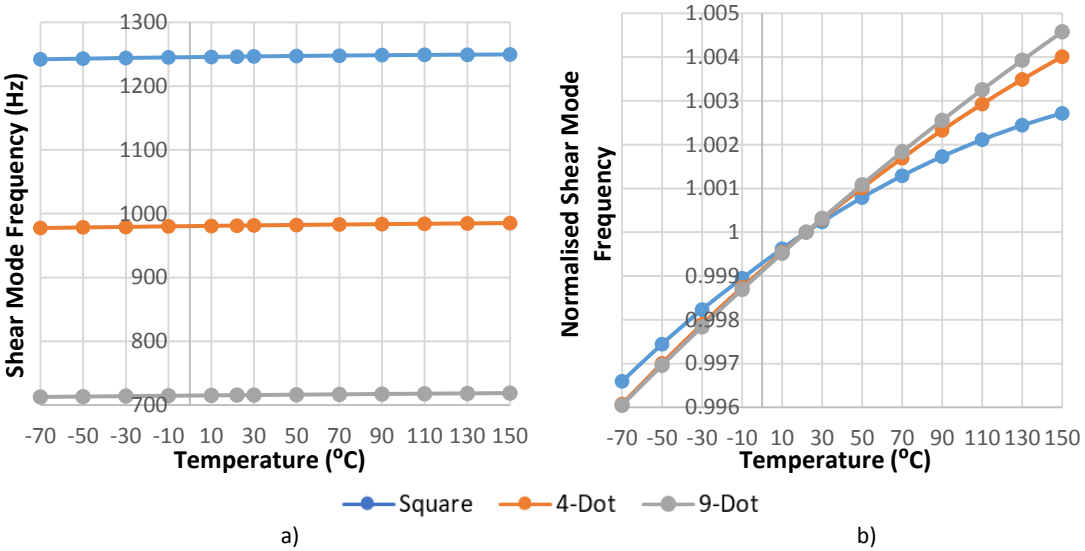


Figure 158 - Shear mode frequency variation, a) magnitude and b) normalised, over temperature for a 1mm thick bond of varying shape

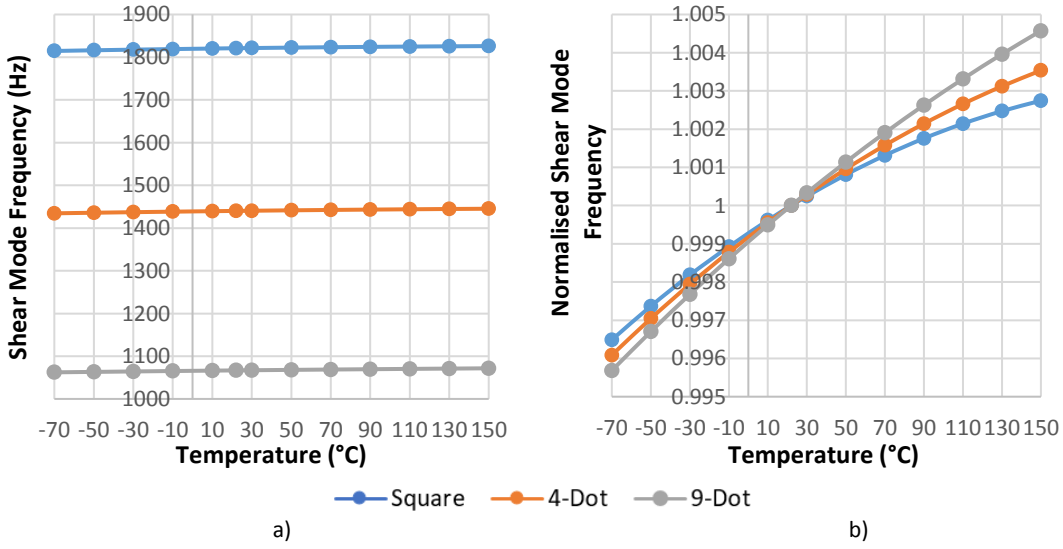
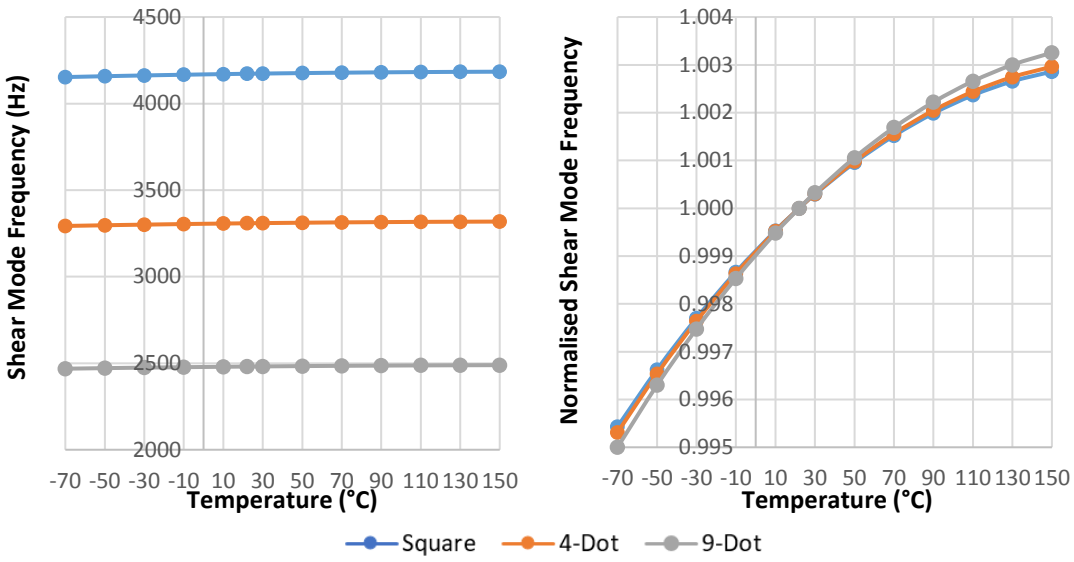


Figure 159 - Shear mode frequency variation, a) magnitude and b) normalised, over temperature for a 0.5mm thick bond of varying shape



a) b)

Figure 160 - Shear mode frequency variation, a) magnitude and b) normalised, over temperature for a 0.1mm thick bond of varying shape

5.4.3.3. Die Bow

Figure 161, Figure 162 and Figure 163 show the die bow variation, both absolute and normalised over temperature for all bond shapes for 1mm, 0.5mm and 0.1mm bond thicknesses respectively. The general bow trends were discussed in Section 6.4.1, where it was found that the dotted bonds induced much lower bows than the square bond, with 9-dot consistently lower than the 4-dot bond. However, it was also seen that the square bond experienced a significant change at the lowest bond thickness, at which the bow changed sign, representing a shift from a concave to convex surface curvature. The convex bow observed for a square bond at this 0.1mm thickness was lower than both the dotted bonds. However, it was also discussed that there were some possible convergence issues with the thinnest bond. It can be seen in the figures that the bow trends over temperature are approximately linear, with slight slowing of the curvature rate at greater temperature changes from the stress-free temperature of 150°C. This non-linearity could link to the non-linearity observed in the shear mode over temperature, as it is reasonable to assume that die curvature would affect the shear mode frequency due to the associated stresses in the bond. The normalised trends for each bond shape are similar to one another at all thicknesses, with agreement improving at reduced thicknesses.

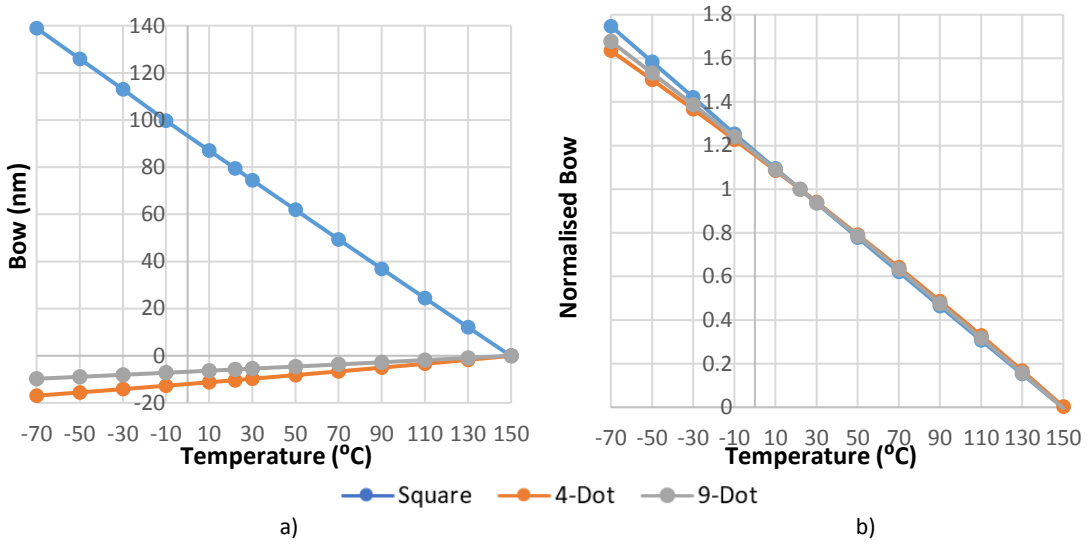


Figure 161 – Die bow variation, a) magnitude and b) normalised, over temperature for a 1mm thick bond of varying shape

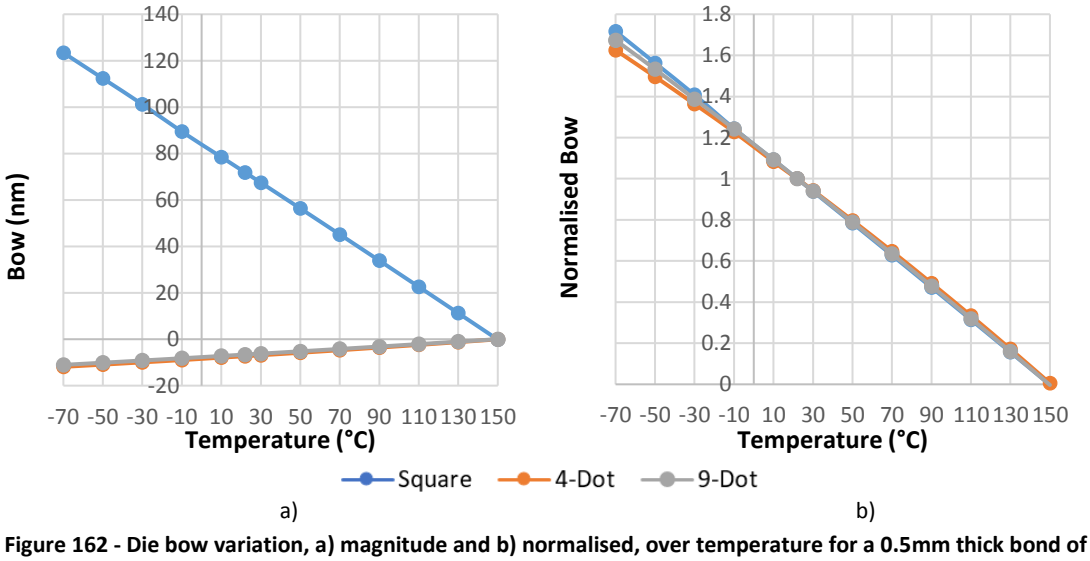


Figure 162 - Die bow variation, a) magnitude and b) normalised, over temperature for a 0.5mm thick bond of varying shape

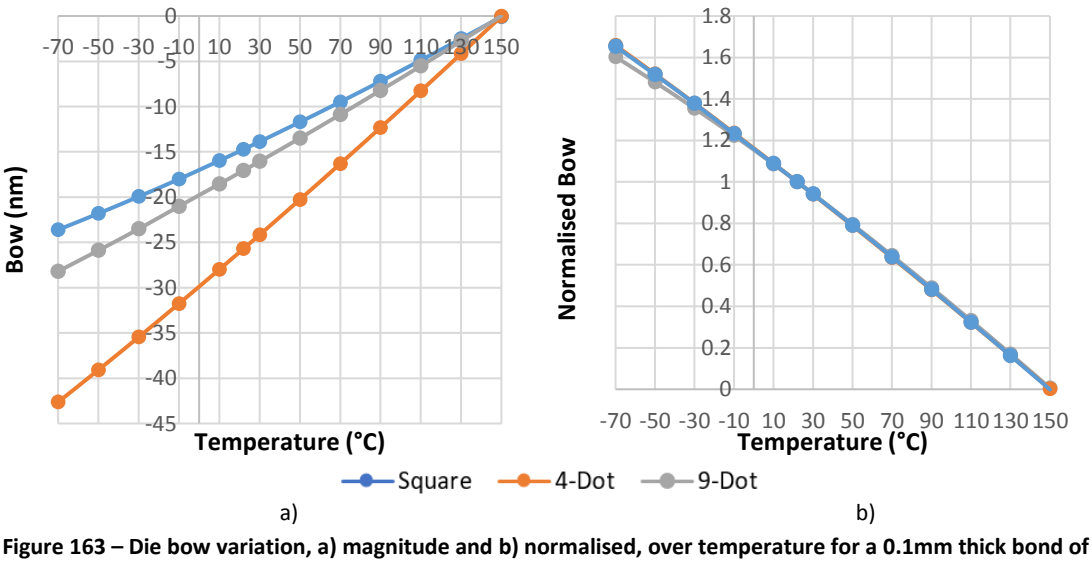


Figure 163 – Die bow variation, a) magnitude and b) normalised, over temperature for a 0.1mm thick bond of varying shape

5.5. Conclusions

The objective of this chapter was to investigate the effects of differing design parameters on the translational mode frequencies and die bow, in an effort to identify specific design features to reduce performance changes over time and temperature. This was to be achieved by identifying bonds with the lowest absolute and normalised trends over temperature, as well as inferring lower change over time by the lowest absolute die bow reducing the scope for viscoelastic mechanisms such as creep to occur.

The key bond design parameters were discussed, including thickness and bond shape and formed the main focus of the investigation. This included explanations of the term slenderness and its measure, shape factor, and how this impacts the stiffness of the bond leading to definitions of apparent modulus and its behaviour with reducing thickness. It was shown that the slenderness stiffening effect could vastly alter the stiffness, and that use of the apparent modulus is important. It was shown that to accurately estimate the apparent modulus of a slender bond, it is important to understand the compressibility of the bond material and therefore know an accurate value of Poisson's ratio. The bond shapes tested included the use of dotted/'discretised' bonds, after it was noted in the literature that a 4-dot bond reduced the bonding induced stress and curvature. The study was extended to observe whether further discretisation of the bond would lead to further improvements, with inclusion of a 9-dot bond. It was shown how the shape factors and therefore apparent modulus of the various bond shapes varied over thickness.

The FE models used in the investigation were described, with details on the contact algorithms, detection methods, symmetry conditions and mesh regime used in order to create a computational and time efficient converged model. With some convergence data shown and discussed, more detailed convergence trends were shown for the thinnest bonds, 0.25 and 0.1mm, due to the requirement of changing the desirable 1:10 element to thickness ratio discussed in Chapter 4 (FE model development), as they exceeded the available computational limits. It was found that the modal frequencies were at a good level of convergence. However, the die bow was less conclusive with 1.5-2% changes observed after further mesh reductions in the square bonds.

5.5.1. Die Bow

Reducing the die bow is a priority in reducing the performance changes of MEMS inertial sensors, due to the relative moment and stressing of the MEMS structures, leading to bias and scale factor changes. Therefore, reducing the change in die bow over temperature will lead to reductions in performance changes over temperature.

The die curvature was seen to vary significantly with bond shape and thickness. However, the normalised changes occurring over temperature were similar for differing designs, and therefore reducing absolute bow at any given temperature will lead to lower changes over temperature. In general, the dotted bonds induce lower bow than the square shape, with the 9-dot lower than the 4-dot at all thicknesses, indicating that bond discretisation is beneficial for reducing bonding stresses and curvatures, and therefore their changes over temperature and time.

The square bond's die bow is reduced as thickness is reduced, contrary to most literature, but an indication of the thermal expansion mismatch effect described by [44]. This is also seen in the 4-dot bond when reduced from 1mm to 0.5mm. However, bow increases are then observed for further thickness reductions. The 9-dot bond consistently follows the trend of increasing bow with reducing thickness, indicating that bond discretisation can reduce or eliminate the thermal expansion mismatch effect. The square 0.1mm thick bond experiences a change in its curvature shape to convex (at other thicknesses concave), inferring that there could be a thickness at which the square bond experiences zero induced curvature. However, convergence issues were identified for this bond design earlier in the chapter.

The bow variation measured around a centred circular path on the die was also observed and it was seen that the level of variation was proportional to the absolute bow experienced. The variation was cyclic with the minimum curvatures observed orientated towards the die edges (0/90°) and the maximum towards the die corners (45°). The relative variation was quite consistent between bond shapes, especially at reduced thicknesses, typical of a MEMS die bond. Therefore, reduction of the absolute die bow at any given temperature reduces the deformation variation over the die's surface.

The use of discretised bonds will therefore lead to lower performance issues such as zero-g offsets and quadrature bias in MEMS accelerometers and gyroscopes respectively. While also improving the stability of performance metrics over temperature, such as bias and scale factor.

5.5.2. Bounce Mode

It was found that the bounce mode increases non-linearly as thickness is reduced and for MEMS scale bonds, the change is dominated by slenderness effects and therefore the bond's apparent modulus variation with thickness. The square bond shape was found to be the stiffest due to its greater cross-sectional area and its higher shape factor causing earlier onset of the slenderness stiffening, leading to greater apparent Young's modulus at all thicknesses compared with the other bond shapes. However, the 4-dot and more so the 9-dot bond shapes experience greater relative change over thickness because of the greater associated percentage change in their apparent moduli.

The bounce mode was found to increase linearly as the temperature is reduced away from the bonding temperature, with the change occurring proportional to the absolute value. The normalised change in the bounce frequency over temperature is seen to increase with slenderness until a limiting thickness, at which a reduction is then seen. It is reasoned that the limiting thickness and normalised change variation over thickness of a bond is linked to its apparent modulus behaviour over thickness and its rate of change at its designed thickness.

This can be described by assuming that a change in temperature simply causes a small change in thickness, and therefore the bounce modes temperature dependency is linked to the bonds apparent modulus sensitivity to thickness change. Figure 164 shows the general apparent modulus variation over thickness for a compressible bond. Highlighted is the thickness at which the greatest rate of change in E'_a is occurring, leading to significant increases normalised bounce mode frequency change over temperature. This thickness is a good indication of the limiting thickness observed due to the dominance of the slenderness stiffening effects on bounce mode change, although is not exact due to the other thickness dependencies of the bounce mode. Using a bond thickness away from this value will produce a bond with lower normalised change over temperature. To improve the absolute variation over temperature an increased thickness is required, due to the absolute variation being proportional to the absolute value of bounce mode frequency.

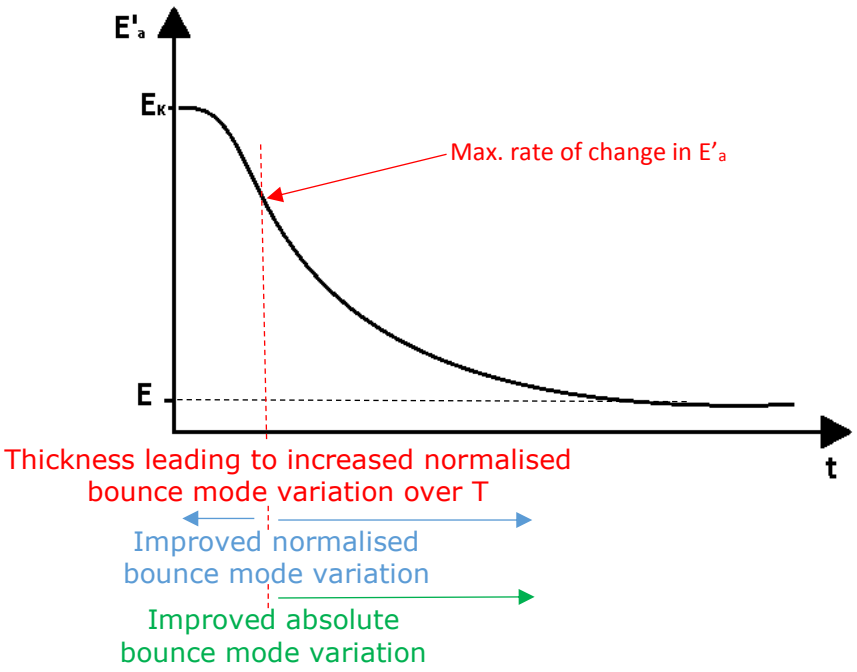


Figure 164 – Diagram illustrating link between E'a thickness sensitivity to Temperature dependency of bounce mode frequency

5.5.3. Shear Mode

The shear mode increases nonlinearly as the thickness is reduced, and unlike the bounce mode there is no slenderness stiffening effect, which is confirmed through comparison with theoretical results. As there are no slenderness effects the three bond shapes experience similar relative changes as the thickness is reduced. As was observed in the bounce mode, the square shape produces the stiffest bond, and 9-dot the least stiff, due to their varying cross-sectional areas.

The geometrical changes caused by temperature changes lead to a reducing shear mode frequency as the temperature is decreased away from the bonding temperature. This trend is non-linear with the reduction accelerating with greater temperature reductions. The normalised changes occurring are much lower in magnitude compared to those observed in bounce. It is seen that thickness changes do not significantly alter the normalised frequency change over the temperature range, however as the bond thickness is reduced the non-linearity increases leading to significant changes in the shape of the temperature trend.

The magnitude of non-linearity and its change over thickness varies with bond shape. The square bond suffers from high non-linearity even at the largest thicknesses, however its change is small as thickness is reduced to 0.25mm. The dotted bonds suffer from a much lower non-linearity in the

thicker bonds, however experience much greater increases as the thickness is reduced. This again links to the behaviours observed for the changing apparent Young's modulus over thickness for differing bond shapes. However, it does not affect the change occurring, as was observed in bounce, but instead the non-linearity of the change occurring.

The square 0.1mm thick bond experiences the only relatively significant change in normalised shear mode frequency over temperature, which coincides with the change in bow shape. Therefore, it appears that a convex die shape leads to greater normalised changes in the shear mode frequency over temperature than a concave surface, even when its curvature magnitude is significantly lower.

6. Chapter 6: Bond Design Variation - Experimental

6.1. Introduction

In Chapter 2, trial experiments were conducted on a single bonded sample, consisting of a 1mm thick square silicone bond, attaching a 1mm thick square copper die to a rigid aluminium base. In this chapter, the testing is expanded to include bond samples having differing die thickness, bond shape and bond thickness, and includes repeating the tests over time. The test regime is extensive and is designed to investigate the effects of bond design on the bonds properties and how they change over time when exposed to differing temperature environments. Trial experiments in Chapter 2 indicated coupling can occur between the translational and rotational motions of the die when excited in purely translational directions, and analytical and FE models in Chapter 3 indicated the coupling was caused by manufacture and assembly imperfections of the bond and die. In the same chapter approximate errors in the estimated material properties caused by imperfections of various types and magnitudes were investigated and discussed. At the end of Chapter 2, changes to the testing procedures and sample preparation were identified in order to generally improve vibration frequency response and surface profile measurements, as well as to reduce the level of coupling. These changes will be discussed when relevant in the following sections.

6.1.1. Objectives

The overall aim of the testing regime is to identify bond design parameters that improve the performance of MEMS inertial sensors, as sensor performance can degrade due to changes in bond properties or deformation state over excitation, temperature, and in particular over time. This chapter is primarily concerned with identifying the parameters that result in the most stable bond properties over excitation and temperature, and over time, when subjected to different temperature environments, including temperature cycling and long term high temperature storage. The bond properties considered include apparent moduli and loss factors, in bounce and shear, as well as the surface profile/curvature of the die (over time only).

To achieve this aim, differing objectives must be fulfilled. Vibration testing is used to assess the linear response range and level of non-linearity for each sample design and the bond properties are characterised over a range of excitation amplitudes. The mechanical properties of each bond design are also identified over temperature. The mechanical property trends over excitation and temperature will be assessed at different instances in time so the effects of repeated temperature cycling, short and long term high temperature storage and further temperature cycling can be observed and identified. The changes in the deformation state of the die will also be assessed over time, by measuring the surface profile, before and after bonding and after being subjected to a high temperature storage environment. This allows the deformation/curvature induced in the die from bonding to be assessed, as well as any possible creep in deformation/curvature of the die due to the combined temperature environments (cycling and storage).

Further to these objectives and the overall aim of the chapter, testing different bond designs provides an opportunity to validate and assess the ability of FE models to accurately simulate the dynamic response of the bond over temperature (Note: time dependence was not considered in the FE study conducted in Chapter 5). The validation and accuracy assessment is achieved by comparing simulated and measured bond properties and bond induced deformations for bonds having different shape and thickness.

6.2. Overview of Experiments

This section describes the various test methods used to characterise bond properties and their trends over differing environmental variables, such as excitation amplitude and temperature, and over time, including vibration tests and surface profile measurements. The different samples to be tested are also described including the variations in design parameters considered, and the full test regime and procedure to which the samples are subjected. As a part of this testing procedure description, the comparisons that are conducted in order to achieve the objectives outlined in the previous section are discussed, as well as extraneous variables that are present in the experiments and how these have been mitigated.

6.2.1. Testing Types and Description

Multiple testing methods and measurements are used in the test regime to characterise the bond properties and 'state' as fully as possible at various points in the experimental procedure, including vibration test and surface metrology methods.

6.2.1.1. Vibration

Vibration experiments are used to assess the mechanical properties of the bond by analysing the frequency response or transmissibility function of a point on the die's surface or edge respectively. However, as in the trial experiments different vibration test methods are used when determining the bonds property trends over differing variables, such as position, excitation amplitude and environmental temperature. The differences between the vibration test methods and procedures used for the differing objectives are discussed in the following sections.

6.2.1.1.1. Multipoint Mode Shape Characterisation

As in the trial experiments and emulated in the FE models, when analysing the effects of bond imperfections, multipoint measurements are used to characterise the motions of the die. This vibration testing method measures the frequency response at several locations, including the approximate centre and extremes (corners and edges) on the surface or edge of the die for bounce or shear respectively, see Figure 165. By measuring at different locations on the die, it is possible to observe the level of coupling and infer an approximate level of bond imperfection and the resulting errors in the derived properties. The tests performed use the FFT method described in Chapter 2, which involves exciting and measuring all frequencies in the desired range simultaneously and allows very short duration tests, permitting all points to be measured quickly. This is important because each sample has 9 or 5 measurement points in bounce or shear respectively. It was found in the trial experiments that transmissibility functions measured using this method suffered from a low signal to noise ratio, and for this reason the source amplitude used here has been increased to 2V, to provide a larger excitation but remain within the linear range at each frequency. In tests the sample is mounted directly onto the shaker armature via an M4 thread, with no connecting rod to remove any unwanted associated resonances in the output transmissibility functions.

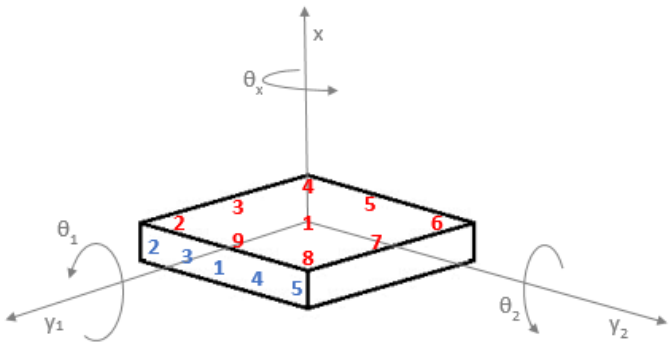


Figure 165 - Figure of multipoint positions bounce and shear

In Sections 6.4.1.1. results from the multipoint tests are displayed as Transmissibility functions, with all measured points for a sample in a given excitation direction plotted in a single figure.

6.2.1.1.2. Linearity

In the linearity tests the frequency response of the die is measured for various base excitation amplitudes, allowing the linear response region of the bond to be observed. Due to the importance of the source amplitude magnitude, a sine sweep measurement method is used and the frequency response measured at the approximate centre of the die surface and edge in bounce and shear respectively, see measurement point 1 in Figure 165. As in the multipoint tests, the sample is attached directly to the shaker armature, with no connecting rod.

In Sections 6.4.1.2. and 6.4.2.2. results from linearity tests are displayed as estimated material property, modulus or loss factor, against excitation amplitude or as a backbone-like figure of modulus against loss factor with the excitation level indicated by the colour of the marker, with blue to red indicating increasing amplitude. The use of these backbone-like plots allows for easy comparison of the temperature trends of the bond properties over time.

6.2.1.1.3. Environmental Temperature

To study the effect of environmental temperature on the properties of the die, the frequency response is measured over a range of temperatures, typically -40 to 120°C. Due to the requirement to vary the temperature of the bond, the test setup for these experiments is modified due to the presence of the temperature chamber, as was discussed and shown in section 2.6.3. see Figure 34.

The chamber and the varying temperature also have a significant effect on the testing procedure used, and improvements to the procedure have been introduced based on observations

made in trial experiments. In trial tests it was found that the chamber introduced extra artefacts and resonances in transmissibility functions, thought to be associated with the fan of the chamber. Also, in cooling tests (for temperatures below room temperature), high levels of noise were present in the results due to the presence of water vapour in the chamber which condensed onto the die surface causing laser signal issues. For this reason, extra steps were taken in cooling tests before measurements are taken. Once the temperature in the chamber reaches equilibrium (which takes approximately 20-30 minutes depending on the oscillation level from the thermocouple reading), the chamber is turned off to stop the fan and ensure there is no nitrogen release, the door is opened to remove water vapour from the chamber and the measurement surface wiped to remove condensate before measurements are taken. These steps must be completed quickly in order to ensure the temperature of the sample does not change before measurements are recorded. The measurement itself must also be taken quickly, and for this reason the FFT method is used, as these can be recorded in less than one second.

In Sections 6.4.1.3. and 6.4.2.2. results from environmental temperature tests are displayed as the estimated material properties, Modulus and loss factor, against temperature or as a backbone-like figure of modulus against loss factor with the temperature indicated by the colour of the marker, with blue to red indicating increasing temperature. The use of these backbone-like plots allows for easy comparison of the temperature trends of the bond properties over time.

6.2.1.2. Surface Profile – Die Curvature

In the trial experiments, surface scans of the die were conducted using both mechanical stylus and optical white light interferometry methods before and after bonding. It was seen that there was a change in the deformation state of the die due to bonding. However, this change was seen to be less than the resolution capability of the mechanical methods. Therefore, in the experiments conducted within this chapter only white light interferometry measurements using the Bruker NP Flex are used.

In Chapter 2, issues with the surface profile measurement procedure and results were identified and possible solutions suggested. These included the poor initial shape of the die, the lack of referencing features on the die to enable before and after scans to be aligned and the change of form analysis, as well as excessive output file sizes inhibiting efficient analysis of the scans. The requirement for high flatness of the manufactured die is achieved through the use of oil immersed EDM to

manufacture the dies. Referencing features will be introduced by manufacturing grooves on two sides, leading to a partial cross hair on the parted-off die to align the scan start location to, see Figure 49. To reduce the size of the output files, the resolution in the x-y die plane is reduced to its lowest setting. This reduction in x-y resolution will lose information on the surface texture and roughness of the die, which is the primary function of the equipment. However, there is no loss in resolution in the z direction and so die surface shape is remains accurate. This reduction in output file size is key to allow efficient manipulation and analysis of the surface height data.

The die surface is scanned at three points in the testing regime, before bonding, after bonding and after exposure to several temperature environments (cycling and storage). The difference between the scans before and after bonding reveals the curvature/deformation induced from bonding, while a comparison of scans after bonding and after temperature testing indicate any change in form from possible viscoelastic effects, or creep occurring throughout the temperature cycling and high temperature storage environments. These comparisons define two key deformation state changes.

These deformation state changes are the key results of these tests and will be displayed as filled contour plots representing the die surface. These results are obtained by manipulating the raw data. The referencing features provide location and orientation data for the die and allow approximate alignment of the two scans. However, due to the manual placing of the die on the scan bed, it is necessary to realign the scans, as well as remove any tilts induced in the scans because of non-parallelism between the scan head and die. In addition, the raw scan data may have bad points due to signal/reflective issues across the dies surface, leaving gaps in the height data at these locations. These issues are corrected by manipulating the raw height data and a Matlab analysis script was developed for this purpose. The analysis script imports the two sets of scan data to be compared and asks the user to select 3 die corner locations, each time displaying a close zoom contour plot of the height data for a given corner. The script then calculates the final corner location such that the four points enclose a rectangular/square area. The enclosed data sets are then assembled into 2D arrays with their rows and columns representing the x and y axes of the die respectively, and replacing the ‘bad’ points with zero terms. The zero terms are located and replaced by the mean value of the neighbouring values, and this process continues iteratively so that the gaps in the data are filled. Only data points that were initially

'bad' are edited, so all data points having real measured height data remain unchanged throughout this process to ensure no change in the shape data after the gaps are filled. The difference between the two scans at each cell is then calculated, resulting in a single array representing the change in form across the die surface. To remove any tilt from this array, line plots at multiple rows are displayed and by selecting two points on each line, the average y tilt gradient is calculated. This process is repeated for column data to calculate the average x tilt gradient. Using the 2 gradients, an array of tilted values is created, representing a flat tilted surface, which is subtracted from the change of form data to remove tilt. If necessary, this process is repeated to remove any remaining tilt from the change of form data.

6.2.2. Test Samples

The tested samples are composed of a rigid aluminium base, with an attached steel square die via a silicone die bond. The shape of the die bond is varied with levels of square, 4-dot and 9-dot, see Figure 129. The intended thicknesses of the die bond are 1mm, 0.5mm and 0.1mm. The shape and thickness of the bond is controlled using a stencil to which the uncured silicone is applied during assembly. However, the viscous mixture was found to stick to the stencil in some cases despite use of a non-stick coating and although guides and spacers were used during die placement, variations in thickness were observed. To improve the accuracy of the property calculations, thickness measurements using Vernier callipers were taken at each corner of the die and averaged to estimate the mean bond thickness.

Table 18 summarises the properties for each sample. Each steel die has cross-sectional dimensions of 10x10mm, but with varying thickness. The majority of samples have ~ 1mm thickness, but two of the samples have 0.5mm thickness in order to reduce its stiffness and hence increase any deformations experienced by the die. During manufacture and assembly, the mass of the bases, dies and final assembled and cured samples were measured using a sensitive set of scales (resolution of 10mg), allowing the bond mass to be calculated. The bond and die mass are key parameters when calculating the apparent moduli. The selected samples were chosen to allow different bond shapes to be compared, along with trends over thickness, as well as comparisons of different die stiffness, allowing conclusions to be drawn on the effect of bond shape and bond thickness and how they interact,

as well as how die stiffness affects die deformation, and how the resulting stress differences affect the dynamic properties of bonds.

Table 18 - Properties of Tested Samples

Sample	Bond Shape	Bond Thickness (mm)	Bond Mass (mg)	Die Thickness (mm)	Die Mass (mg)
1	Square	1.3	86.87	0.95	729.53
2	Square	1.1	67.67	0.95	730.13
3	Square	0.485	39.98	0.95	730.02
4	Square	0.295	21.23	0.95	729.97
5	4-Dot	0.6125	42.64	0.95	730.36
6	4-Dot	0.44	29.95	0.95	730.65
7	9-Dot	0.235	8.00	0.95	730.69
8	9-Dot	0.3925	12.93	0.95	729.77
9	Square	1.0825	73.66	0.45	419.04
10	Square	0.425	38.23	0.45	403.97

6.2.3. Test Procedure

The samples are subjected to an extensive test regime of vibration testing, surface metrology and temperature environments. Table 19 summarises the full test procedure for each sample, where each vibration test is first conducted in bounce and then in a single shear direction.

Table 19 - Full Test Procedure for each sample

Test no.	Test name	Test Description
1	SP1	Die Surface Profile Measurement (Before Bonding)
2	-	Assembly and Bonding
3	SP2	Die Surface Profile Measurement (After Bonding)
4	MV	Multipoint Vibration – Mode Shape Characterisation
5	LV1	Linearity Vibration (1-175mV)
6	TV1	Temperature Vibration – Heating (ambient - 120°C)
7		Temperature Vibration – Cooling (ambient - -60°C)
8	LV2	Linearity Vibration (1-175mV)
9	TV2	Temperature Vibration – Heating (ambient - 120°C)
10		Temperature Vibration – Cooling (ambient - -40°C)
11	LV3	Linearity Vibration (1-175mV)
12	HTS1	High Temperature Storage (72hrs at 120°C)
13	LV4	Linearity Vibration (1-175mV)
14	HTS2	High Temperature Storage (145hrs at 120°C)
15	LV5	Linearity Vibration (1-175mV)
16	TV3	Temperature Vibration – Heating (ambient - 120°C)
17		Temperature Vibration – Cooling (ambient - -40°C)
18	LV6	Linearity Vibration (1-175mV)
19	SP3	Die Surface Profile Measurement (After Temperature Environments)

For a single sample, the designed test regime provides many opportunities to observe changes that may occur to bond properties over time. The three temperature vibration tests (TV1-3) provide the bond properties over the temperature range -40°C to 120°C. The lowest temperature was initially selected to be -60°C but samples 1 and 2 (square ~1mm thick) sheared at the base-bond interface, and so this temperature was increased to ensure no further loss of samples. Comparison of the three temperature profiles provides information on the temperature repeatability of the bond, and how they are changed by temperature cycling and high temperature storage.

The six linearity vibration tests (LV1-6) provide backbone-like trends of the bonds properties (moduli versus loss factor) and provide an indication of the linear range of response and the level of non-linearity if this range is exceeded. A comparison of the different linearity vibration tests indicates how the linear range and non-linearity of response evolves over time and how it changes because of single and repeated temperature cycling and storage. Further linearity vibration tests positioned between high temperature storage provides information on how changes in the bond evolve over the time in storage, i.e. does the change occur in the short-term or is prolonged storage duration required before changes are seen? Another linearity test after the third temperature cycle provides information on further changes to the bond, i.e. do they occur, or does high temperature storage inhibit further changes?

The three surface profile measurements taken, and their comparisons will indicate changes in the dies shape due to bonding and over the duration of the test regime. These allow identification of any induced curvature due to bonding stresses. As well as any changes over time, providing an indication of any creep in the bond which may be associated with property changes observed from the results of the vibration tests, or whether changes are solely caused by changes to the bond material itself.

6.3. Mechanical Characterisation of Bond Properties

In Chapter 2 the dominant modal peak observed in a measured response transmissibility function for bounce and shear was used to estimate the stiffness and damping coefficient based on single degree of freedom Hysteretic Kelvin-Voigt model, consisting of a lumped mass connected to the

ground by a linear spring and hysteretic damper in parallel. A representative diagram for this system can be seen in Figure 22.

6.3.1. Apparent Storage Modulus

As shown in section 2.5.3.1., the apparent storage modulus of a bond in bounce or shear can be expressed as:

$$E_a, G_a = \frac{{\omega_{n_{bounce,shear}}}^2 \left(m_{die} + \frac{m_{bond}}{3}\right) t_{bond}}{A_{bond}}$$

The design parameters, die mass, bond mass, bond thickness and bond area, are known and shown in Table 18 for the various bonds tested. The natural frequency, ω_n, is found from transmissibility data measured in the tests. Quadratic interpolation of the three maximum transmissibility points, is conducted to provide improved estimates for the natural frequency and maximum transmissibility (which is used in loss factor calculation) as shown in chapter 3.

6.3.2. Hysteretic Loss Factor

In Chapter 3, loss factor calculation methods were developed, and investigations conducted to assess the accuracy implications of system and measurement properties, system loss factor and frequency resolution, signal imperfections, noise and artefacts, and bond imperfections, slopes and die misplacements. It was found that the differing calculation methods had varying advantages and disadvantages depending on the signal and sample imperfections observed in a particular transmissibility function, these are discussed in detail for all calculation methods investigated in chapter 3 and concluded in section 3.5. Both the exact inverse transmissibility and second order form of averaged multi-power bandwidth methods are considered in the tests conducted in this chapter, with the most accurate chosen dependent on the transmissibility function analysed.

The second order averaged multi-power bandwidth method is given by:

$$\eta_{mp} = \frac{{\omega_2}^2 - {\omega_1}^2}{2{\omega_n}^2} . \frac{1}{\sqrt{\frac{1-p}{p}}}$$

In the averaged multiple-power bandwidth method the loss factor is calculated over a range of power levels, and the resulting estimates averaged. The power levels used are manually selected for each transmissibility function analysed, such that coupled mode responses and artefacts observed can

be omitted from the analysis. The power bandwidth frequencies, ω_2 and ω_1, are found from the analysed transmissibility function, and are the frequencies at which, $|T^*| = \sqrt{p}|T^*{}_{max}|$, with linear interpolation applied to improve their estimation.

The exact inverse transmissibility method, the loss factor is calculated using:

$$\eta = \frac{1}{|T^*{}_{max}|\sqrt{1-\left(\frac{1}{|T^*{}_{max}|}\right)^2}}$$

6.4. Results and Discussions

The following sections present and discuss the obtained results for the bond design variation experiments. Each sample will be characterised initially, including estimates of the level of imperfection and resulting errors, as well as their property trends with excitation and temperature. Following this, the evolution of property trends for each sample over time will be presented, with comparisons made between samples using their normalised change trends, as well as changes observed in the deformation states of dies.

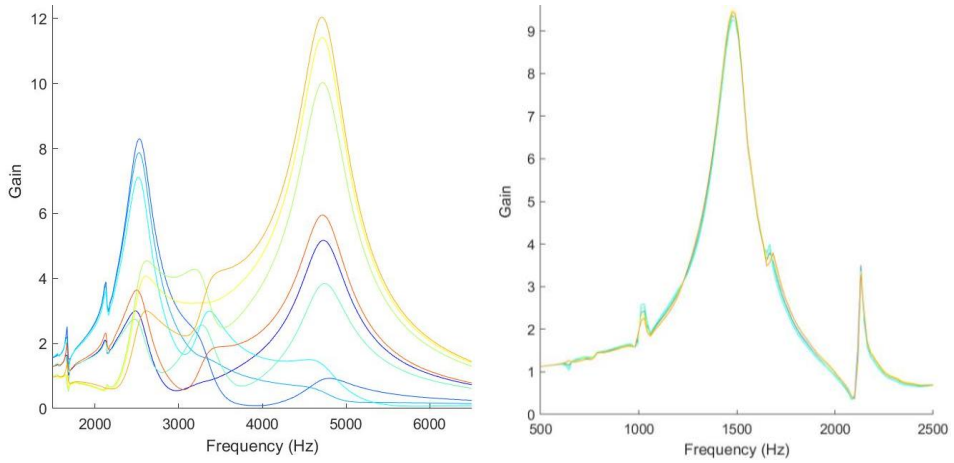
6.4.1. Initial Sample Characterisation and Mechanical Property Trends

In this section results from multipoint transmissibility tests will be shown, as raw transmissibility functions, and used to estimate the level of imperfection present in each sample. Using the results of FE imperfection studies conducted in Chapter 3 along with these estimates, approximate errors will be assigned to each sample for individual properties. Initial property trends over excitation amplitude and temperature for all samples will be shown and compared.

6.4.1.1. Sample and Mode Shape Characterisation (multipoint)

Figure 166 shows the measured multipoint transmissibilities in bounce and shear for sample 1 (1.3mm thick square bond). In bounce it can be seen that there is significant coupling to rocking modes with large responses observed at approximately 2.5 and 3.5 kHz, as well as contaminating rocking motion at the bounce mode at around 4.8 kHz. At this bounce mode peak three bands of response can be seen indicating an imperfection aligned approximately with a shear direction, where the variation between bands are large, suggesting high level of imperfection. The transmissibilities in shear confirm

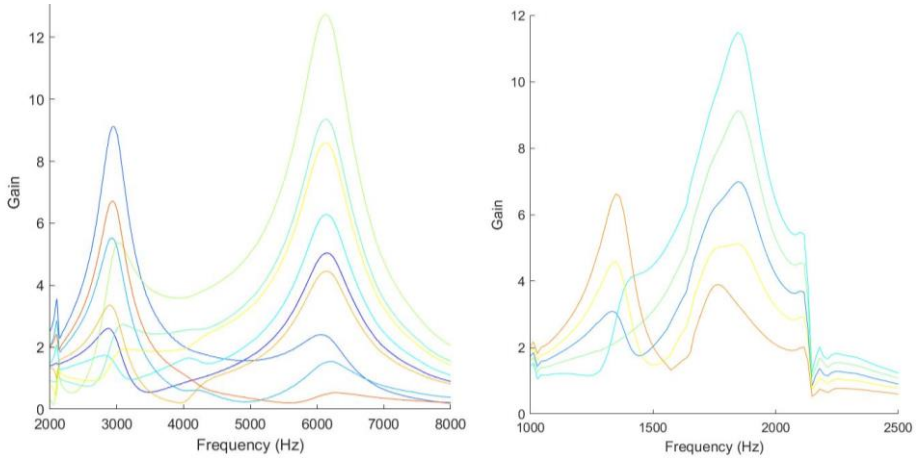
the approximate alignment of the imperfection with the shear direction measured, as coupling to twist is low, with good agreement in response across the dies edge. Using the large slope angle (parallel to a shear axis) imperfection as a guide to the possible errors induced in the property analysis, it can be seen that the approximate behaviour of the imperfection allows for accurate assessment of the loss factors (<1%). However, its large magnitude can cause significant shifts in the natural frequencies and therefore induces high errors in modulus estimations of approximately 23% in bounce and 5% in shear.



a) b)

Figure 166 - Multipoint Transmissibility Functions for sample 1 (1.3mm square) in bounce (a) and shear (b)

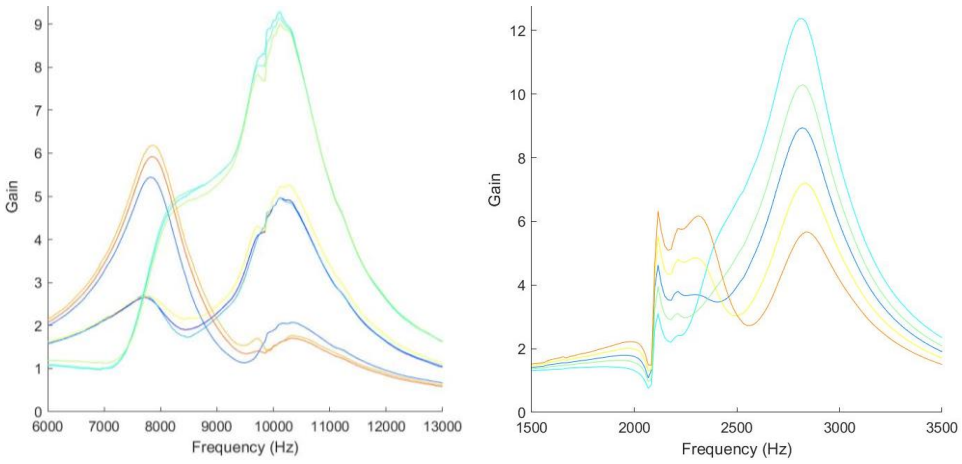
Figure 167 shows the measured multipoint transmissibilities for sample 2 (1.1mm thick square bond) in bounce and shear. The bounce response is similar to that analysed for sample 1, with large coupling observed as well as three bands of response. In this case, however, the variation within each band is greater, indicating less alignment of the imperfection with a shear direction, from observation of the points present in the response bands the alignment is closer to the opposite shear direction compared to sample 1. This greater misalignment is to the shear direction orthogonal to the one being measured and as observed in the shear transmissibility graph, leads to large coupling of twist and both shear modes. The shear response shows behaviour of two close coupled modes, with large frequency shifts and magnitude variations in the peaks measured across the dies edge. These multipoint behaviours are more indicative of a large 2D imperfection, which was seen to cause large errors in the modulus and shear loss factor estimates, although the compressive loss factor can be estimated with approximately 1% accuracy.



a) b)

Figure 167 - Multipoint Transmissibility Functions for sample 2 (1.1mm square) in bounce (a) and shear (b)

Figure 168 shows the multipoint transmissibilities for sample 3 (0.5mm thick square bond), large coupling between bounce and rocking, and twist and shear can be observed. In bounce an almost perfect banded response is seen, indicating the imperfection is aligned with a shear direction. The presence of large coupling between twist and shear demonstrates that the alignment of the imperfection is to the opposite shear direction to that being measured. However due to the 1D nature, there is no coupling to the other shear mode and therefore the shear loss factor can be estimated with less than 2.5% error, while in bounce within 1%, modulus errors are much greater (17 and 23%).



a) b)

Figure 168 - Multipoint Transmissibility Functions for sample 3 (0.5mm square) in bounce (a) and shear (b)

Figure 169 shows the multipoint transmissibilities for sample 4 (0.3mm thick square bond) in shear only, the bounce mode frequency for this bond design exceeds the capabilities of both the shaker and control accelerometer. The response behaviour observed across the dies edge indicates a 1D imperfection aligned to the opposite shear direction, as there is no distortion of the peaks shape due to coupling of the other shear mode. The level of coupling to twist, observed by the level of response

at the twist frequency and the level of gain variation between measurement points at the shear mode, shows a medium magnitude of imperfection, between the cases investigated in Chapter 3.

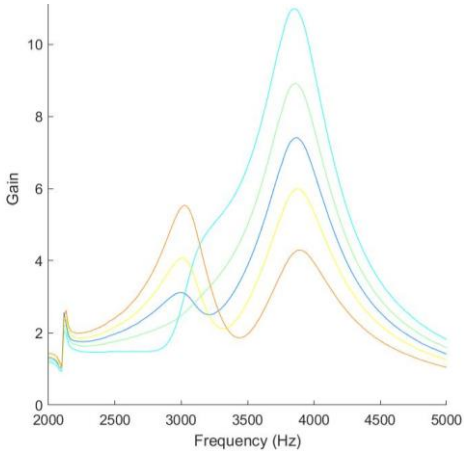


Figure 169 - Multipoint Transmissibility Functions for sample 4 (0.3mm square) in shear

Figure 170 shows the multipoint transmissibilities for sample 5 (0.6mm thick 4-dot bond) in bounce and shear, it can be seen that there is a large level of imperfection insinuated from the large coupling to rocking when excited in bounce and similarly twist when excited in shear. There are three bands of response in bounce, indicating this imperfection is closely aligned to a shear direction. The presence of high coupling in the shear results shows that this alignment is to the opposite shear direction than the one being measured. There is some visible distortion of the shear peak shape, although this tends to be an indication of a 2D imperfection, the presence of a large artefact at approximately 2.1 kHz is more likely to be the cause.

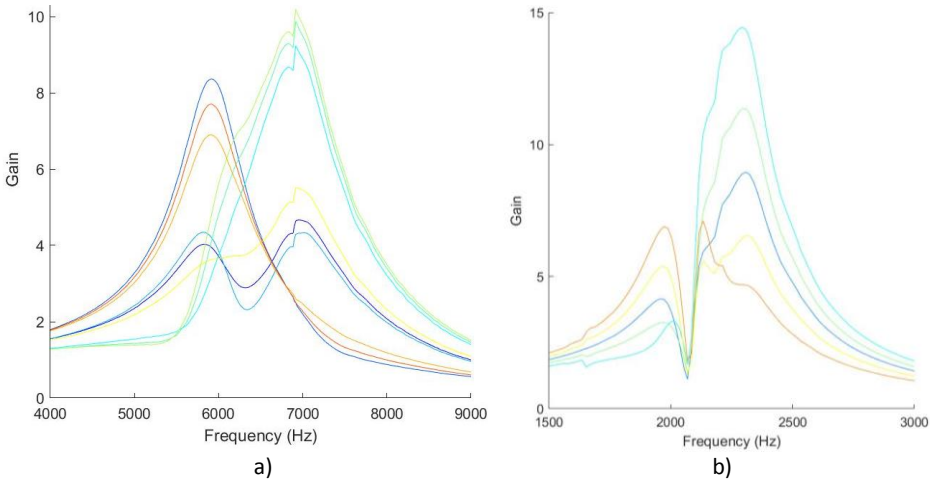


Figure 170 - Multipoint Transmissibility Functions for sample 5 (0.6mm 4-dot) in bounce (a) and shear (b)

Figure 171 shows the measured multipoint transmissibilities for sample 6 (0.4mm thick 4-dot bond) in bounce and shear. They show a large level of coupling and therefore imperfection. This imperfection can be deduced to be 2D in nature, and possibly incorporating a combination of slope and

die misplacement, due to the excitement of both rocking modes in bounce and coupling between twist and both shear modes. A combination type imperfection causes issues in estimation of errors as they can oppose each other allowing for accurate estimates, but also exasperate their effects. In this case it is likely that the bounce loss factor can be found accurately, but due to the significant imperfection modulus estimates will be affected greatly and due to the two close coupled shear modes the shear loss factor will suffer high errors as well.

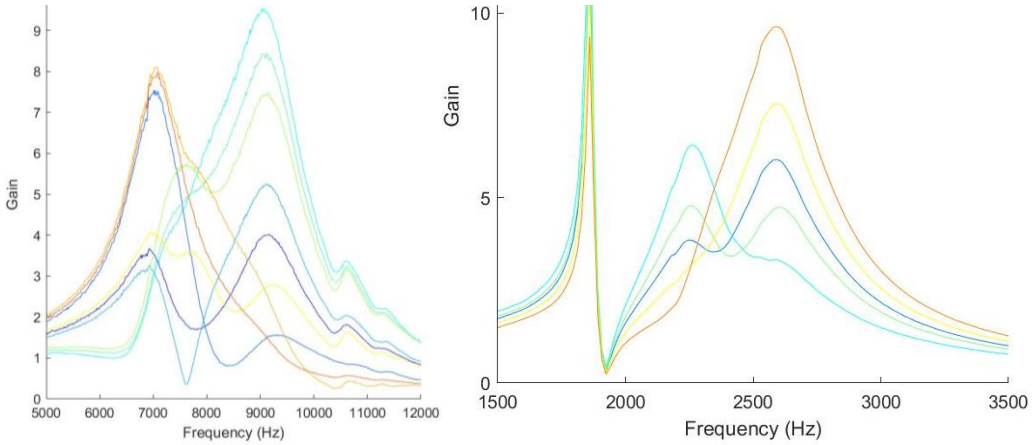


Figure 171 - Multipoint Transmissibility Functions for sample 6 (0.4mm 4-dot) in bounce (left) and shear (right)

Figure 172 shows the measured multipoint transmissibilities in shear for sample 7 (0.2mm thick 9-dot bond). A large level of imperfection is present, due to the significant twist response and the extreme variation in the shear mode peak gain across the die edge. This imperfection is likely to cause high errors in modulus estimation, but as there is no distortion of the shear peak due to coupling with the other shear mode, loss estimates should be accurate.

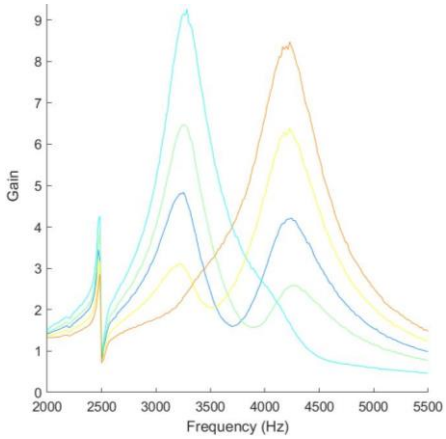
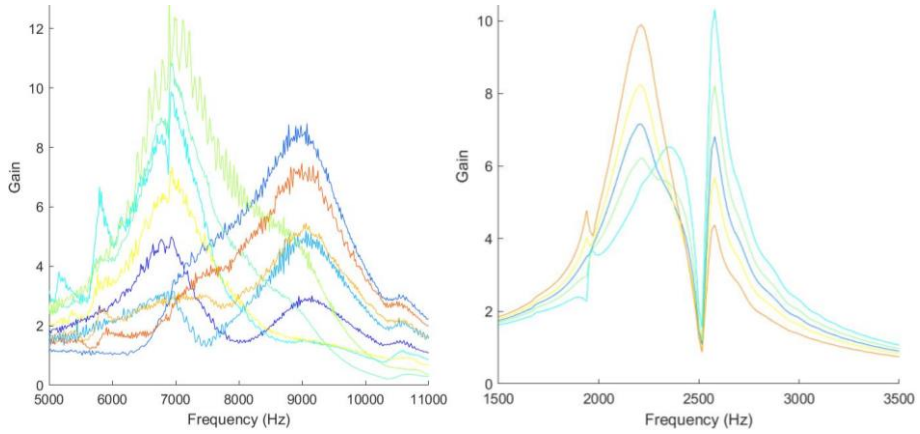


Figure 172 - Multipoint Transmissibility Functions for sample 7 (0.2mm 9-dot) in shear

Figure 173 shows the measured multipoint transmissibilities for sample 8 (0.4mm thick 9-dot bond) in bounce and shear. As observed in many samples, a large level of coupling exists between the

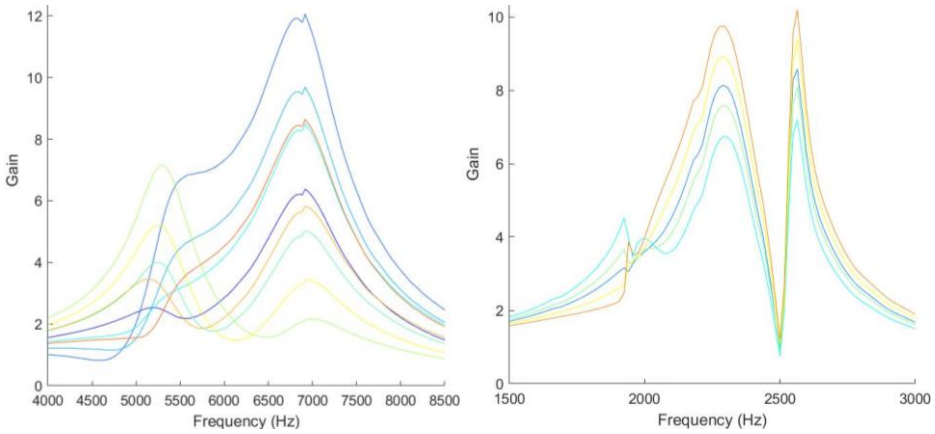
translational and rotational motions, signifying a large level of imperfection. Therefore, any modulus analysis will be affected significantly, the loss factor in bounce is not typically affected greatly due to the distance from the coupled modes. However, in this case the low-level response seen at the central measurement point will have a further detrimental effect. The shear transmissibilities show significant twist response, but the presence of an artefact at the shear mode completely obscures the peak, making further observations difficult.



a) b)

Figure 173 - Multipoint Transmissibility Functions for sample 8 (0.4mm 9-dot) in bounce (a) and shear (b)

Figure 174 shows the measured multipoint transmissibilities in bounce and shear for sample 9 (1.1mm thick square bond with 0.5mm thick die). Once again coupling is present in both tested directions, and from the magnitude of rocking response, the imperfection can be insinuated to be medium in magnitude (between the cases investigated). The shear response shows a low level of twist response, although some distortion of the shear peak can be seen, indicating coupling of the other shear mode. Due to the presence of an artefact it is difficult to ascertain the level of distortion to the shear peak.



a) b)

Figure 174 - Multipoint Transmissibility Functions for sample 9 (1.1mm square, thin die) in bounce (a), shear (b)

Figure 175 shows the measured multipoint transmissibilities for sample 10 (0.4mm thick square bond with 0.5mm thick die) in shear. It can be seen that there is a low response at the twist mode frequency and relatively low peak variation at the shear mode peak. This low level of coupling infers a low level of imperfection, although without the bounce response, this cannot be confirmed, as a good shear response can occur when differing imperfections interact. In either case, the loss estimate will be accurate, with less than 1% error, but the modulus error could vary from 0.5% to 8.5%.

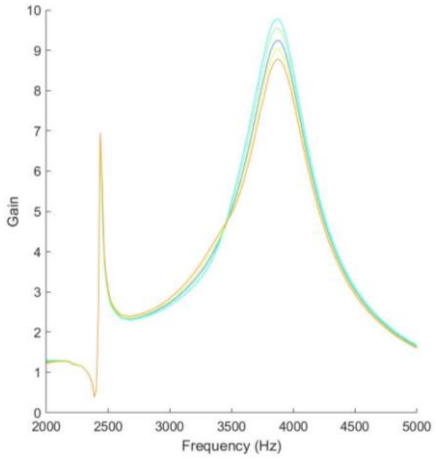


Figure 175 - Multipoint Transmissibility Functions for sample 10 (0.4mm square, thin die) in shear

In this section, the measured multipoint transmissibility functions in bounce and shear have been analysed qualitatively to assess the presence and magnitudes of any coupling. By making comparisons with the investigations studied in Chapter 3 for bonds including imperfections, the approximate type and magnitude of imperfection present in the samples have been inferred. Table 20 summarises the findings, along with estimated errors inferred from the FE investigations in Chapter 3. While these error estimates provide an indication of the errors in the derived material properties, they only provide a guide as the FE investigation was carried out using only a single bond design and the imperfections modelled were limited to a small number.

Table 20 - Coupling observations and inferred imperfection types for the tested samples, along with property error estimates

Sample	Bounce			Shear		
	Imperfection/Coupling Description	E error (%)	η error (%)	Imperfection/Coupling Description	G error (%)	η error (%)
1	Large ~1D	23	1	Large but aligned with measurement	5	0
2	Large ~2D	26	1	Large and misaligned, close coupled shear modes	15	28
3	Large 1D	23	1	Large and orthogonal, no shear coupling	17	2
4				Medium and orthogonal, no shear coupling	5-10	1-2
5	Large ~1D	23	1	Large coupling, artefact	17	2
6	Large 2D combination	27	1	Large, shear coupling	20	12
7				Large, no shear coupling	17	2
8	Large 2D	20-30	1+	Large, artefact	10-20	5-10
9	Large 2D	26	1	Large, distortion, artefact	7-15	15-30
10				Low twist and no shear coupling	0-8	<1

It has been seen in the multipoint analyses, and summarised in Table 20, that all samples manufactured and tested suffer from high levels of coupling and therefore imperfection. This has resulted in relatively high errors for most properties, with the exception of the bounce loss factor. These errors make comparisons between differing samples difficult, due to the uncertainty in their magnitude and the variation observed in different bond samples. This will make any assertions/conclusions into the effect of design parameters difficult. However, provided the imperfections and their effect on their respective property estimates are constant and consistent throughout the tests then it should be possible to observe the property trends over temperature and time and discuss the trends with confidence, although the absolute values may be affected. The high levels of imperfection observed in the multipoint tests will result in very large errors in loss factor if calculated using the inverse transmissibility method, due to its sensitivity to contamination by rotational motion. Therefore, the loss factor errors discussed here (and shown in Table 20), and the loss factor values and trends shown in the following sections refer only to the loss factors calculated using the second order averaged multi-power bandwidth method.

6.4.1.1.1. Comparison to FE modal Frequencies

Figure 176 plots the bounce mode frequencies obtained from the multipoint tests and FE models for different bond shapes against bond thickness. It can be seen that the experimental results for the square bonds are in reasonable agreement with the FE models, including the thin die result (which has been compensated due to the reduced mass effects). The 4-dot bond frequencies are 2kHz higher in the experiments, but the gradient of the change due to thickness between the two samples is similar to that observed in the FE. The 9-dot bond tested has a much greater modal frequency (5kHz) than observed in the FE study, and there is no trend data to be commented on as only one 9-dot bond was within the measurement capabilities of the testing setup.

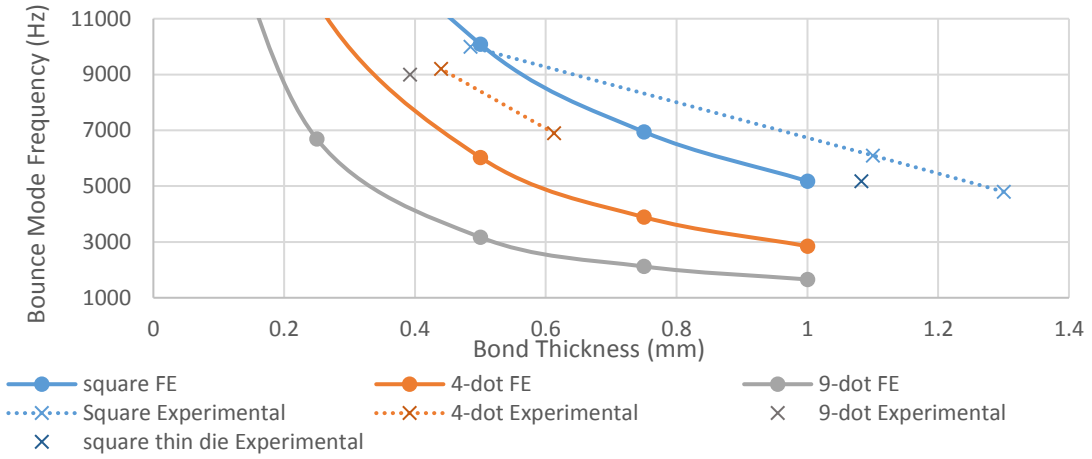


Figure 176 – Comparison of Experimental and FE Bounce mode frequencies of various bond shapes over thickness

Figure 177 plots the shear mode frequencies obtained from the multipoint tests and FE models for different bond shapes against bond thickness. It can be seen that all of the experimental frequencies are significantly higher than their equivalent result in the FE, inferring that the FE model has not captured some constraining effect in the shear direction. This may be caused by geometrical differences between the real and modelled bond shapes, such as the curvature of the bond edges. Or, it could be an indication that, for the scale of bonds investigated, the shear mode is affected by slenderness stiffening effects. The differences are consistent across the bond shapes and therefore could be caused by inaccurate material properties used in the models. There is reasonable agreement between the experiments and FE for the square and 4-dot bond behaviour, with similar gradients of change in the frequency when the thickness is reduced. However, the experimental results for the 9-dot bond shows significant stiffening at larger thickness than that seen in the FE. As only 2 samples were tested it is

unclear whether this is caused by an experimental error or the FE not capturing the true shape factor effects of the bond shape.

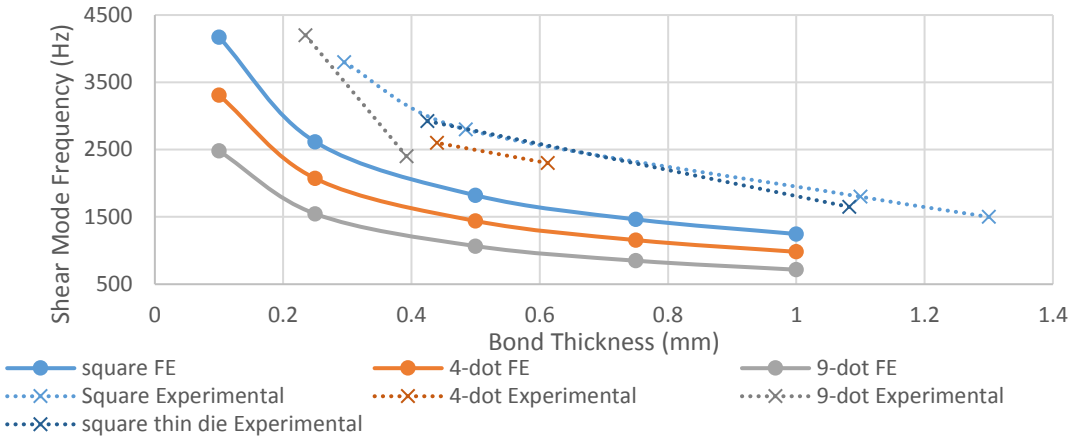


Figure 177 – Comparison of Experimental and FE Shear mode frequencies of various bond shapes over thickness

Comparisons between the experimental and FE results for the modal frequencies of various bond shapes over thickness has shown differences in both the absolute values and thickness trends. There is some agreement between the results, particularly for the square bonds, where good agreement is seen in bounce and the thickness behaviour is captured well in shear despite an offset in absolute value. This offset was observed for all shear results, indicating that further stiffening is required in the shear direction of the model, either through geometrical considerations, improved material properties or some slenderness stiffening effects in shear. Further experimental results are required to comment more on the behaviour of the 4 and 9-dot bonds over thickness.

6.4.1.2. Linearity with Excitation Amplitude

In Chapter 2, the trial experiments showed that the die response in shear and bounce varied under differing base excitation amplitudes. This allowed the non-linear behaviour of the bond to be characterised as the excitation amplitude was increased. The results are displayed as backbone-like plots of modulus and loss factor, one showing absolute properties and one normalised (using properties identified as within the linear region).

Figure 178 plots the bounce mechanical properties of the bond estimated from measured transmissibility functions under increasing levels of excitation. The graph plots the modulus against loss factor with marker colour representing the level of excitation (from blue - 0.1g, to red 17.6g. In absolute terms, it can be seen that the differing bond designs produce bonds with different modulus and loss

factor properties, and that these properties vary differently with the level of excitation. In general, a softening effect is observed, where modulus reduces with increasing excitation, as well as increases in loss factor. Sample 9 is the exception where a reduction in loss is observed. However, this change is very small in comparison to the loss trends of other bond designs. The loss trends vary significantly with bond designs, this can also be seen in the normalised trends, with loss increases of between 1 and 12% from linear to that measured at 17.6g excitation magnitude (excluding sample 9 decreases by <1%). The normalised changes in modulus are less significant with only 1-4% decreases from linear (1-2.5g) to the highest excitation (17.6g).

The highest normalised loss changes are observed in thinner bonds (square and 9-dot 0.5mm thickness). However, this is not consistent across all bonds of that thickness, with the 4-dot 0.5mm thickness bond loss factor changing by only ~1%. After neglecting the two highest relative loss changes mentioned, all others experience a change of less than 4%. Due to these relatively low changes, the correlations seen are only weak, with little consistency observed across samples except for the general direction of the changes occurring, i.e. reducing modulus and increasing loss. This coupled with the large variation in possible errors identified and discussed for the multipoint tests of different samples, leads to difficulty in comparison and deriving conclusions on the effects of individual design parameters.

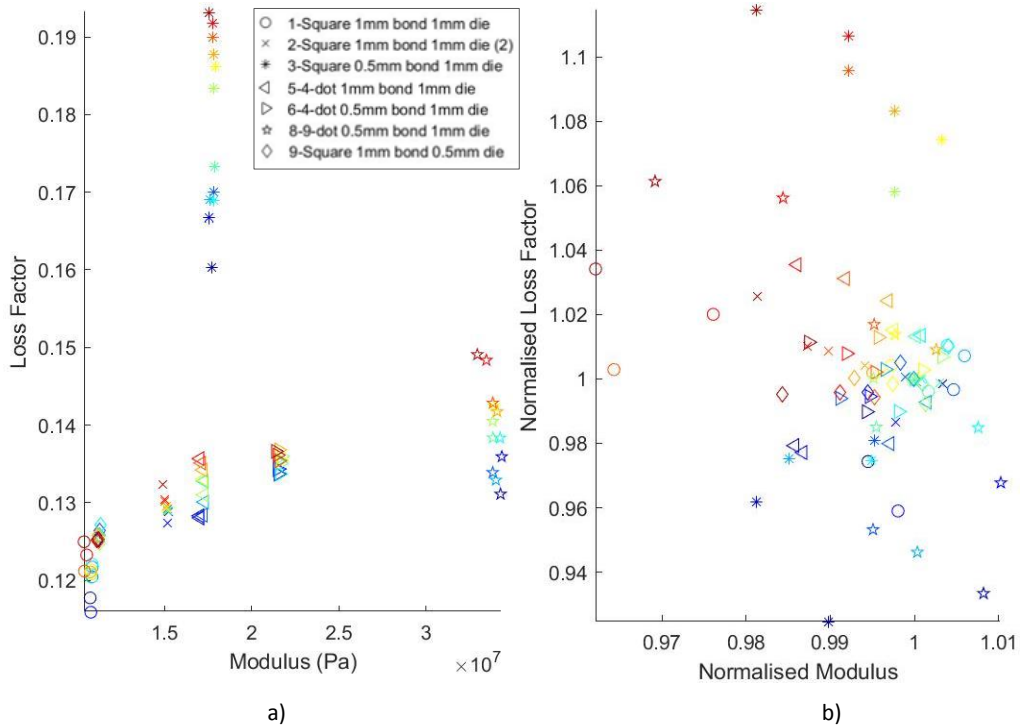


Figure 178 – a) Absolute and b) Normalised Bounce Property changes with excitation amplitude (0.1g (blue)-17.6g (red))

Figure 179 plots the shear mechanical properties of the bond estimated from measured transmissibility functions under increasing levels of excitation, using a similar backbone-like graph to that used for bounce. As observed in the bounce direction, there is a large variation in properties between samples of differing designs, as well as differing linearity trends. In the shear case, all samples show decreasing modulus and increasing loss trends as the excitation magnitude increases. The normalised trends indicate that the changes in properties are much more significant compared to those observed in bounce, with 8-45% increases in loss and 3-17% decreases in modulus. These greater changes produce stronger correlations between the normalised loss and modulus changes and the normalised figure has been annotated to highlight these relationships for differing bond designs. For example, sample 5 shows strong loss factor changes with low modulus variation (A), while sample 8 shows much larger modulus variation for a similar loss factor change (B). Samples 1, 3, 4, 6, 9 and 10 follow the same behaviour (gradient of changes - C), but to different magnitudes of change over the same excitation range. Behaving similarly to these samples, samples 2 and 7 see a slightly increased loss to modulus change ratio (D). Despite observing these differing correlations for various samples, there are no clear associations with design changes.

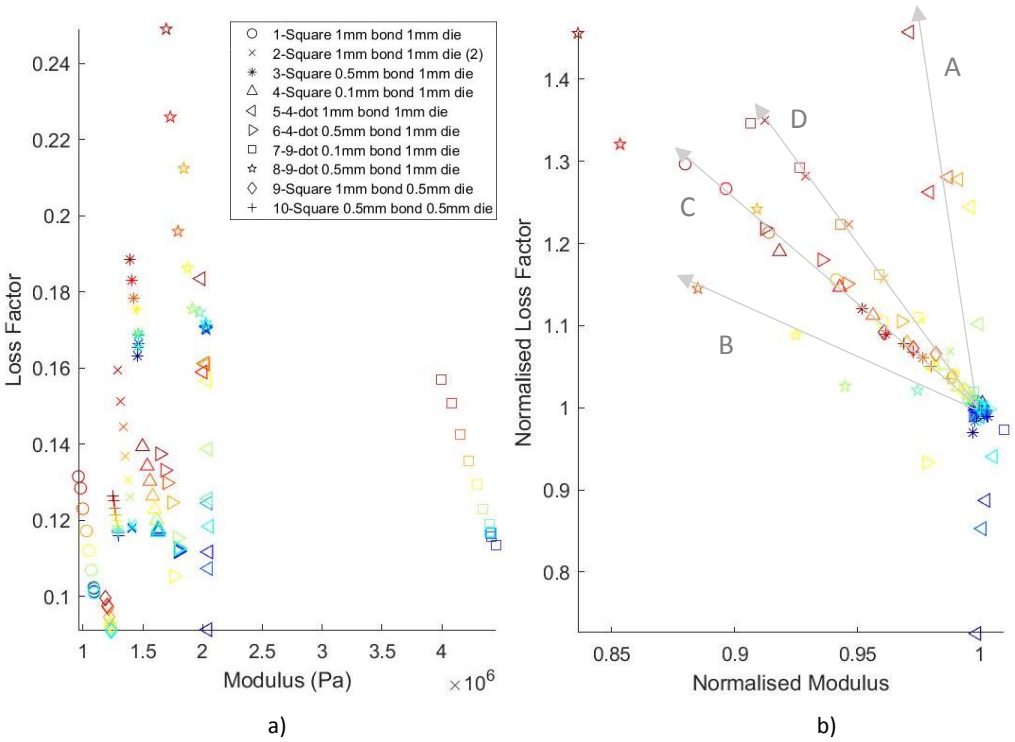
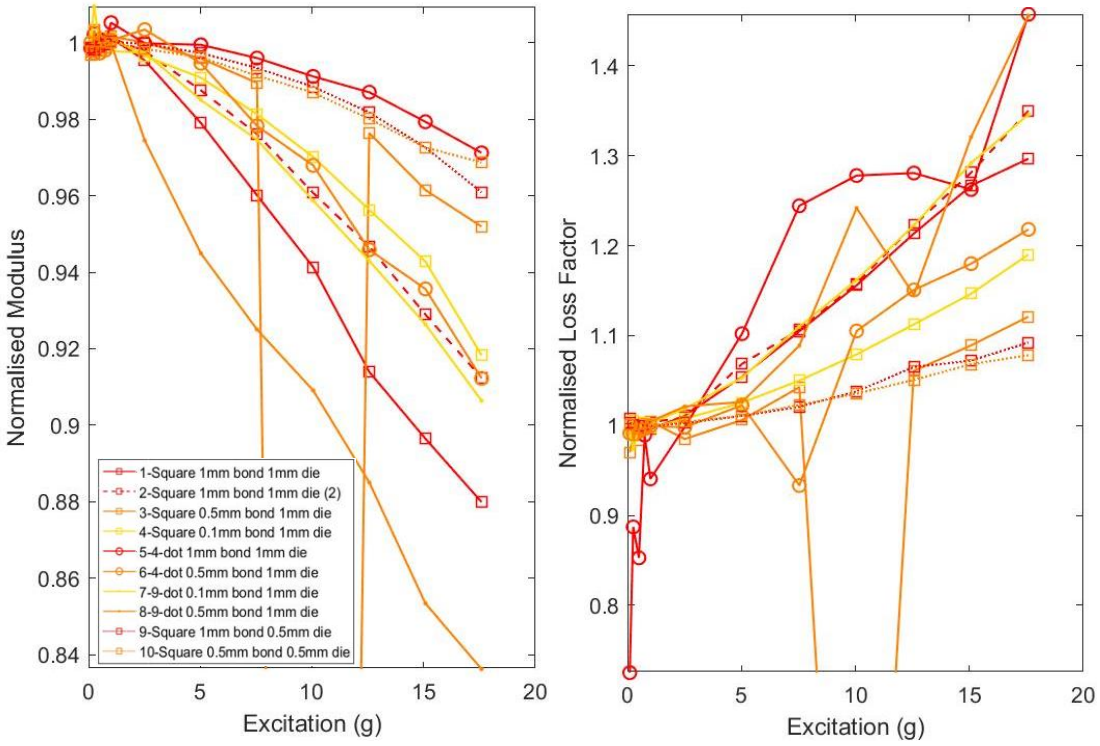


Figure 179 – a) Absolute and b) Normalised Shear Property changes with excitation amplitude (0.1g (blue)-17.6g (red)), A, B, C, and D illustrate differing non-linearity trends observed

Figure 180 shows the individual normalised shear property trends as a function of excitation magnitude. The trends identified previously can be seen clearly in these graphs, with increasing loss and decreasing modulus as excitation increases. These individual property trends allow a few trends associated with effects of sample design parameters to be identified. The samples 9 and 10 utilising the thinner die can be seen to undergo smaller changes in both properties, suggesting a lower level of non-linearity. This is to be expected given that the lower mass in the vibrating system will result in lower amplitudes of motion. Also observed is that two samples with the largest variations experienced in both properties over the excitation range are associated with 9-dot bond shapes, indicating that this bond pattern may be susceptible to larger levels of non-linearity compared to others. However, as mentioned previously, this cannot be proved conclusively due to the varying errors in the calculated properties between different samples.



a) b)

Figure 180 - Individual Normalised shear property trends over excitation magnitude for various bond designs, a) normalised modulus, b) normalised loss factor, normalised using properties within linear range

6.4.1.3. Environmental Temperature

Figure 181 shows the absolute and normalised (to ambient properties) bounce property changes for all tested samples when environmental temperature is change, these are shown in the

same backbone-like plots used in the linearity results, with marker colour defining temperature from -40°C (blue) to 120°C (red). It can be seen in both graphs that as temperature is increased both the modulus and loss decrease. In absolute terms, it can be seen that there is a variation in properties between differing samples as was observed in the linearity and multipoint tests. The normalised plot shows that despite these variations in properties, the changes occurring over temperature are proportional to the property values of that sample, because the trend in the normalised plot is very similar with temperature for all samples. This agreement in normalised changes across the varying bonds and design parameters suggests that the trends over temperature are dominated by the changes in material properties over temperature, which affects all bonds the same, given that they are all composed of the same material. Agreement of the normalised trends between samples is strongest for positive changes in temperature (heating experiments), with greater differences visible for sub-zero temperatures. This could be an indication that certain design parameters can affect the glass transition temperature, leading to earlier/ delayed significant stiffening. However, this can also be explained by the difficulties and greater errors in analysing the cooling tests, due to factors discussed in the trial experiments chapter such as reduced response and poor laser signal due to vapour and condensate in the chamber.

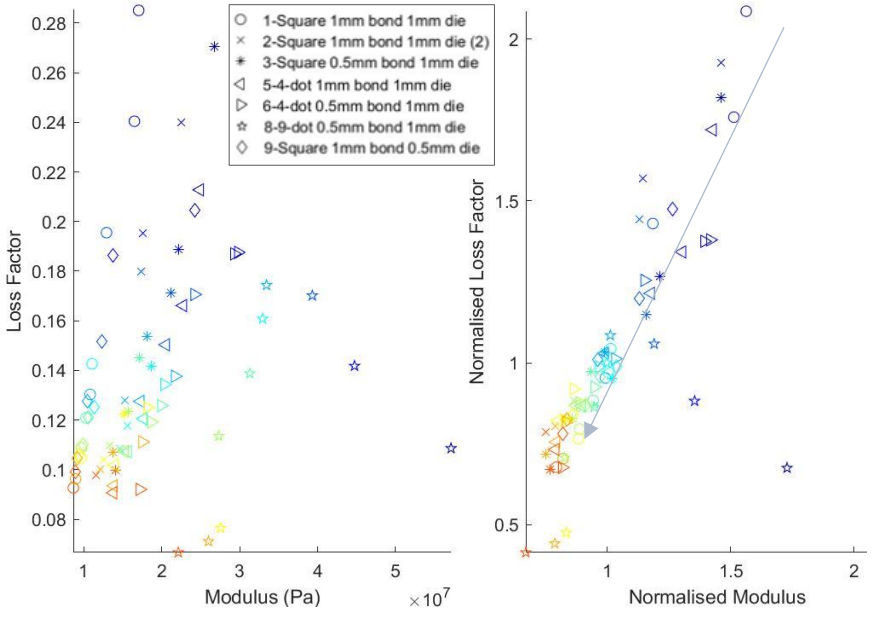


Figure 181 - Backbone style graphs, showing changes in a) absolute and b) normalised (to ambient) bounce properties, modulus against loss factor when environmental temperature is varied (Shown by marker colour from blue to red (-40-120°C))

Figure 182 shows the trends for individual normalised bounce properties, modulus and loss factor, with environmental temperature for various bond designs. These figures confirm the similarity in normalised property changes with temperature observed in Figure 181 and discussed previously. There are no clear differences in the trends observed in Figure 182, which can be associated with design variations, confirming the dominance of the material property changes over temperature. Although it is likely that there are differences due to bond design but have been obscured by the varying errors in the analysis of differing samples.

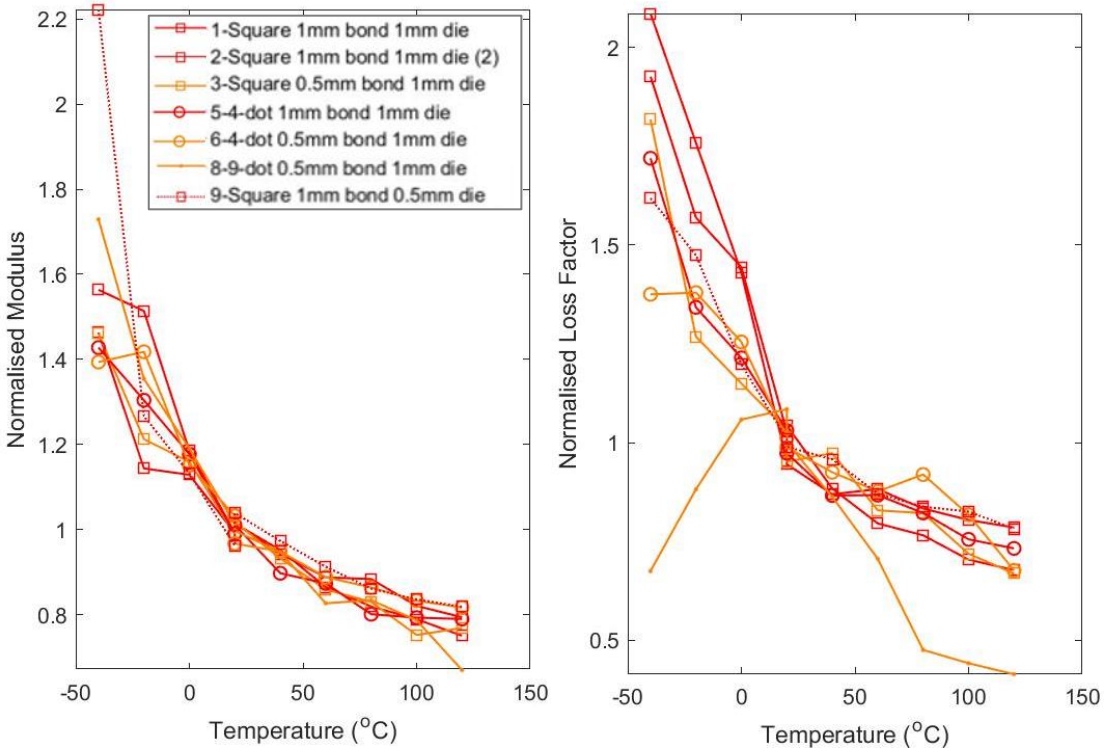
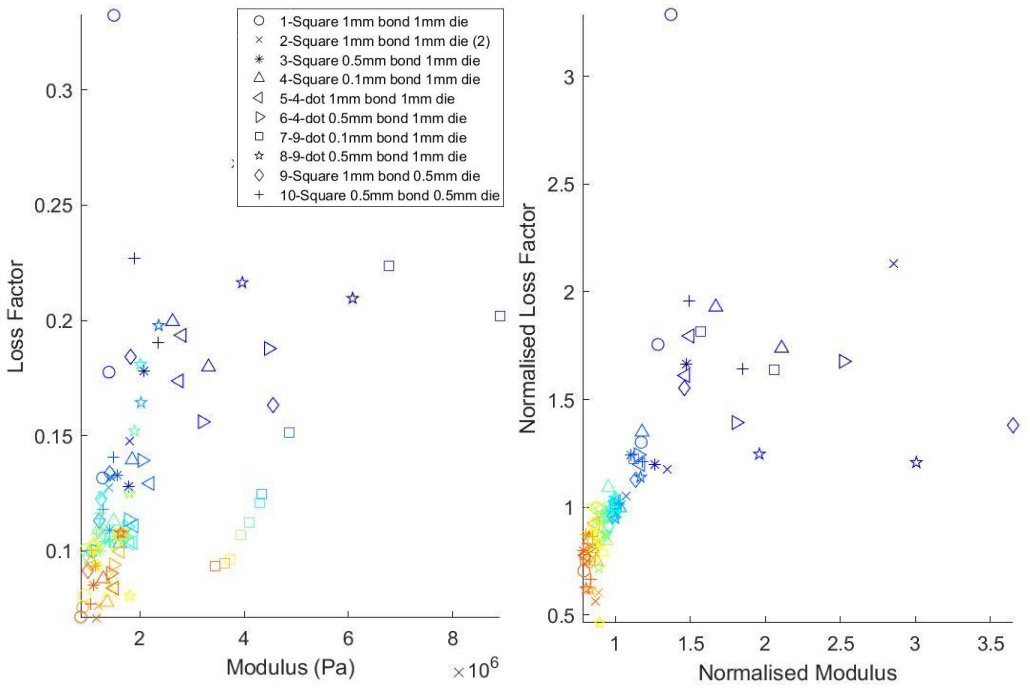


Figure 182 – Normalised (to ambient) bounce property trends over environmental temperature for varying samples, markers denoting bond shapes, colour for bond thickness and dotted lines showing thinner dies, a) normalised modulus, b) normalised loss factor

Figure 183 shows the absolute and normalised shear property trends with environmental temperature, as backbone-like plots of modulus against loss factor. As identified in previous sections the various bond designs have varying properties and trends. However as seen in the initial bounce temperature tests just discussed, the normalised trends are in relatively good agreement across the different bond designs. This gives an indicator that the behaviour over temperature is dominated by the bond material, as opposed to geometrical design parameters.

It can be seen in the normalised plot in Figure 183, that at sub-zero testing temperatures significant shifts in the normalised properties can be seen as well as large variations between samples. The large shifts at -20 and -40°C shows evidence of the bond material approaching or reaching its glass transition temperature. While the variation between samples at these temperatures could indicate different glass transition temperatures or behaviour when this temperature is reached, and that this could be controlled or altered through design parameters of the bond. However, as discussed for the bounce tests, this could also be due, at least in part, to the difficulty in analysing these tests due to signal issues and the lower response observed.



a) b)

Figure 183 - Backbone style graphs, showing changes in a) absolute and b) normalised (to ambient) shear properties, modulus against loss factor when environmental temperature is varied (Shown by marker colour from blue to red (-40-120°C))

Figure 184 shows the same normalised trends displayed in Figure 183, with those lower temperature results omitted, focusing solely on the results at temperatures between 20-120°C. This figure more clearly shows the changes in properties experienced, as well as the agreement between different designs. While slightly differing trends can be observed for various bond designs, no clear or obvious correlations to design parameters can be seen. While this confirms that the material property changes are dominant in the bond property changes, the existence of variation does indicate that the temperature behaviour can be influenced through bond design. However, in the tests conducted here the varying errors across different samples, and experienced at different temperatures, are likely to

have obscured those design effects. These statements are further backed up by the individual shear property trends over temperature shown in Figure 185.

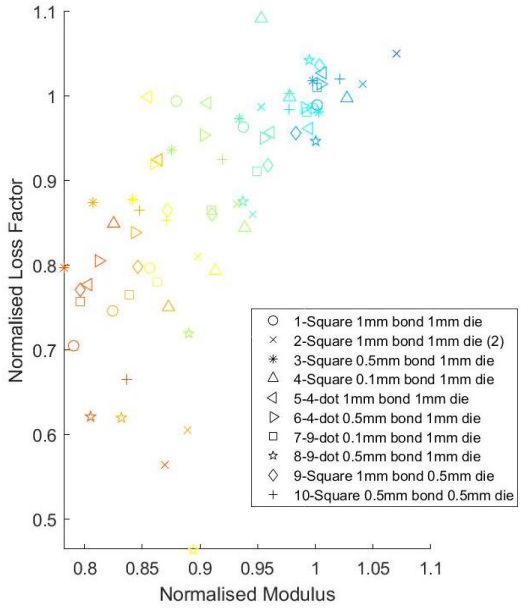
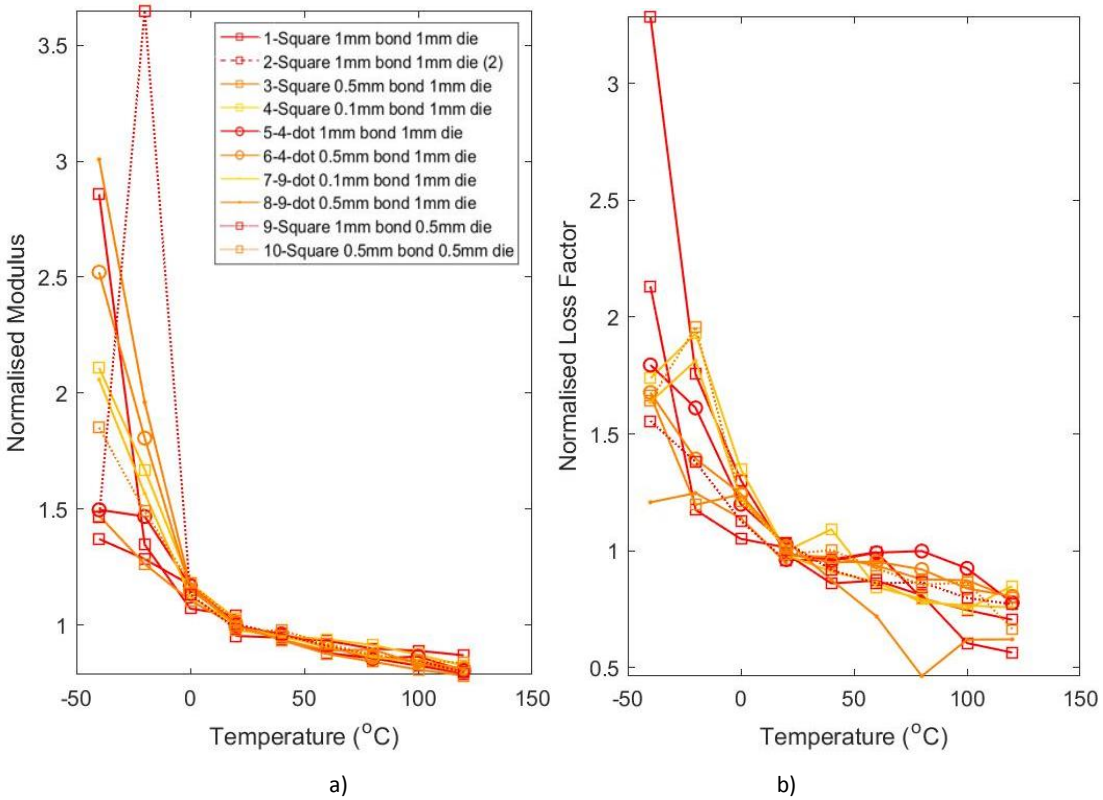


Figure 184 – Normalised (to ambient) Shear property backbone graphs, for environmental temperatures between 20-120°C



a) b)

Figure 185 – Normalised (to ambient) shear property trends over environmental temperature for varying samples, markers denoting bond shapes, colour for bond thickness and dotted lines showing thinner dies, a) normalised modulus, b) normalised loss factor

6.4.2. Sample Changes over Time, Temperature cycling and High Temperature Storage

In this section, the property trends over excitation and temperature over time, 6 linearity trends and 3 temperature trends, will be shown for chosen samples. These trends will be displayed in the same backbone-like curves used throughout the chapter, within these figures it is the general trends between tests that are of concern as opposed to the detailed trends within each specific test over excitation or temperature. Comparison of the normalised changes that occur in the linear/ambient temperature properties over time for differing samples will be shown, with discussions on the possible effects over time and how they may be influenced by various design parameters.

6.4.2.1. Linearity Trends with Excitation Amplitude

Figure 186 shows the bounce property and linearity trend changes between differing linearity tests conducted over time, before and after differing temperature environments, for sample 5. It can be clearly seen that evolution occurs in bond properties over time, and are particularly significant after specific temperature environments. Firstly, it is seen that the properties are relatively stable over the first three linearity tests, which were conducted before any temperature loading, after 1 full temperature cycle (i.e. heating and cooling tests), and then after a further temperature cycle respectively. Between these three tests only small, inconsistent changes in the properties are observed, and while these could be associated with the temperature cycling, they could also be caused by extraneous factors such as differing signal issues causing slight fluctuations in derived properties and their associated errors. However, after these tests significant and consistent changes in the linearity trends can be observed. The differing trends are shown by grey arrows, which highlight the direction of property change with increasing excitation, while the red dashed arrow shows how these trends shift over time.

The most dominant effect observed is a stiffening of the bond with the modulus increasing between each of the remaining linearity tests, with an overall increase of over 2 MPa over the course of the full test regime. The significant shifts (L3-L5) occur after the bond has been stored at high temperatures for long periods (HTS 1+2), while another shift (L6) is seen after a further temperature cycle (T3). Over this same period there is some variation in the loss factor, and the property trends over

excitation. However, these are to a much smaller extent compared to the stiffening observed. Sample 5 has been shown here as an example due to its clear trends for all of the linearity tests conducted. However, the dominant modulus shifts are seen for the majority of samples in bounce between L3-L5, before and after the high temperature storages. The further shift after more temperature cycling is observed in some but not all samples.

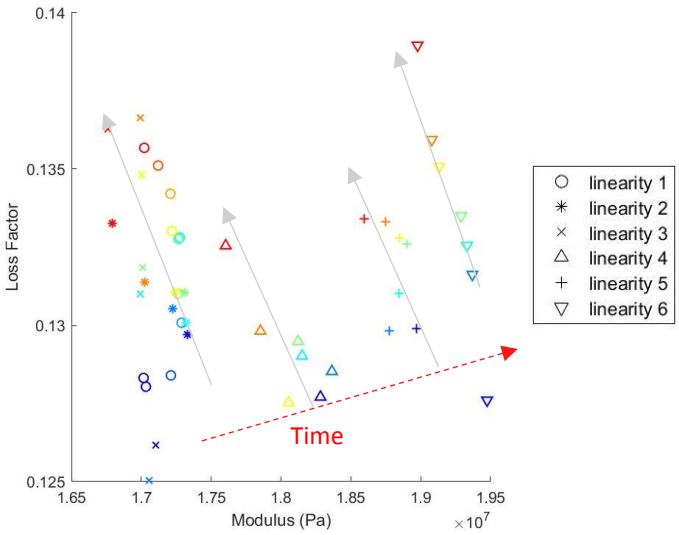


Figure 186 – Linearity trends over time for sample 5 in bounce

Figure 187 shows the shear property and linearity trend changes between differing linearity tests conducted over time, before and after differing temperature environments, for multiple samples. The stronger trends with excitation magnitude, observed in shear compared to bounce and discussed in the initial linearity trend Section 6.4.1.2, allow for greater clarity of the property changes occurring over time for a greater number of samples. It can be seen, in the shown examples, that similar significant shifts in modulus occurs over time, as described for the bounce case. There is large stiffening of all of the tested bonds between L3-L5 tests, during which the samples were subjected to long term high temperature storage. Over this same testing period, there are some changes in the loss factor and the property changes over the excitation ranges. However as mentioned in the bounce case, these are not as significant as the modulus changes and are not consistent across all of the samples. The plot for sample 9 shown in the figure, demonstrates similar stiffening before and after temperature cycles, as well as the storage, and this can be seen for samples 8 and 10 also (not shown in the figure). This could be an indication that some bond designs are more susceptible to property changes over time, although clear associations with specific design parameters are not observable.

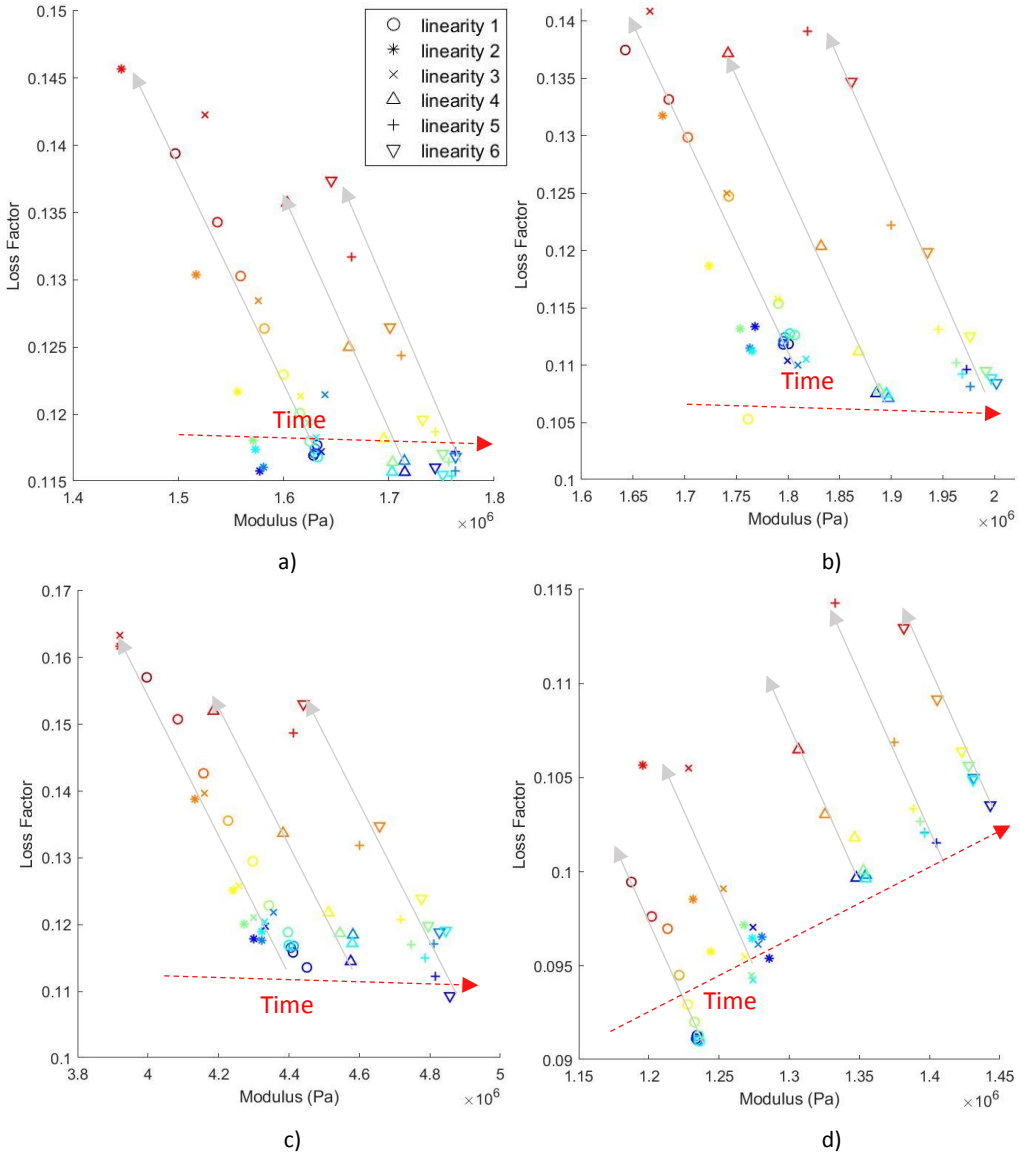
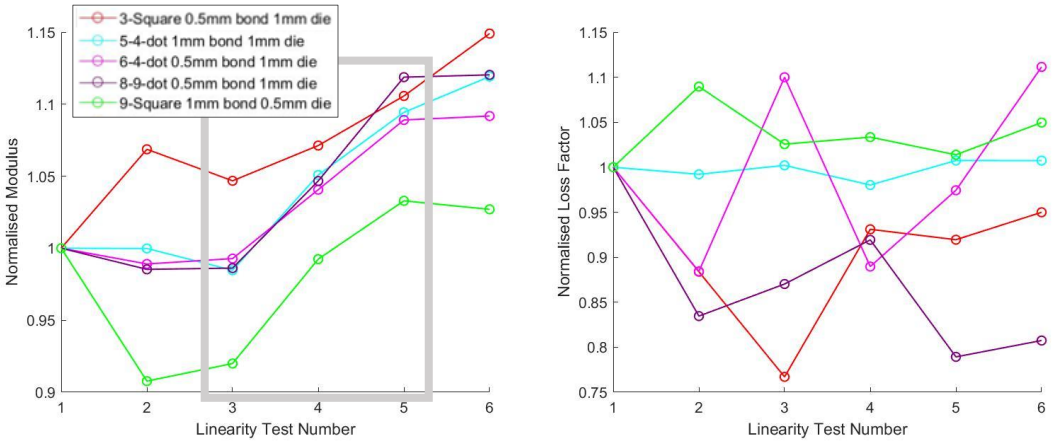


Figure 187 – Linearity Trends over time in shear for samples 4 (a), 6 (b), 7 (c) and 9 (d)

6.4.2.1.1. Linear Properties over time

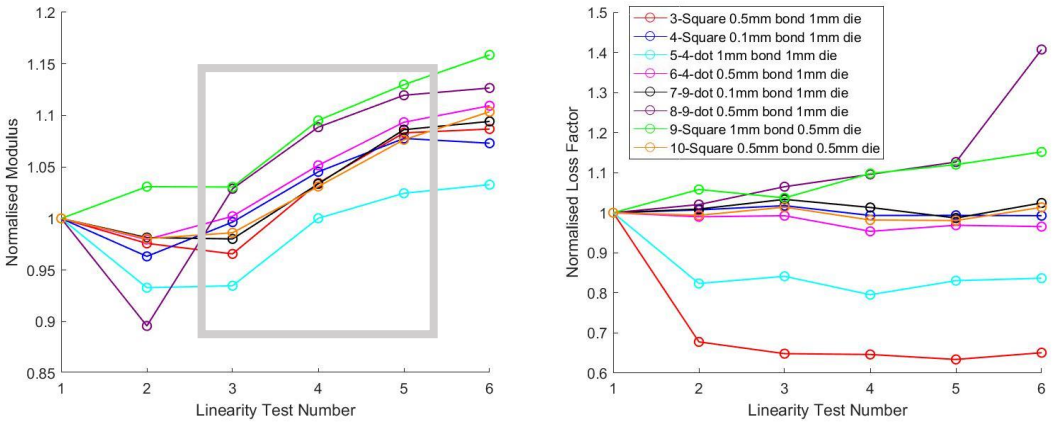
During the analysis process of the linearity tests, linear properties are selected from each trend captured (L1-L6) and significant changes in these properties can be observed over time. Figure 188 and Figure 189 show the normalised linear properties for all samples in bounce and shear respectively against time, where properties are normalised relative to the initial linear property (L1) in each test direction. It can be seen there are large variations in loss factors for all samples, in both directions. However, there is no consistency in these changes either over time or between samples. It is likely that the majority of these variations are caused by the difficulties encountered in the analyses, due to varying errors between samples because of imperfection effects or between tests due to signal problems such as noise and artefacts obscuring peak gains and widths.

However, the stiffening effects discussed in the previous section for high temperature storage of the bonds are observed. These changes are highlighted by the grey box in the figures. During this period of the test regime, it can be seen that the normalised linear modulus increases significantly for all samples and in both testing directions. The results indicate that the apparent moduli, both Young's and shear, are increased by approximately 10% after two phases of storage at elevated temperatures (72 and 145 hours @ 120°C). Interestingly, it appears that the stiffening is relatively constant, with significant shifts in moduli observed after both storage durations. The rate of stiffening is reduced over time, with approximately half the stiffening rate observed in the second storage, with similar stiffening observed but over a duration twice as long.



a) b)

Figure 188 – Normalised (to initial linear properties from test L1) linear bounce properties from linearity tests over time, a) modulus, b) loss factor, grey box highlights the significant stiffening after temperature storage



a) b)

Figure 189 – Normalised (to initial linear properties from test L1) linear shear properties from linearity tests over time, a) modulus, b) loss factor, grey box highlights the significant stiffening after temperature storage

6.4.2.2. Environmental Temperature Trends

Figure 190 shows the bounce property trends over temperature, measured during the three temperature cycling tests conducted over time at various points in the test regime, for samples 5 and 8. In the figure, the plots show the property changes occurring with increasing temperature, with Young's modulus and loss factor both decreasing. Changes in the bond properties over time can also be observed in the plots. The trends for temperature cycles 1 and 2 appear similar. However, a significant shift is seen for temperature cycle 3, which has been conducted after the high temperature storage of the bond samples. The shift in the temperature trend can be seen to be dominated by a modulus increase, echoing the stiffening effect of the HTS environment identified from linearity tests conducted and discussed in the previous section. The example sample trends shown in Figure 190, were chosen due to the clear shifts observable, however all tested samples experience this stiffening effect.

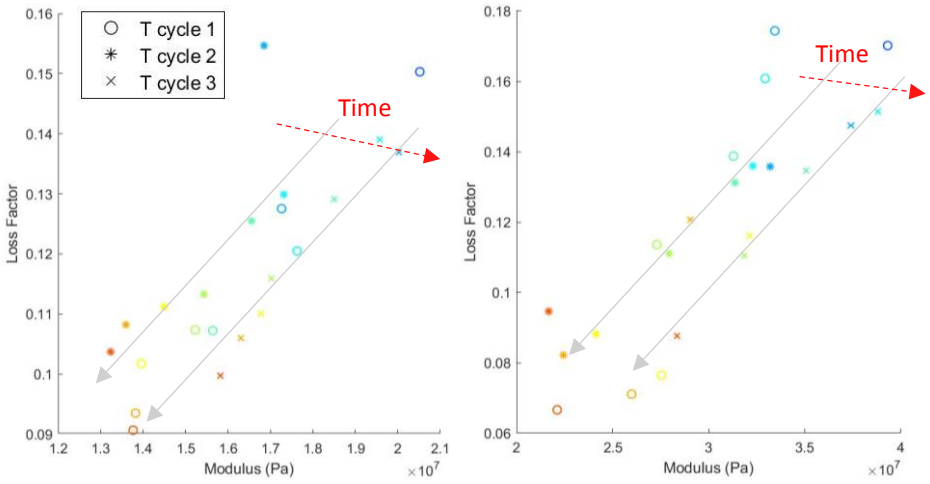


Figure 190 – Temperature Trends over time in bounce for samples 5 (a) and 8 (b)

Figure 191 shows the shear property trends over temperature, measured during the three temperature cycling tests conducted over time at various points in the test regime, for samples 3, 6, 7 and 10. The plots show the loss factor and modulus of the bonds decrease with increasing temperature. The changes in the trends are similar to those described for the bounce properties, with similar trends for cycles 1 and 2, followed by a significant shift in the 3rd cycle after the samples have undergone storage at high temperatures, dominated by an increased modulus. This confirms the stiffening observed in the shear linearity tests after high temperature storage, and mirror the effects seen in bounce tests. Four examples of the shifts are shown in the figure, however all tested samples exhibit this same behaviour.

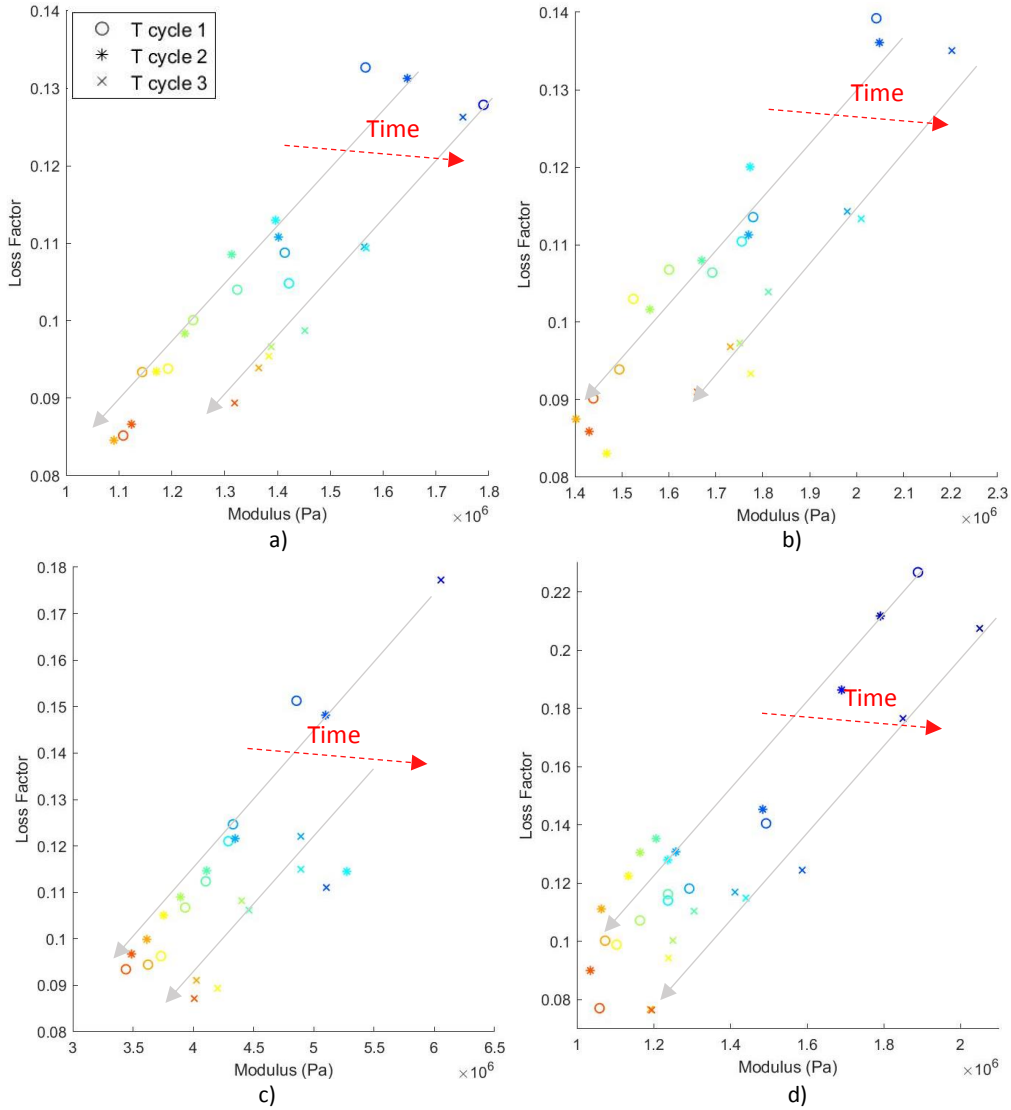
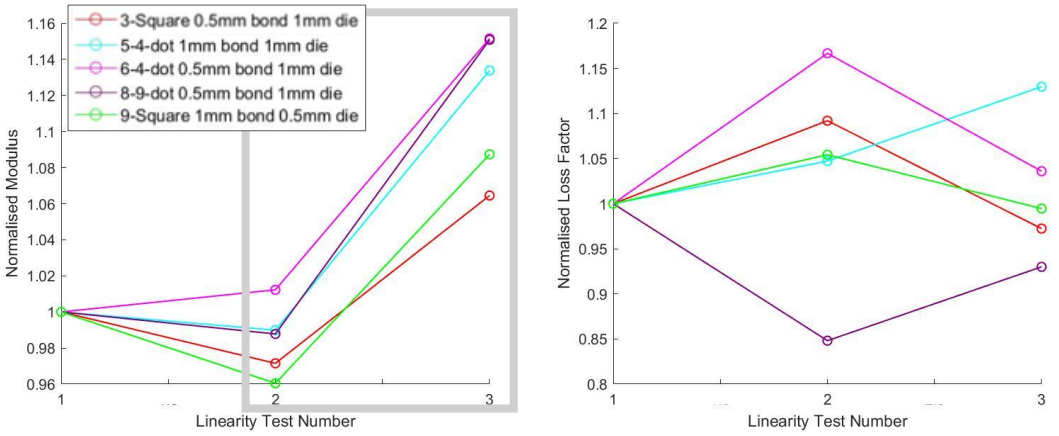


Figure 191 - Temperature Trends over time in shear for samples 3 (a), 6 (b), 7 (c) and 10 (d)

6.4.2.2.1. Ambient Properties over time

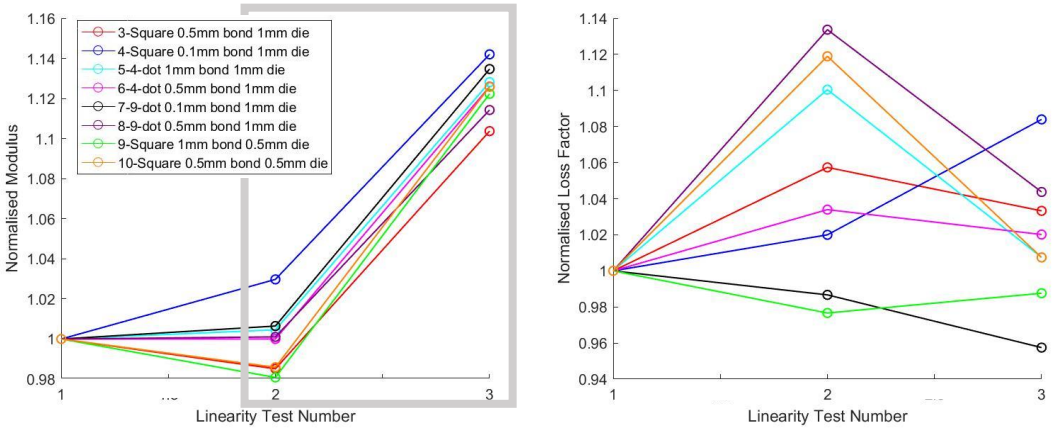
Figure 192 and Figure 193 show the ambient property changes for all samples over time, in bounce and shear respectively. The properties shown were selected from each of the three temperature cycling tests and normalised using the initial measurement, to allow depiction of the relative property changes occurring between each test. While changes occur to the moduli after the 1st temperature cycle, in both test directions, there is no consistency between samples, i.e. some experience small increases, while others decrease. There is a significant increase in modulus between the 2nd and 3rd cycles, during which the bonds were subjected to the high temperature storage. This significant stiffening is observed for all samples in both testing directions. In bounce, the increase varies between samples from approximately 10 – 17%, while in shear the change is more consistent across samples at around 13%.

The ambient loss factor is also seen to vary significantly over the three temperature cycles, with its normalised value changing for each sample in both directions, as shown in Figure 192 and Figure 193. The loss factors, unlike the moduli, experience significant changes after the first cycle, with the majority of samples experiencing increases between 4-17% and 2-13% in bounce and shear respectively. It is also seen that the loss factors decrease by similar amounts in the 3rd temperature cycle measurements. Although these trends are observed for the majority of samples, there are exceptions in both cases and the samples that do not follow the described trends are different in each test direction. The final loss factor values suffer from less than ±5% change compared to those measured during the first temperature tests, this is not significant considering the level of variation observed across all the tests. Therefore, it is difficult to conclusively comment on the time dependency of the loss factor and the effect of the thermal environments.



a) b)

Figure 192 – Normalised (to initial from test T1) ambient bounce properties from temperature tests over time, a) modulus, b) loss factor, grey box highlights the significant stiffening after temperature storage



a) b)

Figure 193 – Normalised (to initial from test T1) ambient shear properties from temperature tests over time, a) modulus, b) loss factor, grey box highlights the significant stiffening after temperature storage

6.4.2.3. Die Surface Profile Change

In this section, the changes experienced in the shape/deformation state of the die for each sample due to bonding and due to possible creep mechanisms will be shown, along with comparisons between samples and discussions on the possible effect of various design parameters. The shape changes are determined by following the analysis procedure described in Section 6.2.1.2. Figure 194 shows the difference in the scans before and after the filling process described earlier. It can be seen that the 'bad' measurement points (red), caused by poor reflection from dies surface or when the depth is outside of the defined measurement range, obscures the shape of the surface. However, the shape can be clearly seen after the filling procedure has been conducted, while no detrimental effects can be observed, confirming its effectiveness while not affecting the 'good' measurement points.

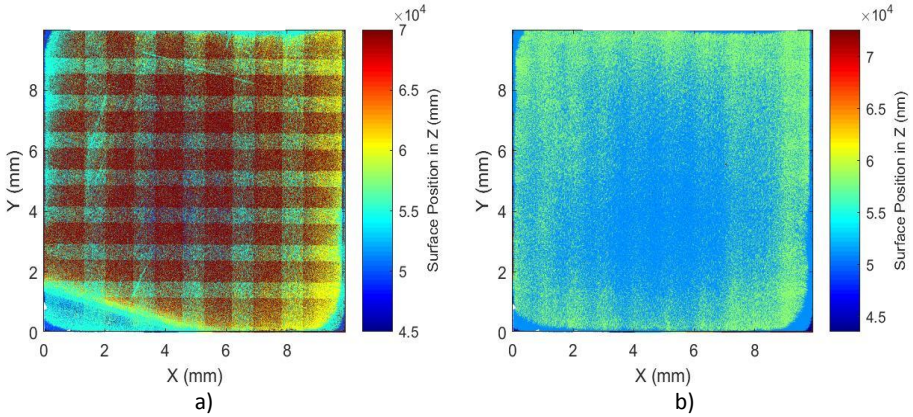


Figure 194 – Example of initial (unbonded) surface scan for sample 1, a) before and b) after filling of bad measurements

Figure 195 shows a 2D profile of the surface measurements, through the centreline of the die, before and after the filling process. These plots confirm the observations made from the contour plots, that the filling procedure has greatly reduced the noise allowing the surface shape to be identified, without affecting the original measurements. However, it can be seen that there is still large levels of residual noise in the data, with a similar magnitude to that of the height variation in the observed shape. This may be reduced further with a greater number of filling iterations (currently 50,000). However, it is clear that there would still be a large level of noise in the data, due to the variation in the 'good' measurement points. This variation is in the order of µm, which is much larger than the advertised nm resolution of the Bruker interferometry system used. Considering the difference in these resolutions, the observed variations could be measurement of the surface roughness, or evidence of further reflection problems of the die surface, as opposed to general test noise in the measurements.

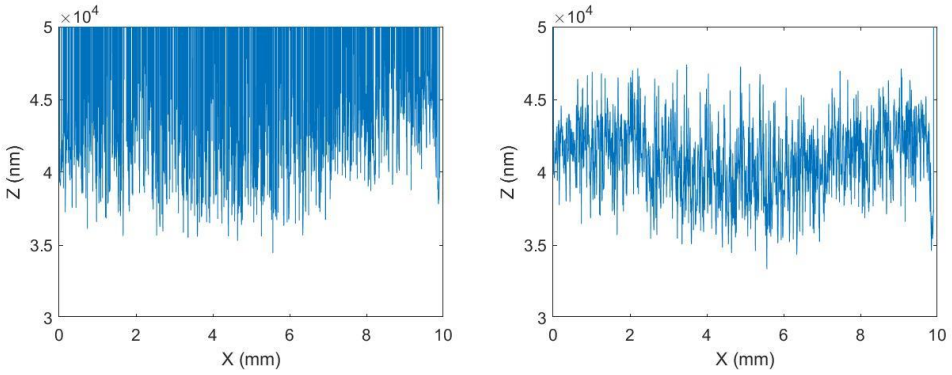


Figure 195 - 2D profile of surface measurements, illustrating noise before (left) and after (right) filling process

The high level of noise present in the profile data will lead to even greater levels in the change of form data, after comparing differing profiles over time. If the noise is caused by surface roughness, it is possible that the variations will cancel. However, this would require perfect alignment of the scans, which is unlikely to such high accuracy. The noise in the change of form plots is too great to observe general changes in the shape, and therefore the plots to be shown in the following sections have undergone further smoothing processes. The final results have undergone smoothing, using a moving average, in 2 dimensions. The moving average uses a small span of 5 neighbouring points (compared to ~2800 across die width), this small span is selected such that any unwanted change, induced by stretching high/low areas, is minimised. This smoothing is performed iteratively (10 iterations) to increase the magnitude of the noise reduction. Use of this further smoothing operation will cause some detrimental effects in the results, reducing the reliability of the absolute scan values, but does allow any general shape changes to be identified and compared.

6.4.2.3.1. Bonding Induced Curvature

Figure 196 shows the smoothed changes to the die's shape after bonding, and it can be seen that there are varying degrees and patterns of possible change occurring across the differing bond designs. Many of these show a concave change such as samples 1, 4, 9 and 10. These samples suggest some expected trends, firstly the concave shape was seen in FE for square bonds for thicknesses greater than 0.1mm, and secondly, that less change occurs for thinner bonds (when comparing 1+4, and 9+10). While others are less clear and more sporadic in their change, such as the saddle like change seen for sample 2. It could be that the significant bond imperfections have affected the patterns of change, as well as the initial shapes of the die being not perfectly flat. The bonding changes shown are large (~600-1200nm), much larger than those observed in FE investigations (~6-80nm).

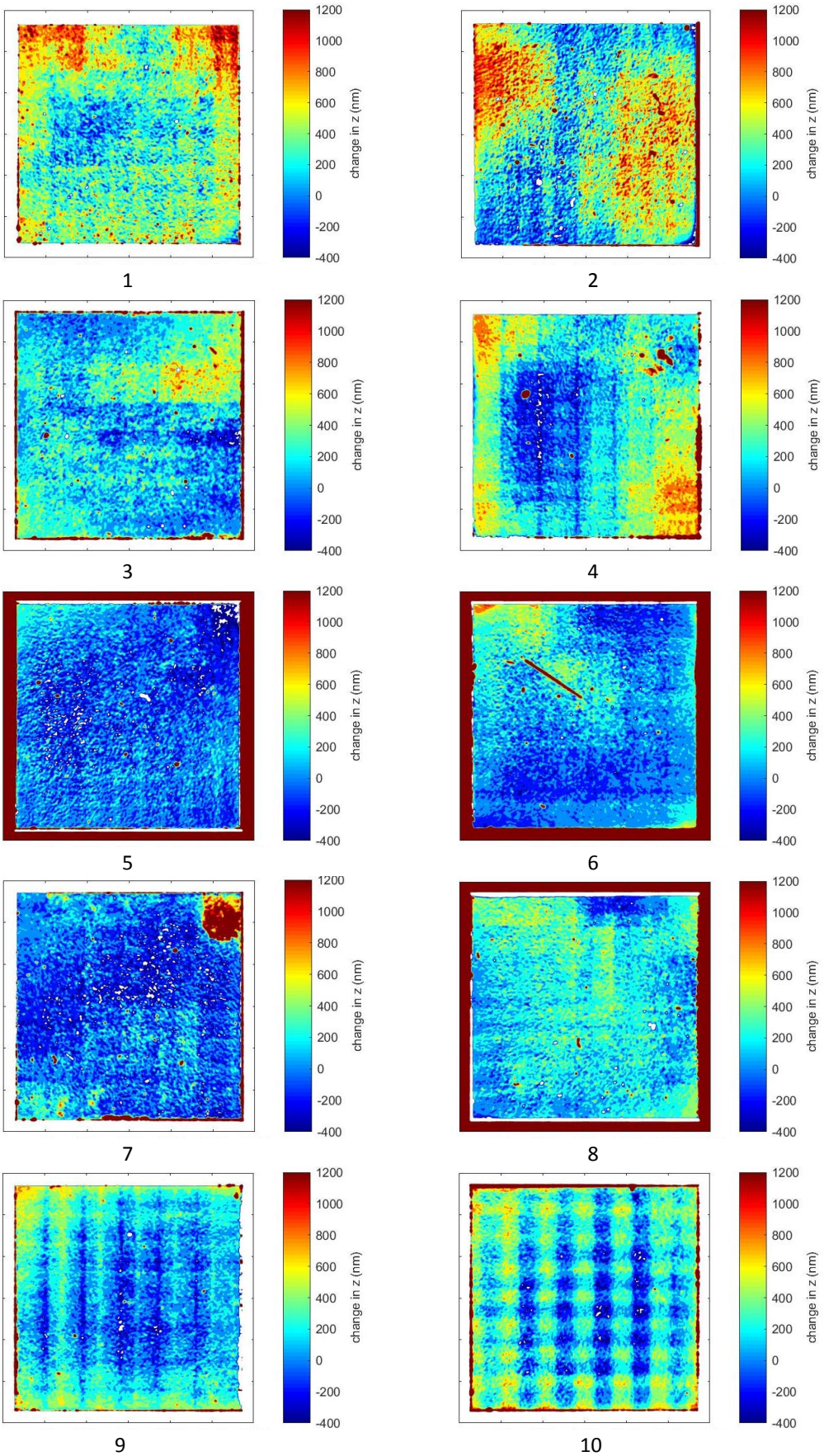


Figure 196 – Change in Die Shape after Bonding for each sample

6.4.2.3.2. Temperature Cycling and High Temperature Storage – Creep

Figure 197 shows the smoothed changes in die shape after high temperature storage. Similar to bonding, there is variation in the magnitudes and patterns of change that occur. Again, there are indications of concave (samples 4, 8, 10) and convex (samples 3, 6) changes, and other more sporadic, non-axisymmetric changes. The changes observed are large, between 600-1200nm, similar to those observed due to bonding. However, there is no clear link between the patterns observed over the two changes. If a creep-like viscoelastic mechanism was occurring, it would be expected that the opposite pattern of change found after bonding, will occur after storage.

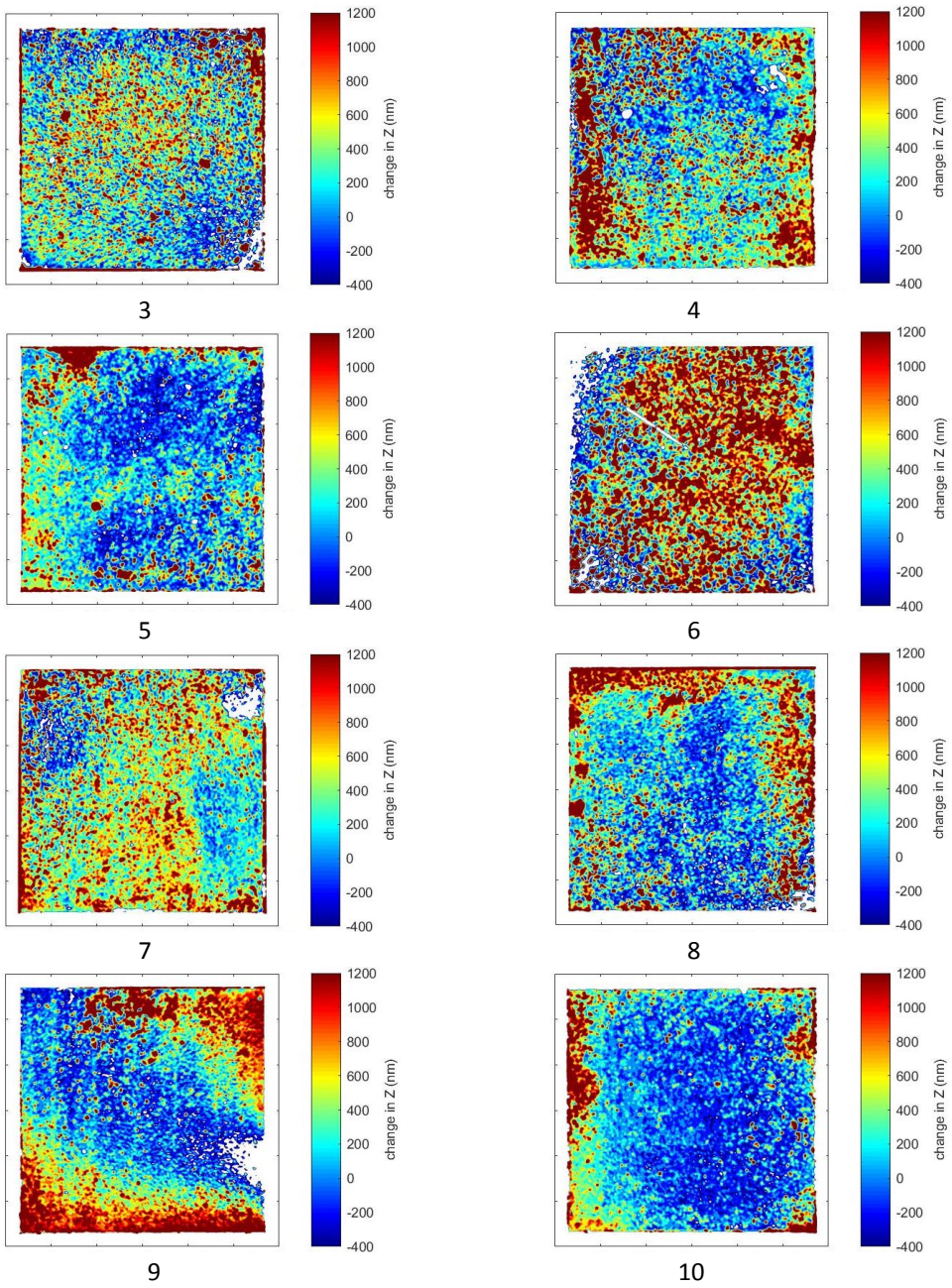


Figure 197 – Change in Die Shape after High Temperature Storage for each sample

The changes observed after storage suffer from more sporadic and localised contour changes, and therefore have suffered from greater problems in measurements, either larger levels of noise or more reflective problems leading to more 'bad' measurements. This is likely to be due to the harsh environments the samples have been exposed to between the two scans (after bonding and after storage). Between the scans the samples have been cycled in temperature multiple times, and during the cooling tests it was seen, and commented on earlier, that the dies have been coated in condensate, which freezes and thaws during and after tests. This has likely affected the die surfaces, with the possibility of oxide layers created sporadically over the surface.

6.5. Conclusions

In this chapter, experimental results and property trends have been shown and discussed for various bond designs over excitation magnitude, temperature and time. In the following sections, the findings will be summarised for characterising bond imperfections, property trends over excitation and temperature, as well as measurement of die shape and how the property trends and die shape evolve over time and after differing thermal environments.

6.5.1. Characterising Bond Imperfections

The frequency responses measured across the dies surface and edge were shown and discussed and it was found that all samples suffer from translational modes contaminated with coupled rotational motions, inferring high levels of imperfections. Comparison of the responses with FE case studies of various imperfections allowed approximate evaluation of the errors associated with each property for each bond design. The estimated errors were large, with modulus errors of 20-30% and 5-20% and loss factor errors of 1% and 0-30% in bounce and shear directions respectively. The large errors and their significant variation between samples makes comparisons difficult and unreliable, leading to difficulties in concluding the effects of individual design parameters.

6.5.2. Linearity

It was seen that changes in the base excitation magnitude leads to consistent trends in the properties of all samples. After a linear response region, indicated and observed by similar derived properties for a range of excitation magnitudes, non-linearity was identified with reducing modulus and

increasing loss experienced when excitation is increased further. These non-linear trends were more evident and significant in the shear direction, with much greater property changes observed over the same tested excitation range. It was observed that the linear regions and the severity of the non-linearity was affected by design parameters, with differing modulus and loss trends observed for differing bonds. Samples incorporating thin dies were seen to experience lower change of properties, and hence have lower non-linearity, due to the lower mass and therefore lower response amplitudes. It was also found that 9-dot bonds experienced among the largest property changes, indicating their susceptibility to significant non-linearity. However, further design effects are difficult to deduce due to the error problems associated with the varying imperfection levels between samples.

6.5.3. Temperature

It was observed that as the environmental temperature was increased the modulus and loss factor reduced for all samples. The normalised property trends showed that these changes were relatively consistent across bond designs, indicating that the temperature dependency is dominated by the temperature dependency of the bond material. However, some variation in the trends were observed, particularly in shear, inferring that the temperature dependency can be altered through design of the bond. There was no clear association of these differing trends with differing design parameters, but these may have been disguised by the varying errors between samples. There were larger trend differences observed for differing bonds at the lowest temperatures, possibly indicating that the bond design could impact the location and effect of the glass transition temperature, although this could also be associated with the greater difficulties in their analysis due to signal problems and the low response.

6.5.4. Property changes over time

Linearity and temperature property trends measured at differing points in the test regime were shown and discussed, and it was found that the changes occurring over the same tested ranges (excitation and temperature) were relatively consistent over time. However, there were significant shifts in the absolute values observed throughout the test regime. After temperature cycles there were small and inconsistent shifts that varied between samples. After high temperature storage, however, large consistent shifts were seen in properties for all samples. These shifts were dominated by an

increase in modulus, representing a stiffening of approximately 10% in both directions. This stiffening was seen over two separate high temperature storages, indicating that this stiffening is continuous. However, the stiffening effect did reduce after the second storage given that its duration was twice as long (similar stiffening was observed after each storage). The stiffening did vary between samples, indicating that it is affected by design. However, no direct links to individual parameters can be drawn due to the varying error issues and the relatively small number of samples. Changes in loss were also observed after thermal cycling and high temperature storage, but these were inconsistent between samples.

6.5.5. Surface Profiles and change over time

Measurements of the die shapes were conducted using white light interferometry, and it was seen that individual surface profiles could be observed at differing stages of the test regime. The analysis procedure for the scan data was evaluated and its ability to fill voids in the data from 'bad' measurements without affecting the shape was confirmed. However, the resolution of the scans were much poorer than expected, with noise/variations across the surfaces in the order of a micron compared to the sub-nanometre resolution advertised by the measurement system. This high noise/variation level could be associated with the surface roughness of the dies or be caused by poor signal/ reflection from the surface. This could be improved through greater control and precision in the dies manufacture. Due to the high levels of noise in the individual scans, changes occurring between scans are obscured, with improvement to the original scans these changes may be seen.

To allow observation of any possible changes occurring in the dies shape over time, 2-dimensional smoothing is used, which is likely to reduce the accuracy and reliability of both absolute values and trends but does allow some indication of changes. Significant changes over time were observed, although they were not consistent across the bond designs. Some samples clearly show concaving of the top surface after bonding, as well as concave and convex changes after high temperature storage. However, many others show more sporadic, unexpected patterns of change, although bond imperfections are likely to significantly affect the patterns observed. Changes after storage are more sporadic or sudden over the surface, which could be signs of surface degradation due to the condensation and freezing experienced during temperature testing.

6.5.6. FE model validation

Some agreements were found between the experimental and FE results, with the bounce frequencies of the square bonds of varying thickness predicted well in FE, the frequency changes over thickness of the 4-dot bonds was also echoed in the FE results but with offsets in absolute values. Differences in the absolute values were seen for all shear mode frequencies, showing that extra stiffening is required in this direction within the FE models. It was hypothesised that this could be due to geometrical effects, inaccurate material properties used in the FE models or slenderness stiffening effects that were not expected in shear. There were also significant differences between the curvature induced after bonding, with corner-centre differences of 5-80nm seen in the FE compared with the 600-1200nm variations measured in scans. However, the FE model is likely to be underestimating the curvature as the cure shrinkage has not been included, and the experimental results may have been significantly affected by the noise and smoothing procedure, as well as the possible surface degradation discussed.

7. Chapter 7: Project Conclusions and Evaluation with Proposed Improvements and Future Work

7.1. Introduction

The packaging of MEMS inertial sensors is an important area of interest for MEMS inertial sensors due to residual stresses and curvature induced in the MEMS structure. Industry has identified the die attach process as a potential area of concern and the possible root cause of performance drifts observed in devices over time and temperature. This study focuses on the design parameters that affect stress development, including bond shape and thickness, as well as, bond material properties, such as moduli, thermal expansion coefficients, their temperature dependence, glass transition temperature and possible viscoelastic behaviour.

7.1.1. Aims

To investigate the changes occurring to an adhesive bond over time and temperature and how these changes are affected by die bond design parameters, the apparent material properties of the bond and the curvatures induced in the die were investigated. Finite Element models and experimental procedures were developed to study bond design effects on the properties of bonds, including time (experiment only) and temperature dependencies. With the aim of providing insights into bond designs that minimise stress and curvature, and provide greater stability of properties over time and temperature.

7.1.2. Methodologies

The project has incorporated a combination of finite element modelling and experimental work to characterise the properties of various bond designs over temperature and time. The bonds investigated consisted of a 10x10x1mm solid, square steel die attached to a rigid base using different designs of slender silicone bond (Dow Corning Q-1225). The thickness of the bond was varied over a nominal range of 0.1-1mm, and the different shapes studied included square, 4-dot and 9-dot configurations. In the FE modelling and experiments, the bonds properties and stress state were

characterised using the translational die modes in bounce and shear directions and die curvature, defined in this project as the vertical height difference between the corner and centre of the die.

An FE model was used to simulate the bonding process, consisting of free thermal expansion of the assembly to the curing temperature of the silicone, at which point rigid constraint of the bonded surfaces was imposed. The assembly was then cooled to ambient temperature inducing curvature of the die due to the stresses developed from the varying contraction rates of the base, bond and die. It should be noted that the curvature in the model is solely caused by the temperature drop from the curing temperature of the constrained assembly, and the cure shrinkage associated with the silicone bond was not modelled. The environmental temperature was varied from -70-150°C at 20°C intervals and the curvature and bounce and shear frequencies recorded. The FE model uses material properties constant over temperature, and so the output trends over temperature are solely caused by geometrical and stress effects, although estimated temperature dependent Young's modulus and variations to key material properties were investigated to observe their effects. Time dependency was not investigated in the FE model.

In the experimental work, the mechanical characterisation of bond properties was achieved through vibration testing, while it was assumed in the analysis that the bond in bounce and shear acted as independent single degree of freedom systems. This assumption allowed the bond to be characterised simply in terms of its apparent modulus and loss factor and provided a simple means of comparison over time and temperature, for the different bond designs.

The transmissibility function was measured across the surface or edge of the sample at multiple points to identify the modes observed in the translation responses of interest and assess the effects of bond imperfection. The modulus and loss factor properties of the bond were determined by analysing the shape and location of the translational mode peak in the transmissibility function. In addition, the bonds were subjected to extensive testing including linearity and temperature tests, where the excitation magnitude and environmental temperature are varied respectively, to observe trends in the bond properties. These tests were repeated over time and before and after storage at high temperature to observe changes in properties caused by temperature cycling and storage. The experimental work also included surface metrology measurements of the same bonded samples. This

involved measuring the shape of the top surface of the die using white light interferometry before and after bonding and after high temperature storage. By comparing the die shape over time, the bonding induced curvature and changes in the curvature due to possible viscoelastic mechanisms after thermal environments were measured.

7.2. Project Work, Outcomes and Evaluation

7.2.1. Finite Element Modelling

7.2.1.1. Development

When investigating the bonding stress using FE modelling it was necessary to develop separate models for the free expansion and bonding as it was observed that large gaps and penetrations were induced at the bond interfaces, leading to erroneous results for the model outputs, when modelled together (utilising the bonding temperature parameter). Extensive interrogation of the model parameters was conducted, including investigation of the contact algorithms and detection methods, contact parameters, symmetry, mesh structure and sizing. It was found that different contact algorithms could be used to achieve the same converged results, but with significantly differing requirements for parameters. It was found that the multi-point constraint (MPC) method provided converged outputs with no control of contact parameters, but was susceptible to overconstraint, which caused errors in the outputs, particularly for the shear mode frequency. To avoid overconstraint, a symmetric quarter model geometry was used.

Differing mesh structures and sizes were investigated and it was found that a contact-sized tetrahedral mesh was the most appropriate. This mesh structure provided the quickest convergence with reducing mesh size, with a good level of convergence achieved for element sizes of 100µm, while greatly reducing the total element numbers compared with part-sized meshes. The element sizes were varied for differing thicknesses of bond, and a ratio of 10 elements across the thickness was used, except when the efficiency of the model was significantly compromised.

7.2.1.2. Environmental Temperature

The translational modal frequencies and the die bow were calculated over the typical operating temperature range of a MEMS inertial sensor. Initially the material properties were kept constant over temperature, and so changes in the model outputs were due to the geometrical changes occurring over temperature. As the temperature reduced, curvature and stresses developed within the assembly caused the bounce and shear mode frequencies to change. The importance of modelling the bonding stresses based on a constrained contraction from the bonding temperature was demonstrated, with significant differences observed in the model outputs and their behaviour over temperature, between pre-stressed and unstressed cases.

7.2.1.3. Material Properties

The Young's modulus, thermal expansion coefficient and Poisson's ratio of the bond material were varied to investigate their effect on the model outputs and their trends over temperature, an estimated temperature dependent Young's modulus was also investigated. These investigations identified beneficial bond material properties for reducing die curvature, as well as the change in curvature and modal properties over temperature. The greatest reduction in die curvature was achieved using a bond with a lower thermal expansion coefficient, and it is thought the curvature will be minimised by matching the thermal expansion of the bond material with that of the adherends (base and die). The curvature can also be reduced significantly by using a low modulus material, where the curvature reduction is directly proportional to the modulus reduction. A lower Poisson's ratio was also found to reduce curvature.

Die curvature and modal frequency change over temperature was dominated by material property temperature dependence, confirming that the thermal stability of the bond properties can be improved by reducing the temperature dependency of the bonds material properties.

When the bond properties are temperature independent, the curvature change over temperature is reduced through the same mechanisms as reducing absolute bow at any given temperature. The most significant reduction in modal frequency change was realised by reducing the thermal expansion coefficient of the bond. This was achieved without affecting the absolute frequency (bond stiffness), and so is more effective than reducing the Young's modulus, which still exhibits the

same normalised change over temperature. Similar to curvature, it is thought that the modal changes will be minimised by matching the thermal expansion coefficients for the bond and adherends.

7.2.1.4. Bond Geometry

The key consideration when changing the bond's geometry is the slenderness or shape factor of the bond, defined as the ratio of the cross-sectional (loaded) area to the force-free area. For bonds having a high shape factor, the constraint of the bonded surfaces leads to stiffer compressive behaviour than expected, leading to the definition of apparent Young's modulus. Empirical relations between material Young's modulus and apparent Young's modulus were discussed in Chapter 5. The apparent modulus of a given bond varies significantly with thickness changing from the material Young's modulus and tending towards the material Bulk modulus. Therefore, in order to accurately model the bond's dynamic and deformation behaviour and it's change with thickness it's mechanical properties must be known to a high level of accuracy, including Young's modulus and Bulk modulus or Poisson's ratio. The rate at which the increase to Bulk modulus occurs is dependent on the bond's shape factor with thickness. Therefore, another requirement for accurate bond modelling is to understand the constraining effects, or shape factor for any given bond shape as a function of thickness.

The importance of Young's modulus on the model outputs was discussed, particularly the stress and curvature developed as the temperature is reduced from the bonding temperature and the resulting effect on the modal frequencies over temperature. The observed significant variation in apparent Young's modulus between differing bond shapes over thickness will have a significant impact on all model outputs and their variation over temperature. This variation was found to be dependent on the shape factor, which in turn is dependent on both the bond shape and thickness, and therefore the effects of these design parameters are strongly linked, making their individual effects difficult to separate without reference to the other. For this reason, their effects are discussed together, focussing on each model output in turn.

7.2.1.4.1. Die Bow

Reducing die bow is a priority when reducing bias and scale factor changes of a MEMS inertial sensor, due to the relative movement and stressing of the MEMS structure. The die curvature varied significantly between bond designs, however the normalised changes over temperature were similar,

and therefore reducing absolute bow will lead to lower changes over temperature. In general, the dotted bonds induce lower levels of bow than the square shape, with the 9-dot lower than the 4-dot for all thicknesses. This indicated that bond discretisation or reducing the bonds shape factor is beneficial for reducing bonding stresses and curvatures, and therefore their changes over temperature and time.

Some bond shapes showed reduced curvature with thickness reductions, particularly square, contrary to most literature, but is an indication of effects observed by Rusanen and Torkkeli, which was attributed to the large thermal expansion mismatch of the bond. It was found that bond discretisation reduced (4-Dot) and eliminated (9-Dot) this effect. The bow reduction observed in the square bond with reducing thickness is extreme with a sign change observed between thicknesses of 0.25 and 0.1mm, indicating a change from concave to convex bow and a thickness at which there is no bow.

In ring-type MEMS gyroscopes, the relative movement of transducers around the ring can lead to quadrature bias. Bow variations around a circular path were investigated, and it was found that the variation is proportional to the absolute bow experienced. The normalised bow variation was relatively consistent across bond shapes and thicknesses. Therefore, reduction of absolute bow, reduces the deformation variation over the die's surface.

In summary, discretised bonds or bonds with lower shape factors are expected to experience fewer performance issues such as zero-g offsets and quadrature bias in MEMS accelerometers and gyroscopes respectively, while also improving the stability of performance metrics over temperature, such as bias and scale factor.

7.2.1.4.2. Bounce Mode

The absolute bounce mode was found to increase non-linearly with thickness reduction, following the increase in apparent Young's modulus due to slenderness stiffening effects. The square bond shape had the highest bounce frequencies, and 9-dot the lowest, as expected given that the square has the largest cross-sectional area as well as the highest apparent modulus at all thicknesses. However, the 4-dot and more so the 9-dot bond shapes experience greater relative change over thickness because of the greater associated percentage change in their apparent moduli.

The bounce mode change over temperature is linear, with the change observed proportional to the absolute value. However, the normalised change occurring over temperature was found to vary with thickness and shape changes. For all bond shapes reducing the thickness leads to an increased percentage change over temperature up to a limiting thickness, after which the normalised change reduced. The changes in normalised change over temperature due to thickness reduction varied between bond shapes, with square experiencing the lowest and 9-dot the highest variations in normalised change (over temperature) as thickness was reduced. Resulting in differing bond shapes experiencing the minimum and maximum normalised change over temperature at each thickness. This can be explained by noting that the temperature change causes the thickness to change and hence bounce frequency to change, resulting in a change in the apparent modulus of the bond. Therefore, the sensitivity of the bounce frequency to temperature change depends on the sensitivity of the apparent modulus to a thickness change. Therefore, to reduce absolute bounce frequency change with temperature, the bond should be designed so that it does not experience significant slenderness stiffening effects. This can be achieved through use of a bond with low shape factor.

7.2.1.4.3. Shear Mode

The shear mode increases non-linearly with reducing thickness, and unlike bounce the shear mode appears unaffected by slenderness stiffening effects as there is no volume change, with the FE results agreeing with theoretical frequency values. As the temperature is reduced the shear mode is seen to reduce non-linearly, with the reduction accelerating for greater temperature changes. This is contrary to the thickness trend. Assuming that a temperature drop would cause a reduction in thickness, it would be expected that the modal frequency would increase. Observing the opposite trend indicates that the stress and curvature induced causes a softening of the bond in shear to overcome the thickness reduction effects.

As there are no slenderness effects, the three bond shapes experience similar relative changes as the thickness is reduced. However, as the bond thickness reduces the non-linearity increases leading to significant changes in the shape of the temperature trend. The level of non-linearity and its rate of increase as thickness is reduced varies for differing bond shapes. The square bond suffers from high non-linearity even for large thicknesses and it does not increase greatly with thickness reductions,

whereas the 4-dot bond has lower non-linearity initially and increases more, this is seen more so for the 9-dot bond. This behaviour again links back to that observed for the apparent modulus changes with reducing thickness for various bonds (slenderness stiffening effects). However, this does not affect the change occurring, as was observed in bounce, but instead the non-linearity of the change occurring.

7.2.2. Vibration Experiments and Analysis

7.2.2.1. Property Analysis

The modulus and loss factor were characterised using transmissibility functions describing the response of the die to base excitation. Bounce and shear directions are excited individually, with die response measurements made in the direction of excitation. The shape, location (frequency) and maximum gain of the modal peak were used to calculate the bond properties, where a single-degree-of-freedom system response was used to analyse the peak based on a Kelvin-Voigt model with hysteretic damping. Apparent Young's and shear modulus values were calculated based on the natural frequencies at which the translational bounce and shear modes occur respectively, using equation (2.2).

Different loss factor calculation methods were developed and used in Chapter 3 and their susceptibility to noise and artefacts and deviation from the assumed SDOF behaviour caused by manufacturing imperfections were investigated. The methods investigated include the inverse transmissibility, the half-power and the averaged multi-power methods, and it was found that the noise induced errors were more significant in the bandwidth methods because the power bandwidth frequencies were adversely affected. However, it was seen that through use of smoothing, in the form of a small span moving average, the errors can be greatly reduced. The inverse transmissibility method was seen to provide improved errors for when noise was present.

It was seen that artefacts, sharp and sudden responses at a single frequency, had differing effects on the different calculation methods, which were dependent on their location relative to the modal peak. A side artefact did not affect the inverse transmissibility method errors. The half-power method was affected with significant error induced, while use of the average multi-power method achieved greater accuracy by choosing a power range to avoid the artefact. The effect of a central artefact was more significant, as it obscured the natural frequency and the maximum gain, leading to

significant errors for all calculation methods. These errors were seen to be greatly reduced for all methods by manually estimating the modal peak location and magnitude.

The trial experiments showed that the translational modes investigated were contaminated by rotational motions, which was hypothesised to be caused by manufacturing and assembly imperfections of the bond and die. Through use of an undamped analytical model, it was shown that an imperfect bond, incorporating an incline, would cause similar coupling and contamination of modes observed in the initial tests.

Various imperfections were created in simple FE models and their resulting frequency response found at various locations on the die, providing qualitative information on how the imperfections affected the response observed. It was seen that the imperfections caused varying gain across different points at the 'translational' mode frequency, while coupled responses were observed at the 'rotational' mode frequencies. In bounce, coupling to rocking was observed, while in shear coupling to twist was seen, and for larger imperfections coupling to the other shear mode is experienced.

The transmissibility functions from these imperfect FE models were analysed and compared to the results for a perfect modelled bond to allow quantitative assessment of the imperfection induced errors. It was seen that for small imperfections, the natural frequency error was small, but for larger imperfections the error became unacceptable. The errors in loss factor were dependent upon the calculation method used. The inverse transmissibility method experienced large, unacceptable errors even for small imperfections and was highly sensitive to measurement position. The averaged multi-power method experienced improved errors in comparison, with small errors for small imperfections, and even for some 1-dimensional large imperfections. For 2-dimensional large imperfections, the errors were significantly increased. This method was relatively insensitive to measurement position.

7.2.2.2. Design Variations and Full Test Regime

Bond samples of varying design, including bond shape, bond thickness and die thickness variations, were subject to vibration testing to observe their characterised property trends over temperature and excitation. The tests were repeated over time and before and after thermal environments to observe any changes in these property trends over time.

Multipoint tests were conducted to identify the translational mode frequencies and to observe and assess any imperfections present in the assemblies. It was found that all samples suffered from contamination of the 'translational' modes and significant coupling, inferring high levels of imperfection. Based on results from the FE imperfection study, approximate errors for the characterised properties were estimated. The estimated errors were large and varied significantly between samples, making comparisons difficult and unreliable. This made it difficult to draw conclusions regarding the effects of individual design parameters.

A testing procedure was developed to investigate and characterise the linear behaviour of bonds and consistent trends were observed for all samples. In the non-linear regime the estimated modulus reduced, and the loss increased as the excitation magnitude increased. The non-linear trends were more significant and observable in the shear direction. The onset and magnitude of the non-linearity varied between samples, indicating the effects of design parameters, while the 9-dot bond samples were among the largest property changes, indicating susceptibility to non-linearity. Further conclusions were obscured by the error implications of the bond imperfections.

A testing procedure for varying the environmental temperature was developed, and it was observed that for increasing temperatures the modulus and loss factor reduced for all samples in both bounce and shear. The normalised property trends were similar across bond designs, indicating the dominance of the temperature dependent properties of the material. There were some variations in property trends, particularly in shear, indicating design effects. However, there were no clear associations with design parameters and are likely obscured by the imperfection errors. There were greater variations between bond designs at the lowest temperatures tested, inferring that the glass transition temperature and its resulting stiffening effect can be altered through bond design. However, it was also seen that cooling tests suffered from increased signal problems such as noise, and low response levels when significant stiffening occurred.

It was found that the linearity and temperature property trends measured over time showed similar changes over the tested ranges. However, shifts in the absolute property values were observed throughout the test regime. After temperature cycling some small shifts were seen, but these were inconsistent and varied between samples. After high temperature storage large consistent property

changes were observed for all samples, dominated by an increase in modulus representing approximately 10% stiffening in both test directions. This stiffening was observed after two separate high temperature storages, although it was observed to slow after the second storage duration. The normalised stiffening that occurred varied between samples, indicating effects of design parameters, but no conclusive trend with given parameters could be drawn. The stiffening was dominated by the material and therefore to significantly reduce time dependency, a bond material with lower or no time dependency must be used. Various changes in loss were also observed after thermal environments, but these were inconsistent between samples.

7.2.3. Die Curvature Measurements

A procedure for measuring the surface curvature of a bonded die using white light interferometry was developed, and analysis processes written. This procedure is theoretically capable of measuring curvatures to nanometre resolution, however, the resolution of the scans was poorer than expected, with significant noise levels exceeding the curvature changes expected to be observed. The cause of this high noise was unknown given the sub-nanometre resolution of the equipment, but it was hypothesised that it could be associated with the surface roughness of the die or be caused by poor reflection from the measured surface. With implementation of die manufacturing methods for improved surface finish, it is thought that greater resolutions will be achieved.

Due to the noise in the individual scans, the changes between scans were obscured. 2-dimensional smoothing was used to provide some indication of changes or patterns of change occurring, although this would likely reduce their accuracy and reliability. The resulting plots indicated that significant inconsistent changes had occurred over time. For some samples concaving was present after bonding, as well as concave and convex changes after high temperature storage, but many showed more sporadic, unexpected patterns of change. The unexpected patterns could be due to bond imperfections, but the sporadic changes tended to occur after testing and high temperature storage and therefore could be an indication of surface degradation occurring due to condensation and freezing experienced during temperature testing.

7.2.4. Comparisons between FE model and Experimental

Comparisons of the ambient temperature modal frequencies found using the FE model and vibration testing were made in Chapter 6. It was found that the bounce mode frequencies and their behaviour with reducing thickness were in good agreement. However, the 4-dot and 9-dot arrangements were found to have significantly higher frequencies in the experimental work. Despite this, the change in frequency of the 4-dot bond with thickness observed in the tests did appear to agree with the FE.

In shear, it was found that all experimental results were higher than those found in the FE modelling. The differences between the model and experimental results were relatively consistent and therefore could be caused by material property differences. Geometrical differences between the bonds modelled and tested could cause the offsets observed, particularly features such as the shape of the bond sides. Another possible cause for the difference is that, despite literature and the FE model saying otherwise, the shear mode is affected by the bond slenderness, leading to the increased frequencies observed in the testing. This would be unexpected due to the lack of a volume change associated with the shear mode shape. However, as the measured mode is not purely translational shear because of the coupling and contaminated motions induced from the imperfections, a volume change may be experienced leading to slenderness stiffening effects. Again, the shear mode frequency behaviour with reducing thickness was in reasonable agreement.

Comparisons of the bonding induced die bow was difficult considering the noise present in the experimental work and the smoothing that was applied. However, some similar deformation patterns were observed (concaving), but the measured values were far greater than those calculated using FE. This discrepancy could be caused by the smoothing itself, or as described for the modal frequencies be due to differences in the bond geometry or material properties, as well as the possible surface degradation observed after cooling tests. Also, the FE model does not incorporate shrinkage of the bond during curing, which could significantly alter the bow values.

7.3. Bond Design for Improved Performance

In this section the key findings relating to the bonds design to reduce performance changes in MEMS inertial sensors are summarised. The bond features described here have been found to reduce die curvature from bonding or the change in bond properties over temperature. A reduced die curvature was also observed to reduce curvature change over temperature, curvature variation in a circular path on the die, as well as over time due to lower scope for viscoelastic mechanisms to occur. It has been established that these effects can lead to performance changes in MEMS inertial sensors.

A low thermal expansion coefficient of the bond material provided the most significant reduction in die curvature from varying the bond material properties, and greatly reduced the percentage change in bond properties over temperature. It is thought that minimisation of performance effects will be gained through approximate matching of the bond and adherends thermal expansion rates. A reduced Young's modulus was also seen to reduce die curvature and absolute bond property change, however was less effective than thermal expansion reduction as the percentage change in bond properties was constant.

Results from experimental and FE work indicated that changes in bow and bond properties over temperature were dominated by the temperature dependency of the bond material properties. While, the changes in modulus observed in experiments after high temperature storage appeared dominated by bond material time dependency, due to the low variation in change observed across differing bond designs. Therefore, time and temperature related performance drifts can be most significantly reduced through the selection of a bond material with lower time and temperature dependencies, i.e. a material that does not suffer from changing modulus over time due to further curing or aging effects.

The 9-Dot bond shape showed the lowest die curvature of the investigated shapes, and it was indicated that further discretisation of the bond would lead to further reductions. To reduce the temperature dependency of the bond properties, the bond should be designed such that it does not experience significant slenderness stiffening effects. To achieve this and the small thicknesses used in MEMS devices a very low shape factor is required and can be achieved through a high perimeter to cross-sectional area ratio of the bond shape.

7.4. Improvements and Future Works

This section suggests and discusses improvements, changes and future works that could be applied to achieve the full aims and objectives of this project. This will include comments on the overall project structure, as well as changes to provide improvements to existing work and suggestions for further investigations.

It is clear that the ability to draw conclusive detailed outcomes was inhibited by the scope of the project, which in hindsight was too broad with too many varying objectives. The project incorporated Finite Element modelling and multiple experimental streams to observe and assess the effects of many design parameters, including considerations of temperature and time dependencies on both static and dynamic outputs. The many varying aspects led to the project becoming highly exploratory, without deep and focussed investigation of a single specific aspect. This was compounded by the lack of established modelling and testing procedures for bonds of the scale investigated, which took significant amounts of time to develop.

The project was designed as it was because of the dependencies between the design parameters of the bond, shape and thickness, and their effects on material behaviour, as well as the relationship between the die curvature and modal frequencies. The project confirmed and highlighted the significance of these relationships. However, to fully achieve the initial aims, it would have been helpful to split the project into separate focussed projects allowing deeper understanding of the effects occurring.

Future work should focus on separate design parameters initially without time dependency to first fully understand the thickness effects of a single bond shape, with more detailed investigation into the stresses developed in the bond and their distribution, as well as the curvatures. This should be followed up with a separate project investigating the effects of alternative bond shapes and their behaviour with thickness. With the changes over time to be considered at a later stage.

7.4.1. Finite Element Modelling

Improvements to the Finite Element model developed within this project are possible with small focussed investigations. Significant improvements would be gained through accurate assessment

of the bond material properties and their change over temperature, in particular for Young's modulus, thermal expansion coefficient and Poisson's ratio. As well as providing accurate properties, insights into material behaviour will be gained allowing a more appropriate material model to be identified and used.

The effect of geometric imperfections between the tested and modelled bonds is another area for further investigation. This could be achieved within the FE model by emulating the manufactured bonds, through detailed inspection, while also investigating the sensitivity of the model to geometry changes. For example, the radii of the square bond corners or of the dots, or the presence of convex curvature of the 'free' sides of the bond.

Inclusion of the cure shrinkage of the silicone bond would provide greater accuracy of the bonding effects and could be applied as an artificial thermal expansion coefficient at the cure temperature. This would increase the curvatures observed in the modelling, improving their agreement with those measured experimentally.

Greater computational capability would enable further mesh refinements to be realised for the bonds currently modelled, providing greater opportunities to achieve convergence for the thinnest bonds. It would also allow greater reductions in thickness to be modelled reliably and efficiently. This would enable the zero-deformation point for the square bond shape to be investigated in detail, along with further investigations to understand why this sign change of curvature occurs. This would provide valuable insights into development of stress-free bonds.

Differing effects and behaviours over temperature were identified between convex and concave die shapes. This should be investigated further to better understand why these differing shapes are induced and the relationship to the design parameters of the bond and its material properties. With understanding of the differing shapes performance effects in MEMS inertial sensors, the design of the MEMS elements can be better informed. This is because the differing die shapes are likely to affect the MEMS element deformation and stressing differently, depending on its designed anchored points for the fixed and moving electrodes.

Investigations having greater focus on the stress, as well as the curvature, and its distribution in the bond would enhance understanding of the changes to the die curvature and translational modes over temperature.

Variation of the bond material properties within the FE model development identified the material properties that significantly affect curvature induced from bonding and the changes occurring to the translational mode frequencies, particularly the thermal expansion mismatch between the bond and adherends. Extension of this investigation to include a wider range of material properties should be investigated, including matching the thermal expansion coefficients for the bond and adherends to provide valuable insight into beneficial bond properties for improved performance stability over temperature, as well as further understanding of the deformations induced in the die due to bonding. This can be further expanded to include bond design variations, including thickness and bond shape, to observe their differing behaviours to bond material changes.

The addition of material time dependency information to the model, through experimental measurement of any viscoelastic behaviours, such as creep and stress relaxation, would provide information on the changing model outputs over time.

The changes observed over time and temperature were found to be caused predominantly by the time and temperature dependencies of the flexible silicone adhesive, therefore other methods for creating flexibility within the bond should be investigated. This should include the design of adherends, either the substrate, the die or both, to include stress isolation structures that are able to deform, in a controlled manner, to accommodate thermal expansion mismatches, allowing rigid adhesives with lower time and temperature dependency to be used.

Finally, the inclusion of detailed MEMS structure and electrostatics in the FE model, such as an accelerometer comb or gyroscope ring structure, would provide direct knowledge of the performance effects of changing bond properties and curvature over time and temperature.

7.4.2. Experimental

The most significant obstacles to fully achieving the aims of the experiments were the manufacturing imperfections present in the samples that affected the die response and property characterisation. Reduction or elimination of these sample imperfections would lead to the greatest

improvements in outcomes from the current project. This can be achieved by either reducing the magnitude of possible imperfections or by reducing their effect.

To reduce the absolute imperfections, greater precision is required in their manufacture. Automation of bond creation can be applied, through precision deposition or using printed or spun bonds, allowing very small thicknesses and complex bond shapes to be created accurately. To ensure there are no die assembly imperfections, the die would also need to be placed mechanically to achieve good positional accuracy.

Larger-scale samples could be used to reduce the effects of any imperfection, and provide larger response in vibration testing, as well as greater curvatures induced by bonding, and changes due to high temperature storage. These larger responses and curvature are more observable and will reduce the significance of the noise observed in the results. While reduction of the die stiffness, through thickness reduction or a lower modulus material can further exaggerate the curvatures experienced. The use of these samples should still be valid and comparable to MEMS scale bonds, as long as the slenderness ratios are maintained.

Changes to the manufacture of the die can also improve the noise and resolution of various results. Through the use of grinding and polishing the surface finish of the die can be improved, reducing roughness and increasing flatness. In turn, noise in both the vibration response and curvature measurements will be reduced due to improved reflection/signal of the laser and white light.

Simple test setup changes can also be made to improve the results. This is primarily concerned with the precision and range capability of equipment, as well as reduction of signal issues such as noise and artefacts. The temperature chamber used is thought to be a cause of noise and artefacts in the results. This included spurious vibrations from the fan and laser signal issues and surface degradation from the vapours and condensate experienced during cooling tests. Use of a sealed chamber, without a fan, in which the coolant and the resulting vapours could not interact with the laser or sample would eliminate these problems.

Changing the electromagnetic shaker and control accelerometer to models capable of higher frequency excitation and measurement (piezoelectric shaker) will increase the capability of the test setup to test and characterise bonds having lower thicknesses. While using a shaker with a greater load

capacity would allow larger excitation magnitudes improving the results and observation of non-linearity and the resulting property trends. A shaker with multiple fixing points on its armature, as well as enhanced fixturing, with measurement of orientation, would improve and ensure more accurate translational excitation with greater alignment to a specified direction. The improvement in the shaker used and the enhanced attachment of the bond sample is also likely to cause a reduction in signal imperfections observed.

Using a laser vibrometer with scanning capability, which measures the response over a specified area would allow automatic assessment of the die mode shapes, and identification of any coupling due to sample imperfection. This function, depending on the size of the capture area, may also enable testing of multiple samples simultaneously, improving the efficiency of the experiments and reducing the time that samples are exposed to potentially harmful environments.

Although investigated thoroughly, further improvements and investigation of property characterisation methods could be conducted. Within this project, the transmissibility function was used to characterise the apparent properties of the bond, using the inverse transmissibility magnitude and bandwidth methods and the behaviour is represented by a single-degree-of-freedom system. However, there are further methods available that were not considered within the scope of this project. For example, the modal circle fit method for calculation of the loss factor, which uses Nyquist response data, while phase data could also be used to identify the natural frequency. Expansion of the analysis model to a multiple degree of freedom system could also enhance the analysis and additional investigations into signal processing techniques could be carried out to reliably and effectively remove signal imperfections from the measured response and excitation signals.

Splitting of the project as suggested at the beginning of this section would lead to shorter test regimes, particularly if time dependency was not considered until a later project. This would enable testing of a far greater number of samples, including repeats and control samples, greatly improving the observability of trends and their reliability.

Further to the experimental improvements discussed, future experimental investigations would provide greater insights into bond design effects, including variation of the bond adhesive and validation experiments for the future FE investigations proposed.

References

[1] S. Y. Bae, K. J. Hayworth, K. Y. S. K. Yee and D. V. Wiberg, “High Performance MEMS Micro-Gyroscope,” in *PROCEEDINGS OF SPIE VOLUME 4755: Design, Test, Integration, and Packaging of MEMS/MOEMS*, 2002.

[2] S. Asokanthan, S. Ariaratnam, J. Cho and T. Wang, “MEMS vibratory angular rate sensors: Stability considerations for design,” *STRUCTURAL CONTROL AND HEALTH MONITORING,* vol. 13, pp. 76-90, 2006.

[3] J. Lau, C. Lee, C. Premachandran and Y. Aibin, Advanced MEMS Packaging, McGraw Hill, 2010.

[4] T. Sethuramalingham and A. Vimalajuliet, “Design of MEMS Based Capacitive Accelerometer,” in *International Conference on Mechanical and Electrical Technology*, Singapore, 2010.

[5] B. Chouvion, S. McWilliam, A. Popov and C. Fox, “Review and comparison of different support loss models for microelectromechanical systems resonators undergoing in-plane vibration,” *Journal of Mechanical engineering science,* vol. 226, pp. 283-295, 2012.

[6] F. Ayazi and K. Najafi, “A HARPSS Polysilicon Vibrting Ring Gyroscope,” *Journal of Microelectromechanical Systems,* vol. 10, no. 2, pp. 169-179, 2001.

[7] S. Wong, C. Fox, S. McWilliam, C. Fell and R. Eley, “A preliminary investigation of thermo-elastic damping in silicon rings,” *Journal of Micromechanics and Microengineering,* vol. 14, pp. 108-113, 2004.

[8] N. Sanatdoost, V. Masek and L. Zhang, “A Z-axis MEMS Gyroscope With Improved Sensitivity,” in *Sensors Applications Symposium, IEEE*, Galveston, TX, 2013.

[9] G. Wua, D. Xu, B. Xiong and Y. Wang, “Effect of air damping on quality factor of bulk mode microresonators,” *Microelectronic Engineering,* vol. 103, pp. 86-91, 2013.

[10] Z. Hua, B. Gallacher, J. Burdess, C. Fell and K. Townsend, “A parametrically amplified MEMS rate gyroscope,” *Sensors and Actuators A: Physical,* vol. 167, pp. 249-260, 2011.

[11] A. Trusov, I. Prikhodko, S. Zotov, A. Schofield and A. Shkel, “Ultra-High Q Silicon Gyroscopes with Interchangeable Rate and Whole Angle Modes of Operation,” in *IEEE Sensors*, 2010.

[12] Y. Xu, R. Wang, S. Durgam, Z. Hao and L. Vahala, “Numerical models and experimental investigation of energy loss mechanisms in SOI-based tuning-fork gyroscopes,” *Sensors and Actuators A: Physical,* vol. 152, pp. 63-74, 2009.

[13] S. Wong, C. Fox and S. McWilliam, “Thermoelastic damping of the in plane vibration of thin silicon rings,” *Journal of Sound and Vibration,* vol. 293, pp. 266-285, 2006.

[14] K. Harish, B. Gallacher, J. Burdess and J. Neasham, “Simple parametric resonance in an electrostatically actuated microelectromechanical gyroscope: Theory and Experiment,” *Journal of Mechanical Engineering Science,* vol. 222, pp. 43-52, 2008.

[15] S. Yoona, S. Leea and K. Najafia, “Vibration sensitivity analysis of MEMS vibratory ring gyroscopes,” *Sensors and Actuators A: Physical,* vol. 171, pp. 163-177, 2011.

[16] B. Gallacher, J. Hedley, J. Burdess, A. Harris, A. Rickard and D. O.King, “Electrostatic correction of structural imperfections present in a microring gyroscope,” *Journal of Microelectromechanical systems,* vol. 14, no. 2, pp. 221-234, 2005.

[17] Silicon Sensing, “Silicon Sensing,” Silicon Sensing, 2014. [Online]. Available: www.siliconsensing.com. [Accessed 06 05 2014].

[18] Y. Dong, P. Zwahlen, A. Nguyen, F. Rudolf and J. Stauffer, “High Performance Inertial Navigation Grade Sigma-Delta MEMS Accelerometer,” in *Position Location and Navigation Symposium (PLANS)*, Indian Wells, CA,, 2010.

[19] H. S. Hsieh, H. C. Chang, C. F. Hu, C. L. Cheng and W. Fang, “A novel stress isolation guard ring design for the improvement of a three axis piezo-resistive accelerometer,” *Journal of Micromechanics and Microengineering,* vol. 21, pp. 1-11, 2011.

[20] Park, Y, S. Park, B. Choi, H. Ko and T. Song, “MEMS Fabricated Accelerometers With Feedback Compensation,” in *Proceedings of the 16th IFAC World Congress*, Czech Republic, 2005.

[21] H. Xuemei and T. Linhong, “Research and Analysis of Bias Voltage on Variable-Capacitance Micro-Mechanical Accelerometer,” in *Intelligent Information Hiding and Multimedia Signal Processing*, Harbin, 2008.

[22] S. Senturia, Microsystem Design, London: Kluwer Academic Publishers, 2001.

[23] T. Juneau, A. Pisano and J. Smith, “Dual Axis Operation of a Micromachined Rate Gyroscope,” in *International conferecnce on Solid State Sensors ad Actuators*, Chicago, 1997.

[24] S. T. Hossain, *Thermoelastic damping and support loss in MEMS ring resonators,* Nottingham: Nottingham University Thesis, 2016.

[25] R. Gerke, MEMS and Microstructures in Aerospace Applications, Chapter 8: MEMS Packaging, CRC Press, 2005.

[26] J. Joo and S. Choa, “Deformation Behaviour of MEMS Gyroscope Sensor Package Subjected to Temperature Change,” in *IEEE Transactions on Components and Packaging Technologies*, 2007.

[27] I. Sadaba, “Residual Stress Effects in Micro-Engineered Sensors,” University of Nottingham, Nottingham, 2004.

[28] A. Malshe, C. O'Neal, S. Singh, W. Brown, W. Eaton and W. Miller, “Challenges in the Packaging of MEMS,” *International Journal of Microcircuits and Electronic Packaging,* vol. 22, no. 3, pp. 233-241, 1999.

[29] X. Chen, W. Cui and W. Xue, “Process Modelling and Device Package Simulation for Optimisation of MEMS Gyroscopes,” *Computer Aided Design and Applications,* vol. 6, no. 3, pp. 375-386, 2009.

[30] C. Liu, H. Chang, H. Liao, K. Li, C. Lin, W. Chen and T. Lin, “Novel Approaches of Wafer level Packaging for MEMS Devices,” in *IEEE 62nd Electronic Components and Technology Conference*, San Diego, CA, 2012.

[31] K. Persson and K. Boustedt, “Fundamental Requirements on MEMS Packaging and Reliability,” in *8th International Symposium on Advanced Packaging Materials, IEEE*, 2002.

[32] B. Kim, R. Melamud, R. Candler, M. Hopcroft and T. Kenny, “MEMS Packaging for Reliable Resonators and Oscillators,” in *IEEE Microwave Symposium*, Montreal, 2012.

[33] S. Walwadkar, P. Farrell, L. Felton and J. Cho, “Effect of Die-Attach Adhesives on the Stress Evolution in MEMS Packaging,” in *International Symposium on MicroElectronics*, Boston, 2003.

[34] X. Zhang, S. Park and M. Judy, “Accurate Assessment of Packaging Stress Effects on MEMS Sensors by Measurement and Sensor-Package Interaction Simulations,” *Journal of MicroElectroMechanical Systems,* vol. 16, no. 3, pp. 639-649, 2007.

[35] B. Wang, “Considerations for MEMS Packaging,” in *High Density Microsystem Design and Packaging and Component Failure Analysis*, Shanghai, 2004.

[36] S. Farrens and S. S, “Wafer Level Packaging: Balancing Device Requirements and Material Properties,” in *Proceedings of Pan Pacific Microelectronics Symposium*, 2008.

[37] G. Li and A. Tseng, “Low Stress Packaging of a Micromachined Accelerometer,” *IEEE Transactions on Electronics Packaging Manufacturing,* vol. 24, pp. 18-25, 2001.

[38] S. Choa, M. Lee and Y. Cho, “Effects of Packaging Induced Stress on MEMS Devices and its Improvements,” *Key Engineering Materials,* Vols. 326-328, pp. 529-532, 2006.

[39] I. Sadaba, F. C and S. McWilliam, “An Investigation of Residual Stress Effects due to the Anodic Bondong of Glass and Silicon in MEMS Fabrication,” *Journal of Applied Mechanics and Materials,* Vols. 5-6, pp. 501-508, 2006.

[40] J. Taweeplengsangsuke, J. Hsiung and R. Pearson, “Modeling the Die Attach Adhesives Process,” in *Symposium on Advanced Packaging Materials*, 1998.

[41] S. Walwadkar and J. Cho, “Evaluation of Die Stress in MEMS Packaging: Experimental and Theoretical Approaches,” *Transactions on Components and Packaging Technologies,* vol. 29, no. 4, pp. 735-742, 2006.

[42] F. Sarvar, D. Hutt and D. Whalley, “Application of Adhesives in MEMS and MOEMS Assembly: A Review,” in *nternational IEEE Conference on Polymers and Adhesives in Microelectronics and Photonics*, Zalaegerszeg, 2002.

[43] T. Koniger, “Highly Flexible Die Attach Adhesives for MEMS Packaging,” in *Microelectronics Packaging Conference (EMPC)* , Grenoble, 2013.

[44] O. Rusanen and A. Torkkeli, “Adhesives as a Thermomechanical Stress Source - Comparing Silicones to Epoxies,” in *Adhesive Joining and Coating Technology in Electronics Manufacturing*, Binghamton, NY, 1998.

[45] C. Lo, O. Yoke, C. Yong and L. Seong, “Assembly Challenges for Low Modulus Die Attach Material for MEMS Devices,” in *Electronics Packaging Technology*, Singapore, 2009.

[46] J. Song, Q. Huang, M. Li and J. Tang, “Effect of Die Bonding on MEMS Device Performance: System Level Modelling and Experimental Verification,” *Journal of MicroElectroMechanical Systems,* vol. 18, no. 2, pp. 274-286, 2009.

[47] T. Marinis and J. Soucy, “Time Lapse Measurements of Stress Relaxation in MEMS Sensor Die Bonds,” in *Electronic Components and Technology Conference*, Reno, NV, 2007.

[48] I. Sadaba, C. Fox and S. McWilliam, “A Study of Residual Stress Effects due to Adhesive Bonding of MEMS Components,” *Journal of Applied Mechanics and Materials,* Vols. 5-6, pp. 493-500, 2006.

[49] D. Farley and A. Dasgupta, “Characterisation of Non-Conductive Adhesives,” in *Thermal, Mechanical and Multiphysics Simulation and Experiments in Micro-Electronics and MicroSystems*, 2005.

[50] T. Marinis, J. Soucy and D. Hanson, “Isolation of MEMS devices from package stresses by use of compliant metal interposers,” in *Electronic Components and Technology Conference*, San Diego, 2006.

[51] J. Song, J. Tang and Q. Huang, “Effect of Die Bonding on MEMS Characteristics; Cell Library Study,” in *Electronic Packaging Technilogy*, Shenzhen, 2005.

[52] Y. Shang, J. Wang, D. Chen, Q. Shi and G. Li, “Closed-loop Control of a SOI-MEMS Resonant Accelerometer with Electromagnetic Excitation,” *Key Engineering Materials ,* vol. 503, pp. 211-215, 2012.

[53] J. Song, Q. Huang, M. Li and J. Tang, “Influence of Environmental Temperature on the Dynamic Properties of a Die Attached MEMS Device,” *Microsystem Technlogies,* vol. 15, no. 6, pp. 925-932, 2009.

[54] M. Lishchynska, C. O’Mahony, O. Slattery, O. Wittler and H. Walter, “Evaluation of Packaging Effect on MEMS Performance: Simulation and Experimental Study,” *TRANSACTIONS ON ADVANCED PACKAGING,* vol. 30, no. 4, pp. 629-635, 2007.

[55] J. Mehner, V. Kolchuzhin, I. Schmadlak, T. Hauck, G. Li, D. Lin and T. Miller, "The Influence of Packaging Technologies on the Performance of Inertial MEMS Sensors," in *IEEE Transducers*, Denver, CO, 2009.

[56] R. B. L. Hopf, J. Menze, M. Zundel, E. Mazza and A. Ehret, "Experimental and theoretical analyses of the age dependent large strain behaviour of Sylgard 184 (10:1) silicone elastomer," *Mechanical behaviour of biomedical materials,* pp. 425-437, 2016.

[57] E. Tatar, S. Alper and T. Akin, "Effect of Quadrature Error on the Performance of a Fully Decoupled MEMS Gyroscope," in *MEMS*, Cancun, 2011.

[58] D. Ewins, Modal Testing: Theory, practice and application, Baldock, Hertfordshire: Research Studies Press, 2000.

[59] K. McConnell and P. Varoto, Vibration Testing: Theory and Practice, Hoboken: Wiley, 2008.

[60] S. R. S. Inc., *Operating Manual and Programming Reference: Model SR785 Dynamic Signal Analyzer,* Sunnyvale, California: Stanford Research Systems inc., 1998.

[61] C. Beards, Engineering Vibration Analysis with application to Control Systems, Butterworth-Heinemann, 1995.

[62] A. Gent and P. Lindley, "The compression of bonded rubber blocks," *Proceedings of the institution of mechanical engineers,* vol. 173, pp. 111-122, 1959.

[63] J. Horton, G. Tupholme and M. Gover, "Axial loading of bonded rubber blocks," *Journal of applied mechanics,* vol. 69, pp. 835-843, 2002.

[64] A. Gent and E. Meinecke, "Compression, Bending and Shear of Bonded Rubber Blocks," *Polymer engineering and science,* vol. 10, no. 1, pp. 48-53, 1970.

[65] J. Diani, B. Fayolle and P. Gilormini, "A review on the Mullins effect," *European Polymer Journal,* pp. 601-612, 2009.

[66] R. Warley, D. Feke and I. Manas-Zloczower, "Transient Effects in Dynamic Modulus Measurement of silicone Rubber, Part 2: Effect of mean strains and strain history," *Journal of Applied Polymer Science,* vol. 104, pp. 2197-2204, 2007.

[67] G. Papagiannopoulos and G. Hatzigeorgiou, "On the use of the half-power bandwidth method to estimate damping in building structures," *Soild Dynamics and Earthquake Engineering,* vol. 31, pp. 1075-1079, 2011.

[68] ANSYS, Inc., *Contact Technology Guide,* Canonsburg, PA: ANSYS, 2009.

[69] ANSYS, Inc., *Workbench User Guide,* Canonsburg, PA: ANSYS, 2012.